High magnetic field studies of 2DEG in graphene on SiC and at the $LaAlO^3/SrTiO^3$ interface

Yang Ming

Université de Toulouse

THÈSE

En vue de l'obtention du

DOCTORAT DE L'UNIVERSITÉ DE TOULOUSE

Délivré par : *l'Institut National des Sciences Appliquées de Toulouse (INSA de Toulouse)*

Présentée et soutenue le *16/04/2018* **par :**

Ming Yang

High magnetic field studies of 2DEG in graphene on SiC and at the $LaAlO_3/SrTiO_3$ interface

-

Étude des gaz d'électrons bidimensionnels sous champ magnétique intense dans du graphène sur SiC et à l'interface entre les oxydes complexes $LaAlO_3$ et $SrTiO_3$

JURY

Prof. Uli Zeitler	Université Radboud	Rapporteur
Dr. Wilfrid Poirier	Laboratoire National de Métrologie et d'Essais	Rapporteur
Dr. Laetitia Marty	Institut Néel	Examinatrice
Prof. Virginie Serin	Université Paul Sabatier	Examinatrice
Dr. Walter Escoffier	INSA-Toulouse	Examinateur
Dr. Benoit Jouault	Université de Montpellier	Examinateur Invité
Prof. Michel Goiran	Université Paul Sabatier	Directeur de Thèse

---

École doctorale et spécialité :
SDM : Nano-physique, nano-composants, nano-mesures - COP 00

Unité de Recherche :
Laboratoire National des Champs Magnétiques Intenses (UPR 3228)

Directeur(s) de Thèse :
Prof. Michel GOIRAN et *Dr. Mathieu PIERRE*

Rapporteurs :
Prof. Uli Zeitler, *Dr. Wilfrid Poirier*

Acknowledgments

The past three and half years of my PhD study has been the most important period in my life. I am so fortunate to enter the group "Nano-objects and nanostructure semiconductors" as a PhD student in LNCMI and learn from people with different background. I hereby take this chance to express my great gratitude to all the people who have taught, helped and accompanied me throughout the past years.

This thesis is supported by the China Scholarship Council and I would first thank this institution for the financial support during the past years. I shall also thank the director of LNCMI: Geert Rikken for hosting me and supporting my PhD study in the lab.

I would like to express my gratitude to Michel Goiran and Walter Escoffier for their supervision. They are always available whenever I have questions and problems. They have offered continuously support to me without any reserve, not only in work, but also in personal life. I feel extremely lucky to work with them for their patience, kindness, enlightened attitudes and all their other virtues.

I would like also to thank all the members of the jury: Prof. Uli Zeitler, Dr. Wilfrid Poirier, Prof. Virginie Serin, Dr. Laëtitia Marty, Dr. Benoit Jouault for their evaluation on this thesis.

I am grateful to the other members of the group in LNCMI: Mathieu Pierre, Florian Vigneau, Bruno Camargo, Rubi Km and Banan Kerdi for their assistance, tutorial and discussions, with thank to Mathieu for his gentle guidance for sample fabrication, programming and experimental setup. Thank you, Bruno for introducing me to the e-beam lithography and all the advice you gave me. Thank you, Florian for all your help in my professional and personal life. The peaceful atmosphere in the group makes the everyday work easy and joyful.

I would like to thank all my collaborators, especially Prof. Ariando, Dr. Benoit Jauoult, Dr. Alesandro Cresti for their great supports on providing high quality samples, data analysis and discussions. They bring me the most valuable insights and perspectives in physics through the collaboration projects.

I acknowledge the sponsorship from the NEXT project for my visit to Prof. Ariando's lab at National University of Singapore, with special thanks to Dr. Kun Han for teaching me the PLD sample growth and taking care of me during my stay.

I want to thank all the staff members in LNCMI: researches, engineers, technicians and secretaries for their friendliness. All the people have been kind to me and willing to offer generous help whenever I seek for them during the work. I especially want to thank Duncan Maude for his support on the dilution refrigerator and the useful discussion which inspired me a lot.

I also want to thank all the postdocs and PhD students in the lab: Wojciech Tabis, Anatolie Mitioglu, Michael Hartman, Siham Benhabib, Alessandro Surrente, Miyata Atsuhiko, Armelle Poux, Stefano Scotto, Krzysztof Galkowski, Zhuo Yang

and Nan Zhang for the happy hours together in work and outside work.

Finally, I would like to thank my family, especially my wife Mengmeng Qi, my parents and parents in law, for their love, understanding, trust and supports.

Contents

Introduction **1**

1 Two-Dimensional Electron Gas system **3**
1.1 Two-Dimensional Electron Gas . . . 3
1.2 Electronic properties and transport in 2DEG . . . 4
1.2.1 Free electron model . . . 4
1.2.2 Boltzmann transport equation . . . 8
1.2.3 Quantum corrections to classical transport . . . 13
1.3 Landau level quantization . . . 16
1.3.1 Landau levels . . . 16
1.3.2 Landau level degeneracy . . . 17
1.3.3 Landau level broadening . . . 18
1.3.4 Shubnikov-de Haas oscillations . . . 20
1.4 The quantum Hall effect . . . 22
1.4.1 The integer quantum Hall effect . . . 24
1.4.2 Edge states in the quantum Hall regime . . . 24
1.4.3 The breakdown of the quantum Hall effect . . . 25
1.4.4 Variable range hopping in the quantum Hall regime . . . 27

2 Experimental techniques **29**
2.1 High magnetic field . . . 29
2.2 The LNCMI facility . . . 30
2.3 Cryogenics . . . 31
2.4 Sample holder and electrical addressing . . . 32
2.5 Transport measurements . . . 34

3 Graphene on SiC **37**
3.1 Introduction to graphene . . . 38
3.1.1 Atomic structure of graphene . . . 38
3.1.2 The Dirac-like energy dispersion . . . 39
3.1.3 The Landau levels of graphene . . . 42
3.1.4 The quantum Hall effect in graphene . . . 43
3.2 Graphene on Silicon Carbide . . . 45
3.2.1 Epitaxial growth of graphene on Silicon Carbide . . . 45
3.2.2 Sample preparation . . . 46
3.2.3 Charge transfer in graphene on Silicon Carbide . . . 47
3.3 Electronic properties of graphene on SiC . . . 49
3.3.1 Temperature dependence at zero magnetic field . . . 49
3.3.2 Longitudinal and Hall resistance in the QH regime . . . 51

3.3.3 Temperature dependence of magneto resistance in the QH regime . . . 53
3.4 Anomalous oscillations of the magnetoresistance . . . 55
3.4.1 Experimental features . . . 55
3.4.2 Temperature dependence . . . 56
3.4.3 The origin of the anomalous oscillations . . . 58
3.5 Model and simulations . . . 59
3.5.1 Charge transfer in inhomogeneous G/SiC . . . 59
3.5.2 Anomalous oscillations and breakdown of the QHE . . . 64
3.6 Quantum Hall effect at low filling factor . . . 65
3.7 Conclusion . . . 67

4 The $LaAlO_3/SrTiO_3$ Interface 71
4.1 Introduction to $LaAlO_3/SrTiO_3$ . . . 72
4.1.1 Origin of the 2DEG . . . 74
4.1.2 Electronic band structure . . . 76
4.2 Sample preparation and characterization . . . 79
4.2.1 Sample preparation . . . 79
4.2.2 Resistance vs temperature characteristics . . . 80
4.3 Magneto-transport and electronic properties . . . 81
4.3.1 Monotonous magnetoresistance and Hall effect . . . 81
4.3.2 Shubnikov-de Haas oscillations . . . 83
4.3.3 Discussion . . . 85
4.4 Band structure spectroscopy . . . 92
4.4.1 Gate dependent magneto-transport at sub-Kelvin temperature 93
4.4.2 Effective mass versus carrier density . . . 95
4.4.3 Analysis and model . . . 97
4.4.4 Extension of the experimental results at 55 T and 500 mK . 101
4.5 Conclusion . . . 102

Conclusion 105

A List of works 107

B Résumé de la thèse en français 111
B.1 Gaz d'életons bidimensionnel . . . 111
B.2 Techniques expérimentales . . . 114
B.3 Graphène sur carbure silisium . . . 114
B.4 L'interface entre $LaAlO_3/SrTiO_3$ . . . 123
B.5 Conclusion . . . 133

Bibliography 135

Introduction

Two dimensional electron gas (2DEG) system are attracting significant attentions for fundamental research and electronic applications. The confinement of the electrons allows the emergence of new properties, which are much different from those in bulk conductors. Conventional 2DEG were reported at the Si/SiO_2 interface of semiconductor and in heterostructures AlGaAs/GaAs and related III-V compounds. The transport properties of the 2DEG in silicon-based metal-oxide-semiconductor field-effect transistor (Si-MOSFET) make them the most successful and fundamental element of logic circuit in electronic devices. Driven by the craving for better performance of electronics, vast investigations have been drawn on the study of high mobility 2DEG and consequently new physics have emerged such as the quantum Hall effect. Nowadays the Si-based technology is approaching its ultimate performance limit as the size of each individual transistor is reduced to a few nanometers. At the same time, the ever increasing demand for "big data" requires faster processors and larger storage memories. Scientists and engineers are motivated to look for new type of 2DEG to replace the silicon for future electronic devices in order to meet the information age requirements.

The discovery of graphene by Novoselov and Geim in 2004 has opened up a new research area of true two dimensional crystals which were believed to be not thermodynamically stable. The electronic mobility in graphene was found to reach 10^6 cm^2/Vs when deposited on hexagonal boron nitride (hBN) or suspended. The Dirac-like nature of electrons in graphene gives rise to many exotic transport properties which are rarely or never observed in other systems. However, the use of graphene in logic circuits is impossible due to the lack of band gap which is extremely important for field effect transistor to ensure a large on/off switching ratio. Anyhow, its excellent mechanic, optical and transport properties make it a promising candidate for a broad range of other applications. When graphene is grown on a silicon carbide substrate (SiC), a magnetic field dependent charge transfer from the SiC substrate was reported to increase the carrier density in graphene and to pin the Fermi energy between the zeroth and first Landau levels. This effect gives rise to a broad quantum Hall plateau, making graphene/SiC the perfect candidate for the definition of resistance standard in metrology. Further investigations of this system, and in particular the quantum Hall effect breakdown mechanisms, are thus of primary importance.

Nearly the same time, another new type of high mobility 2DEG at the interface between two complex oxides $LaAlO_3$ and $SrTiO_3$ was discovered and became a focus of many research works. The emergence of new properties, never observed in the two mother bulk compounds, opened new research interests on these systems. The 2DEG at the $LaAlO_3/SrTiO_3$ interface was commonly accepted to rise from the $3d$ orbitals of Ti with strong directional anisotropy compared to the conventional 2DEG at the interface of semiconductor heterostructures (which are composed of

isotropic s or p electron orbitals). The interplay of the broken translation symmetry at the interface, the spin-orbit coupling and the electron-phonon interactions gives rise to a complex band structure at the origin of various properties such as superconductivity, magnetism, spin charge conversion and metal-insulator transitions. Beyond $LaAlO_3/SrTiO_3$, the large family of the ABO_3 perovskite crystals brings a wider range of exotic properties such as ferroelectricity, ferromagnetism, colossal magnetoresistance, and high-temperature superconductivity. The rich physical properties in the complex oxide interfaces make them also promising candidates with multifunction devices. Nowadays, the fine details of the electronic band structure and the origin of its emergent properties are still not fully understood, despite great efforts dedicated to these systems during the past years.

This thesis is devoted to the investigation of the electronic properties of the two aforementioned 2DEG, taking advantage of very high magnetic field (up to 80 T) and low temperature (down to 40 mK). High field magneto-transport constitutes a potent tool to understand the underlying physics and reconstruct the electronic band structure. The thesis is organized as follows.

In chapter 1, I will first give a general introduction of the transport properties from classical and semiclassical approaches, as well as the quantum corrections to the transport in 2DEG. I will also discuss the Landau quantization and the quantum Hall effect in details.

In chapter 2, I describe the experimental details concerning the generation of high magnetic field at the LNCMI faculty of Toulouse, the cryogenic environment and the experimental techniques related to the transport measurement in pulsed magnetic field.

In chapter 3, I will discuss the anomalous quantum Hall effect and its breakdown in graphene/SiC. An introduction concerning the band structure and transport properties of general graphene is firstly given. I later focus on the particular system of graphene/SiC and discuss the high field results. A model developed by our collaborators: Dr. Benoit Jouault and Dr. Alessandro Cresti is described, which fully explains the anomalous transport properties in graphene/SiC.

In chapter 4, the quantum transport of the 2DEG at the $LaAlO_3/SrTiO_3$ interface is discussed. A brief review of the 2DEG at the $LaAlO_3/SrTiO_3$ interface is given: the crystal structure, the origin of 2DEG, the band structure and the effect of spin-orbit coupling. Through analyzing the high field SdH oscillations and Hall effect, I address the role of Rashba effect as well as the link between the mobility and the orbital symmetry. Later, I discuss the back-gate dependence and explain the transport experimental results from theoretical band-structure taking into account the strong spin-orbit coupling effect.

Chapter 1

Two-Dimensional Electron Gas system

Contents

1.1 Two-Dimensional Electron Gas 3
1.2 Electronic properties and transport in 2DEG 4
1.2.1 Free electron model 4
1.2.2 Boltzmann transport equation 8
1.2.3 Quantum corrections to classical transport 13
1.3 Landau level quantization 16
1.3.1 Landau levels 16
1.3.2 Landau level degeneracy 17
1.3.3 Landau level broadening 18
1.3.4 Shubnikov-de Haas oscillations 20
1.4 The quantum Hall effect 22
1.4.1 The integer quantum Hall effect 24
1.4.2 Edge states in the quantum Hall regime 24
1.4.3 The breakdown of the quantum Hall effect 25
1.4.4 Variable range hopping in the quantum Hall regime 27

In this chapter, I will review the electronic properties and transport in 2DEG. I will start with the Drude model and then take into account the distribution function and quantum corrections. Subsequently, the Landau level quantization under high magnetic field is introduced and its effect on the electronic properties is discussed. Finally, a brief introduction to the Quantum Hall effect is presented.

1.1 Two-Dimensional Electron Gas

Two dimensional electron gas (2DEG) has drawn intense attention and continues to receive significant interests since the development of metal-oxide-semiconductor field effect transistor (MOSFET) in the 1960s. The electrons confined in one dimension and can be considered as free in the plane defined by the other two dimensions. In semiconductors the low carrier density goes with a large Fermi wavelength (a few nm) that is close to the confinement size, implying profound modification of

the band-structure. Furthermore, the high mobility achieved in some 2D structures allows a large mean free path which can be of the order of the sample's size.

The first 2DEG was realized in silicon inversion layer in MOSFET [Fowler 1966], which shows a mobility of the order of 10^4 cm^2/Vs [Bishop 1982]. A Si-MOSFET is made of a p-type Si substrate with a SiO_2 layer on top that serves as an insulator between the metallic electrode (gate) and the p-doped Si. In this system, the 2DEG is created at the Si-SiO_2 interface due to the interfacial potential. An applied positive voltage on the metallic gate leads to the formation of an inversion layer. The conductance of the device is strongly affected, allowing the first fundamental ingredient of modern integrated circuits. Later, a higher mobility (up to 10^6 cm^2/Vs) 2DEG was reported in the III-V semiconductor heterostructures such as the interface of AlGaAs/GaAs [Dingle 1974]. Such an extremely high mobility is the result of the separation of the mobile carriers with their parent donors, defining the so-called modulation doping effect [Störmer 1979]. The exploration of these 2DEG systems has revealed novel transport properties which can only be explained in the framework of quantum physics. The most relevant discoveries are the integer quantum Hall effect which was found in Si-MOSFET by Von Klitzing *et al.* in 1980 [Klitzing 1980] and the fractional quantum Hall effect found in AlGaAs/GaAs by Tsui *et al.* in 1982 [Tsui 1982].

1.2 Electronic properties and transport in 2DEG

The electrical conductivity of a conducting material is governed by the motion of the charge carriers, most commonly electrons or/and holes. From the macroscopic manifestation of charge transport, we can try to approach the underneath and fundamental electronic band structure. In the following, I will discuss how the electronic properties translate into the transport properties from different models.

1.2.1 Free electron model

The transport of charges in a material can be described by the Drude model, which was proposed in 1900 by the German physicist Paul Drude. This model is a classical treatment of electrons based on the kinetic theory of gas, neglecting the electron-electron interactions (independent electron approximation) and electron-nuclei interactions (free electron approximation). In this model, the charge carriers (electrons) are regarded as point-like particles and their collective motion in a conductor, under an external electric or magnetic field or a temperature gradient, manifest as a current flow at the macroscopic scale.

Effect of an applied electric field

Let us consider a system of N electrons which are free to move in a conductor of volume V in response to an electric field $\boldsymbol{E}$. They are colliding with the scattering centers (immobile ions, defects). In the absence of electric field, the electrons are

moving randomly and the average velocity is $\langle \boldsymbol{v} \rangle$=0. After applying an electric field and considering the Newton's equation of motion, the electrons will acquire a drift velocity $\boldsymbol{v_d}$ between two collisions. If we define τ as the mean free time between two collisions, the drift velocity $\boldsymbol{v_d}$ writes

$$\boldsymbol{v_d} = -\frac{e\boldsymbol{E}}{m}\tau. \tag{1.1}$$

The current density $\boldsymbol{j}$ is written as

$$\boldsymbol{j} = -ne\boldsymbol{v_d} = \frac{ne^2\tau}{m}\boldsymbol{E} \tag{1.2}$$

where n=N/V is the charge carrier density in the conductor and m is the electron rest mass. The conductivity σ of the conductor is defined as

$$\sigma = \boldsymbol{j}/\boldsymbol{E} = \frac{ne^2\tau}{m} = n\mu e \tag{1.3}$$

where $\mu = \dfrac{e\tau}{m}$ is the mobility in unit of m^2/Vs. The mobility characterizes how quickly electrons move through a conductor, when driven by an external electric field. According to the simple Drude model, the charge transport is proportional to the product of the carrier density (e. g. the number of electrons participating to transport) and their mobility, an intrinsic quantity derived from the mean relaxation time τ. The derivation of τ from first principles is examined in several dedicated models, which go beyond the scope of this oversimplified introduction of the Drude model.

Effect of an applied magnetic field

Classically, the electrons experience the Lorentz force and move in circular orbitals when placed in a uniform magnetic field. The equation of motion with the electron mass m and charge $-e$ is

$$m\frac{d\boldsymbol{v}}{dt} = -e\boldsymbol{v} \times \boldsymbol{B}. \tag{1.4}$$

Let us consider a magnetic field in the $\boldsymbol{z}$-direction $\boldsymbol{B} = (0, 0, B)$. After projection of Eq. 1.4 into the $\boldsymbol{x}$ and $\boldsymbol{y}$ unit vector we end up with a system of coupled differential equations

$$\begin{cases} m\ddot{x} = -eB\dot{y} \\ m\ddot{y} = eB\dot{x} \\ \ddot{z} = 0. \end{cases} \tag{1.5}$$

If we neglect the speed in the $\boldsymbol{z}$ direction ($\dot{\boldsymbol{z}} = \boldsymbol{z} = 0$) the general solution of the

movement of the electron is

$$\begin{cases} x(t) = X - Rcos(\omega_c t + \phi) \\ y(t) = Y + Rsin(\omega_c t + \phi) \end{cases} \tag{1.6}$$

where $\omega_c = \dfrac{eB}{m}$ is the cyclotron angular frequency. From Eq. 1.6, electrons move along a circle of radius $R = \dfrac{v_0}{\omega_c}$ (v_0 is the electron speed at $t = 0$) centered at coordinates (X, Y) while ϕ is a phase term. The magnetic field does not provide (or remove) any energy in the system. Classically, it simply bends the electrons' trajectory into circular orbits without affecting their initial energy.

Classical Hall effect

When electrons are subjected to both electric and magnetic fields, their motion will be the combination of the two motions discussed above. In a finite sized conductor with a fixed current flowing in the $\boldsymbol{x}$ direction and a magnetic field applied in the $\boldsymbol{z}$ direction, the curved motion of electrons gives rise to a charge accumulation at one side (in the $\boldsymbol{y}$ direction) and leaves the other side an opposite charge. This phenomenon is called Hall effect and was discovered by Edwin Hall in 1879. Due to the charge accumulation, a transverse voltage V_H is established, and the resulting electric field $\dfrac{dV_H}{dy}$ will compensate the Lorentz force to prevent the current flow in the $\boldsymbol{y}$ direction (j_y=0) at equilibrium.

Eq. 1.1 is modified as

$$\frac{m\boldsymbol{v}}{\tau} = -e(\boldsymbol{E} + \boldsymbol{v} \times \boldsymbol{B}) \tag{1.7}$$

and its projection onto the $\boldsymbol{x}$ and $\boldsymbol{y}$ unit vectors provide a set of coupled differential equations:

$$\begin{cases} \dfrac{mv_x}{\tau} = -eE_x - ev_y B \\ \dfrac{mv_y}{\tau} = -eE_y + ev_x B. \end{cases} \tag{1.8}$$

Combining Eq. 1.2 and Eq. 1.3 into Eq. 1.8 we obtain

$$\begin{cases} \sigma_0 E_x = j_x + \omega_c \tau j_y \\ \sigma_0 E_y = -\omega_c \tau j_x + j_y \end{cases} \tag{1.9}$$

which can be rewritten in a matrix form:

$$\boldsymbol{E} = \frac{1}{\sigma} \begin{pmatrix} 1 & \omega_c \tau \\ -\omega_c \tau & 1 \end{pmatrix} \boldsymbol{j}. \tag{1.10}$$

We can invert this matrix to obtain *Ohm's law*:

$$\boldsymbol{j} = \boldsymbol{\sigma} \cdot \boldsymbol{E} = \begin{pmatrix} \sigma_{xx} & \sigma_{xy} \\ \sigma_{yx} & \sigma_{yy} \end{pmatrix} \begin{pmatrix} E_x \\ E_y \end{pmatrix}. \tag{1.11}$$

Eq. 1.11 is a generalization of Eq. 1.2 in the presence of magnetic field. The novelty is that the conductivity σ is not a scalar anymore but a $2\times$ 2 matrix, called the conductivity tensor. The structure of the matrix, with equal but opposite off-diagonal components, follows from rotational invariance. The explicit expression for the conductivity tensor is

$$\boldsymbol{\sigma} = \frac{\sigma_0}{1+\omega_c^2\tau^2} \begin{pmatrix} 1 & -\omega_c\tau \\ \omega_c\tau & 1 \end{pmatrix} \tag{1.12}$$

where σ_0 is the Drude conductivity without magnetic field (Eq. 1.3). The off-diagonal terms in the matrix account for the Hall effect: at equilibrium, a current in the $\boldsymbol{x}$ direction is associated with an electric field with a component in the $\boldsymbol{y}$ direction.

The resistivity tensor $\boldsymbol{\rho} = \begin{pmatrix} \rho_{xx} & \rho_{xy} \\ \rho_{yx} & \rho_{yy} \end{pmatrix}$ is defined as the inverse of the conductivity tensor $\boldsymbol{\sigma}$ through the relation $\boldsymbol{\sigma} \cdot \boldsymbol{\rho} = \boldsymbol{I}$ where $\boldsymbol{I}$ is a 2×2 identity matrix. The inversion of the tensor gives important relations between conductivity and resistivity:

$$\begin{aligned} \rho_{xx} &= \frac{\sigma_{xx}}{\sigma_{xx}^2+\sigma_{xy}^2} \Longleftrightarrow \sigma_{xx} = \frac{\rho_{xx}}{\rho_{xx}^2+\rho_{xy}^2} \\ \rho_{xy} &= -\frac{\sigma_{xy}}{\sigma_{xx}^2+\sigma_{xy}^2} \Longleftrightarrow \sigma_{xy} = -\frac{\rho_{xy}}{\rho_{xx}^2+\rho_{xy}^2}. \end{aligned} \tag{1.13}$$

By combining Eq. 1.11 with Eq. 1.13 we obtain

$$\begin{aligned} \rho_{xx} &= \frac{1}{n\mu e} \\ \rho_{xy} &= \frac{\omega_c\tau}{n\mu e}. \end{aligned} \tag{1.14}$$

Alternatively, the transverse resistivity ρ_{xy} is written as

$$\rho_{xy} = \frac{\omega_c\tau}{n\mu e} = \frac{eB}{m}\frac{\tau}{n\mu e} = -\frac{B}{ne} = R_H B \tag{1.15}$$

with $\mathrm{R}_H = -\dfrac{1}{ne}$ is called the Hall coefficient. R_H depends only on the carrier density in a conductor, and is unaffected by other parameters such as the effective mass, the sample geometry or the scattering time. Due to its independence from extrinsic parameters and mobility, the Hall effect has become a standard tool to determine the carrier density in electrical conductors.

In 2D, the resistivity (conductivity) is related to the resistance (conductance)

through the following equations:

$$\begin{aligned} R_{xx} &= \frac{V_{xx}}{I} = \frac{L}{W} \cdot \frac{E_x}{j_x} = \frac{L}{W}\rho_{xx} \\ R_{xy} &= \frac{V_{xy}}{I} = \frac{E_y}{j_x} = \rho_{xy} \end{aligned} \tag{1.16}$$

where L and W are the length and width of the sample, ρ_{xx} and ρ_{xy} are the longitudinal and Hall resistivity respectively.

The Drude model is an oversimplified theory to explain the transport of electrons in metals and semiconductors. It provides an easy way to calculate the carrier density of a conductor with the Hall effect and simply estimates the scattering time in a conductor from the conductivity. However this model predicts no magnetoresistance in contrast with experimental observations. This is because the electrons are treated with a unique drift velocity and the transverse electric field induced by the Hall effect, which exactly compensates the Lorentz force, cancels the curved motion to keep the electrons traveling straightly along the voltage drop. In a real system, the presence of the magnetic field affects the energy dependent scattering time and changes the resistance in a very complicated manner [Fawcett 1964]. Some other failures of the Drude model show in the thermal transport measurements. In the 1920s, Sommerfeld improved the free electron model by introducing the Fermi-Dirac distribution and Pauli exclusion principle of the electrons, which are treated as fermions rather than a gas of free particles [Ashcroft 2010].

1.2.2 Boltzmann transport equation

In the Drude model, all electrons are treated on the same footing and the temperature of the system is not defined. Once the electron's dynamic is known, the macroscopic properties of the whole electron gas are derived by multiplying the extensive parameters by N, the number of electrons. The temperature and the eventual carrier density gradients are not taken into account. To refine the model, a statistical description of the electron gas is required, where the temperature defines the energy distribution of the electrons. We can either use the Boltzmann or the Fermi-Dirac distribution function. The latter derives from a quantum mechanical treatment of fermions which is appropriate for electrons.

Boltzmann transport equation

Let us first define a classical distribution function $f(\boldsymbol{r}, \boldsymbol{p}, t)$ in the phase space with the position $\boldsymbol{r}$ and the momentum $\boldsymbol{p}$ of the electron. The mean number of electrons located within a volume d^3r centered at $\boldsymbol{r}$ and within a momentum volume d^3p centered at $\boldsymbol{p}$ at time t is

$$dN = f(\boldsymbol{r}, \boldsymbol{p}, t) d^3r d^3p. \tag{1.17}$$

The time evolution of the electron system usually comes from two parts. The first part is the drift term under external fields and temperature gradients, which must obey the continuity equation. Indeed the electrons at $f(\boldsymbol{r}, \boldsymbol{p}, t)$ must come from the states of $f(\boldsymbol{r} - d\boldsymbol{r}, \boldsymbol{p} - d\boldsymbol{p}, t - dt)$. We thus have

$$f(\boldsymbol{r}, \boldsymbol{k}, t) = f(\boldsymbol{r} - d\boldsymbol{r}, \boldsymbol{p} - d\boldsymbol{p}, t - dt).$$

The second part is the effect of electron collisions, which break the continuity flow in the system. If we write this part as $(\frac{\partial f}{\partial t})_{coll}$, then the time evolution of the distribution function becomes

$$f(\boldsymbol{r}, \boldsymbol{p}, t) = f(\boldsymbol{r} - d\boldsymbol{r}, \boldsymbol{p} - d\boldsymbol{p}, t - dt) + (\frac{\partial f}{\partial t})_{coll} dt.$$

We expand the first part in the right-hand side and get

$$f(\boldsymbol{r}, \boldsymbol{p}, t) = f(\boldsymbol{r}, \boldsymbol{p}, t) + [-\frac{\partial f}{\partial t} - \frac{\partial f}{\partial \boldsymbol{r}} \cdot \dot{\boldsymbol{r}} - \frac{\partial f}{\partial \boldsymbol{p}} \cdot \dot{\boldsymbol{p}}]dt + (\frac{\partial f}{\partial t})_{coll} dt.$$

which simplifies into

$$\frac{\partial f}{\partial t} + \frac{\partial f}{\partial \boldsymbol{r}} \cdot \dot{\boldsymbol{r}} + \frac{\partial f}{\partial \boldsymbol{p}} \cdot \dot{\boldsymbol{p}} = (\frac{\partial f}{\partial t})_{coll}.$$

The first term in the left-hand part is the time dependent distribution term. The second and third terms represent the drift components induced by external fields and carrier density gradients. The right-hand part is the collision term (or the scattering term), which relaxes the system back to equilibrium. At stationary state, the distribution function is independent of time so that the first part in the left-hand side is $\frac{\partial f}{\partial t} = 0$. The steady Boltzmann equation follows

$$\dot{\boldsymbol{r}} \cdot \nabla f + \dot{\boldsymbol{p}} \cdot \nabla_p f = (\frac{\partial f}{\partial t})_{coll}. \tag{1.18}$$

Fermi-Dirac distribution in the Boltzmann transport equation

At equilibrium (in the absence of temperature gradients and external fields), the electrons follow the Fermi-Dirac distribution function

$$f(\varepsilon(k)) = \frac{1}{e^{(\varepsilon(k) - \varepsilon_F)/k_B T} + 1} \tag{1.19}$$

where ε_F is the Fermi energy and k_B is the Boltzmann constant. We now introduce the Fermi-Dirac distribution function in to Eq. 1.18. For this propose, the momentum $\boldsymbol{p}$ will be replaced by the wavevector $\boldsymbol{k}$ and Eq. 1.17 is modified into

$$dN = \frac{2}{(2\pi)^3} f(\boldsymbol{r}, \boldsymbol{k}, t) d^3r d^3k \tag{1.20}$$

where the factor $\frac{2}{(2\pi)^3}$ characterizes the quantized k-space volume of $\frac{1}{(2\pi)^3}$ occupied by two electrons of opposite spins. We also use the de Broglie relation $\boldsymbol{F} = \hbar\frac{d\boldsymbol{k}}{dt}$ and $\boldsymbol{v} = \frac{1}{\hbar}\nabla_{\boldsymbol{k}}\varepsilon(\boldsymbol{k})$ to derive the Boltzmann equation with Fermi-Dirac distribution:

$$\frac{1}{\hbar}\mathbf{F}\cdot\nabla_{\boldsymbol{k}}f + \boldsymbol{v}\cdot\nabla f = (\frac{\partial f}{\partial t})_{coll}. \tag{1.21}$$

Electrical conductivity in the relaxation time approximation

In order to solve the Boltzmann equation, we need to have an explicit expression for the collision term. The relaxation time approximation considers that the system will relax towards equilibrium within the relaxation time τ after the external field or temperature gradients are turned off. We assume that the decay to equilibrium follows an exponential time-behavior following the equation

$$\frac{\partial f}{\partial t} = -\frac{f - f_0}{\tau}$$

with the solution

$$f - f_0 = f_1 = f_1(t=0)e^{-\frac{t}{\tau}} \tag{1.22}$$

where f_0 is the equilibrium distribution and f_1 is the deviation of the distribution function from equilibrium, which we assume to be much smaller than f_0. Combining Eq. 1.21 and Eq. 1.22 we have the simplified Boltzmann equation

$$\frac{1}{\hbar}\boldsymbol{F}\cdot\nabla_{\boldsymbol{k}}f_0 + \boldsymbol{v}\cdot\nabla f_0 = -\frac{f_1}{\tau}. \tag{1.23}$$

To calculate the electrical conductivity, we consider the simplest case where a static electric field is applied without thermal gradients, we inject the relations $\frac{1}{\hbar}\nabla_{\boldsymbol{k}}f_0 = \frac{1}{\hbar}\frac{\partial f_0}{\partial\varepsilon}\nabla_{\boldsymbol{k}}(\varepsilon(\boldsymbol{k})) = \boldsymbol{v}\frac{\partial f_0}{\partial\varepsilon}$ and $\nabla f_0 = \frac{\partial f_0}{\partial\varepsilon}\nabla\varepsilon$ into Eq. 1.23 to yield

$$\boldsymbol{F}\cdot\boldsymbol{v}\frac{\partial f_0}{\partial\varepsilon} + \boldsymbol{v}\nabla\frac{\partial f_0}{\partial\varepsilon} = -\frac{f_1}{\tau}. \tag{1.24}$$

Replacing $\boldsymbol{F}$ by $e\boldsymbol{E}$, the out of equilibrium distribution function reads

$$f_1 = e\tau\frac{\partial f_0}{\partial\varepsilon}\boldsymbol{v}\cdot\boldsymbol{E}' \tag{1.25}$$

where $\boldsymbol{E}' = \boldsymbol{E} - (1/e)\nabla\varepsilon_F$ as the effective electrical potential. Since $f(\boldsymbol{k}) = f_0(\boldsymbol{k}) + f_1$ and considering that f_1 is small compared to f_0, we write

$$f(\boldsymbol{k}) = f_0(\boldsymbol{k}) + \frac{e\boldsymbol{E}'\tau}{\hbar}\cdot\frac{\partial f_0}{\partial\boldsymbol{k}} \approx f_0(\boldsymbol{k} + \frac{e\boldsymbol{E}'\tau}{\hbar}).$$

The out of equilibrium state is interpreted as the displacement of the Fermi

surface under external electric field. Since the distribution f_0 at equilibrium state results in no current, the current density is then found from the distribution function $f_1(\boldsymbol{k})$ by calculating of the average value of $\boldsymbol{j} = \langle -ne\boldsymbol{v} \rangle$ over all k-space from Eq. 1.20 and Eq. 1.25:

$$\boldsymbol{j} = -\frac{2e}{(2\pi)^3} \int \boldsymbol{v} f_1 d\boldsymbol{k} = -\frac{2e^2\tau}{(2\pi)^3} \int \boldsymbol{v}\boldsymbol{v} \frac{\partial f_0}{\partial \varepsilon} \boldsymbol{E}' d\boldsymbol{k}. \tag{1.26}$$

Neglecting the diffusion current density so that $\boldsymbol{E}' = \boldsymbol{E}$, we obtain the conductivity tensor

$$\boldsymbol{\sigma} = -\frac{2e^2\tau}{(2\pi)^3} \int \boldsymbol{v}\boldsymbol{v} \frac{\partial f_0}{\partial \varepsilon} d\boldsymbol{k} \tag{1.27}$$

Assuming a parabolic dispersion relation $\varepsilon = \hbar^2 k^2 / 2m^*$ and an isotropic media, so that $\langle v_z^2 \rangle = v^2/3$, the conductivity scalar is obtained after integrating Eq. 1.27 by parts:

$$\sigma = -\frac{2e^2\tau}{3(2\pi)^3 m^*} \int_0^\infty dk 4\pi k^3 \frac{\partial f_0}{\partial k} = \frac{2e^2\tau}{3(2\pi)^3 m^*} (-4\pi k^3 f_0 \mid_0^\infty + 3 \int_0^\infty dk 4\pi k^2 f_0) \tag{1.28}$$

where the first term is zero for $k = 0$ and for $k = \infty$ since $f_0(k \longrightarrow \infty) = 0$. Finally we get the conductivity

$$\sigma = \frac{2e^2\tau}{3(2\pi)^3 m^*} \times 3 \int_0^\infty dk 4\pi k^2 f_0 = \frac{2e^2\tau}{(2\pi)^3 m^*} \times \int_0^\infty f_0 d\boldsymbol{k} = \frac{ne^2\tau}{m^*} \tag{1.29}$$

with $n = [2/(2\pi)^3] \int f_0 d\boldsymbol{k}$ is the electron density. Although this relation is similar to Eq. 1.3 describing the free electron model in the previous section, the physical meaning is quite different. The term $\dfrac{\partial f_0}{\partial \varepsilon}$ in Eq. 1.27 indicates that the transport properties originate only from the electrons at the Fermi level and not from all the electrons in the conductor. Here m^* is the effective mass instead of the bare electron mass, which depends on the material's band structure, and τ is the relaxation time at the Fermi energy. Beyond the relaxation time approximation, the electron scattering is treated using microscopic models (electron-phonon scattering, charged impurity etc.) and the conductivity would depend experimentally on temperature.

From Eq. 1.26, we can write the current density

$$\boldsymbol{j} = \sigma \boldsymbol{E} - \frac{1}{e} \sigma \nabla \varepsilon.$$

The first term is the current density induced by the external electric field, and the second term can be viewed as the diffusion current density. From the Fick's Law $\boldsymbol{j}_{diff} = -eD\nabla n$ and the relation $\nabla n = \nabla \varepsilon \dfrac{dn}{d\varepsilon}$, we obtain the Einstein relation

$$\sigma = e^2 D \frac{dn}{d\varepsilon} = e^2 D g(\varepsilon) \tag{1.30}$$

where D is the diffusion coefficient and $g(\varepsilon)$ is the density of states evaluated at the Fermi level.

Transport equation in low magnetic field

In the free electron model, a conductor shows no magnetoresistance under external magnetic field since the induced Hall field exactly compensates the Lorentz force. This result is a consequence of the assumption that all electrons share the same relaxation time. In a real system, the relaxation time itself is a function of the charge carrier energy, and the conductivity depends on the relaxation time distribution. In a magnetic field, the Lorentz force is introduced in Eq. 1.23 and the simplified Boltzmann equation becomes (neglecting temperature gradient)

$$\frac{e}{\hbar}(\boldsymbol{E}+\boldsymbol{v}\times\boldsymbol{B})\cdot\nabla_k f=-\frac{f_1}{\tau}. \tag{1.31}$$

We can obtain the current density by solving Eq. 1.31 using the similar integration in Eq. 1.26 and project the vector $\boldsymbol{j}$ into the $\boldsymbol{x}$ and $\boldsymbol{y}$ unit vectors:

$$\begin{cases} j_x=\dfrac{ne^2}{m^*}\left(\dfrac{\tau E_x}{1+\omega_c^2\tau^2}-\dfrac{\omega_c\tau^2E_y}{1+\omega_c^2\tau^2}\right) \\ j_y=\dfrac{ne^2}{m^*}\left(\dfrac{\tau E_y}{1+\omega_c^2\tau^2}+\dfrac{\omega_c\tau^2E_x}{1+\omega_c^2\tau^2}\right). \end{cases} \tag{1.32}$$

When the magnetic field is low, *i.e.* $\omega_c\tau\ll 1$, the j_x component can be written as

$$\begin{aligned} j_x&=\frac{ne^2}{m^*}[\tau E_x(1-\omega_c^2\tau^2)-\omega_c\tau^2E_y(1-\omega_c^2\tau^2)] \\ &\approx\frac{ne^2}{m^*}[\tau E_x-\omega_c\tau^2E_y-\omega_c^2\tau^3E_x] \end{aligned} \tag{1.33}$$

neglecting the terms in B greater than second order. For the j_y component, we neglect the $\omega_c^2\tau^2$ terms in the denominator and obtain

$$j_y=\frac{ne^2}{m^*}[\tau E_y+\omega_c\tau^2E_x].$$

At equilibrium, the total current density along the y direction should be 0, thus we get $E_y=-\omega_cE_x\langle\tau^2\rangle/\langle\tau\rangle$ by taking the average over energy. Then the j_x component in Eq. 1.33 becomes

$$j_x=\frac{ne^2E_x}{m^*}\left[\langle\tau\rangle-\omega_c^2\langle\tau^3\rangle+\omega_c^2\frac{\langle\tau^2\rangle^2}{\langle\tau\rangle}\right]$$

and the conductivity is derived as

$$\begin{aligned}\sigma =& \frac{ne^2}{m^*}\langle\tau\rangle - \frac{ne^2}{m^*}\omega_c^2\left[\langle\tau^3\rangle - \frac{\langle\tau^2\rangle^2}{\langle\tau\rangle}\right] \\ =& \sigma_0 - \frac{e^2}{m^{*2}}\sigma_0\left[\frac{\langle\tau^3\rangle\langle\tau\rangle - \langle\tau^2\rangle^2}{\langle\tau\rangle^2}\right]B^2\end{aligned} \tag{1.34}$$

The magneto conductance $\dfrac{\Delta\sigma}{\sigma_0} = \dfrac{\sigma-\sigma_0}{\sigma_0} = -\dfrac{\rho-\rho_0}{\rho_0}$ reads

$$-\frac{\Delta\sigma}{\sigma_0} = \frac{\Delta\rho}{\rho_0} = \frac{e^2}{m^{*2}}\left[\frac{\langle\tau^3\rangle\langle\tau\rangle - \langle\tau^2\rangle^2}{\langle\tau\rangle^2}\right]B^2. \tag{1.35}$$

Eq. 1.35 indicates that in the low magnetic field range, the magnetoresistance displays a quadratic dependence on magnetic field, which has been observed in many metals.

1.2.3 Quantum corrections to classical transport

The conductivity obtained in Eq. 1.29 is a result of a semiclassical treatment, in which the quantum mechanical Fermi-Dirac statistic is taken into account, while the dynamics of the electrons at the Fermi level is assumed to be classical. The temperature dependence of the Drude resistivity $\rho(T) = \dfrac{m^*}{ne^2\tau(T)}$ is found in the temperature dependence of scattering time τ, provide the electron density is assumed constant. In diffusive transport, electrons mainly experience two types of scattering: elastic and inelastic scattering.

Let us discuss, for example, case of non-interacting spin-less electrons in a disordered crystal at non-zero temperature. The main source of inelastic scattering is due to electron-phonon interaction, which is temperature dependent. When the temperature is decreased, the electron-phonon scattering is suppressed, leading to a decrease in the resistivity. At low enough temperature, the residual resistivity is due mainly to elastic scattering (with static impurities or other crystalline defects) and should be temperature-independent in the classical theory. Thus, based on the above discussion we should observe a decrease of resistivity as the temperature decreases followed by a saturation at low temperature ($\sim$ 40 K). However, experimentally it was found that the resistivity starts to rise again at a low temperature. The increase is very small in large samples, but becomes quite pronounced in narrow channels or 2DEG. This anomalous resistivity results from long-range coherence in the diffusive motion of electrons and is linked to the wave-like nature of electrons.

Elastic scattering does not change the energy of electrons, but only change their momentum, making the electrons scatter from a Bloch state $\boldsymbol{k}$ to an equal energy state $\boldsymbol{k}'$ with determined phase shift. In contrast, for inelastic scattering processes, electrons cannot interfere with themselves anymore and therefore the coherence is broken. The electronic transport is coarsely related to the following characteristic lengths: (1) the mean free path l, which is the average distance between two elastic

scattering events; (2) the phase coherence length l_ϕ which is the average distance over which phase coherence is maintained; (3) the sample length L. When the temperature decreases, the inelastic scattering is reduced and the phase coherence length l_ϕ becomes much larger than the mean free length. Therefore electrons will maintain their phase coherence after several elastic scatterings. According to the Feynman path description of diffusion [Feynman 2010], the electrons can move from one point $\boldsymbol{r}$ to another point $\boldsymbol{r}'$ along different trajectories by random walk. The probability P to reach $\boldsymbol{r}'$ from $\boldsymbol{r}$ is given by the square of the sum of all probability amplitudes A_i for each possible trajectory:

$$P = \left|\sum_i A_i\right|^2 = \sum_i |A_i|^2 + \sum_{i \neq j} A_i A_j^*. \tag{1.36}$$

where the probability amplitude A_i contains a phase term $A_i = |A_i| e^{i\varphi_i}$. The first term in Eq.1.36 represents the classical probability for an electron at position $\boldsymbol{r}$ to reach the position $\boldsymbol{r}'$ and the second term is the quantum interference between all possible trajectories.

In most cases, the quantum interference term averages out to zero because of the very large number of different trajectories with uncorrelated phases. However, when the $\boldsymbol{r}$ and $\boldsymbol{r}'$ coordinates are identical (the electron makes a loop), the forward path (probability amplitude A^+) and backward path (probability amplitude A^-) are time reversed. This makes the two paths having the same probability amplitude A and the same phase. The coherent backscattering probability becomes $P(0) = |A^+|^2 + |A^-|^2 + 2A^+A^- = 4|A|^2$, which is twice of the classical probability $2|A|^2$. The enhanced probability for an electron to return to the origin point (coherent backscattering) decreases the diffusion constant and thus decreases the conductivity. This effect has been interpreted as a precursor of localization in strongly disordered systems and has thus become known as weak localization.

The weak localization correction $\Delta\sigma$ to the Drude conductivity σ is proportional to the probability of an electron to return to its origin point. In the two-dimensional case, this probability is $P(0,t) = \dfrac{1}{4\pi D t}$ where D is the diffusion coefficient. The weak localization correction in conductivity can be written as below

$$\Delta\sigma \propto -\int_{\tau_0}^{\tau_\varphi} \frac{dt}{4\pi D t} \tag{1.37}$$

where $\tau_0 = \dfrac{l}{v_F}$ is the elastic scattering time, l is to the mean free path and $\tau_\varphi = \dfrac{l_\varphi^2}{D}$ is the phase coherence time. Since the phase coherence length increases with decreasing temperature and, we can heuristically assume the temperature dependence of the phase coherence time to be $\tau_\varphi \propto T^{-p}$ with p is a constant depending on the type of scattering events. Thus we infer the temperature dependence of the weak localization correction

$$\Delta\sigma \propto -\kappa\hbar p \times \ln(\frac{1}{T}) \tag{1.38}$$

where κ is a parameter depending on the disorder level in the system. In two dimensions, the quantum correction of the Drude conductivity diverges logarithmically at low temperature.

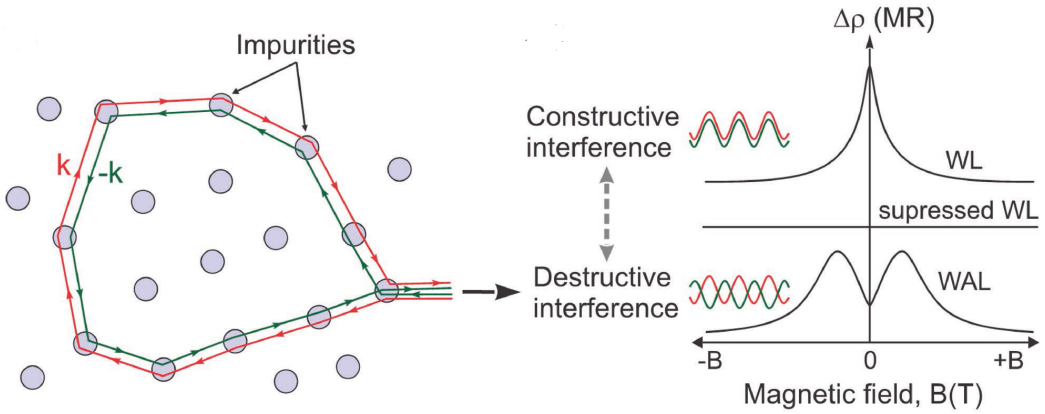

Figure 1.1: Skematic view for the backscattering of a particle in two-dimension systems. The two time reversed loops have opposite quantum phases leading to constructive interference. The quantum interference enhances the probability for the particle to return to its origin point and decrease (increase) the conductivity (resistivity) at B = 0. In the presence of spin-orbit coupling, the quantum interference is destroyed. The magnetic field will first cancel the effect of the spin-orbit coupling and re-establish the quantum interference in the system at very low field range, before initialing the weak localization. Extracted from [Jnawali 2017].

If we apply a perpendicular magnetic field to the 2D system, the two time-reversal paths for the particle to return to its origin gains a phase difference and the constructive quantum interference will be destroyed. The phase difference between the two loops is $\Delta\varphi = \dfrac{2eBS}{h} = \dfrac{2S}{l_m^2} = 4\pi\dfrac{\Phi}{\Phi_0}$, which is twice of the loop area divided by the square of the magnetic length l_B, or 4π times of the elementary of the flux quantum $\Phi_0 = h/e$. The system shows a negative magnetoresistance in a very small field range due to the suppression of the weak localization by the magnetic field (shown in Fig. 1.1).We can introduce another characteristic time, the magnetic relaxation time $\tau_B = \dfrac{\hbar}{4BDe}$, which is the time required to make the phase difference $\Delta\varphi = \dfrac{2\pi BD\tau_B}{\Phi_0}$ equal to $\dfrac{1}{2}$. Above a certain critical field B_c the magnetic relaxation time is much shorter than τ_φ and the weak localization effect is fully destroyed. The weak localization is usually proven and studied experimentally by the negative magnetoresistance under low magnetic field and the analysis of B_c provides a way to estimate τ_φ .

In the weak localization regime, the presence of spin-orbit coupling introduces a spin-dependent phase difference for the two time reversed trajactories and destroys

the phase coherence in the system. This effect is called the weak antilocalization (WAL) [Golub 2016]. When the magnetic field is progressively established, the external field will first cancel the suppression of the weak localization brought by the spin-orbit coupling and the system shows a positive magnetoresistance in a very small field range (shown in Fig. 1.1).

1.3 Landau level quantization

In the classical treatment of electrons' dynamic under mangetic field discussed in section 1.2.1, the electrons have a circular trajectory with the radius being inversely propotional to the magnetic field strength. When the magnetic field is high, i.e. $\omega_c\tau \gg 1$, the magnetic field cannot be treated as a pertubation and neither the classical nor the semi-classical approches are valid. We need to solve the Schrödinger equation and incorporate the magnetic field in the Hamiltonian of the system. The angular momentum (and hence the energy) will be quantized into discrete values. The description of the electrons in terms of Bloch wavefunction is not approprate, and one actually refers to as Landau levels [Girvin 1999].

1.3.1 Landau levels

The Hamiltonian of independent electrons is written as

$$H = \frac{\boldsymbol{p}^2}{2m} + V(\boldsymbol{r}) \tag{1.39}$$

where $\boldsymbol{p}$ is the canonical momentum while V($\boldsymbol{r}$) is the lattice periodic potential. In magnetic field, the Hamiltonian is modified by applying the Peierls substitution which consist in replacing the canonical momentum $\boldsymbol{p}$ by the gauge-invariant kinetic momentum [Jackson 1999]

$$\boldsymbol{p} \rightarrow \Pi = \boldsymbol{p} + e\boldsymbol{A} \tag{1.40}$$

where $\boldsymbol{A}$ is the vector potential so that $\boldsymbol{B} = \boldsymbol{\nabla} \times \boldsymbol{A}$. In the following the lattice potential V($\boldsymbol{r}$) is treated as a perturbation and is absorbed into the effective mass. The kinetic momentum is proportional to the electron velocity $\boldsymbol{v}$, which must naturally be gauge invariant because it is a physical quantity.

The Schrödinger equation reads

$$\frac{1}{2m^*}(\frac{\hbar}{i} + e\boldsymbol{A})^2\psi = \varepsilon\psi. \tag{1.41}$$

Now we set the vector potential as $\boldsymbol{A} = (0, Bx, 0)$ (Landau Gauge), so that the magnetic field is along the $\boldsymbol{z}$ direction. The Schrödinger equation is modified accordingly:

$$H\psi(\boldsymbol{r}) = \frac{\hbar^2}{2m^*}[-\frac{\partial^2}{\partial x^2} + (\frac{1}{i}\frac{\partial}{\partial y} - \frac{eB}{\hbar})^2 + \frac{\partial^2}{\partial z^2}]\psi = \varepsilon\psi. \tag{1.42}$$

Since the Hamiltonian operator couples the coordinates $\boldsymbol{x}$ and $\boldsymbol{y}$, but leaves the $\boldsymbol{z}$-coordinate alone, we can write the wavefunction as

$$\psi(x, y, z) = e^{ikz}\phi(x, y). \tag{1.43}$$

Let us define $\varepsilon^{'} = \varepsilon - \frac{\hbar^2}{2m^*}k_z^2$ in Eq. 1.42 which yields:

$$[-\frac{\hbar^2}{2m^*}\frac{d^2}{dx^2} + \frac{1}{2}m^*\omega_c^2(x + l_B^2 k_y)^2]\phi(x) = \varepsilon^{'}\phi(x). \tag{1.44}$$

We forget about the $\boldsymbol{z}$ direction so that the following now accounts only for 2DEG. From the Eq. 1.44 the Hamiltonian is similar to a harmonic oscillator in the $\boldsymbol{x}$ direction, and is independent of the $\boldsymbol{y}$ direction motion. The frequency of the harmonic oscillator is again the cyclotron frequency $\omega_c = eB/m^*$, and the center sits on

$$x_0 = -\frac{\hbar}{eB}k_y = -l_B^2 k_y \tag{1.45}$$

with $l_B = \sqrt{\frac{\hbar}{eB}}$ is the first cyclotron radius (or the magnetic length). The eigenenergies of the harmonic oscillator are [Shankar 2012]

$$\varepsilon_N^{LL} = \hbar\omega_c(N + \frac{1}{2}) \tag{1.46}$$

where N=0, 1, 2, $\cdots$ is an integer. The discrete energy levels of the eigenstates are called Landau Levels. The corresponding explicit wavefunctions are

$$\psi_{n,k}(x, y) \propto H_N(x + k_y l_B^2)e^{-(x+k_y l_B^2)^2/2l_B^2} \tag{1.47}$$

with H_N the usual Hermite polynomial wavefunctions of the harmonic oscillator. The wavefunctions look like strips, extended in the $\boldsymbol{y}$ direction but exponentially localized around $x_0 = -k_y l_B^2$ in the $\boldsymbol{x}$ direction.

The energy of electrons is quantized in the $\boldsymbol{xy}$ plane and the separation between the nearest Landau levels is $\hbar\omega_c$. When considering the presence of the electron spin, the Landau levels will split into two sublevels with an additional Zeeman energy $E_Z = \pm\frac{1}{2}g\mu_B B$, where the g is the effective Landé g-factor and μ_B is the Bohr magneton.

1.3.2 Landau level degeneracy

For a 2DEG system with a simple parabolic band dispersion $\varepsilon(k) = \hbar^2 k^2/2m^*$, the density of states (DOS) of the electrons without magnetic field is (neglecting the spins)

$$g(\varepsilon) = \frac{m^*}{2\pi\hbar^2} \tag{1.48}$$

as shown in Fig. 1.2. In the presence of a magnetic field, the density of states evolves and tends to peak at energies corresponding to Landau levels. Due to the lack of the energy dependence on $\boldsymbol{k}$ of the Landau levels, the degeneracy of each level is enormous.

In order to calculate the degeneracy of the landau levels, we assume that the sample is rectangular with dimensions L_x, L_y and that the left hand edge is at $x = -L_x$ and the right hand edge is at $x = 0$. From the Eq. 1.43, we can assume periodic boundary conditions in the $\boldsymbol{y}$ direction $\psi(y) = \psi(y + L_y)$ and have $\Delta k_y = 2\pi/L_y$. Because the wavefunctions (Eq. 1.47) are exponentially localized around $x_0 = k_y l_B^2$, the extension of each wave function in the $\boldsymbol{x}$ direction writes $\Delta x_0 = \Delta k_y l_B^2 = \frac{2\pi l_B^2}{L_y}$. For a finite sample restricted to $0 \leq x \leq L_x$ we would expect the number of the allowed states to be

$$D = \frac{L_x}{\Delta x_0} = \frac{L_x L_y}{2\pi l_B^2} = \frac{eBA}{h} \tag{1.49}$$

where $A = L_x L_y$ is the area of the sample. Therefore, we conclude that for each Landau level, there are $\frac{eB}{h} = \frac{1}{2\pi l_B^2}$ states per unit area. We notice in Eq. 1.49 that $\Phi = BA$ is the total magnetic flux in the sample, while $\phi_0 = \frac{h}{e}$ is known as the "flux quantum" and thought as the magnetic flux contained within the area $2\pi l_B^2$. Thus Eq. 1.49 can be alternatively written as

$$D = \Phi/\phi_0 \tag{1.50}$$

from which the degeneracy of Landau level is regarded as the number of flux quanta in the sample. Interestingly, there is exactly one quantum state per flux quantum piercing the 2DEG. If we redistribute the Landau level degeneracy over the energy interval $\hbar\omega_c$ between two LLs, we have $\frac{1}{2\pi l_B^2}/\hbar\omega_c = \frac{m^*}{2\pi\hbar^2}$, which is equal to the density of sates of the 2DEG without magnetic field (Eq. 1.48). Hence, the total density of states in a 2DEG system is not changed by the magnetic field, only its energy distribution is modified from constant to a series of δ functions as shown in Fig. 1.2. When the magnetic field is increased, the degeneracy in each Landau level increases and the electrons tend to fill the lower Landau levels to minimize the energy of the system. If the carrier density is fixed, the Fermi level will jump abruptly to lower Landau level as soon as its degeneracy is sufficient enough at a finite value of the magnetic field, to hold all the charge carriers. This quantization is universal and independent of all microscopic details such as the type of semiconductor material, the purity of the sample and so forth.

1.3.3 Landau level broadening

In a real system, perturbations caused by the impurities in the crystal and/or the electron-electron interactions break the translation symmetry and bring a po-

tential energy fluctuation through the sample. As a consequence, the Landau levels are broadened and a non-zero density of states is present in between the Landau levels. The broadening is characterized by Γ, which is related to a quantum scattering lifetime τ_D through the uncertainty relation $\Gamma \sim \hbar/\tau_D$. The Landau levels are no longer described by δ functions, but by Gaussian (Eq. 1.51) or by Lorentzian (Eq. 1.52) functions [Usher 2009]:

$$g(\varepsilon) = \frac{m}{2\pi\hbar^2}\frac{\hbar\omega_c}{\pi\Gamma}\sum_{N=0}^{\infty} exp\left[-\frac{(\varepsilon-\varepsilon_N^{LL})^2}{2\Gamma^2}\right], \tag{1.51}$$

$$g(\varepsilon) = \frac{m}{2\pi\hbar^2}\frac{\hbar\omega_c}{\sqrt{2\pi}\Gamma}\sum_{N=0}^{\infty}\frac{1}{1+(\frac{\varepsilon-\varepsilon_N^{LL}}{\Gamma})^2}. \tag{1.52}$$

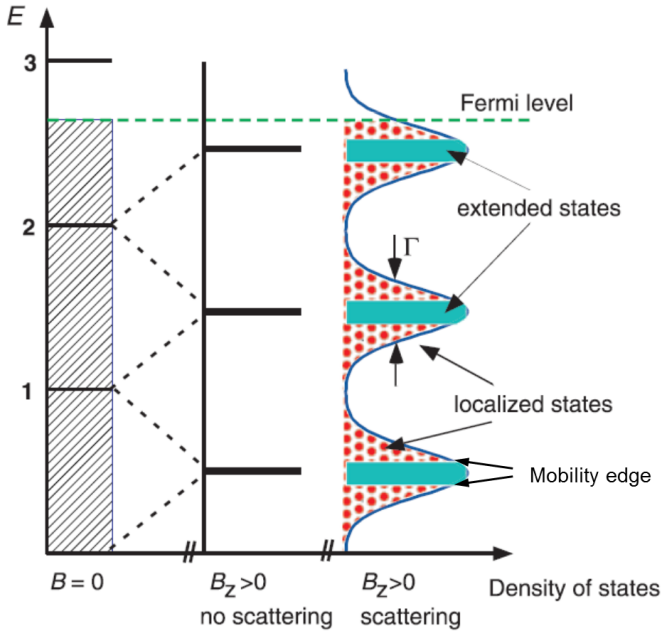

Figure 1.2: Landau quantization of 2DEG without spin. The constant density of state (left) develops into a serie of peaks which are refered to as Landau levels in the absence of disorder (middle) under magnetic field. The introduction of disorder in the system broadens the Landau levels into peak-line shapeliness, allowing non-zero density of states in between the Landau levels. The broadening of the Landau levels can be modelized by a Gaussian or a Lorentzian function with a typical parameter Γ, which is related to the quantum scattering time of the 2DEG. The states at the center stripe of the Landau levels are called extended states, and the states far away from the center are localized states. The extended states and the localized states are separated by the mobility edge. Extracted from [Jeckelmann 2001].

The broadening of the Landau levels allows the Fermi energy to vary con-

tinuously from higher (lower) Landau level when the magnetic field is decreased (increased) or the carrier density is increased (decreased). As shown in the right hand side of Fig. 1.2, there are two types of quantum states inside the broadened Landau levels: extended states in a stripe at the center and localized states away from center. The energy boundary between the extended states and localized states is called the mobility edge. In localized states, electrons are localized along closed equipotential lines which can be a few l_B and do not contribute to the transport properties. When the Fermi level falls in the extended states, the material is conducting, whereas if it falls in the localized states it behaves as an insulator. The presence of the localized states plays an important role in the quantum Hall effect (in Section. 1.4), without which the Hall resistance would show continuous increase in magnetic field, instead of plateaus.

1.3.4 Shubnikov-de Haas oscillations

In a 2DEG with parabolic dispersion relation, the density of states is constant in the absence of magnetic field, and develops energy increasing peaks-like shapeliness (Landau levels) as the magnetic field increases. In simple words, an analogy can be made with an elastic rubber decorated with equally spaced marks at equilibrium. One end of the elastic rubber is fixed and defines the origin of the energy scale along its length, whereas each mark represent a Landau level. Increasing the magnetic field is similar as pulling the free end of the rubber. The energy of the Landau levels increases and the energy gap between Landau levels also increases. For a fixed Fermi energy, the Landau levels will subsequently cross the Fermi level as the magnetic field increases. According to the Einstein relation (Eq. 1.30), the conductivity is proportional to the density of states at the Fermi level and therefore the magneto-resistivity will display an oscillating behavior (see Fig. 1.3). This effect was first observed by Shubnikov and de Haas (1930) in Bismuth and then named as Shubnikov-de Haas (SdH) oscillations. The SdH oscillations are a consequence of the Landau level quantization of the energy spectrum and thus can be only observed at high enough magnetic field ($\omega_c\tau > 1$) and low temperature ($\hbar\omega_c > k_BT$).

We start with the Kubo-Greenwood expression for the conductivity [Kunc 2015]

$$\sigma = \int_{-\infty}^{+\infty} \sigma(\varepsilon)(-\frac{\partial f_0}{\partial \varepsilon})d\varepsilon \tag{1.53}$$

with $f(\varepsilon)$ is the Fermi-Dirac distribution function (Eq. 1.19). The conductivity $\sigma(\varepsilon)$, obtained from the Boltzmann theory in high magnetic field ($\hbar\omega_c \gg 1$) reads: $\sigma(\varepsilon) = \dfrac{ne^2}{m^*\omega_c^2\tau_{\varepsilon_F}}$. Combining the Einstein relation (Eq. 1.30) with the Landau level-like DOS in Eq. 1.51 or 1.52 and the relation $\dfrac{\sigma_{xx}(B)-\sigma_0}{\sigma_0} = \dfrac{R_{xx}(B)-R_0}{R_0}$, the explicit expression of the oscillatory part of the resistance is described by the

Lifshitz-Kosevich formula

$$\Delta R = 4R_0 R_T R_D sin\left[2\pi\left(\frac{f_{SdH}}{B} - \frac{1}{2}\right) \pm \frac{\pi}{4}\right] \tag{1.54}$$

where R_0 is the zero magnetic field resistance and $\Delta R = R_{xx}(B) - R_0$, f_{SdH} is the frequency of the oscillations. The thermal factor

$$R_T = \frac{2\pi^2 m_c k_B T}{\hbar e B} / sinh\left(\frac{2\pi^2 m_c k_B T}{\hbar e B}\right) \tag{1.55}$$

is related to effect of the finite temperature. This factor tends to damp the oscillation amplitude when the temperature increases (see Fig. 1.3(b)). The term $m_c = \frac{\hbar^2}{2\pi}\frac{\partial S}{\partial E}$ is the cyclotron resonance mass where S is the cyclotron orbit area. It is worth noting that the cyclotron effective mass m_c is different from the effective mass m^* in general, because m^* is a matrix-valued function of the wavevector $\boldsymbol{k}$ while m_c is a property of the entire orbit and depends on energy. Only for a spherical Fermi surface we have m_c equals to m^*. For a non-spherical Fermi surface m_c is a various combination the effective masses in different directions in the plane normal to the magnetic field. In the following chapters however, as an approximation, we shall make no distinction between the effective mass and the experimentally available cyclotron mass.

The Dingle factor

$$R_D = exp\left(-\frac{2\pi^2 m_c k_B T_D}{\hbar e B}\right) = exp\left(-\frac{\pi}{\omega_c \tau_D}\right) \tag{1.56}$$

(where T_D is the Dingle temperature) is related to the quantum scattering time $\tau_D = \frac{\hbar}{\Gamma}$. It sets the oscillation amplitude decay as magnetic field decreases (see Fig. 1.3(c)). By fitting the temperature dependence of the amplitudes of the oscillation, we can extract the cyclotron mass and the quantum scattering time (quantum mobility) of the system.

When the magnetic field increases, a maximum of conductivity appears each time the Fermi level is aligned with a Landau level, $\varepsilon_F = \varepsilon_N^{LL}$. We can rewrite this expression and make the inverse magnetic field B_N explicit so that

$$\frac{1}{B_N} = \frac{e\hbar}{m^* \varepsilon_F}(N + \frac{1}{2}). \tag{1.57}$$

The maximum of conductivity is encountered periodically with period $T_{SdH} = \frac{1}{B_{N+1}} - \frac{1}{B_N} = \frac{e}{nh}$, where n is the carrier density. This periodicity provides us a very powerful tool to calculate the carrier density by measuring the SdH oscillations frequency through the Onsager relation $n = \frac{g_s g_v e}{h} f_{SdH}$ with g_s and g_v the spin and valley degeneracy, respectively. Furthermore the magnetic field angle dependence of the SdH oscillations provides information regarding the topology of the

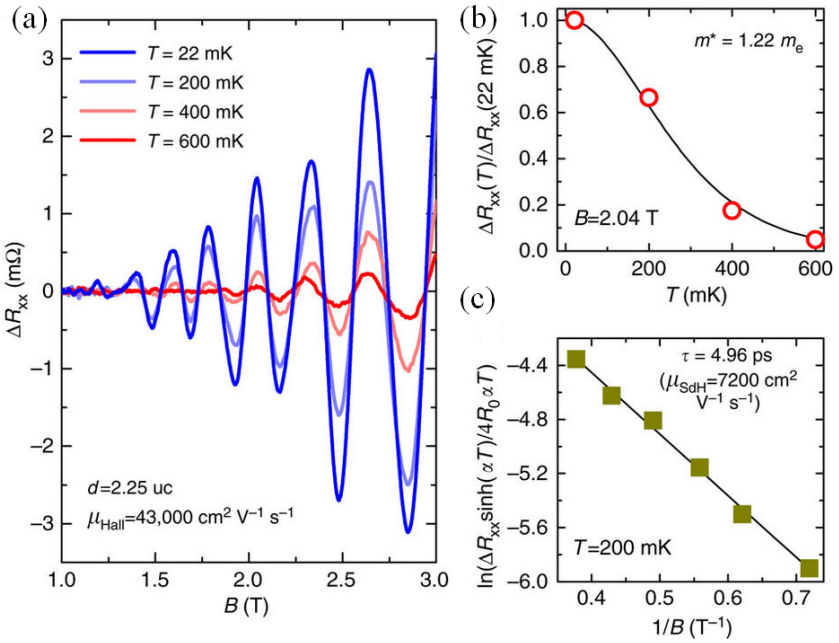

Figure 1.3: (a) The temperature dependence of typical SdH oscillations in high mobility 2DEG at the spinel/perovskite interface of $\gamma - Al_2O_3/SrTiO_3$. The amplitude decays rapidly as the temperature increases and magnetic field decreases. (b) The temperature dependence of the oscillations' amplitude at a fixed magnetic field. Fitting with the LK formula (Eq. 1.54), one can extract the cyclotron mass of the electrons in the system. (c) The magnetic field dependence of the oscillations' amplitude at a fixed temperature, from which one can extract the Dingle temperature and hence the quantum scattering time in the system. Extracted from [Chen 2013].

Fermi surface, since the carrier density is directly related to the Fermi vector. For example, in 2DEG, most of the transport properties only depend on the perpendicular component of the magnetic field because of the 2D Fermi surface. If the magnetic field is titled with an angle θ with respect to the sample plane, the SdH oscillations' frequency and position of peaks shows a $\cos\theta$ relation compared with the perpendicular configuration [Caviglia 2010b]. In 3D case, the angle dependence of SdH oscillations is a powerful tool to construct the Fermi surface in different directions [Eto 2010].

1.4 The quantum Hall effect

In 1980, Klaus von Klitzing [Klitzing 1980] discovered that the Hall resistance shows a series of plateaus at $R_H = \dfrac{h}{\nu e^2}$ with a integer value ν, when measuring a two dimensional electron gas in a MOSFET (metal-oxide-semiconductor field-effect

transistor) inversion layer under very low temperature (4.2 K) and high magnetic field (up to 15 T) (Fig. 1.4(a)). Two years later in 1982, Daniel Chee Tsui *et al.* [Tsui 1982] discovered another serie of plateaus with a fractional values of ν in a higher mobility 2DEG sample in GaAs/AlGaAs heterostructure (Fig. 1.4(b)). The manifestation of a quantized Hall resistance over a range of magnetic field (plateau) are called the integer (ν is an integer) and fractional (ν is fraction with odd denominator) quantum Hall effect, which are two of the most remarkable condensed-matter phenomena discovered in the 20th century. For the discovery of the quantum Hall effects, Klaus von Klitzing was awarded the 1985 Nobel Prize in Physics and Robert B. Laughlin, Horst L. Störmer and Daniel C. Tsui were awarded the 1998 Nobel Prize in Physics.

The QHE is a strictly quantum phenomenon which can be only observed in a two dimensional electron gas (2DEG) or two dimensional hole gas (2DHG). The SdH oscillations requires the quantization of density of states while the QHE requires the quantization of electron motion in addition. Based on the conditions of Landau level quantization, the two requirements for observing the QHE are: firstly, a high charge carrier mobility to make sure that the electrons (or holes) can complete many cyclotron orbits ($\mu B \gg 1$) before being scattered; secondly, a high magnetic field and low temperature to make sure that the Landau level energy gap is large compared with the thermal activation energy $k_B T$ ($\hbar\omega_c > k_B T$).

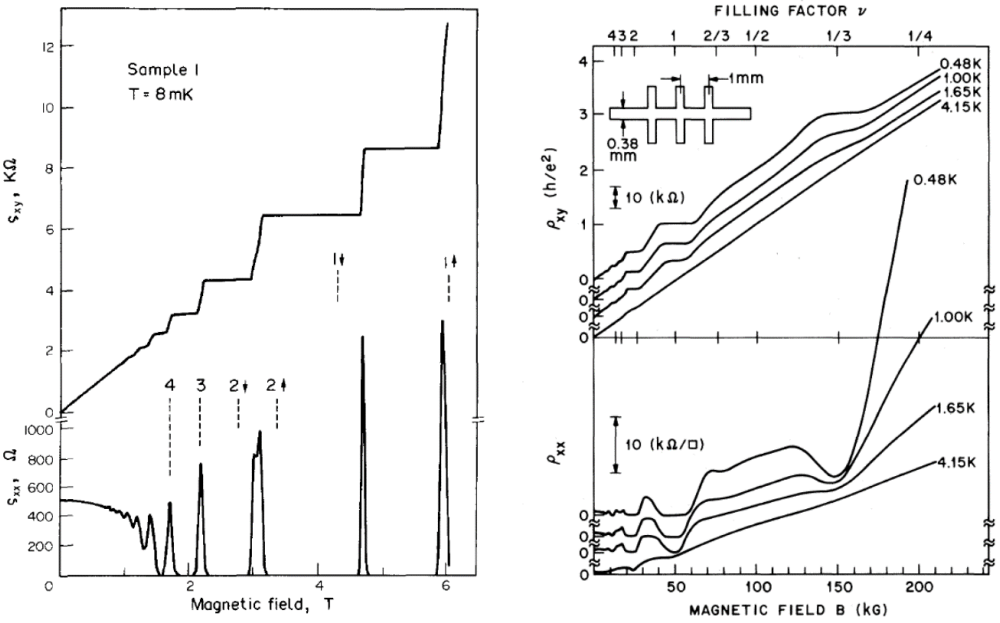

Figure 1.4: The integer quantum Hall effect (IQHE) and the fractional quantum Hall effect (FQHE). Extracted from [Ebert 1982, Tsui 1982].

1.4.1 The integer quantum Hall effect

The integer quantum Hall regime is achieved when the longitudinal resistance is null and the Hall resistance is quantized at an integer value of $\frac{h}{e^2}$:

$$\begin{aligned} R_{xx} &= 0; \\ R_{xy} &= \frac{h}{\nu e^2} \end{aligned} \tag{1.58}$$

where ν is called the filling factor.

Referring to the Eq. 1.12, the resistivity tensor $\boldsymbol{\rho}$ and the conductivity tensor $\boldsymbol{\sigma}$ in the quantum Hall regime can be written as

$$\boldsymbol{\rho} = \begin{pmatrix} 0 & -\frac{h}{\nu e^2} \\ \frac{h}{\nu e^2} & 0 \end{pmatrix} \tag{1.59}$$

and

$$\boldsymbol{\sigma} = \begin{pmatrix} 0 & \frac{\nu e^2}{h} \\ -\frac{\nu e^2}{h} & 0 \end{pmatrix} \tag{1.60}$$

leading to $\rho_{xx} = 0$ and $\sigma_{xx} = 0$. This results looks counter-intuitive but remains valid as long as $\sigma_{xy} \neq 0$. In this situation, the dissipation power in the 2DEG is null:

$$\boldsymbol{j} \cdot \boldsymbol{E} = \boldsymbol{j} \cdot \boldsymbol{\rho} \cdot \boldsymbol{j} = 0. \tag{1.61}$$

Indeed, the current is flowing perpendicularly to the electric field without doing any work. Since $\sigma_{xx} = 0$, no current is flowing in the longitudinal direction, like an insulator, while $\rho_{xx} = 0$ means that the current is dissipationless, like a perfect conductor.

The exact, universal quantization of the Hall resistance regardless of detailed sample geometry and impurity configuration enables the establishment of a metrological resistance standard, and serves as the basis for an independent determination of the fine structure constant.

1.4.2 Edge states in the quantum Hall regime

To understand the phenomenology of the plateaus in the quantum Hall effect, we refer to the concept of Landau level quantization of the energy spectrum discussed above. According to the previous theoretical discussion (section 1.3.3), the bulk system is insulating when the Fermi level sits in the localized states and conducting when the Fermi level sits in the extended states. A real 2D sample is never infinite in size and boundaries actually play an essential role in the Quantum Hall effect [Halperin 1982].

From a classical viewpoint, electrons will all cycle under magnetic field in the

same direction, say anti-clockwise. At the sample edges, the electrons will collide and bounce back on the boundaries. Since all the motions are anti-clockwise, the result is a skipping orbit motion in which the particles travel along the one-dimensional boundary of the sample and move only in a same direction from one end of the sample to the other one. In the case of scattering centers, the electrons will collide the "boundary" of the scattering potential and move in a closed loop centered around the scatterer. If the scattering center is placed far from the sample boundary, the electrons can be viewed as trapped by the scatterers and do not contribute to transport. If the scattering center is located close to the boundary, electrons will simply cycle around and continue their progression along the boundary. Since the edge states are chiral, backscattering is forbidden along the edges (see fig. 1.5) and the current is dissipationless (*i.e.* zero resistance).

From a quantum mechanical point of view, the presence of the boundary modifies the Hamiltonian and adds an additional potential energy in the Landau levels for the electrons at the boundaries (Eq. 1.46) which can take shape as illustrated in Fig. 1.5(c). When the Fermi level is set between two bulk Landau levels, let's say between the ν^{th} and $(\nu{+}1)^{th}$ Landau levels, the electrons in the bulk make cyclotron motions along the equipotential lines caused by the presence of the scatterers. Electrons are localized on closed equipotential lines and do not contribute to the net current. These states are called the localized states with localization length ξ. There are 2 Fermi points for each Landau level and each Fermi point form a perfect 1D edge conductance channel, thus there are ν channels on each edge. Different from the localized states in the bulk, the electrons at the edges carry a chiral current. The conductance in the Quantum Hall regime is described by Landauer-Büttiker formula in multiprobe systems [Büttiker 1988]:

$$\begin{cases} \sigma_{xx} = \infty, \\ \sigma_{xy} = \nu \dfrac{e^2}{h} \end{cases} \tag{1.62}$$

where ν is the filling factor, which is equal to number of Landau levels below the Fermi energy. When the Fermi level is between the ν^{th} and $(\nu{+}1^{th})$ bulk Landau levels, the transport is dominated by the edge channels, hence the Hall resistance shows a quantized value of $\frac{1}{\nu}\frac{h}{e^2}$. When the magnetic field or the carrier density changes the Hall resistance does not change and shows a plateau as long as the Fermi level is between two Landau levels. When the Fermi level is aligned with the Landau levels and enters the extended states, the electrons in bulk will become delocalized and start to contribute to transport according to the Boltzmann theory.

1.4.3 The breakdown of the quantum Hall effect

Soon after the first discovery of the quantum Hall effect, a lot of investigations were put forward to prove the exact quantization of the Hall resistance and for its possible application as resistance standard in metrology. High precision mea-

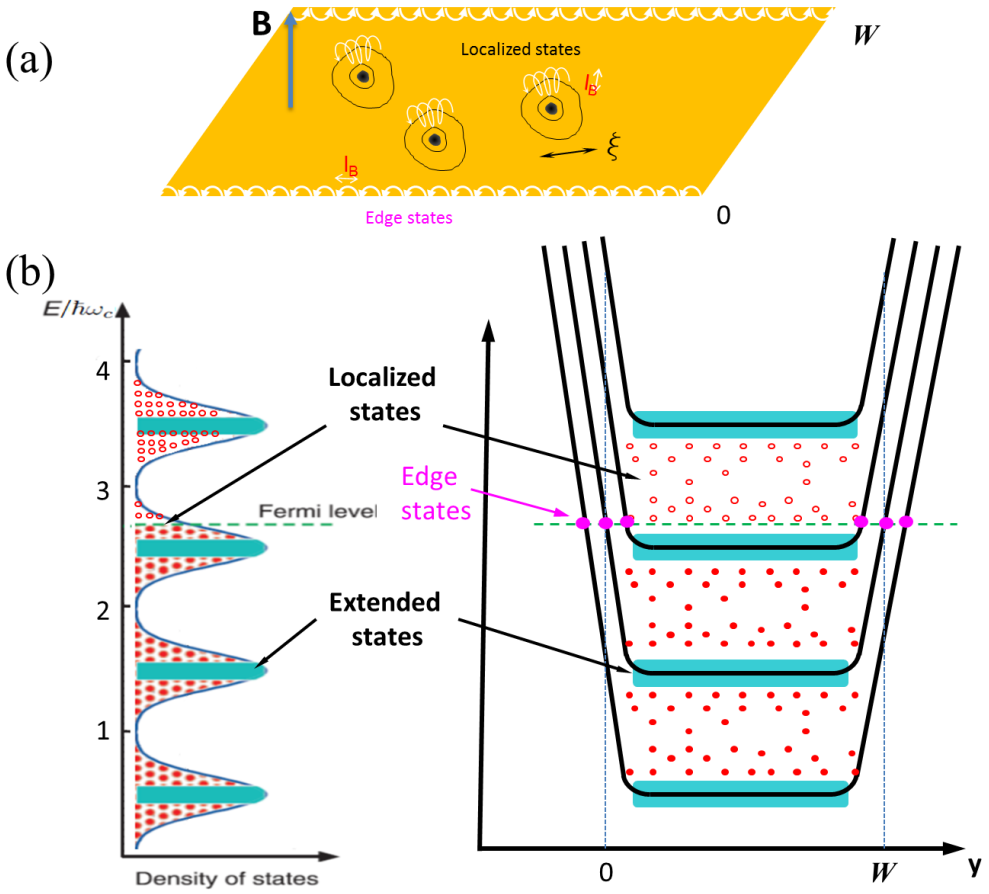

Figure 1.5: (a) The classical viewpoint of the quantum Hall effect. In magnetic field, the electrons at the boundary of the sample bounce against the boundary and form a chiral current near the edge. The electrons inside the sample cycle along the equipotential lines of the scattering centers and are therefore trapped. The typical length of the trapping equipotential is called the localization length ξ. (b) The sketch of DOS in the presence of a magnetic field in a real finite size 2D sample. In order to confine the 2DEG inside the sample, we need to introduce an addition potential along the sample's y direction. The diverging potential will cross the Fermi level at the boundaries and thus the electrons at the boundaries will be delocalized when the Fermi level sits between two Landau levels. As a result, the transport is dominated by the small number of the edges state electrons, showing a zero R_{xx} and a plateau in R_{xy}. When the Fermi level approaches the Landau levels, the bulk electrons become delocalized and start to contribute to the transport. Then the sample shows a finite R_{xx} and a classical Hall effect.

surements of the quantum Hall effect become crucial and require a current as high as possible. However, a sudden breakdown of the quantum Hall effect occurs if the sample current exceeds a certain limit I_c. At this critical current, the system becomes dissipative: the longitudinal resistance ρ_{xx} changes abruptly by several orders of magnitude and the Hall resistance shows a deviation from the quantized values. This phenomenon naturally attracted attention because of its relevance in standard applications as well as the potential to elucidate the fundamental physics of the quantum Hall effect.

A number of mechanisms have been suggested for the explanation of the breakdown of the QHE, including the Zener tunneling of electrons to higher Landau levels, electron heating effects, Cherenkov-like acoustic phonon emissions, heat instability of electron systems. Among them, the most commonly used model is the bootstrap-type electron heating model proposed by Komiyama and Kawaguchi [Komiyama 2000], which is based on the heat instability of the electron system. In the quantum Hall regime at finite temperature, a small fraction of electrons populate the higher energy Landau levels, above ε_F. They rapidly relax their energy so that the stability of the QHE is preserved: the energy fluctuations of the electrons system remain weak and stable. However, the situation changes when the Hall effect field reaches a critical value E_y^c. Due to E_y^c, the excited electrons are accelerated and the rate of energy gain is higher than the rate of energy loss. The electron temperature increases rapidly due to the electron-electron interaction and the QHE breaks down. Above E_y^c, an infinitesimal fluctuation is amplified by the electric field and the electron system undergoes a transition to a dissipative state. In the quantum Hall regime, R_{xy} is quantized and E_y is propotional to the current I, the bootstrap-type electron heating induced quantum Hall effect breakdown occurs at different critical currents I_c=$E_y^c/(h/\nu e^2)$ for different filling factors ν [Alexander-Webber 2012].

In the quantum Hall regime, the Hall electric field E_y was found to be concentrated near the edge of the sample [Fontein 1991]. When the current I is approaching the critical current I_c, the critical field E_y^c is firstly reached near the edge and the current will then redistribute itself to avoid the dissipative edge regions. The dissipative regions will increasingly expand towards the interior region with increasing current. The quantum Hall effect breakdown occurs only when the dissipative region extends across the full width of the sample so that the dissipationless current path is no longer available. The breakdown of the quantum Hall effect was found to depend on the sample geometry in two different classes: the critical current I_c scales linearly with the width W of a sample with low mobility [Boisen 1994]; or I_c increases sublinearly and is almost saturated at relatively small I_c values with increasing W of a sample with high mobility [Balaban 1993].

1.4.4 Variable range hopping in the quantum Hall regime

Localized electrons do not contribute to transport at zero temperature. However, at finite temperature, they can be thermally activated to extended states at the

next Landau level or to another empty localized state. The charge transfer between localized states introduces a conductance in the quantum Hall regime and gives rise to finite longitudinal resistance. Depending on the temperature the conductance originates from different mechanisms. When the temperature is high enough, the conductance is dominated by the thermal activation and the electrons favor to hop to the nearest states. The conductance in the thermal activation model is described by the Arrhenius law [Polyakov 1994]:

$$\sigma_{xx} = \sigma_0 exp(-\Delta E/T) \tag{1.63}$$

where ΔE is the energy gap between two Landau levels.

At low temperature, the transport is often well described by the Variable Range Hopping (VRH) theory proposed by Sir Nevill Mott in 1968 [Mott 1968]. In the VRH theory, electrons are likely to hop to a remote localized state with a small energy difference rather than to the nearest site with high energy difference. In the quantum Hall regime, as we discussed before (section 1.4.2) the electrons in the bulk are strongly localized on a typical length ξ around equipotential lines brought by disorder. The quantum Hall regime can be regarded as the Anderson localization regime and hence the temperature dependence of the longitudinal conductivity is described by the Mott-VRH model [Rosenbaum 1991]:

$$\sigma_{xx} = \frac{\sigma_0}{T} exp(-(T_0/T)^{\frac{1}{d+1}}) \tag{1.64}$$

where d is the dimension of the system. When the Coulomb interaction is not negligible between two hopping states, a power-law dependent density of states near the Fermi energy must be introduced. This problem was investigated by Efros Shklovskii and the hopping conductivity is modified accordingly to the ES-VRH model [Efros 1975, Shklovskii 1984]:

$$\sigma_{xx} = \frac{\sigma_0}{T} exp(-(T_0/T)^{\frac{1}{2}}) \tag{1.65}$$

which is valid for all dimensions. In both Eq. 1.64 and Eq. 1.65, σ_0 is a parameter, T_0 is the hopping temperature, which is related to the localization length. By fitting the temperature dependence of the longitudinal conductivity in the quantum Hall regime with the (ES-)VRH model, one can obtain the localization length ξ by the following relation

$$k_B T_0 = Ce^2/4\pi\epsilon_r\epsilon_0\xi \tag{1.66}$$

where ϵ_0 is the vacuum dielectric constant, ϵ_r is the dielectric constant for the sample and $C \simeq 6.2$ is a constant.

Chapter 2

Experimental techniques

Contents

2.1 High magnetic field 29
2.2 The LNCMI facility 30
2.3 Cryogenics 31
2.4 Sample holder and electrical addressing 32
2.5 Transport measurements 34

In this chapter, I will present the experimental details concerning the generation of high magnetic field at the LNCMI facility of Toulouse, the cryogenic environment and the experimental techniques related to the transport measurement in pulsed magnetic field.

2.1 High magnetic field

Magnetic field is a fundamental element in the universe. Although quite weak, the earth's magnetic field has been used for navigation purpose since more than 2000 years ago, and acts as a protection shield against the solar wind and radiations from the universe. It was proven extremely crucial for the development of the current form of life on earth. Since the discovery of the *Faraday's law of electromagnetic induction* and the electrification by the end of the 19^{th} century, the magnetic field has entered to everyone's daily life with many electromagnetic devices. In the area of scientific research, due to its interaction with electron systems, magnetic field is also a very important tool in condensed matter physics, to reveal the fundamental states of matter through the study of optics, magnetism, transport and other properties of materials.

The magnetic induction is measured in unit of tesla (T) in the SI system and Gauss (G) in the CGS system, where 1 T = 10000 G. To comply with the community jargon, we will write magnetic field to actually refer as the magnetic induction in the rest of this manuscript. The strength of the earth magnetic field is between 25 μT to 60 μT, while the magnetic field of a permanent magnet is usually of the order of 0.1 T (Neodymium magnet can produce a magnetic field up to 1.5 T). People have developed many kinds of magnets to achieve much higher magnetic field than the permanent magnets. According to the Biot-Savart law, the magnetic induction

B produced by a current $\boldsymbol{I}$ along a closed path $d\boldsymbol{l}$ at a position **r** is

$$\boldsymbol{B}(\boldsymbol{r}) = \frac{\mu_0 \boldsymbol{I}}{4\pi} \int_C \frac{d\boldsymbol{l} \times \boldsymbol{r}}{r^3} \tag{2.1}$$

where μ_0 is the vacuum magnetic permeability. The magnetic field strength is proportional to the current. In magnets based on coil technology, it is both limited by the Joule heating effect and the Laplace Force. In order to achieve very high magnetic field, people have developed different technologies, such as the the superconducting magnets (up to 20 T) [Hanai 2014], hybrid magnets (up to 45 T) [Mao 2003, Fazilleau 2012], pulsed magnets (up to 100 T) [Sims 2008, Béard 2013a], single turn coil (up to 300 T) [Portugall 1999], electro-magnetic flux compression (up to 700 T) [Nakamura 2013] and explosive flux compression (highest record 2800 T) [Boyko 1999].

2.2 The LNCMI facility

The LNCMI is a large scale facility dedicated to the generation of intense magnetic field. The laboratory is composed of two buildings on two different sites. The site of Grenoble is dedicated to static magnetic field whereas the site in Toulouse deals with pulsed magnetic field. In the following, I shall discuss only the pulsed magnetic field techniques which have been used during this thesis. The LNCMI can provide a pulsed magnetic field up to 90 T generated by a resistive coil which is powered by many capacitor units (shown in Fig. 2.1(a)). Nowadays, three capacitor banks are installed in LNCMI-T which can store an energy of 14 MJ, 6 MJ and 1MJ [Béard 2013b]. The capacitor banks are first charged up to 24 kV and then discharged through a coil (Fig. 2.1(c)) in a time scale between 100 ms and 500 ms using an electrical circuit shown in Fig. 2.1(b). Due to the use of both high voltage and high current, the data acquisition system is located in a closed experimental cell and is remote-controlled from a safe place by the researchers. All the electrical devices close to the experiment are powered by an uninterruptible power supply unit and are therefore isolated from the national electricity network during the capacitor charge and discharge cycle (a magnetic field pulse). The duration time of the pulsed field depends on the energy stored in the capacitor banks as well as on the coil and generator characteristics. We can change the pulse time in choosing different generators modules and coils (Fig. 2.1(e)). The coils are immersed in liquid nitrogen (Fig. 2.1(d)) to lower their resistance and to improve their mechanical strength [Frings 2008]. Nitrogen channels are designed in the latest generation of fast cooling magnets to speed up the cooling process which reduces the waiting time to about 1 hour in between two shots at 60 T.

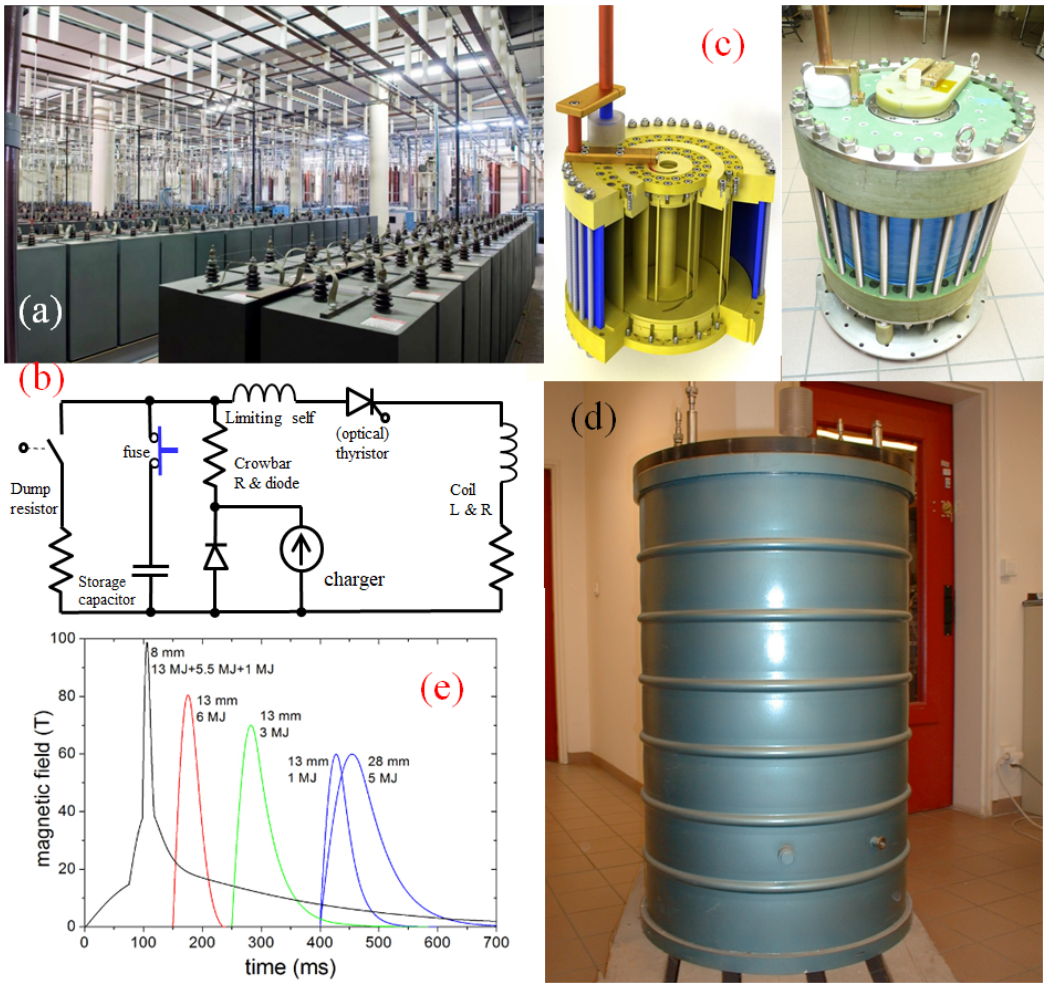

Figure 2.1: (a) Photo of the 14 MJ capacitor bank in LNCMI-T. (b) Electrical circuit of magnetic field generation. (c) CAD view (left panel) and photo (right panel) of a 60 T home-made nondestructive magnet. (d) Nitrogen cryostat to contain liquid nitrogen for cooling magnets. (e) Profile of magnetic field pulses with different power supply and magnets configuration (bore diameter) in LNCMI-T.

2.3 Cryogenics

Two different cryostats (^{4}He cryostat and ^{3}He cryostat) have been used for the high pulsed field experiments in this thesis. ^{4}He cryostat (Fig. 2.2(a)) provides a temperature environment range from 1.5 K to 300 K with ^{4}He as cooling medium. The liquid helium is separated into two parts, the top reservoir and the bottom sample chamber, which are connected through a needle valve handled outside the cryostat to control the helium replenishment. The sample can be immersed directly into liquid helium in the sample chamber, or isolated from liquid helium in a vaccum

sock. A resistive heater located close to the sample, allows a control of temperature from 4.2 K (liquid He temperature) to 300 K. On the other hand, by reducing the vapor pressure of liquid helium in the sample chamber, the temperature can be reduced down to 1.5 K. The ^{3}He cryostat is shown in Fig. 2.2(b) and can achieve a base temperature of 300 mK with the use of a rare isotope of helium ^{3}He. The ^{3}He gas is cooled and condensed by bringing it in contact with a pumped ^{4}He reservoir at 1 K (1 K pot). Once the sample chamber is filled with liquid ^{3}He at 1 K, a lower temperature (300 mK) is generated by reducing the vapor pressure of the liquid ^{3}He reservoir with an external pumping system. A dilution refrigerator not discussed here with a base temperature of 30 mK and a 16 T superconductivity magnet has also been used for very low temperature measurement during this PhD.

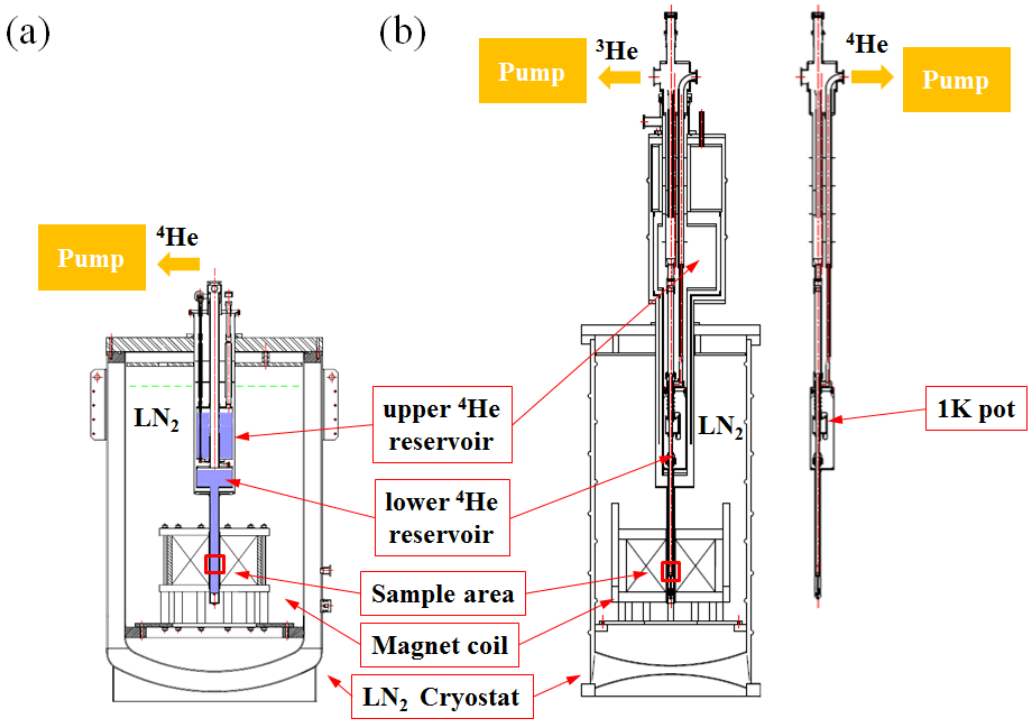

Figure 2.2: (a) ^{4}He cryostat and (b) ^{3}He cryostat.

2.4 Sample holder and electrical addressing

Before conducting magneto-transport experiments, the samples need to be prepared and electrically connected in a special way. First, the sample is glued to a round ceramic disk with 8 or 10 serigraphied gold pads located at the periphery (Fig. 2.3(a)). The ceramic disk acts as a flat sample holder and as a platform for the wedge bonding process (Fig. 2.3(b)) with gold or aluminum wire. The ceramic plate with sample on top, is then glued to a 10 (or 8) pins commercial socket. The

electrical connections between the ceramic pad and the socket are realized by silver paste. It is worth noting that, due to the fragility (sensitivity to electrostatic discharge) of the sample, the sample should be always grounded through a 1 MΩ resistance during all the connection process to avoid any electrostatic shock current which may destroy the sample.

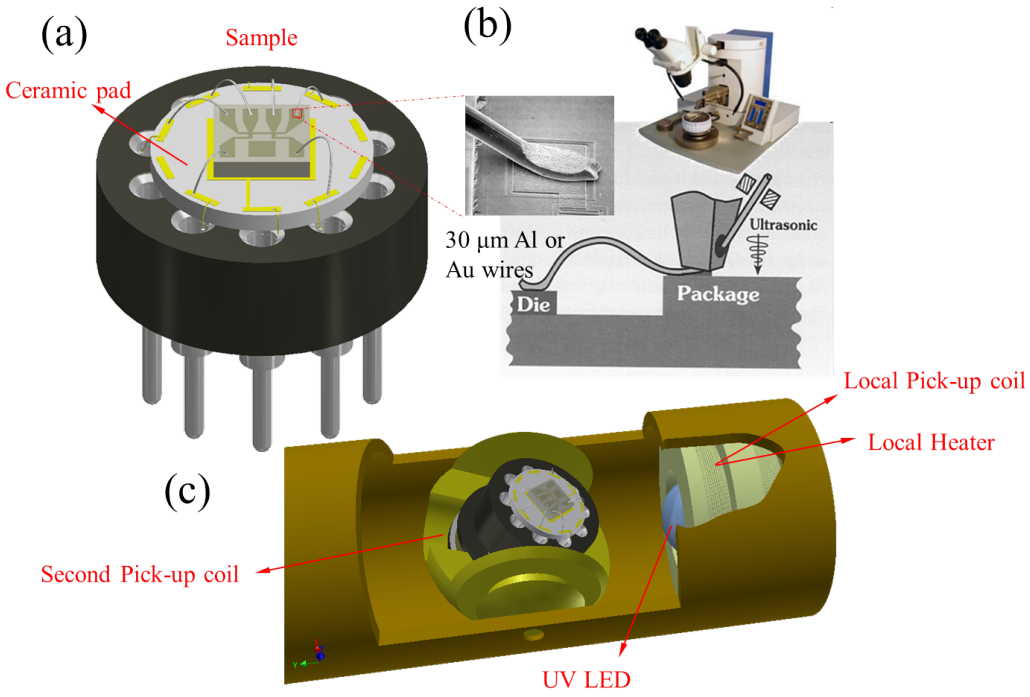

Figure 2.3: (a) Scheme of the sample connection on a connected commercial socket and ceramic pad for high field magneto-transport measurement. (b) Wedge bonding method with Aluminum or Gold wires for the connection between the sample and the ceramic pad. (c) Illustration of the inset's tail with the sample holder connected to the rotation stage.

Once ready, the socket and the sample are mounted onto our measurement inserts. The inserts are specially designed for pulsed field experiments at low temperature. The bottom part of the inserts are made with glass fiber instead of metal to avoid any eddy current induced by the pulsed field. Moreover, all the wires are twisted in pairs to reduce the parasitic induced voltage during the pulse. The magnetic field is captured with a pick-up coil close to the sample, which measures the induced voltage $V_{ind} \propto \frac{dB}{dt}$. The temperature is measured by Lakeshore Silicon diode sensor (DT-670) close to the sample and controlled by a Lakeshore or Cryocon temperature controller. The inserts are equipped with a rotation stage, which can change the sample angle in a range of 90°, from parallel to perpendicular with respect of the magnetic field (Fig. 2.3(c)). The angle of the sample with respect to

the magnetic field is measured through a second pick-up coil embedded below the socket, which rotates together with the sample. Finally, a UV LED with a wavelength of 248 nm is mounted at the end of the insert to change *in-situ* the sample's characteristics when appropriate.

2.5 Transport measurements

The transport measurements are conducted using 4 electrodes to remove the contact and wire resistance contribution. The current is injected through the two ends of the sample (2 probes), and the longitudinal magnetoresistance R_{xx} is measured using the two other probes. Furthermore, additional 2 probes located on both sides of the sample are used to measure the Hall resistance. The current is provided by a voltage source and a large resistance (typically 1 MΩ and in all cases much larger than the sample's resistance) placed in series in the circuit. We use two different kinds of voltage source for different measurement configurations:

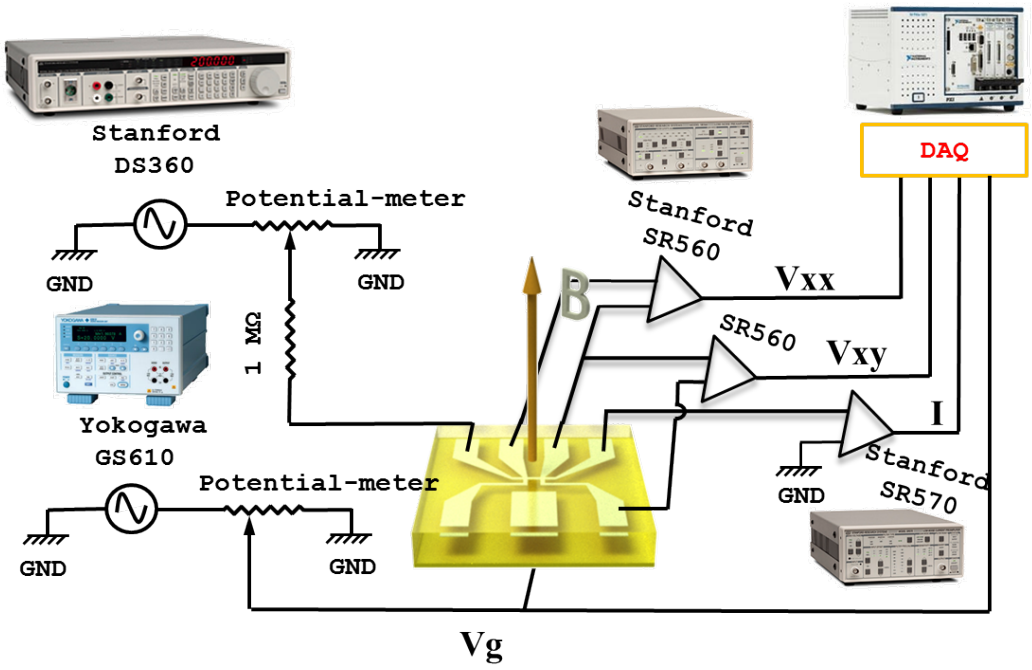

Figure 2.4: Scheme of transport measurement under high magnetic field. The current is provided by a voltage source (Stanford DS360) and a large resistance (of typical 1 MΩ) through the two ends of the sample. Longitudinal resistance R_{xx} and Hall resistance R_{xy} are recorded simultaneously by measuring the corresponding voltage drops which are amplified by Stanford SR560 preamplifiers. The current is measured by a current amplifier Stanford SR570. The gate voltage is applied by a high voltage source (Yokogawa GS610) when required. All the data are acquired together by a high speed acquisition system and stored in computer.

- DC measurement. The injected current is constant and the measured voltages are proportional to the sample's resistance. This technique gets rid of the inductance and capacitance of the circuit. However, it is sensitive to the induced voltage created by the time-varying magnetic flux inside the circuit cross-section perpendicular to the magnetic field. In this case, a fraction of the pure induced voltage measured by a pick-up coil in the close vicinity of the sample is subtracted to the raw recorded signals. The fraction (e.g. the ratio between the total area of the pick-up coil and the area of the sample's wiring loop) is chosen so that the magnetoresistance are identical when the magnetic field increases and decreases (see figure 2.5). This technique provides a reliable measurement scheme, however the signal-to-noise ratio remains limited by the strength of the induced voltage.

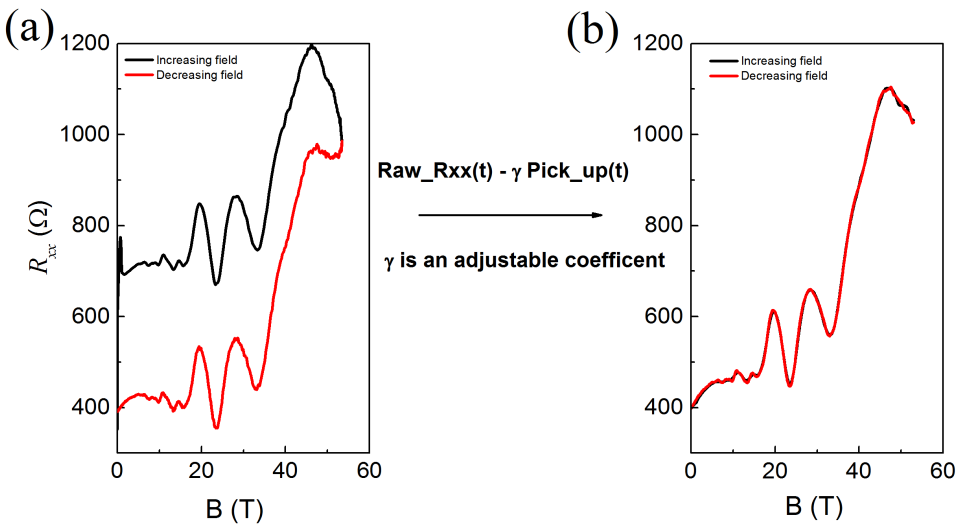

Figure 2.5: Raw data as a function of magnetic field before (a) and after (b) the compensation of the induced voltage in the DC measurement scheme.

- AC measurement. The injected current is sinusoidal with frequency $f_1 > 5$ kHz. The parasitic induced voltage is naturally removed during demodulation since the natural frequency range of the pulsed field ($0 < f_0 < 1$kHz) is much lower than the current modulation frequency f_1. A home-made numerical lock-in is used to perform the demodulation. This technique provides a higher signal-to-noise ratio and allows the measurement of small magnetoresistance oscillations. On the other hand, the back-ground signal as well as the amplitude of the oscillations, is often distorted (as compared to DC measurements) because of unwanted capacitance/inductance associated with the electrical circuit, which become relevant at high frequency. We systematically check that the AC/DC measurement schemes provide almost similar results

when dealing with small magnetoresistance oscillations (neglecting extra-noise in DC measurement).

Chapter 3

Graphene on SiC

Contents

3.1 Introduction to graphene 38
3.1.1 Atomic structure of graphene 38
3.1.2 The Dirac-like energy dispersion 39
3.1.3 The Landau levels of graphene 42
3.1.4 The quantum Hall effect in graphene 43
3.2 Graphene on Silicon Carbide 45
3.2.1 Epitaxial growth of graphene on Silicon Carbide 45
3.2.2 Sample preparation 46
3.2.3 Charge transfer in graphene on Silicon Carbide 47
3.3 Electronic properties of graphene on SiC 49
3.3.1 Temperature dependence at zero magnetic field 49
3.3.2 Longitudinal and Hall resistance in the QH regime 51
3.3.3 Temperature dependence of magneto resistance in the QH regime 53
3.4 Anomalous oscillations of the magnetoresistance 55
3.4.1 Experimental features 55
3.4.2 Temperature dependence 56
3.4.3 The origin of the anomalous oscillations 58
3.5 Model and simulations 59
3.5.1 Charge transfer in inhomogeneous G/SiC 59
3.5.2 Anomalous oscillations and breakdown of the QHE 64
3.6 Quantum Hall effect at low filling factor 65
3.7 Conclusion 67

In this chapter, I will present the high field (up to 80 T) magnetotransport study on graphene/SiC. This work has been performed under the collaboration with Dr. Benoit Jouault from University of Montpellier. This sample shows an extreme broad quantum Hall plateau and anomalous magnetoresistance oscillations in the quantum Hall breakdown regime. We proposed a model based on the sample inhomogeneity and the charge transfer mechanism in this system to explain the experimental results. The content of this chapter have been partly published in Phys. Rev. Lett. 117, 237702(2016).

Graphene shows a unique half-integer quantum Hall effect with conductivity plateaus $\sigma_{xy} = 4(N + 1/2)e^2/h$, where the factor 4 stands for the spin and valley degeneracies and $N = 0, \pm1, \pm2...$ is an integer [Goerbig 2011]. The peculiar Landau levels energy spectrum $E_N = sgn(m)\sqrt{2e\hbar v_F^2|N|B}$ in graphene (which can be written as $E_N \simeq \pm 420\sqrt{|N|B[T]}$K in unit of Kelvin) induces large energy gaps at low LL indices and allows us to explore exotic transport phenomena even at relatively high temperature [Novoselov 2007]. The substrate on which graphene is deposited plays a central role in determining the features of the observed QHE. In low mobility graphene on SiO_2, the presence of electron-hole puddles at the charge neutrality point (CNP) prevents any divergence of the longitudinal resistance at filling factor $\nu < 2$, whereas the Hall resistivity fluctuates around zero due to charge compensation [Poumirol 2010]. On the other hand, in high mobility graphene deposited on boron nitride flakes, a complete degeneracy lifting of the Landau levels can be observed and the corresponding spin-valley textures have been identified [Bolotin 2009, Dean 2011]. In this thesis, we consider graphene on SiC substrate (G/SiC) grown by SiC sublimation method. In this system, the quantum Hall resistance plateau at $h/2e^2$ is exceptionally robust with respect to the magnetic field [Tzalenchuk 2010]. In the following, we will first review the theoretical description of graphene and later address the transport properties of graphene on SiC.

3.1 Introduction to graphene

3.1.1 Atomic structure of graphene

Graphene is a 2D layer of carbon atoms arranged in a honeycomb structure, which was first studied theoretically by Wallace *et al.* in 1947 [Wallace 1947] and experimentally isolated nearly 60 years later by Novoselov *et al.* and Zhang *et al.* [Novoselov 2004, Zhang 2005]. This single atomic layer of carbon can be viewed as the basic structural element for other allotropes of carbon (Fig. 3.1): (1) the graphene layers are stacked upon each other via van der Waals force to form three-dimensional graphite [Geim 2007]; (2) a graphene sheet is rolled up to form a one-dimensional carbon nano-tube [Belin 2005, Dresselhaus 1992]; (3) the boundary of a graphene area are sew together to form the zero-dimensional Fullerenes [Kroto 1985].

Graphene has a hexagonal lattice formed by carbon atoms with two inequivalent atoms A and B in its primitive unit cell defined by the unit vectors $\boldsymbol{a_1}$ and $\boldsymbol{a_2}$ (Fig. 3.2). The distance between two nearest carbon atoms is a_0 =1.42 Å. The coordinates of the primitive lattice vector in the $\boldsymbol{xy}$ cartesian frame are

$$\boldsymbol{a_1} = a(\frac{\sqrt{3}}{2}, \frac{1}{2}), \boldsymbol{a_2} = a(\frac{\sqrt{3}}{2}, -\frac{1}{2}) \tag{3.1}$$

with the lattice constant $a = \sqrt{3}a_0$ =0.24 nm.

The reciprocal graphene lattice is also a honeycomb-like lattice. The primitive

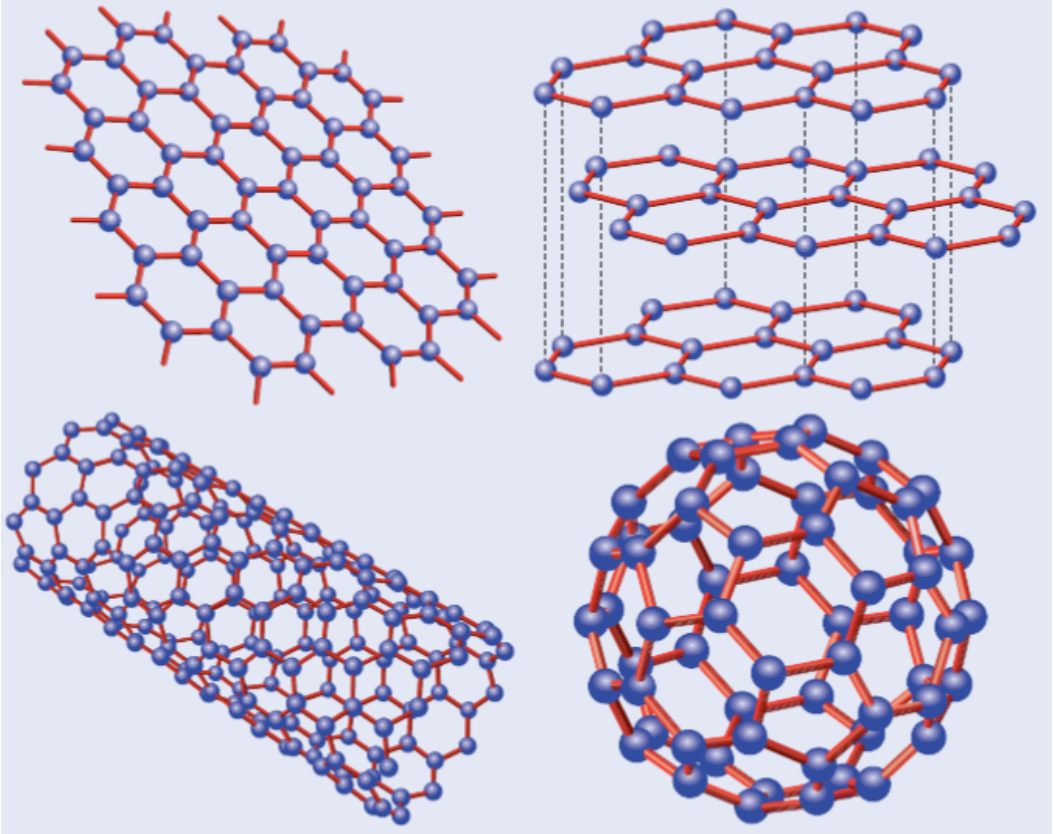

Figure 3.1: Atomic structure of carbon allotropes: Graphene, Graphite, Carbon nanotubes and Fullerenes. Extracted from [Castro Neto 2006].

vectors defined by $a_i b_j = 2\pi\delta_{ij}$ can be written as

$$\boldsymbol{b_1} = \frac{2\pi}{a}(\frac{1}{\sqrt{3}}, 1), \boldsymbol{b_2} = \frac{2\pi}{a}(\frac{1}{\sqrt{3}}, -1) \tag{3.2}$$

The first Brillouin Zone(BZ) is hexagonal, centered at the Γ point and cornered by the K and the K′ points. The coordinates of the K and K′ points with respect to the Γ point are

$$\boldsymbol{K} = (\frac{2\pi}{3a}, \frac{2\pi}{3\sqrt{3}a}), \boldsymbol{K'} = (\frac{2\pi}{3a}, -\frac{2\pi}{3\sqrt{3}a}) \tag{3.3}$$

3.1.2 The Dirac-like energy dispersion

The band structure of graphene can be calculated using the tight banding approximation [Wallace 1947, McClure 1956], considering hopping between the nearest-neighbor atoms. The three nearest-neighbor vectors in the real space are given by

$$\boldsymbol{\delta_1} = a(1, 0), \boldsymbol{\delta_2} = \frac{a}{2}(-1, \sqrt{3}), \boldsymbol{\delta_3} = \frac{a}{2}(-1, -\sqrt{3}), \tag{3.4}$$

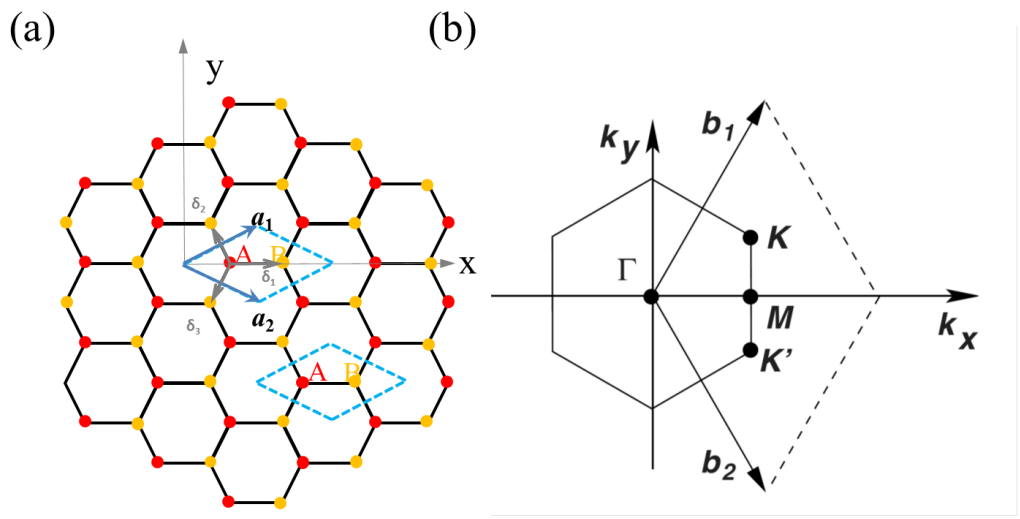

Figure 3.2: (a) Honeycomb lattice of graphene. The vectors $\boldsymbol{\delta_1}$, $\boldsymbol{\delta_2}$, and $\boldsymbol{\delta_3}$ connect the nearest-neighbors (NN) carbon atoms, separated by a distance a=0.142 nm. The vectors $\boldsymbol{a_1}$ and $\boldsymbol{a_2}$ are basis vectors of the triangular Bravais lattice. (b) Reciprocal lattice of the triangular lattice. The primitive lattice vectors are $\boldsymbol{b_1}$ and $\boldsymbol{b_2}$. The first Brillouin zone (BZ) is characterized by its center Γ and the two inequivalent corners K and K′. Extracted from [Castro Neto 2009, Mousavi 2014].

In the framework of the tight-binding model, the potential of the atoms is so large that the electrons are tightly bound to ionic cores and they can only hop between the nearest neighboring atoms [Finnis 2003]. The electron wavefunction ϕ in graphene lattice can be written as a linear combination of atomic wave functions for isolated carbon atoms arranged in a hexagonal lattice. Because of the presence of the two inequivalent atoms (A and B) in the unit cell, the electron wavefunction in graphene is a linear combination of the Bloch wave functions of the two corresponding atomic wave function $\phi_A(\boldsymbol{k}, \boldsymbol{r})$ and $\phi_B(\boldsymbol{k}, \boldsymbol{r})$:

$$\Psi(\boldsymbol{k}, \boldsymbol{r}) = \sum_{\alpha=A,B} c_\alpha(\boldsymbol{k}) \Phi_\alpha(\boldsymbol{k}, \boldsymbol{r}) \tag{3.5}$$

with

$$\Phi_\alpha(\boldsymbol{k}, \boldsymbol{r}) = \frac{1}{\sqrt{n}} \sum_R e^{-i\boldsymbol{k}\cdot R} \phi_\alpha(\boldsymbol{r} - \boldsymbol{R})$$

Here n is the number of unit cells, $\boldsymbol{R}$ runs over all possible linear combinations of the primitive lattice vectors and $\phi_\alpha(\boldsymbol{r} - \boldsymbol{R})$ is the π-orbital wavefuction at the α =A, B carbon atom site. We note that within the sp^2 hybridization of carbon atoms forming a graphene sheet, only the out-of-plane π bond will be considered. The three in-plane σ bonds ensure the cohesion of the graphene crystal and give rise to high energy bands which can be omitted for the description of the electronic

properties. It is worth noting that the hexagonal lattice of graphene can be viewed as the superposition of two triangular sublattices, containing identical carbon atoms.

In Fig. 3.2, we observe that a carbon atom of sublattice A(B) has three nearest neighbor atoms belonging to the sublattice B(A). Therefore the tight binding Hamiltonian is written as

$$H = -t \sum_{\langle i,j \rangle, \boldsymbol{s}} (a^{+}_{\boldsymbol{s},i} b_{\boldsymbol{s},j} + H.c.) \tag{3.6}$$

where $a_{i,\boldsymbol{s}}$ ($b_{i,\boldsymbol{s}}$) and $a^{+}_{i,\sigma}$($b^{+}_{i,\sigma}$) represent the anihilation and creation of an electron with spin $\boldsymbol{s}(\boldsymbol{s} = \uparrow, \downarrow)$ on site $\boldsymbol{R}_i$ on A(B) sublattice. The parameter t is the nearest-neighbor hopping energy (hopping between different sublattices) which is around 2.7 eV [Reich 2002]. The solution of the Shrödinger equation with Hamiltonian (Eq. 3.6) and wavefunction (Eq. 3.5) yields the energy band structure of graphene:

$$E_{\pm}(\boldsymbol{k}) = \pm t\sqrt{3 + f(\boldsymbol{k})} \tag{3.7}$$

where

$$f(\boldsymbol{k}) = 2cos(\sqrt{3}k_x a) + 4cos(\frac{\sqrt{3}}{2}k_y a)cos(\frac{3}{2}k_x a). \tag{3.8}$$

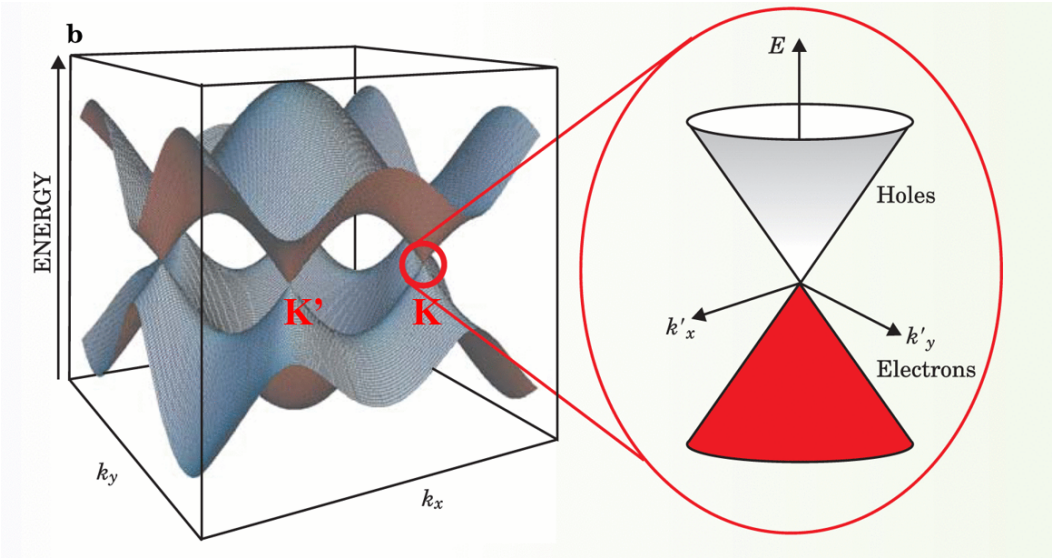

Figure 3.3: Energy dispersion of graphene in the first Brilouin zone from the tight-binding approximation calculation (left). A zoom of one of the Dirac point is shown (right), where the Dirac cone is evidenced. Extracted from [Wilson 2006].

In Eq. (3.7), the plus sign applies to the upper (conduction) band and the minus sign the lower (valence) band. The full band structure is plotted in the left inset of Fig. 3.3, where the upper and lower bands cross at the corners (three equivalent points K and three equivalent points K$'$) of the first Brillouin Zone. In

the vicinity of these crossing points, the energy spectrum shows a linear dispersion relation and the energy gap is zero at $\boldsymbol{k} = \mathbf{K}$. Close to the K (or K$^{'}$) points, we set $\boldsymbol{k} = \mathbf{K} + \boldsymbol{q}$, with $\mid \boldsymbol{q} \mid \ll \mid \mathbf{K} \mid$, where $\mathbf{K}$ is the crystal momentum. The dispersion relation can be developed into

$$E_{\pm}(\mathbf{k}) = E_{\pm}(\mathbf{K} + \mathbf{q}) = \pm\frac{3}{2} \mid t \mid aq + O(q^2) \approx \hbar v_F \mid \mathbf{q} \mid \tag{3.9}$$

where $\boldsymbol{q}$ is the momentum measured relatively to the crossing points and $v_F = 3ta/2\hbar \simeq 1 \times 10^6 m/s$. Alternatively the effective Hamiltonian around the K and K$^{'}$ points is

$$H(q) = \frac{3}{2}ta \begin{pmatrix} 0 & \pm q_x + iq_y \\ \pm q_x - iq_y & 0 \end{pmatrix} = \pm\hbar v_F \boldsymbol{\sigma} \cdot \boldsymbol{q} \tag{3.10}$$

where the σ is the Pauli matrix. The $\mathbf{K}$ and $\mathbf{K}^{'}$ points are called the Dirac points and the dispersion relation around the Dirac point are called the Dirac cones. The zero gap indicates that graphene can be continously switched from negative charge carriers (electrons) to positive charge carriers (holes) by tuning the Fermi energy with respect to the Dirac cone, while the linear energy dispersion relation mimics the behaviors of relativistic massless half-spin particles as in the case of neutrinos in high energy physics. The peculiar electronic structure of graphene plays a central role in the transport properties, with no analogue in condensed-matter physics.

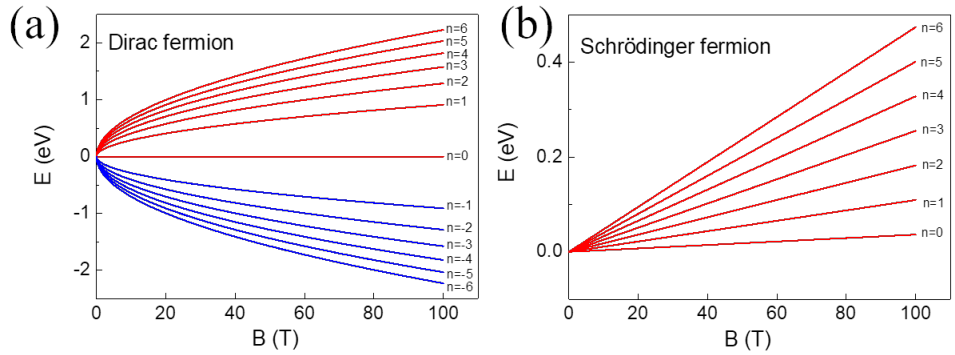

Figure 3.4: The Landau energy spectrum of (a) Dirac fermions and (b) Schrödinger fermions in magnetic field.

3.1.3 The Landau levels of graphene

Let us consider the energy spectrum of graphene in perpendicular magnetic field. The Hamiltonian 3.10 of graphene in a magnetic field can be written as

$$H(\Pi) = \pm v_F(\Pi_x \sigma^x + \Pi_y \sigma^y) \tag{3.11}$$

with $\Pi_x = \frac{\hbar}{\sqrt{2}l_B}(a^+ + a)$ and $\Pi_y = \frac{\hbar}{i\sqrt{2}l_B}(a^+ - a)$. The energy eigenvalues are [McClure 1956]

$$E_n = \pm\sqrt{2e\hbar v_F^2 \mid N \mid B} \tag{3.12}$$

where N is the Landau level index. This Landau level spectrum (shown in Fig. 3.4) is quite different from the conventional Landau energy ladder of Schrödinger fermions (Eq. 1.46), and in particular the non-equidistant energy gaps between LLs and the B-independent zero energy of the zeroth Landau level. The large energy gap between the zeroth Landau level and the first Landau level $E_1 - E_0 = \sqrt{2e\hbar v_F^2 B}$ allows us to observe the integer quantum Hall effect in graphene at room temperature, for moderate (30 T) magnetic field [Novoselov 2007].

3.1.4 The quantum Hall effect in graphene

The integer quantum Hall effect in graphene was observed experimentally by Novoselov *et al.* [Novoselov 2005] and Zhang *et al.* [Zhang 2005] in exfoliated graphene on Si/SiO_2 substrate. Unlike the integer quantum Hall effect in conventional semiconductors [Klitzing 1980], the Hall resistance shows a series of plateaus $R_{xy}^{-1} = \pm 4(N + \frac{1}{2})\frac{e^2}{h}$ (Fig. 3.5) at filling factor

$$\nu = \pm 4(N + \frac{1}{2}), N = 0, \pm 1, \pm 2... \tag{3.13}$$

Here the number 4 corresponds to the 2-fold spin and 2-fold valley (pseudospin) degeneracy in graphene, and the factor $\frac{1}{2}$ is a result of the zeroth Landau Level being equally populated by both electrons and holes.

Soon after the report of the anomalous half-integer quantum Hall effect in graphene, new quantum Hall states at ν=0, ±1, ±4 were observed under high magnetic field ($B > 20$ T) corresponding to a lifting of the spin and valley degenerate Landau levels (see Fig. 3.6). Zhang *et al.* [Zhang 2006] attributed the $\nu = \pm 4$ states to the spin degeneracy lifting within a single particle description. Jiang *et al.* [Jiang 2007] claimed that the $\nu = \pm 1$ states originate from the valley degeneracy lifting driven by the electron-electron interactions, and the ν=0 relates to the spin degeneracy lifting. In high mobility samples deposited on hexagonal Boron Nitride (hBN), the quantum Hall effect was observed at all the integer filling factors [Young 2012] since the small energy gaps between the non-degenerate LL are not hidden anymore by energy broadening effects due to disorder. The lifting of $n = 0$ Landau level is complex and involves ferromagnetic states with entangled spin and valley states.

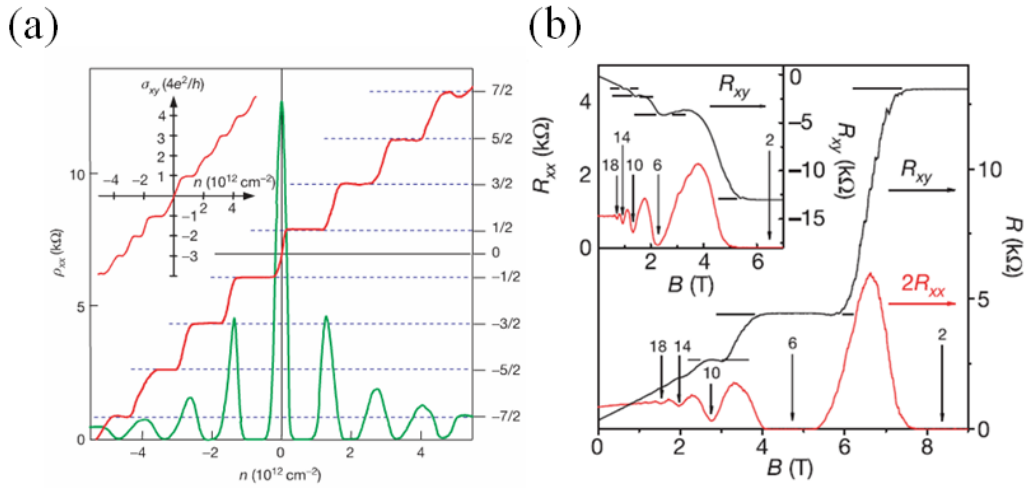

Figure 3.5: (a) The longitudinal resistivity ρ_{xx} and the Hall conductivity σ_{xx} as a function of the carrier density in mono-layer graphene at $B = 14$ T and $T = 4$ K. The inset shows the Hall conductivity σ_{xx} for a bi-layer graphene. The quantum Hall plateau appears at filling factor $\nu = \pm 4(N + \frac{1}{2})$ in mono-layer graphene and at $\nu = \pm 4N$ in bi-layer graphene. Extracted from [Novoselov 2005]. (b) The quantum Hall effect in n-doped (p-doped in the inset) mono-layer graphene as a function of magnetic field. Extracted from [Zhang 2005].

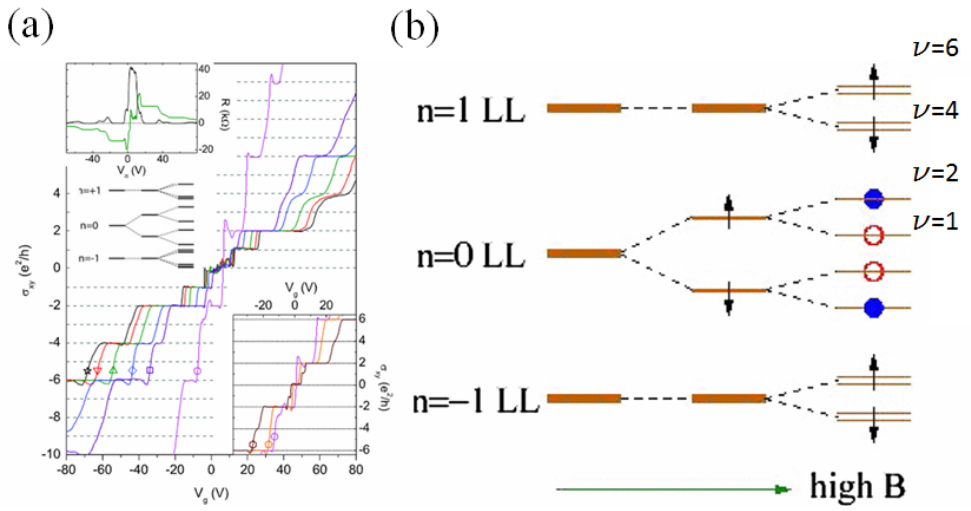

Figure 3.6: (a) The quantum Hall effect in graphene measured at different magnetic fields. New plateaus at filling factor $\nu = 0, \pm 1, \pm 4$ are resolved at higher magnetic field ($B > 20$ T). (b) The hierarchy of the Landau levels of graphene under magnetic field. The up (down) arrows indicate the spin of the charge carriers and the solid (open) dots indicate the different valley. The plateaus at $\nu = \pm 4$ are a result of spin degeneracy lifting and $\nu = \pm 1$ are associated to the valley degeneracy lifting. Extracted from [Zhang 2006, Jiang 2007].

3.2 Graphene on Silicon Carbide

Graphene is a promising candidate to replace the Si-FET and III-V semiconductors based heterostructures to define the international standard of resistance, in terms of the electron charge e and the Planck's constant h. In the quantum Hall regime, the Hall resistance, which is an integer fraction of the exact value $R_K = h/e^2$, is accurate, universal (material-independent) and robust (constant over a broad range of magnetic field, temperature and current). The highest experimental accuracy achieved in exfoliated graphene flakes on SiO_2 is 5×10^{-7} at 350 mK by Guignard *et al.* at filling factor $\nu = 2$ [Guignard 2012]. It is still far from the metrological required accuracy of 10^{-9} [Delahaye 2003]. The main issue for exfoliated graphene being an appropriate system to define the resistance standard is the small area of the flakes which limits the maximum non-dissipative current to sustain the system in the quantum Hall state. In a special designed graphene on GaAs substrate, Woszczyna *et al.* [Woszczyna 2012] even achieved a precision of 6×10^{-9} at 60 mK in a large size graphene sample. However, the breakdown current of 10 μA is too small compared with the quantum Hall breakdown current in other semiconducting quantum Hall resistance standard systems.

During the past decade, many other methods have been developed to produce graphene, such as chemical vapor deposition (CVD) [Bae 2010], SiC sublimation [Berger 2006], or the exfoliation of graphene from graphite by chemical exfoliation methods [Eda 2008, Hernandez 2008]. The CVD and the SiC sublimation methods can produce large areas of graphene up to a few centimeters square compatible with the scale-up requirements of the electronic industry. The quantum Hall effect in graphene on SiC substrate shows the same Hall resistance plateaus as graphene on SiO_2 substrate at filling factor of $\nu = 4(N + \frac{1}{2})$ [Wu 2009, Shen 2009, Tzalenchuk 2010, Lafont 2015]. However, a very broad plateau at filling factor $\nu = 2$ is observed [Jobst 2010, Janssen 2011, Alexander-Webber 2013]. The epitaxial graphene on SiC substrate was thus proposed [Tzalenchuk 2010] and realized [Ribeiro-Palau 2015] as the candidate to overcome the impediments of exfoliated graphene, taking the advantages of the large sample area and the unique interaction between the graphene layer and the SiC substrate [Kopylov 2010].

Our aim is to investigate the robustness of the $\nu = 2$ quantum Hall regime under very high field, to unveil the role of the charge transfer between graphene and its substrate and to identify the mechanisms governing the breakdown of the quantum Hall effect at large current density.

3.2.1 Epitaxial growth of graphene on Silicon Carbide

The samples were grown by Graphensic AB company on a 4H-SiC substrate through the SiC sublimation method. When heated up to high temperature (above 1500°C) under ultra high vacuum, the surface of SiC crystals undergo decomposition due to sublimation. Since silicon has the highest vapor pressure, the Si atoms will sublimate from the surface of the SiC and leave carbon atoms at the surface.

The remaining carbon atoms will re-bond together to form one or several layers with honeycomb-lattice symmetry possessing in-plane sp^2 bonding. During the SiC sublimation, the graphene formation conditions and the resulting electronic properties are quite different for the two substrate faces which are terminated either by Si or C atoms. The formation of graphene on the C-face is very rapid at the growth temperature of 1500-1650 °C in vacuum. On this face, there will be domains of multilayer graphene with size of several microns. They are mostly p-doped with a typical Hall mobility of 5000-6000 cm^2/Vs. On the other hand, the formation of graphene on the Si-face starts at 1550 °C, is much slower and more homogeneous than on the C-face. The graphene layers on the Si-face are always n-doped with a mobility of 1300-1600 cm^2/Vs due to the doping of a $6\sqrt{3} \times 6\sqrt{3}$ supercell layer of "dead" carbon layer under the first graphene layer, which will be further refereed as the "buffer layer". The slower graphene formation rate on the Si-face makes the formation process controllable in order to obtain a homogenous single layer graphene. Moreover, depending on the SiC sublimation conditions, the buffer layer shows different levels of defects. Under lower growth temperature ($T \sim 1600°C$), the buffer layer shows more defects resulting in a highly n-doped graphene whereas under higher temperature (2000°C) and in high argon pressure, it shows an improved integrity with little n-doping effect. Our studies are focused on graphene grown on the Si-face under argon atmosphere.

3.2.2 Sample preparation

After the graphene growth by SiC sublimation, the samples are coated with PMMA (poly methylmethacrylate-co-methacrylate acid) layer for patterning using electron-beam lithography. Oxygen reactive ion etching (RIE) is then applied to remove the graphene unprotected by the resist and to shape the device into a Hall bar. A bilayer of Pd/Au (60 nm/20 nm) is deposited in an electron-beam deposition system to form electrodes with Ohmic contacts to graphene, using the Ti layer for adhesion. Large bonding pads are formed with thicker Ti/Au (20 nm/200 nm) bilayer following a RIE etch which was performed prior to the metal deposition for better adhesion of the metal pads to the SiC substrate. The Hall bar has a width of 100 μm and a total length of 420 μm (Fig. 3.8(a)). It has three pairs of Hall probes, separated by 100 μm. Finally, the samples are covered for protection by 300 nm of PMMA layer. Next, a photo-chemical gate is applied with the coating of a 300 nm resist called ZEP520A (poly methylstyrene-co-chlor-omethylacrylate) on the top of the PMMA protection layer [Lara-Avila 2011, Tzalenchuk 2011]. The ZEP520A layer acts as a floating gate while the PMMA acts as spacer layer. Under deep ultraviolet (UV) light, the ZEP520A resist undergoes a photo-induced scission-type reaction and provides potent electron acceptors (Fig. 3.8(b)). As a consequence, the number of electrons in graphene is reduced very significantly by this gating. Annealing the samples at a temperature just above the glass transition temperature (170 °C) of the polymers reverses the effects of UV light and restores the electrons back to the graphene layer, returning the graphene carrier density back to its initial

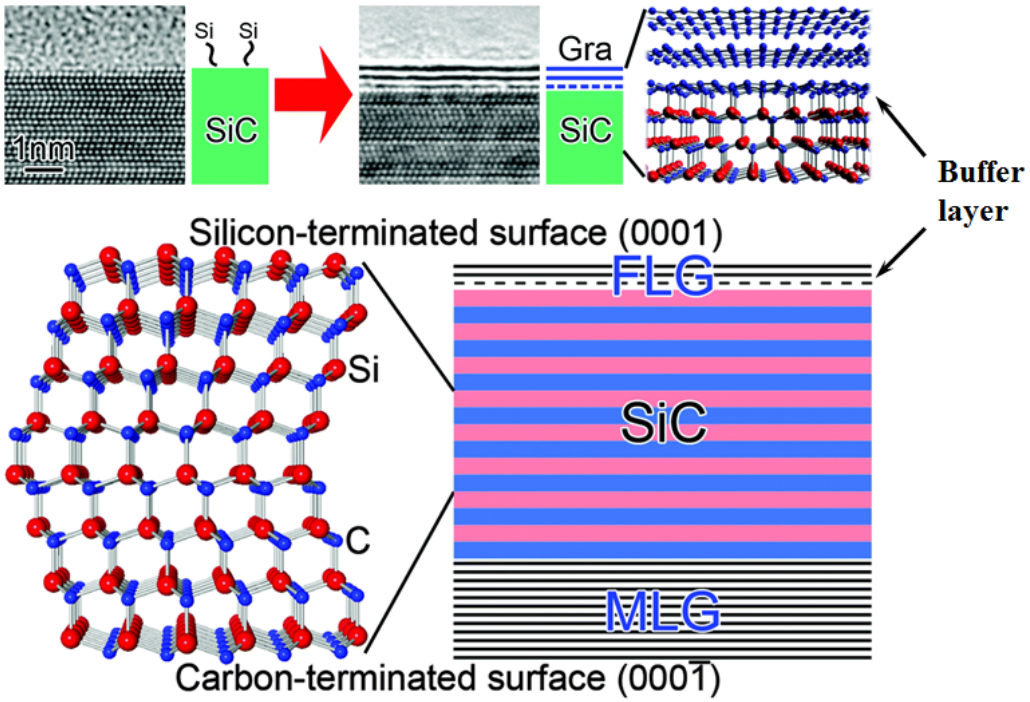

Figure 3.7: Epitaxial growth of graphene by SiC sublimation method. Upon heating, the Si atoms sublimate from the SiC surface, leaving the carbon atoms on the surface. On the C-face the growth rate is fast and results in multilayered graphene. The formation of graphene on the Si-face is slow and there is a buffer layer under the first layer of graphene. Extracted from [Norimatsu 2014].

value prior to UV exposure.

3.2.3 Charge transfer in graphene on Silicon Carbide

The presence of the buffer layer under the first graphene layer plays a very important role in the stabilization of the $\nu = 2$ quantum Hall plateau in a wide range of magnetic field. Indeed, the two layers are seperated only by a distance d=0.3 nm and interact via strong electrostatic coupling. A magnetic field dependent charge transfer between the buffer layer and graphene increases the carrier density in graphene and pins the filling factor at $\nu = 2$ in a large magnetic field range [Kopylov 2010, Janssen 2011]. This hypothesis ensures the alignment of the Fermi energy between the $N = 0$ and $N = 1$ LL. The charge transfer is driven by the difference in work function A between the undoped graphene and the buffer layer, treated as isolated systems. The amount of transferred charges from the buffer layer to graphene is equal to $(A - \varepsilon_F)\gamma$ where γ is the density of donor states per unit area in the buffer layer. In return, the graphene layer will be charged by a carrier density n_s. In addition, the chemical top gate modifies the carrier density in the graphene layer, so that n_s is actually replaced by $n_s + n_g$. Therefore, the charge

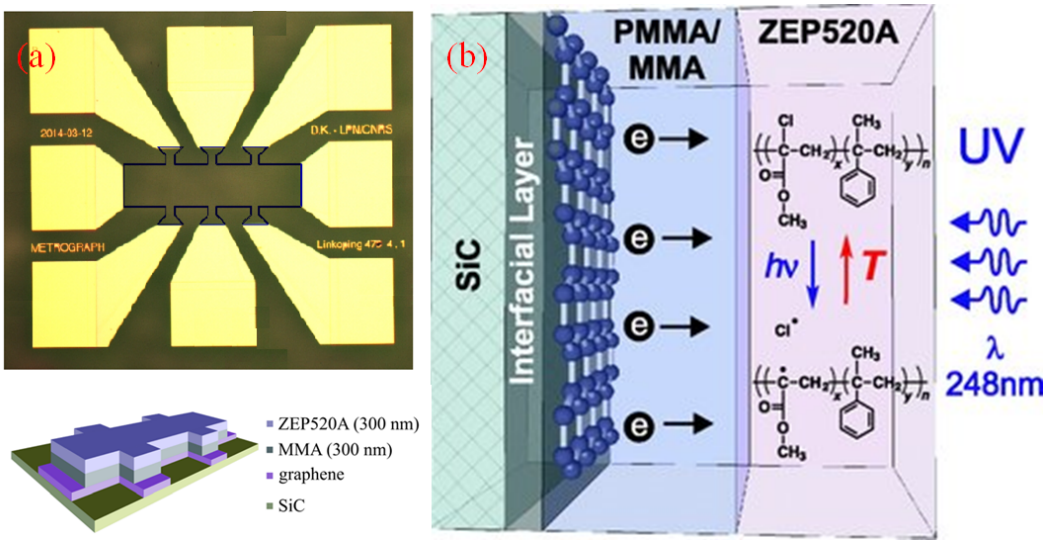

Figure 3.8: (a) The top view and side sketch of the graphene Hall bar. The sample has 3 pairs of Hall contacts seperated by 100 nm. The total length of the sample is 420 nm and the width is 100 nm. Graphene sample is then coated by PMMA/ZEP520A layer for photo chemical gating in order to tune the carrier density. (b) The mechanism of the photochemical gating methods with PMMA/ZEP520A resist. The resist will provide potent electron acceptors to reduce the electron carrier density under UV exposure and restore the electrons when heated up to the glass transition temperature. Extracted from [Yang 2016a, Lara-Avila 2011]

balance equation reads

$$(A - \varepsilon_F)\beta = n_s + n_g.$$

Since β links the energy of the system to the carrier density, an analogue with the plane capacitance model can be established. The term β can be rewritten in terms of a capacitance per unit area C through the relation

$$A - \varepsilon_F = \frac{1}{\gamma}(n_s + n_g) = \frac{e^2}{C}(n_s + n_g).$$

The capacitance per unit area in the system can be expressed in terms of the classical capacitance and quantum capacitance per unit area: $C_c = \frac{\epsilon_0}{d}$ and $C_q = \gamma_e e^2$ where ϵ_0 is the the vacuum permittivity and γ is the density of interface states. Thus we have

$$A - \varepsilon_F = e^2\left[\frac{1}{C_q} + \frac{1}{C_c}\right](n_s + n_g) = e^2\left[\frac{1}{\gamma_e e^2} + \frac{d}{\epsilon_0}\right](n_s + n_g)$$

$$A - \varepsilon_F = \frac{e^2 d}{\epsilon_0}(n_s + n_g) + \frac{1}{\gamma}(n_s + n_g)$$

Finally an alternative to the charge balance equation is

$$\gamma_e \left[A - \frac{e^2 d}{\epsilon_0}(n_s + n_g) - \varepsilon_F \right] = n_s + n_g \tag{3.14}$$

where the left-hand side accounts for the depletion of the surface donor states while the right-hand side sets the carrier density in graphene [Kopylov 2010].

In contrast to graphene deposited on SiO_2 or BN, the distance between the buffer layer and graphene is very small so that the quantum capacitance dominates the electrostatic coupling. Since the quantum capacitance depends on the magnetic field through a redistribution of the electronic states into Landau levels, the charge transfer between the buffer layer and graphene is also magnetic field dependent, as pointed out by Janssen *et al.* who reported an anomalous strong pinning of the filling factor at $\nu = 2$ for a broad range of magnetic field up to 15 T. They used Eq. 3.14 to determine the residual carrier density in graphene for an infinite magnetic field, *i.e.* when $\varepsilon_F = 0$. By adjusting the parameter n_g to their experimental results, they noticed that $n_\infty = \dfrac{A\beta}{1 + e^2\beta/C_c} - n_g$ can be up to 30 % higher than the initial carrier density at zero field (the parameters A and β were set to 0.4 eV and $\gamma = 5.04 \times 10^{12}$ eV^{-1}cm^{-2} respectively) (Fig. 3.9(b)). This observation confirms that a charge transfer takes place in graphene on SiC as the magnetic field varies and provides a natural explanation for the establishment of a broad Hall plateau at $\nu = 2$.

In the following, we will refine the above model and consider inhomogenously doped graphene samples. We extended the measurement up to 80 T on samples with lower carrier density in order to observe the breakdown of this anomalous broad Hall plateau. Furthermore, since the native carrier density n_s (*i.e.* without the influence of the chemical gate) of graphene could be measured together with $(n_s + n_g)$, we derive new values of A and γ (taken as fitting parameters) and we compare them to the literature.

3.3 Electronic properties of graphene on SiC

3.3.1 Temperature dependence at zero magnetic field

The temperature dependence of the longitudinal resistance $R_{xx}(T)$ is shown in Fig. 3.10. From room temperature to ∼100 K, R_{xx} decreases linearly. As the carrier density in the sample does not change with temperature (the low field Hall resistance remains constant), the linear decrease in R_{xx} was attributed to the suppression of the inelastic electron-phonon scattering. Below 50 K, the resistance shows an upturn with a logarithmic increase. This is the signature of weak localization when the phase coherence length l_ϕ exceeds the mean free path in the sample. The weak localization effect is also confirmed by the negative magnetoresistance under very low field (< 1 T) as shown in the inset of Fig. 3.10. The negative MR at low field range disappears at 60 K, which is consistent with the temperature evolution of the

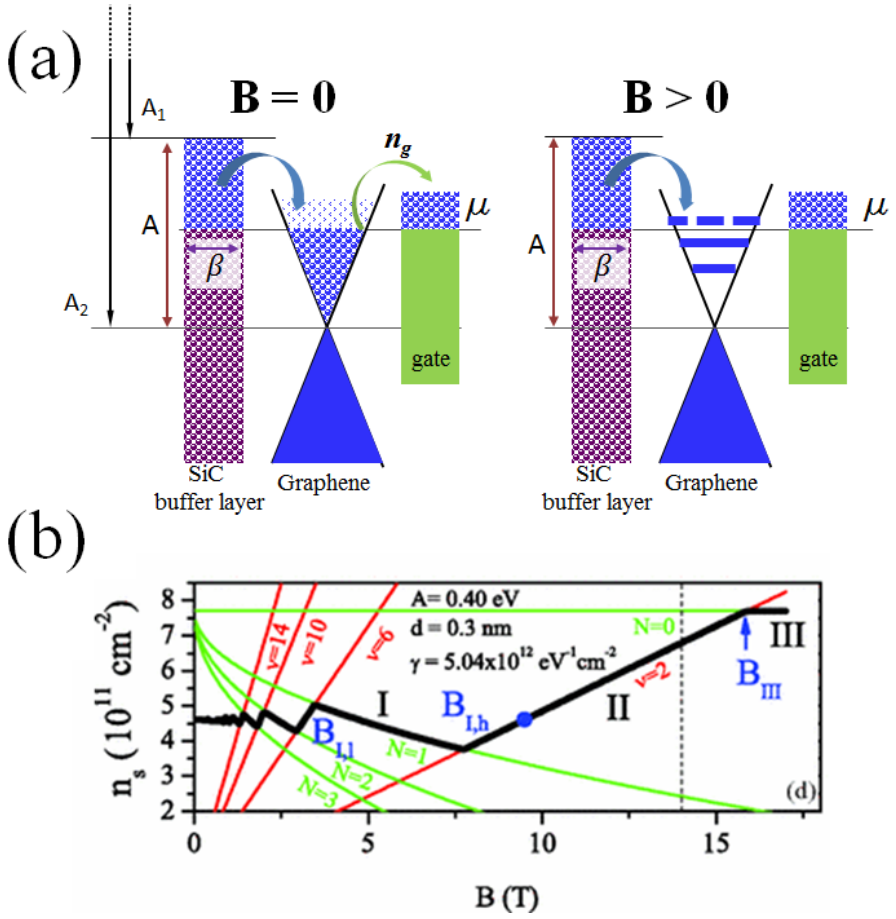

Figure 3.9: Sketch of the charge transfer model in graphene on SiC. (a) A_1 and A_2 represent the work function of isolated SiC buffer layer and isolated undoped graphene, respectively. At equilibrium, charges are transferred from the buffer layer to graphene in order to equilibrate the chemical potential μ. This effect is counterbalanced by the presence of a chemical gate on top of graphene, which reduce the carrier density by n_g. Under magnetic field, the chemical potential (Fermi level) is affected by the quantization of graphene density of states into LL, and thus the charge transfer is affected. (b) The carrier density (black curve) evolution as a function of magnetic field. The carrier density increases linearly from $B \sim 7.5$ T up to 16 T as a result of charge transfer from the surface donnor states of the SiC substrate. Extracted from [Janssen 2011].

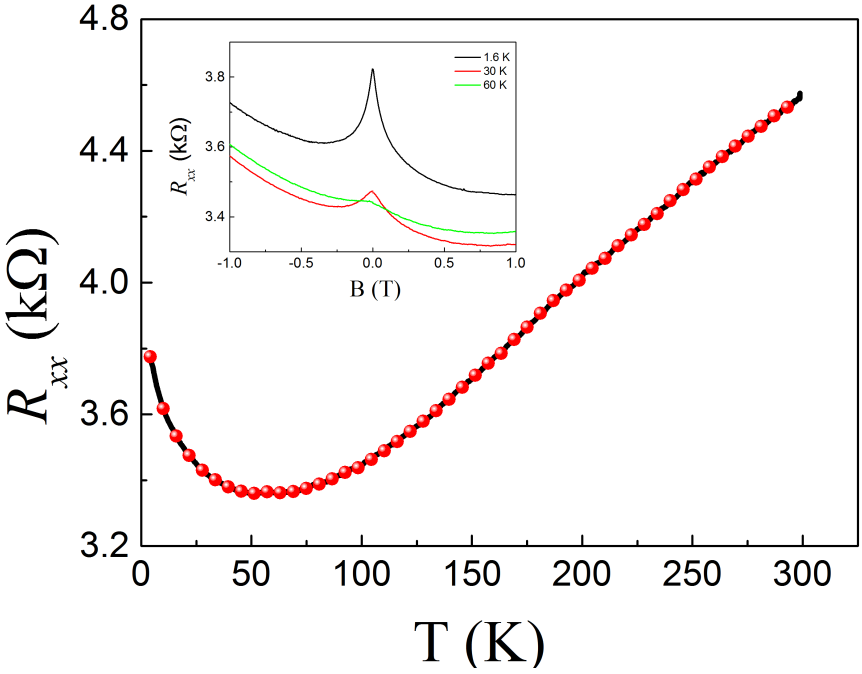

Figure 3.10: (a) The longitudinal resistance R_{xx}(T) as a function of temperature from 300 K to 4.2 K. The weak localization occurs at T $\simeq$ 50 K where R_{xx} shows a minimum. The inset shows the MR for three selected temperatures. The weak localization is visible in the range B $<$ 1 T at low temperature.

resistance at zero field, where the upturn occurs at 50 K.

The weak localization in graphene has been predicted different from conventional 2DEG: it is not only dominated by the inelastic scattering, but also depends on the elastic intervalley scattering since this process conserves the chirality of the electrons [McCann 2006]. Depending on the intervalley scattering rate, graphene shows a presence of weak localization or a suppression of weak localization [Morpurgo 2006]. In the graphene sample obtained by mechanical exfoliation method, the intervalley scattering is weak and the π Berry phase contributes to antilocalization [Morozov 2006]. For epitaxial graphene, the warping of the graphene layers brings deformation of the band structure and cancels the contribution of the antilocalization. Thus, together with the inelastic scattering, a weak localizaiton is observed [Wu 2007].

3.3.2 Longitudinal and Hall resistance in the QH regime

Fig. 3.11 shows the longitudinal and Hall resistances R_{xx} and R_{xy} measured as a function of the magnetic field at temperature T = 4.2 K. The longitudinal resistance is normalized to a square. For $B \geq$ 7 T, an extremely wide quantum

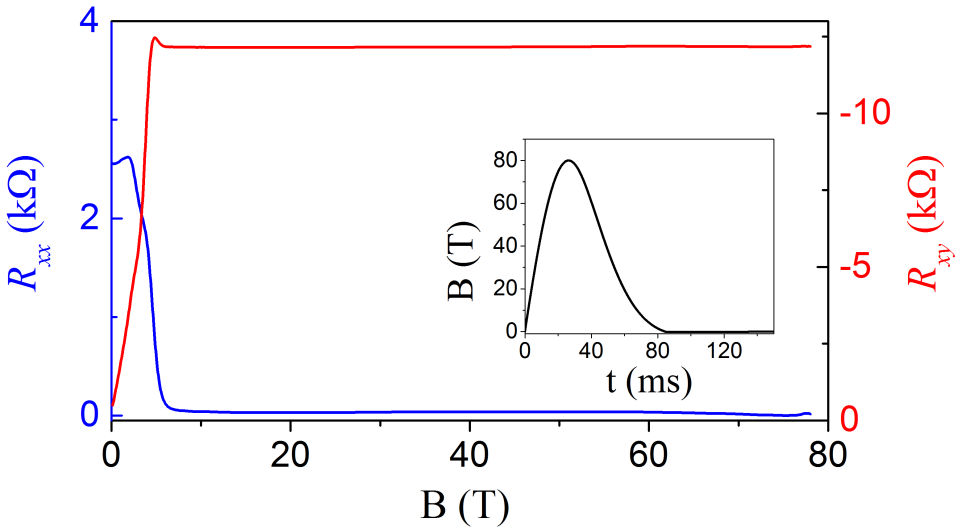

Figure 3.11: Longitudinal resistance R_{xx} and Hall resistance R_{xy} measured at T = 4.2 K up to B = 78 T, with a current I = 20 μA. Inset: pulse of magnetic field used in this experiment.

Hall plateau at $R_{xy} = h/2e^2$ is observed up to the highest available magnetic field (78 T). As expected, the quantum Hall plateau coincides with a complete vanishing of R_{xx}. A small mixing between R_{xx} and R_{xy}, due to the anisotropy of the conductivity induced by the SiC steps [Schumann 2012][Pallecchi 2014], is noticed as a small additional bump in R_{xy} at $B \simeq 7$ T. This mixing can been removed by (anti)symmetrizing the measured resistances recorded in the two opposite directions of the magnetic field: $\bar{R}_{xx(xy)} = [R_{xx(xy)}(B) \pm R_{xx(xy)}(-B)]/2$ as shown in Fig. 3.12.

This phenomenon is in qualitative agreement with the model proposed in [Kopylov 2010], based on a charge transfer taking place between graphene, the chemical gate, and the interface states between SiC and graphene. In particular, it was shown in [Alexander-Webber 2013, Janssen 2011, Lafont 2015] that the carrier concentration in similar systems can increase by 30 % from B = 0 T to B = 16 T, stabilizing the Fermi level in between the N = 0 and N = 1 LL for a broad range of magnetic field. However, at higher magnetic fields, when only the zeroth LL located is populated, the model predicts a saturation of the electron density, which is hardly compatible with our experimental findings. Indeed, by assuming a constant carrier density $n = 8.5 \times 10^{11}$ cm^{-2} at $B_{min} \sim 18$ T, we would have $\nu = 0.45$ at B = 78 T. Therefore, the large plateau observed in Fig. 3.11 questions the charge transfer model and deserves further attention.

3.3.3 Temperature dependence of magneto resistance in the QH regime

Fig. 3.12 shows the symmetrized magnetoresistances at different temperatures. The longitudinal resistance $\bar{R}_{xx}$ has a minimum around $B_{min} \simeq 18$ T when T increases above 30 K. We assume that, as in two-dimensional semiconductor systems, this minimum occurs when the Fermi energy is at midgap between two adjacent Landau levels. This implies that the filling factor ν equals 2 at B_{min} and the carrier density increases from $3.4 \times 10^{11} cm^{-2}$ (the initial carrier density is extracted from the classical Hall effect) at $B = 0$ T up to $8.5 \times 10^{11} cm^{-2}$ at $B = B_{min}$.

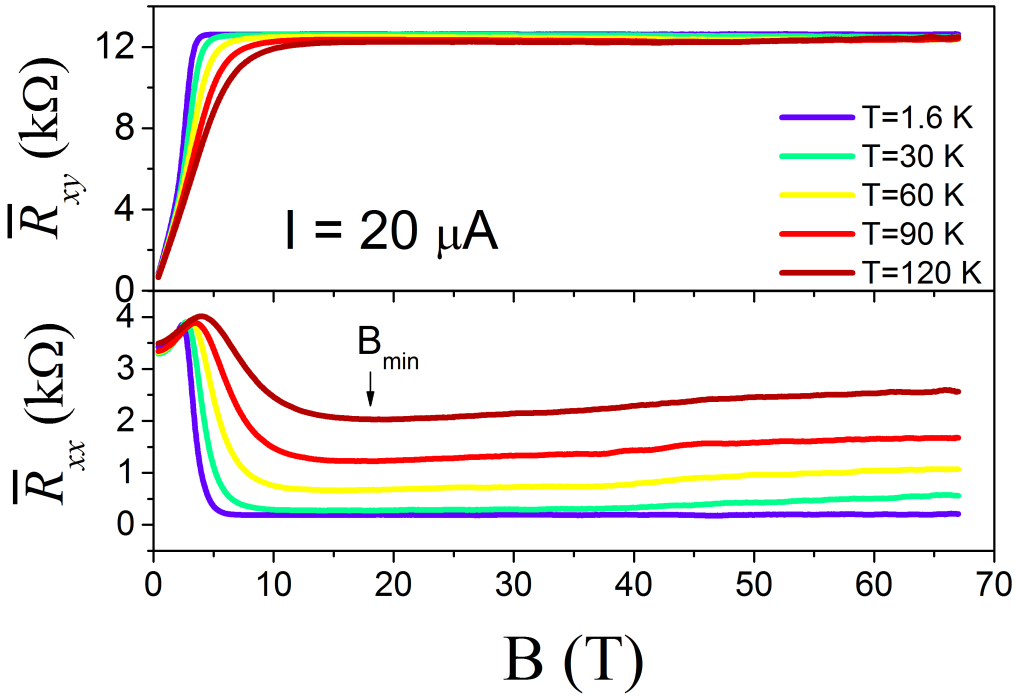

Figure 3.12: Longitudinal and transverse symmetrized resistances from T= 1.6 K up to T = 120 K. A current of 20 μA was used.

At low temperature, charge transport in the quantum Hall regime is often described by the Efros-Shklovskii Variable Range Hopping (ES-VRH) theory [Efros 1975, Shklovskii 1984], where the conductivity reads

$$\sigma_{xx} = \frac{\sigma_0}{T} exp(-(T_0/T)^{\frac{1}{2}}) \tag{1.68}$$

Here, σ_0 is a characteristic parameter, T_0 is the hopping temperature, which is related to the localization length ξ by the relation $k_B T_0 = Ce^2/4\pi\epsilon_r\epsilon_0\xi$, ϵ_0 is the

vacuum dielectric constant; $\epsilon_r \simeq 7$ is the relative dielectric constant averaged between the dielectric constants of the resist and SiC; and C $\simeq$ 6.2 is a constant [Furlan 1998]. ES-VRH has already been observed in various graphene samples below $T = 100$ K [Lafont 2015, Giesbers 2008, Bennaceur 2012, Janssen 2013]. In Fig. 3.13, $T\sigma_{xx}$ vs $\frac{1}{\sqrt{T}}$ is plotted for different magnetic fields. The analysis shown in Fig. 3.13(a) uses only the data in the range $T \geq 30$ K, where measurement errors are negligible, and $T \leq$120 K, where conduction by activation to the extended states can be safely neglected. The data are satisfactorily fitted by the above equation over two decades.

A close look at Fig. 3.13(a) reveals that the experimental data points taken at the highest temperature (120 K) are not perfectly aligned with the others. At these high temperatures, thermal activation (TA) should be taken into account to get a perfect fit of most of the data collected on these samples. In Fig. 3.13(b), we performed a more complex fit, which includes both ES-VRH and TA given by $\sigma_a = \sigma_a^0 exp(-E_a/k_BT)$. The data fit with the ES-VRH contribution alone was already fair; however the fit with the combined TA and ES-VRH contributions becomes excellent, as expected with additional fitting parameters.

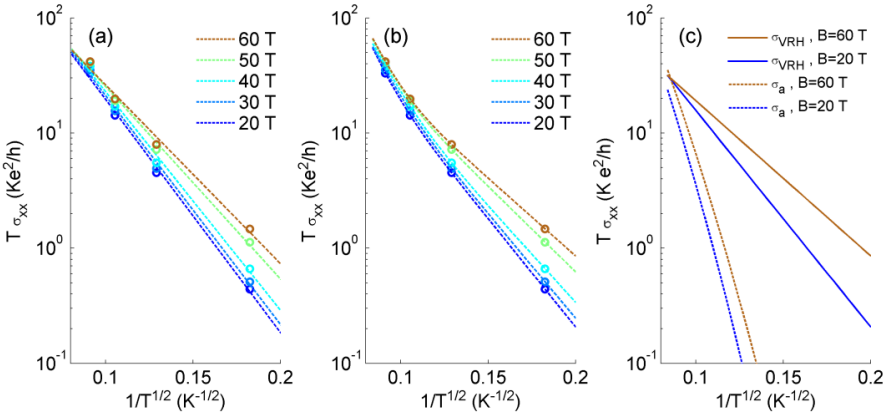

Figure 3.13: (a) Open symbols: measured conductivity $T\sigma_{xx}$ *vs* $T^{-1/2}$ from B = 20 T up to B = 60 T with a step of 10 T. Dashed lines: linear fits with the ES-VRH model. (b) The VRH fitting of the same data in (a), considering the effect of the thermal activation, which can improve the fit for high temperature range (T > 100 K). (c) The contribution of the VRH and TA (Thermal activation) to the conductivity at B=20 T and 60 T. The TA component is negligible compared to the VRH one at low temperature (T<100 K).

For each value of the magnetic field, the localization length ξ, the σ_0 coefficient and the hopping temperature T_0 are extracted from the VRH fits, in Figs. 3.14(a) and 3.14(b). At low magnetic field $B \simeq 20$ T, ξ is comparable to the magnetic length $l_B = \sqrt{\hbar/eB}$. At higher magnetic field, ξ increases only slightly. In the quantum Hall regime, the localization length is expected to vary accord-

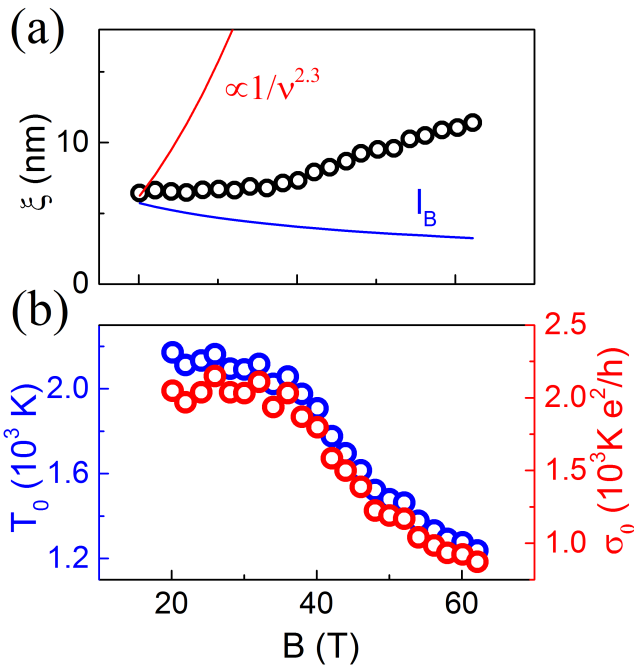

Figure 3.14: (a) Open symbols: localization length ξ extracted from the VRH fit. The blue and red lines are the magnetic length l_B and the quantum percolation theory prediction $\sim 1/\nu^{2.3}$, respectively. (b) Parameters T_0 and σ_0 extracted from the VRH fits.

ing to $\xi \propto \Delta E^{-\gamma}$, where ΔE is the mobility gap between the nearest delocalized states and the Fermi energy and $\gamma = 2.3$ is the quantum percolation exponent [Huckestein 1995]. Assuming a constant charge density and a density of localized states independent of energy, the localization length ξ_B^{TH} would vary as $1/\nu^{2.3} \sim B^{2.3}$, yielding $\xi^{th}_{B=60T}/\xi^{th}_{B=20T} \simeq 12$. By contrast, the experimental variation of ξ in the 20-60 T range is about $\xi^{th}_{B=60T}/\xi^{th}_{B=20T} \simeq 2$, thus suggesting a carrier density increase even for $B > B_{min}$.

3.4 Anomalous oscillations of the magnetoresistance

3.4.1 Experimental features

The breakdown of the quantum Hall effect in graphene/SiC has also been investigated while varying the current in the range 50-400 μA (see Fig. 3.15). Significant deviations of R_{xx} and R_{xy} from the zero resistance and $h/2e^2$ respectively, are noticed when the current is large. At $I = 100$ μA, $R_{xx} > 3$ Ω over the whole magnetic field range, yielding a longitudinal voltage ($V_{xx} > 300$ μV) too large to be compatible with metrological measurements. This defines a critical breakdown current density $j_c \simeq 1$ A/m, one order of magnitude lower than the highest reported values for graphene on SiC [Alexander-Webber 2013].

Furthermore, in the quantum Hall breakdown regime, the magnetoresistance shows weak oscillations instead of a flat minimum associated to the $\nu = 2$ quantum Hall state. The oscillations are 1/B-periodic (shown in Fig. 3.17(a)) with a frequency $f = 128$ T corresponding to a carrier density $n = 1.15 \times 10^{13}$ cm^{-2} through the Onsager relation $n = 4(e/h)/\Delta(1/B)$. Such a carrier density is very close to

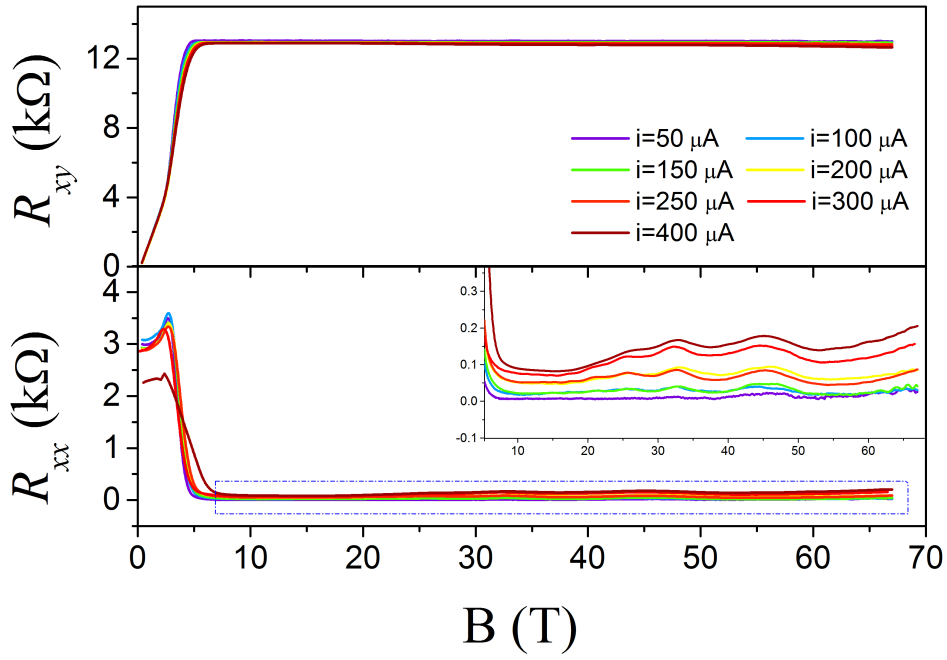

Figure 3.15: The current dependence of the longitudinal and transverse resistance in the quantum Hall breakdown regime. The inset shows the derivation of the longitudinal resistance from zero in the quantum Hall regime. 1/B periodic oscillations are visible and the amplitude of the oscillations increases as the current increases.

the as-grown sample before the photo-chemical gating, which was of the order of 10^{13} cm^{-2}. The current dependence of the amplitude of the oscillations deserves attention. As shown in Fig. 3.15, the amplitude becomes stronger as the current increases. This behavior is in contradiction with the basic properties of Shubnikov-de Haas oscillations, where a current increase results in the amplitude damping due to heating. As discussed below, we will demonstrate that these oscillations do not compare with SdH oscillations, and that their origin is rather linked to complex phenomena involving the breakdown of the quantum Hall regime.

3.4.2 Temperature dependence

In order to get more insights on the origin of the anomalous resistance oscillations, temperature dependence measurements have also been performed for a current of I= 150 μA close to the quantum breakdown regime (Fig. 3.16). Overall, the R_{xx} shows a similar behavior as compared to low current in Fig. 3.12 but additional 1/B periodic oscillations are superimposed. The magnetoresistance at T = 40 K, with the strongest oscillation amplitude, is plotted as a function of the inverse magnetic field in Fig. 3.17(a). Vertical dashed lines provide evidence for

the perfect 1/B periodicity of the oscillations. The oscillations persist up to very high temperature T = 120 K. Contrary to SdH theory, the oscillation amplitude first increases as the temperature increases, reaches a maximum at T=40 K and then decreases to zero at 120 K (Fig. 3.17(c)).

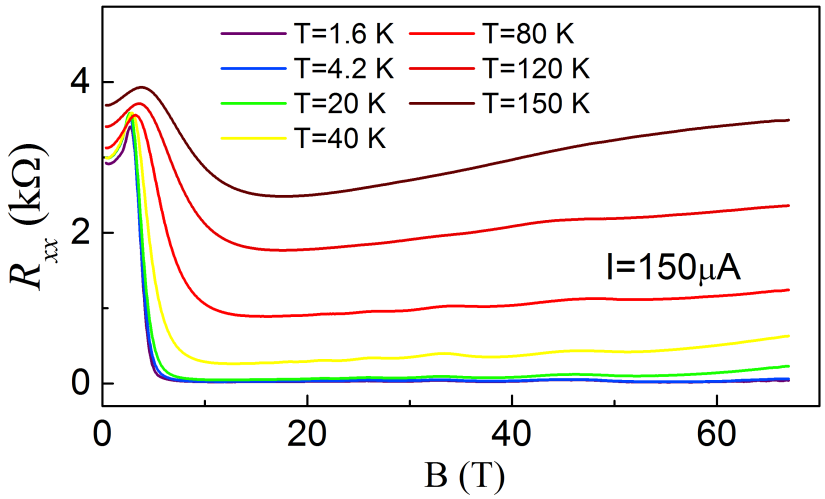

Figure 3.16: The temperature dependence of the longitudinal resistance in the quantum Hall effect breakdown regime with a current of 150 μA. The R_{xx} deviates from zero resistance in the ν=2 quantum Hall regime at high temperature. The superimposed 1/B periodic oscillations persist up to high temperature (T = 120 K).

As discussed in section 1.3.4, the SdH oscillations are associated to the sequential emptying of the LLs in magnetic field. According to the Einstein relation $\sigma_{xx} = \rho_{(E_F)}.e^2.D$, the conductivity is maximum when the Fermi energy is aligned with a Landau level, i.e. when the density of states $\rho_{(E_F)}$ is maximum. In the case of low-doped graphene, as $\rho_{xy} \gg \rho_{xx}$, the maxima of ρ_{xx} will result in maxima of σ_{xx}. On the contrary, the resistivity is minimum when the Fermi energy sits in between two Landau levels. We follow the customary practice to define the index field B_N for each maximum in R_{xx} and plot the reciprocals $1/B_N$ as a function of an integer N. Here, N corresponds to the index of LL at the Fermi energy (Fig. 3.17(b)). The data fit a straight line with a slope corresponding to the inverse oscillation frequency and intercepts $N_{B\to\infty} = 1/2$ in the N horizontal axis when extrapolated to $1/B \to 0$. Such a result is expected for Schrodinger fermions, whereas the phase of the oscillations is shifted by π ($N_{B\to\infty} = 0$) for Dirac fermions [Novoselov 2005, Zhang 2005], due to the presence of a non-dispersing Landau level at zero energy equally shared by electrons and holes. In the present case, the result $N_{B\to\infty} = 1/2$ provides further evidence for an alternative to the simple SdH scenario in G/SiC in order to account for the origin of the oscillations.

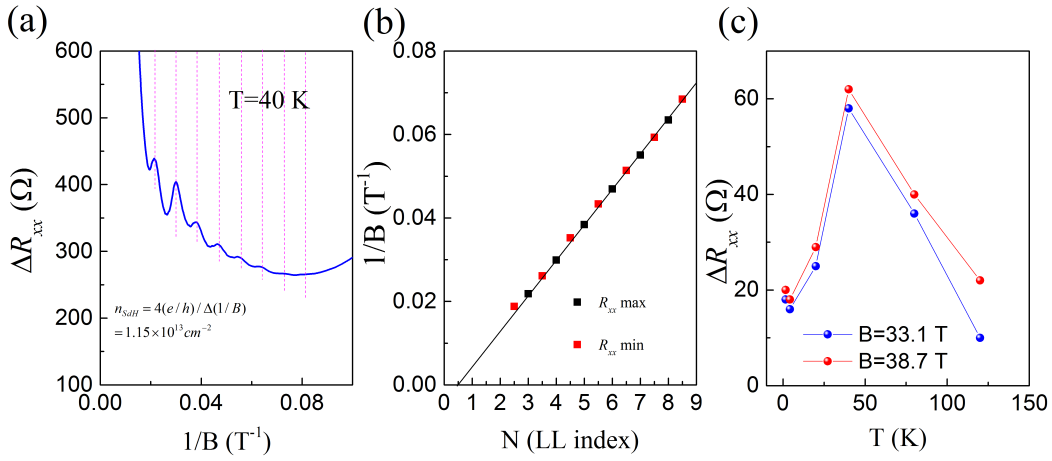

Figure 3.17: (a) The longitudinal resistance R_{xx} at T=40 K as a function of inverse magnetic field. The oscillations show a $1/B$-periodicity. (b) The Landau fan diagram of the oscillation at $T = 40$ K. The integer N (N+0.5) corresponds to maximum (minimum) of the R_{xx} oscillation. The curve extrapolates to 1/2, indicating a Berry phase of 0. (c) The temperature dependence of the oscillation amplitude at B=33.1 T and 38.7 T. The amplitude first increases as the temperature increases and then decreases, showing a maximum at $T = 40$ K.

3.4.3 The origin of the anomalous oscillations

Interestingly, the 1/B-periodic oscillations in R_{xx} at high field are found not reproducible after one or several thermal cycles. In Fig. 3.18, the oscillations show two different behaviors before and after a thermal cycle at 80 K, as shown by comparing the solid and dash lines respectively. The frequency and amplitude are totally different for the two experimental sets.

In order to gain more information about the effect of thermal cycling, we compare the oscillations in different conditions. Fig. 3.19(a,b) make a comparison between two consecutive magnetic field shots (same day, almost one hour between two shots) for the same orientation of magnetic field and for opposite currents $I = \pm$ 150 μA. The vertical offset is not significant and is due to a variation of the preamplifier offset when the input current is reversed. Apart from this offset, the four-probe longitudinal resistances R_{xx}^{4p} display the same behavior. In particular, the period and the amplitude of the oscillating features remain similar. Therefore, Fig. 3.19(a,b) demonstrate the good reproducibility of the measurement for both current directions, provided the sample did not experience any thermal cycling. By contrast, Fig. 3.19(c,d) show the comparison between magnetic field pulses performed on two consecutive days where the temperature rose up to 80 K and 150 K respectively. The magnetoresistances are not reproducible anymore and we conclude that thermal cycles above 80 - 150 K induce irreversible changes in the sample.

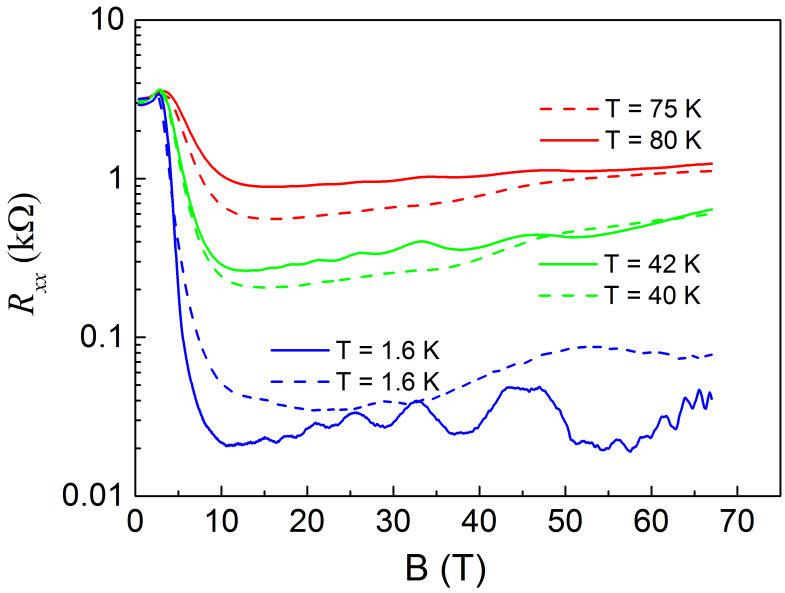

Figure 3.18: The comparison of the oscillations at three temperatures before (solid line) and after (dashed lines) a thermal cycle at 80 K.

The amplitude of the oscillations is actually roughly related to the overall integrity of the resist. This is evidenced in Fig. 3.20, which displays very large amplitude of the oscillations. An optical microscope image of the sample after the measurements shows large cracks in the resist due to a fast cooling down process. For some samples, we did not observe macroscopic resist cracks, however, we postulate that the chemical gating is not homogeneous and microscopic detachments of the resist lead to disconnected graphene puddles with native high carrier density (HD), whereas the rest of the Hall bar remains covered by the resist and has a low electron density (LD). Additionally, graphene detachment from the substrate induced by the SiC steps [Low 2012], bilayer patches [Panchal 2016], or residual contamination [Eriksson 2012] may also induce an inhomogeneous carrier density. Indeed, the 1/B periodic oscillations were not detected in all samples. In a few other samples, not presented, the appearance of the 1/B oscillations could also be related to the progressive appearance of cracks in the resist.

3.5 Model and simulations

3.5.1 Charge transfer in inhomogeneous G/SiC

The model described below is based on the charge transfer proposed by Kopylov *et al.* and takes into account the presence of non-equally doped zones (puddles) resulting in a non-homogenous carrier density distribution. The charge transfer

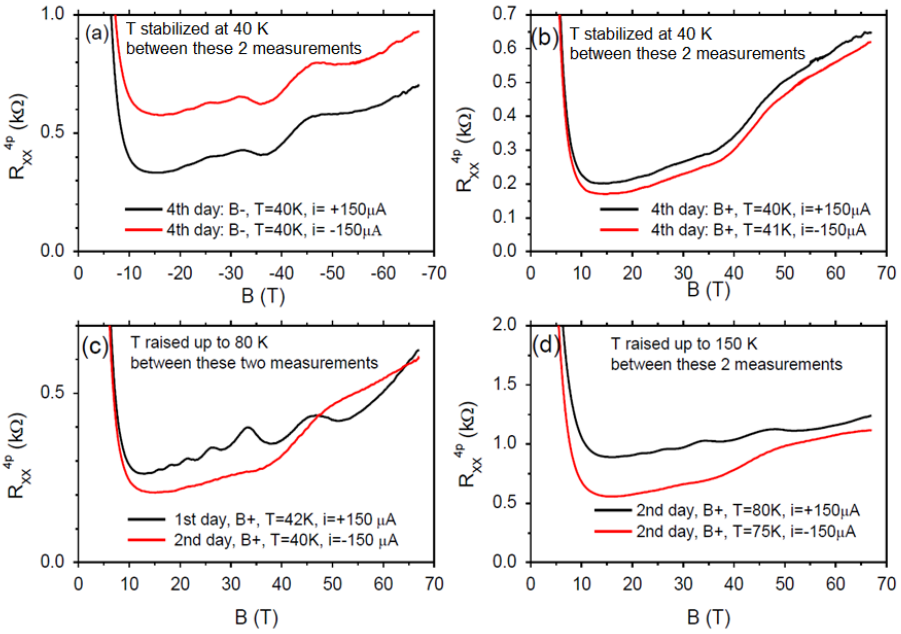

Figure 3.19: Comparison of various longitudinal magnetoresistances, in various experimental conditions. (a) and (b) The temperature T was stabilized at 40 K during and between the measurements at $B < 0$ and $B > 0$, respectively. (c) and (d) The temperature was raised up to 80 K and 150 K between two similar measurements performed at 40 K and 80 K, respectively.

equation Eq. 3.14 can be rewritten to

$$n = -n_g + \beta(A - \mu) \tag{3.15}$$

where μ is the chemical potential of graphene's electrons (considering that the charge neutrality point in graphene is at zero energy) and $\beta = \gamma\epsilon_0/(\epsilon_0 + e^2 d\gamma)$ is an effective density of states, where d is the distance between graphene and buffer layer, ϵ_0 is the vacuum dielectric constant, γ is the density of donor states in the buffer layer.

We assume that the graphene layer is inhomogeneously doped and we introduce the presence of low and high charge carrier density regions, namely LD and HD respectively. The presence of only two types of charge puddles is essential in this model. Indeed, a broad distribution of charge density would average out the effects related to charge transfer between the puddles. Eq. 3.15 applies either in the LD or HD regions and thus the equation's symbols will be completed with a superscript i =LD, HD. Let us first consider the case $B \simeq 0$. The highly doped regions are not influenced by the polymer layer (local detachments or cracks) and therefore we have $n_g^{HD} = 0$. The carrier density $n_0^{HD} = 1.15 \times 10^{13}\text{cm}^{-2}$ and the chemical potential

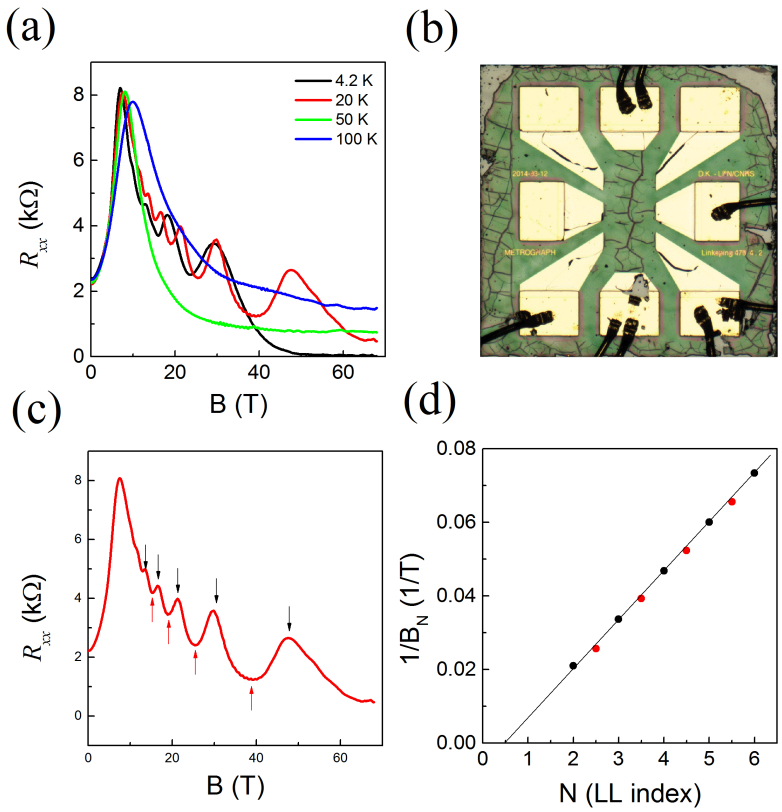

Figure 3.20: (a) Magnetoresistance at $T = 4.2$, 20, 50 and 100 K. (b) The optical image, shows the damaged structure of the covering resist examined after the electrical measurements. (c) Extrema of the longitudinal magnetoresistance at T = 20 K and (d) the corresponding Landau plot evidencing a zero Berry phase .

$\mu_0^{HD} = \hbar v_F \sqrt{\pi n_0^{HD}}$ are determined from the period of the longitudinal oscillations in the quantum Hall breakdown regime. This assertion will be justified *a posteriori*. In the low doped region, the carrier density $n_0^{LD} = 3.4 times 10^{11} \mathrm{cm}^{-2}$ is given by the low field Hall effect. Also, the polymer acts as a gate and induces a non-zero carrier density n_g^{HD} in graphene. To summarize, Eq. 3.15 at $B = 0$ becomes

$$\begin{cases} n_0^{HD} = \beta(A - \mu_0^{HD}) \Rightarrow \beta = \dfrac{n_0^{HD}}{A - \mu_0^{HD}} \\ n_0^{LD} = -n_g^{LD} + \beta(A - \mu_0^{LD}) \end{cases}$$

and thus we have the relations:

$$\begin{cases} n_0^{HD} = \beta(A - \mu_0^{HD}) \\ n_g^{LD} = -n_0^{LD} + n_0^{HD} \dfrac{A - \mu_0^{LD}}{A - \mu_0^{HD}}. \end{cases} \tag{3.16}$$

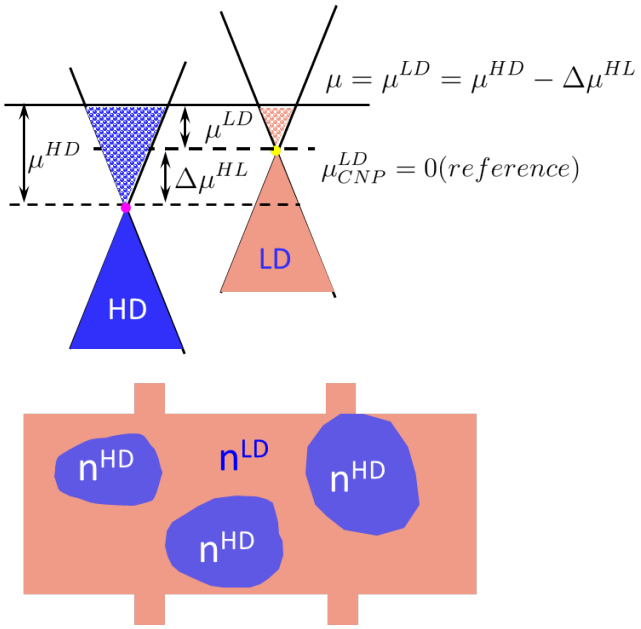

Figure 3.21: The sketch of the presence of the HD and LD regions in the sample. The chemical potential at the LD graphene CNP μ^{LD}_{CNP} is set to zero as a reference.

When the magnetic field increases, electrons will redistribute over all the puddles to keep the same chemical potential μ in the sample. In the following, the chemical potential reference $\mu^{LD}_{CNP} = 0$ is set at the charge neutral point of the LD region, so that $\mu = \mu^{LD}$. We define $\Delta\mu^{HL}$ the chemical potential difference between the CNP in the HD and LD puddles, which always remains constant. The total carrier density $\bar{n}$ reads

$$\bar{n} = (1-\alpha)n^{LD} + \alpha n^{HD} \tag{3.17}$$

where $\alpha = S^{HD}/(S^{LD} + S^{HD})$ is the proportion of HD region. Combining Eq. 3.15 and 3.17 gives:

$$\bar{n} = (1-\alpha)[-n_g^{LD} + \beta(A-\mu)] + \alpha\beta[A - \mu - \Delta\mu^{HL}]. \tag{3.18}$$

The carrier density n^{LD} and n^{HD} in Eq. 3.17 are explicitly expressed as a function of B and μ using the following expressions:

$$n^{LD} = \int_0^{\mu} g_{(\varepsilon,B,\Gamma)} d\varepsilon \tag{3.19}$$

and

$$n^{HD} = \int_0^{\mu} g_{(\varepsilon+\Delta\mu^{HL},B,\Gamma)} d\varepsilon. \tag{3.20}$$

where $g_{(\varepsilon,B,\Gamma)} = \dfrac{eB}{2\pi h}\sum_N 4\dfrac{\Gamma}{(\varepsilon-\varepsilon_N)^2+\Gamma^2}$, corresponds to the LL band structure of graphene (with Lorenzian broadening Γ) at position $\varepsilon_N = sgn(N)\sqrt{2e\hbar B v_F \mid N \mid}$.

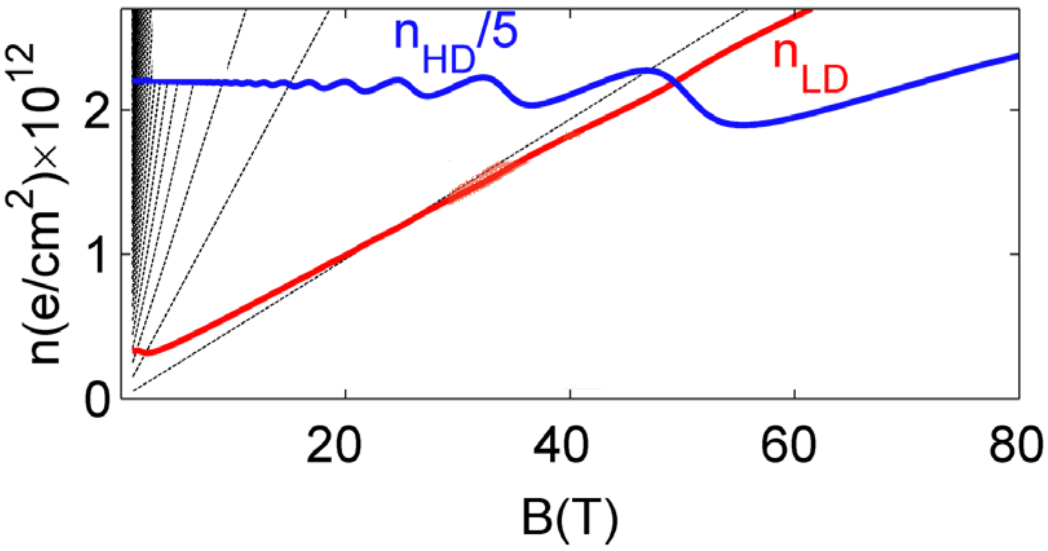

Figure 3.22: Carrier density in the LD and HD regions obtained from the Eq. 3.21. The carrier density in the LD region increases without saturation up to the high magnetic field whereas it oscillates in the HD region.

The combination of Eq. 3.17, Eq. 3.18, Eq. 3.19 and Eq. 3.20 provides the master equation Eq. 3.21 which is solved numerically for each value of magnetic field and adjusted to the experimental data with A, Γ and α being the only fitting parameters:

$$(1-\alpha)\int_0^{\mu} g_{(\varepsilon,B,\Gamma)}d\varepsilon+\alpha\int_0^{\mu} g_{(\varepsilon+\Delta\mu^{HL},B,\Gamma)}d\varepsilon=(1-\alpha)\left[-n_g^{LD}+\beta(A-\mu)\right]+\alpha\beta\left[A-\mu-\Delta\mu^{HL}\right] \tag{3.21}$$

Once the magnetic field evolution of the chemical potential $\mu(B)$ is known, the determination of the carrier density in the LD and HD regions is straightforward (Fig. 3.22). The carrier density in the LD region increases without saturation, implying a charge transfer between the HD and LD regions and being responsible for the stability of the Hall plateau at $\nu = 2$ for $B > B_{min}$. In contrary, the carrier density in the HD region oscillates with 1/B periodicity and refers to as a magnetic field dependent charge transfer between the LD and HD regions. The oscillations of n_B^{HD} translates into oscillations of the magnetoresistance through a modulation of the filling factor with an opposite phase in the LD regions.

3.5.2 Anomalous oscillations and breakdown of the QHE

Within a quantum Hall plateau at filling factor ν, the net conductivity is written as in Eq. 1.60

$$\boldsymbol{\sigma} = \begin{pmatrix} 0 & \frac{\nu e^2}{h} \\ -\frac{\nu e^2}{h} & 0 \end{pmatrix}.$$

Then the current density $\boldsymbol{j}$ becomes

$$\boldsymbol{j} = \boldsymbol{\sigma} \cdot \boldsymbol{E} = \begin{pmatrix} 0 & \frac{\nu e^2}{h} \\ -\frac{\nu e^2}{h} & 0 \end{pmatrix} \cdot \begin{pmatrix} E_x \\ E_y \end{pmatrix} = \begin{pmatrix} \frac{\nu e^2}{h} E_y \\ \frac{\nu e^2}{h} E_x \end{pmatrix}.$$

The current density j_x in the x direction is proportional to the electric field in the y direction $j_x = \nu \frac{e^2}{h} E_y$. This current is flowing without dissipation and for any smooth varying electrical field $E_y(y)$, the above relation remains locally valid. Integrating the sheet current density $j_x(y)$ over a certain width $y_2 - y_1$, the total current is given by

$$I_x = \int_{y_1}^{y_2} j_x dy = \nu \frac{e^2}{h} \Delta\phi_y$$

where $\Delta\phi_y$ is the electrostatic potential drop between y_1 and y_2.

Let us now consider a G/SiC Hall bar containing several HD puddles as shown in Fig. 3.23. When the magnetic field increases, the filling factor is stabilized to $\nu = 2$ in the LD regions (by the charge transfer from the SiC buffer layer) where localized states sit in. On the other hand, Landau levels are progressively depopulated in the HD regions. When the chemical potential is aligned with a LL, the HD regions become compressible with a much higher conductivity than its LD counterpart. The HD regions behave as an equipotential surface and the electric field is normal to the HD/LD interface. In the quantum Hall regime, the current flows almost perpendicular to the electric field and therefore cannot enter in the HD regions, which behave as insulators. Since the current flowing through the Hall bar is constant, the presence of HD puddles induces an increase of the local current density, at the current path bottleneck. This effect is sketched in Fig. 3.23, which shows a numerical simulation of the equipotential lines of a Hall bar decorated with compressible disks in the quantum Hall regime. Macroscopically, this effect translates into a reduction of the effective Hall bar width W_{eff} over which the current flows. In the VRH theory, the current acts as an effective temperature $T_{eff} = eR_H I\xi/2k_B W_{eff}$. Experimentally, T_{eff} is determined by matching the conductivity $\sigma_{xx}(I) = \sigma_{xx}(T_{eff})$. At $B < 20$ T, when the $1/B$-periodic oscillations are small, T_{eff} appears to be roughly linear vs I. The relation $\sigma_{xx}(I) = \sigma_{xx}(T_{eff})$ yields $T_{eff} \simeq 0.05\text{-}0.1 \times (I[\mu A])$[K] which corresponds to an effective Hall bar width W_{eff} = 15 μm considerably smaller than the nominal Hall bar width (100 μm). Similar discrepancy between W_{eff} and W was observed in [Lafont 2015, Furlan 1998], again

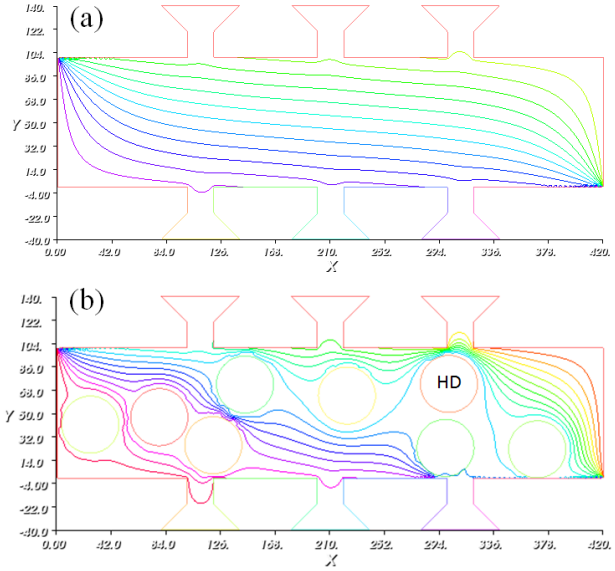

Figure 3.23: (a) Finite Elements Method numeric simulation of equipotential lines of a Hall bar (W = 100 μm, L = 420 μm) in the quantum Hall regime at B = 20 T. (b) The same simulation in a Hall bar decorated by eight disks of radius R = 22 μm inside which $\boldsymbol{E} = 0$. The ballistic chiral current flows only in the low density region near the edge and avoids the high density regions. The gradient of the Hall voltage can be locally very high and the effective width of the Hall bar is considerably reduced.

suggesting a very inhomogeneous current distribution in the samples.

The localization length varies as $\xi = a\mu^{-\gamma}$, where a is chosen to have $\xi_{B=60T}$ = 12 nm, see Fig. 3.14, and μ is given by the calculation, see Fig. 3.24(a). Introducing ξ in T_{eff} and T_{eff} in Eq. 1.65, R_{xx} is calculated at various currents and magnetic fields, as shown in Fig. 3.24(b). The 1/B periodic oscillations are indeed reproduced, with the correct experimental phase and amplitude. The best agreement with the data is found by choosing A = 0.4 eV, α = 30%, and Γ = 15 meV. The large α value points towards a largely inhomogeneous sample and is consistent with the small W_{eff}/W value. The determination of a more quantitative relation between α and W_{eff} would require a detailed knowledge of the current distribution.

3.6 Quantum Hall effect at low filling factor

In graphene on SiC, the stabilization of the $\nu = 2$ Hall plateau over a very broad range of magnetic field relies on the charge transfer between the buffer layer and graphene. For the sample discussed in the previous section, the plateau extends till $B \simeq 80$ T, which constitutes the maximum experimentally available magnetic field. However, since the charge "reservoir" of the buffer layer is not infinite, this

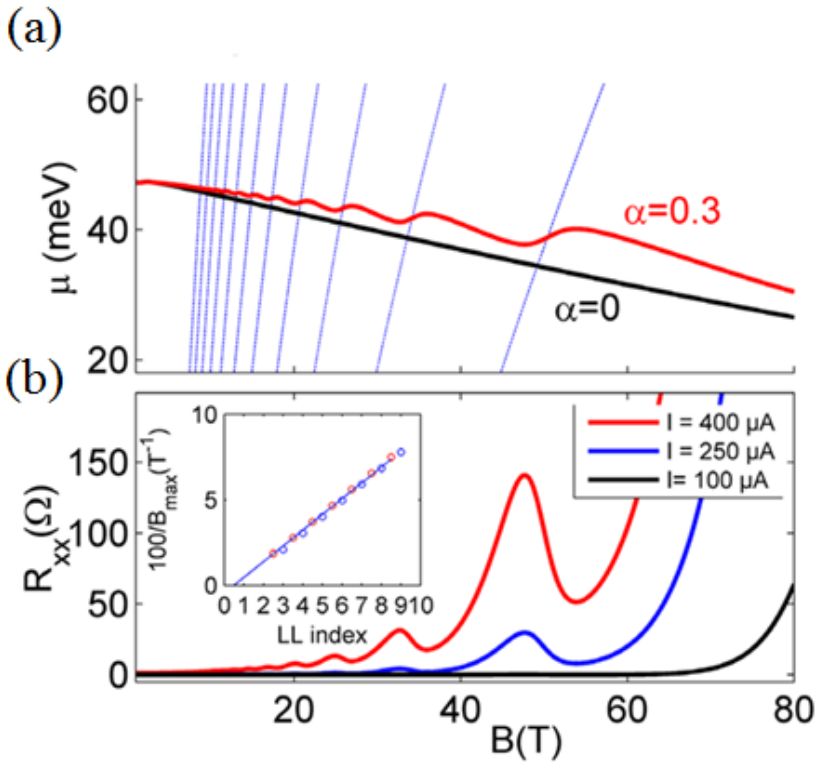

Figure 3.24: (a) Chemical potential μ as a function of B for $\alpha = 30\%$ (red line) and $\alpha = 0$ (black line). The thin blue dashed lines represent the positions of the Landau Levels in the HD puddles. (b) Longitudinal resistance R_{xx} as a function of B, at various currents, calculated within the model described in the text. The curves from the bottom to the top correspond to currents of 100, 250, and 400 μA, respectively. The inset is a Landau plot (blue circles: maxima indexed with integers; red circles: minima indexed with half-integers).

process must stop with ever increasing magnetic field. For technical, financial and deadline reasons, it is difficult (but not impossible!) to increase further the magnetic field. On the other hand, another strategy to address the low filling factor regime is to measure a sample with lower initial carrier density.

The carrier concentration in graphene could be reduced from 2.3×10^{12} cm^{-2} to 4.4×10^{10} cm^{-2} by using a corona gun. Basically, some low energy ions are projected into the PMMA capping layer of the sample. The implanted total charge decays rapidly during a transitional period of a few hours, and then remains stable. The final carrier density of graphene depends both on the initial (pristine) carrier concentration and on the ion dose implanted in the PMMA layer. Even if the electron density can be significantly reduced using this method, the p-doped regime is, however, very difficult to reach.

Fig. 3.25 shows the evolution of the Hall resistance for various values of the

carrier concentration. Starting from $n = 2.3 \times 10^{12}$ cm^{-2} (blue line), the curves are shifted to lower magnetic field when the electron density decreases (they would actually lie on the same trace if plotted as a function of the filling factor). Interestingly, we observe a deviation from the quantized plateau when the carrier density starts to reach very low values. The deviation is first small up to a magnetic field threshold, and then becomes prominent at higher field. Overall, the deviation and the magnetic field threshold are increasing and decreasing functions of the carrier density. When the system is very close to the charge neutrality point (red curve), we do not observe any quantized plateau anymore, and the Hall coefficient actually changes sign. In this case, we observe a magnetic field dependent transition from a n-doped to a p-doped state.

This set of curves demonstrates that, as anticipated from simple arguments, the $\nu = 2$ Hall plateau does not last forever. Beyond the charge transfer mechanism which is specific to graphene on SiC, this result can be explained simply by considering the position of the Fermi energy with respect to the $N = 0$ Landau level. As the magnetic field increases, the degeneracy of the landau level becomes very large and the Fermi energy decreases, approaching $E = 0$. In the very close vicinity of the charge neutrality point, the separation between the electron and hole states does not exactly lie at zero energy, but overlaps within a finite energy range. Usually, this energy range is linked to the presence of electron-holes puddles and scales inversely with the electronic mobility. Under very high magnetic field, when the Fermi energy enters into the energy range with mixed states, both electrons and holes are participating to transport, which clearly affect the Hall resistance quantization rules [Poumirol 2010, Nachawaty 2017]. Close to the charge neutrality point, the exact magneto-transport fingerprint depends on the microscopic sample details, and more precisely on the amplitude and spatial extension of the fluctuating potential landscape. This analysis is beyond the scope of this PhD work, and it is left for the future since it requires further extensive data with varying disorder and carrier density.

So far, the spin and/or valley degeneracy lifting has never been observed in graphene on SiC, even at low filling factors. It makes almost no doubt that the low mobility rather than the charge transfer mechanism prevents its experimental observation. However, "seeing is believing" and high magnetic field studies of clean samples are welcomed to solve this issue.

3.7 Conclusion

We have studied the stability of the quantum Hall plateau in very large Hall bars (100 μm width) made from a chemically gated graphene film grown on SiC substrate. In the quantum Hall regime, the quantized plateau of the Hall resistance at $h/2e^2$ starts at $B \simeq 7$ T and persists up to $B \simeq 80$ T. At high current density, the longitudinal resistance displays small and periodic oscillations when plotted versus 1/B, with zero Berry phase. The extracted carrier density is con-

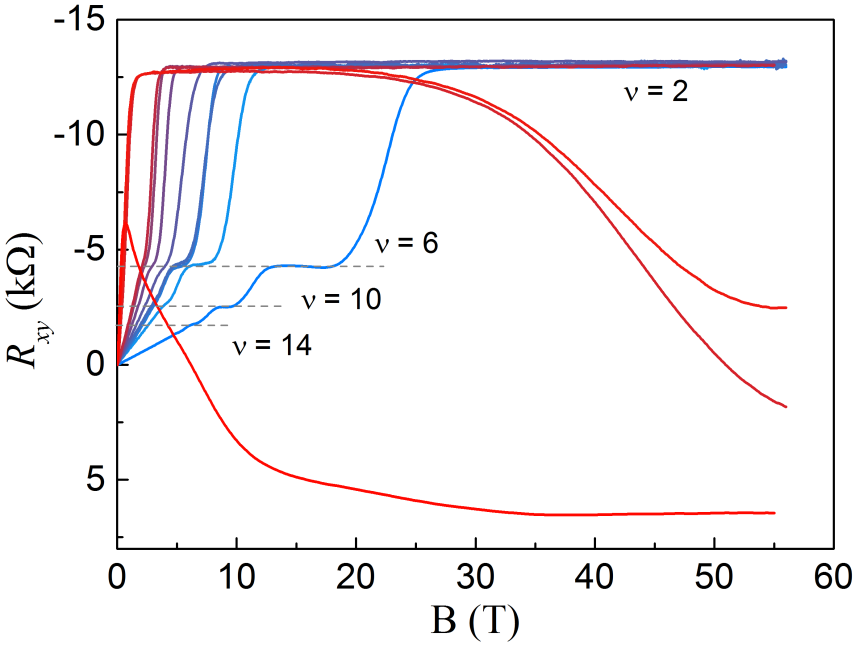

Figure 3.25: Quantum Hall effect of the graphene/SiC under high magnetic field with varying carrier density. At high carrier density range, the sample shows well established quantum Hall plateaus (ν=2, 6, 10...) with a long ν=2 one. As the carrier density decreases, the ν=2 plateau becomes longer and starts to collapse at very low carrier density state.

sistent with the one of as-grown graphene on SiC, *i.e.* without the chemical gate. We relate the longitudinal resistance oscillations to the presence of inhomogeneous doping across the sample where patches of pristine (*i.e.* non-gated) graphene are present. Numerical simulations, based on a charge transfer between the SiC substrate, the gated graphene layer and the patches of ungated graphene, reproduce well the experimental data and indicate that the patches cover up to 30% of the total sample's surface. These in-plane inhomogeneities, in the form of high carrier density graphene pockets, modulate the breakdown of the quantum Hall effect and decrease the breakdown current. The model also suggests a linear evolution of the carrier density as the magnetic field is increased, thus stabilizing the quantum Hall regime at a filling factor of 2 for a broad magnetic field range. The explanation we propose can be readily extended to other quantum systems in which inhomogeneity/charge reservoirs are present. Additionally, new devices embedding charge reservoirs on purpose can also be envisioned, to enhance the stability of the quantum Hall effect, and to explore the physical processes that take place under high magnetic field systems.

In graphene on SiO_2, carrier density puddles are also present but magnetoresistance oscillations in the $\nu = 2$ quantum Hall regime have never been observed. Indeed, first of all, the charge transfer between the buffer layer and graphene is essential. This mechanism ensures an extra-broad magnetic field range over which the LD region remains in the $\nu = 2$ quantum Hall regime. In the HD regions, on the other hand, the high index Landau levels continue to cross the Fermi energy as the magnetic field increases with $1/B$ periodicity. The presence of only two types of charge puddles with different carrier densities, namely LD and HD, is also required instead of a broad distribution of carrier density puddles as in SiO_2 substrates. This binary system allows for a charge transfer between the puddles when magnetic field changes. In turn, the chemical potential varies accordingly. Since the localization length is linked to the chemical potential near the quantum Hall breakdown regime, such variations translate into weak $1/B$ periodic oscillations of the conductance. In graphene on SiO_2, the broad distribution of charge density puddles would average out the charge transfer mechanism, yielding no clear oscillations. Furthermore, the magnetic field range over which the quantum Hall plateau at $\nu = 2$ is established would be too narrow to observe several oscillations.

Chapter 4

The $LaAlO_3/SrTiO_3$ Interface

Contents

4.1 Introduction to $LaAlO_3/SrTiO_3$ 72
4.1.1 Origin of the 2DEG 74
4.1.2 Electronic band structure 76
4.2 Sample preparation and characterization 79
4.2.1 Sample preparation 79
4.2.2 Resistance vs temperature characteristics 80
4.3 Magneto-transport and electronic properties 81
4.3.1 Monotonous magnetoresistance and Hall effect 81
4.3.2 Shubnikov-de Haas oscillations 83
4.3.3 Discussion 85
4.4 Band structure spectroscopy 92
4.4.1 Gate dependent magneto-transport at sub-Kelvin temperature 93
4.4.2 Effective mass versus carrier density 95
4.4.3 Analysis and model 97
4.4.4 Extension of the experimental results at 55 T and 500 mK . . 101
4.5 Conclusion 102

In this chapter, I will present the magnetotransport study on the 2DEG at the $LaAlO_3/SrTiO_3$ interface. This work is under a collaboration with Prof. Ariando's group at National University of Singapore. From the high field experimental data, we address the electronic properties and the role of Rashba effect. The back-gate dependence study at sub-Kelvin temperature helps us to understand the complex band structure in this system. Part of the results have been published in Appl. Phys. Lett. 109, 122106 (2016).

Complex oxide constitute a rapidly developing field of research, with potential applications in electronics [Mannhart 2010, Hwang 2012] or solar energy harvesting [Assmann 2013]. There is currently a focus on the interface between the band insulators $LaAlO_3$ (LAO) and $SrTiO_3$ (STO) for their promising application in multifunctional devices, which hosts a conducting two-dimensional electron gas (2DEG) [Ohtomo 2004]. It is mainly believed to originate from the polar catastrophe [Mannhart 2008], which results in a charge transfer between the polar oxide [100] LAO and the nonpolar oxide [100] STO. This charge transfer prevents a divergence of the electrostatic potential in LAO associated with the intra-layer built-in

electric field. Charge accumulation is therefore predicted at the interface with intriguing consequences such as the emergence of magnetism and superconductivity [Brinkman 2007, Reyren 2007]. The electronic states at the LAO/STO interface have a complex structure which is based on the $3d$ orbitals of Ti atoms. The symmetry-lowering at the interface lifts the Ti t_{2g} band degeneracy so that the band derived from d_{xy} orbital is lower in energy than the ones derived from the d_{xz} and d_{yz} orbitals. Depending on the total two-dimensional carrier density, the band occupation and the spatial distribution of the carriers [Huang 2013] are critical to envision band engineering for oxide electronics [Förg 2012, Stornaiuolo 2015]. A well established tool to investigate the band structure is the magneto-transport in the quantum regime. The development of fabrication technologies combined with the possibility to tune the carrier density utilizing either a capping layer [Huijben 2013] or an ionic liquid gating [Zeng 2016] have allowed for a sufficiantly high-mobility 2DEG to observe Shubnikov-de Haas (SdH) oscillations in magneto-transport experiments [Caviglia 2010b, McCollam 2014, Fête 2014], opening new perspectives for the investigation of the charge carriers' properties in relation with their band-structure. However, quantum transport studies remain scarce in the literature and the large variability in the results (originating from the large range of samples studied) does not yet offer a clear picture of electron transport in LAO/STO. In this chapter, I will discuss high field magneto-transport experiments on LAO/STO samples provided by Prof. Ariando's group at National University of Singapore. We interpret our experimental data obtained on a set of samples with low or medium carrier density by the presence of low and high mobility electrons both contributing to transport, and confirm the role of Rashba spin-orbit coupling. In addition, magneto-transport data at sub-Kelvin temperature on a sample where the carrier density is tuned via the application of a gate voltage show more complex SdH oscillations. From the analysis of the gate dependent SdH oscillation pattern, we tentatively explain the complex band structure at the Fermi energy.

4.1 Introduction to $LaAlO_3/SrTiO_3$

In 2004, a high mobility conducting two-dimensional electron gas (2DEG) at the atomically abrupt interface between two band insulators, $LaAlO_3$ and $SrTiO_3$, was reported by Ohtomo and Hwang [Ohtomo 2004]. This observation has immediately triggered a large number of studies on this family of heterostructures. During the past decade, several properties of the 2DEG at the LAO/STO interface such as superconductivity [Reyren 2007, Caviglia 2008, Bell 2009, Kozuka 2009], magnetism [Brinkman 2007], metal-to-insulator transition [Thiel 2006, Cen 2008], correlated electron behaviour [Breitschaft 2010], coupled electron hole bilayers [Pentcheva 2010] and gate-tunable Rashba effect [Caviglia 2010a], have been observed and investigated. These properties and the origin of the 2DEG at the interface between $LaAlO_3$ and $SrTiO_3$ have triggered considerable research and opened up new routes for promising applications in oxide electronics.

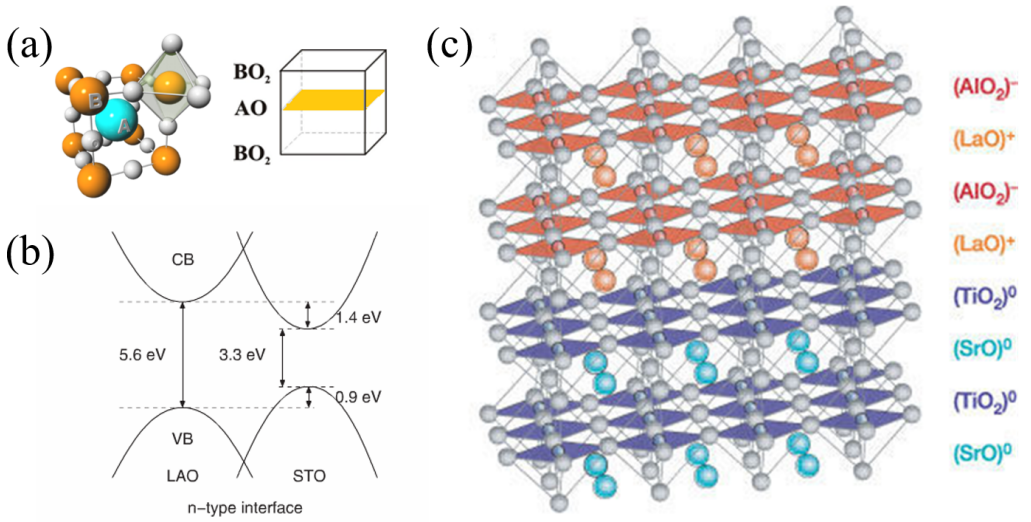

Figure 4.1: (a) The structure of the perovskite ABO_3, where A is either La or Sr atoms, B is Al or Ti atoms. (b) The band alignment of two insulators: LAO and STO. (c) Scheme of the LAO/STO interface, showing the composition of each layer and the ionic charge state of each layer. Extracted from [Ohtomo 2004, Popović 2008].

Both $LaAlO_3$ and $SrTiO_3$ have a perovskite structure sketched in Fig. 4.1(a). $LaAlO_3$ is a rhombohedral perovskite at low temperature (< 700 K) with a lattice constant $a = 5.357$ Å and lattice angle $\alpha = 60°$ [Geller 1956]. It can be described as pseudocubic structure with a lattice constant of 3.791 Å. It is a band insulator with a band gap of 5.6 eV. $SrTiO_3$ is cubic at room temperature with a lattice constant of 3.905 Å. The TiO_6 octahedra have perfect 90° angles. At about 105 K, $SrTiO_3$ undergoes a phase transition into a tetragonal structure where the neighboring TiO_6 octahedra are slightly rotated in opposite directions. $SrTiO_3$ has an indirect band gap E_{g1} =3.25 eV from the maximum of the valence band (VB) at R point to the minimum of conduction band (CB) at Γ point (see figure 4.1) and a direct band gap E_{g2} =3.75 eV at Γ point [Van Benthem 2001]. The small lattice mismatch of 3% between the two compounds allows the epitaxial growth of $LaAlO_3$ films on $SrTiO_3$.

In the (001) direction, the perovskite ABO_3 structure (A={La, Sr} and B={Al, Ti} in the $LaAlO_3$ and $SrTiO_3$, respectively) can be viewed as an alternate stacking of AO and BO_2 layers. $LaAlO_3$ is a polar material formed of charged LaO^{+1} and AlO_2^{-1} layers, while $SrTiO_3$ is non-polar with two neutral sublayers of SrO^0 and TiO_2^0. The atomically abrupt interface between $LaAlO_3$ and $SrTiO_3$ has thus two different configurations: the n-type interface ($SrO^0/TiO_2^0/LaO^{1+}/AlO_2^{1-}$) (Fig. 4.1) and the p-type interface ($TiO_2^0/SrO^0/AlO_2^{1-}/LaO^{1+}$). In both cases, there is a polar discontinuity at the interface, which seems to be the key element to explain the conductivity properties at the interface between these two insulators. Interestingly, a non-zero conductivity can be only found at the n-type interface whereas the p-type

interface is always insulating.

4.1.1 Origin of the 2DEG

The origin of the unexpected 2DEG has been a controversial question and a subject of numerous experimental and theoretical studies. Several mechanisms can be at play.

The most accepted scenario to explain the presence of free charges at the interface, is referred to as the polar catastrophe [Nakagawa 2006]. Since $LaAlO_3$ is polar and therefore made of alternating charged planes, an electric field naturally develops between the planes. Depending on the nature of the initial plane ($La^{3+}O^{2-}$ or $Al^{3+}O_2^{4-}$) in contact with $SrTiO_3$ at the interface, the electric field is either positive or negative. The integration of this built-in electric field along the thickness of $LaAlO_3$ yields an ever increasing (decreasing) potential, which shifts the electronic states in the LAO layers upward (downward). The divergence of the electrostatic potential is supressed either with a structural or an electronic reconstruction. When the interface is made of $La^{3+}O^{2-}$ and $Ti^{4+}O_2^{2-}$ planes, a charge -e/2 per unit cell is transferred to the first TiO_2 layer, where the valence of the Ti atoms changes from Ti^{4+} to $Ti^{3.5+}$. However, when the interface is made of $Al^{3+}O_2^{4-}$ and $Sr^{2+}O^{2-}$ planes, the fixed valence of Sr^{2+} atoms forbids the transfer of half a positive charge and therefore prevents the formation of a 2DHG. In this case, atomic reconstruction will happen to avoid the polar catastrophe in the system. This model is supported by two major experimental facts. Firstly, theoretical calculations predict that the electronic reconstruction occurs only when the thickness of $LaAlO_3$ is larger than 4 stoichiometric layers. This assertion has been experimentally confirmed, since the interface becomes conducting only when this thickness threshold is reached [Thiel 2006, Liu 2013]. Secondly, the model forbids the emergence of a 2DHG which has, indeed, never been experimentally observed. Although the polar catastrophe model is qualitatively attractive, a large discrepancy (of roughly one order of magnitude) is found between the predicted and measured carrier density of the 2DEG. In the polar catastrophe scenario, the transfer of half an electron will result in a very high carrier density up to 3.2×10^{14} cm^{-2}, whereas the experimental recorded values are of the order of 10^{13} cm^{-2}. Some other experimental observations question the validity of the polar catastrophe model. For example, a non-zero conductivity has also been reported in amorphous [Chen 2011] and in the [001] direction [Annadi 2013] $LaAlO_3/SrTiO_3$ interface, despite the fact that no polar catastrophe is expected in these systems.

Several authors [Kalabukhov 2007, Siemons 2007] claimed that the possible origin of the 2DEG can also be the presence of oxygen vacancies at the interface created during the deposition process as a result of high energy particles bombardment. This scenario was inspired from the fact that oxygen vacancies have been known for a long time to lead to conductivity in $SrTiO_3$ [Schooley 1965]. Indeed, annealing pure $SrTiO_3$ substrate in an oxygen partial pressure P_{O_2} larger than 10^{-4} mbar removes the oxygen vacancies and turns $SrTiO_3$ into an insulator

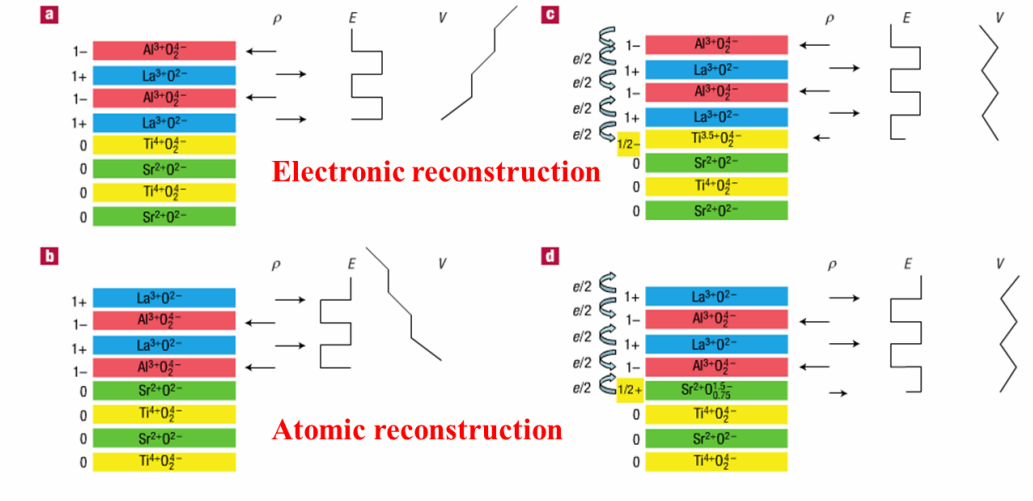

Figure 4.2: The polar catastrophe model at atomically abrupt LAO and STO interfaces along (001) direction. (a,b) are n- and p-type interfaces before reconstruction, respectively. (c,d) are corresponding interfaces after reconstruction. Because the Ti ions have multivalence, the electronic reconstruction is possible in the LaO/TiO_2 interface, while the atomic reconstruction is the only option for the AlO_2/SrO interface. The electonic reconstrution in the LaO/TiO_2 interface induces the 2DEG and the conducting properties whereas the atomic reconstruction brings in an insulating AlO_2/SrO interface. Extracted from [Nakagawa 2006].

[Kalabukhov 2007]. Several works have been done to investigate the samples grown under different P_{O_2}. The sheet resistance of the interface, as well as the carrier density and the mobility, were found to be strongly dependent on P_{O_2} [Brinkman 2007]. Contrary to the bulk STO, a conducting interface is reported in all the studies [Kozuka 2009, Caviglia 2008, Caviglia 2010b, Ariando 2011] where the growth has been performed under $P_{O_2} \geq 10^{-4}$ mbar. The samples deposited under very low $P_{O_2} (\leq 10^{-5}$ mbar) show very high 3D-like electron density [Herranz 2007]. Therefore, we can conclude that the conductivity in the samples deposited under very low P_{O_2} is induced at least partly by the presence of the oxygen vacancies, while it is not the case in the samples deposited under higher P_{O_2}.

A third mechanism which must be taken into account is the intermixing of the La^{3+} and Sr^{2+} ions, which results in a rough interface as observed by electron energy loss spectroscopy [Nakagawa 2006] and X-ray diffraction [Willmott 2007]. This interdiffusion gives rise to several conducting $La_{1-x}Sr_xTiO_3$ unit cells formed at the n-type $LaAlO_3/SrTiO_3$ interfaces. Nevertheless, when applied to the p-type $LaAlO_3/SrTiO_3$ interface, this model fails to explain the insulating properties.

So far, the polar catastrophe is considered as the most efficient mechanism to explain the origin of the 2DEG at the $LaAlO_3/SrTiO_3$ interface. All the samples investigated during this thesis have been annealed in oxygen after fabrication in

order to reduce the contribution of the oxygen vacancies.

4.1.2 Electronic band structure

A detailed theoretical analysis demonstrates that the 2DEG resides on the STO side and spreads over several stoichiometric layers, rather than being confined to the first layer as suggested by the polar catastrophe model [Delugas 2011]. Therefore, we start our discussion by considering the band-structure of $SrTiO_3$. The band-structure of $SrTiO_3$ is complex since it emerges from the 3d $Ti^{3+/4+}$ atomic orbitals, with strong electronic interactions.

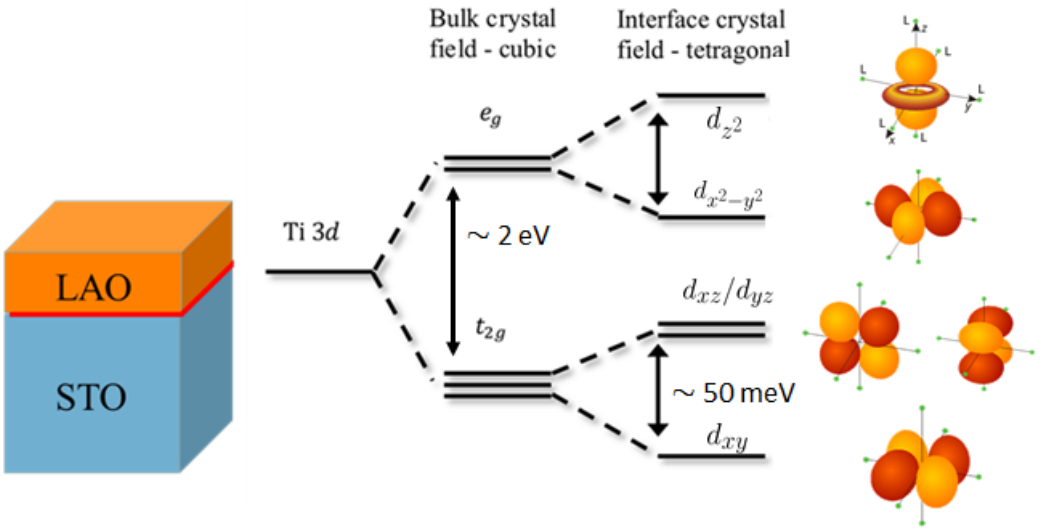

Figure 4.3: The band-structure of the 2DEG is derived from the Ti 3d orbitals of STO. Each Ti atom is caged by an oxygen octahedron (the oxygen atoms are indicated by the little green dots). Due to the bulk crystal field, the octahedral symmetry is broken, the d-orbitals split into two sets: high energy bands derived from e_g (d_{z^2} and $d_{x^2-y^2}$) orbitals and low energy bands t_{2g} (d_{xz}, d_{yz} and d_{xy}) orbitals. At the interface of the $LaAlO_3/SrTiO_3$, the interface crystal field further splits the t_{2g} bands into lower energy d_{xy} singlet and higher energy d_{xz}, d_{yz} doublet.

In bulk $SrTiO_3$, the conduction band is derived from the $3d$ orbitals of the Ti atoms (d_{xy}, d_{xz}, d_{yz}, d_{z^2} and $d_{x^2-y^2}$) and the valence band is derived from the $2p$ orbitals of the oxygen atoms (p_x, p_y, p_z). For isolated Ti atoms without any crystal field, the Ti $3d$ orbitals are 5-folds degenerate. In the $SrTiO_3$ bulk cubic lattice, the Ti atoms are caged in a octahedron cornered by 6 oxygen atoms. The cubic crystal field breaks the quintuplet of states into a triplet and a doublet. The triplet t_{2g} is composed of orbitals (d_{xy}, d_{xz} and d_{yz}) with lobes oriented at 45° with respect to the Ti-O bond and the doublet e_g ($d_{3z^2-r^2}$ and $d_{x^2-y^2}$) with lobes pointing towards the oxygen atoms.

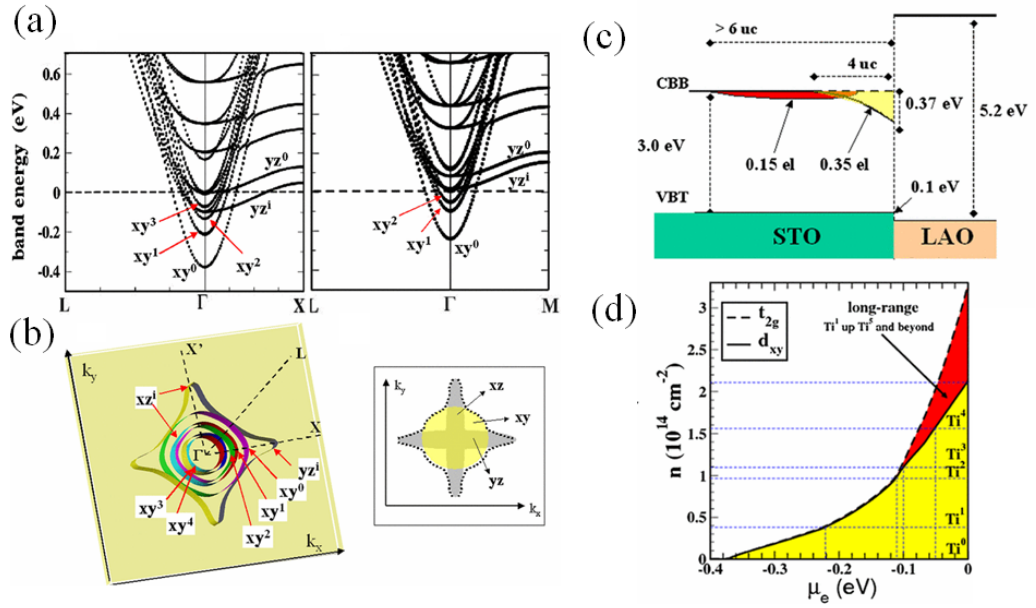

Figure 4.4: (a) Calculated energy bands for high (left) and low (right) carrier density. (b) Fermi surfaces of the 2DEG at the interface of $LaAlO_3/SrTiO_3$. (c) The band alignment of the $LaAlO_3/SrTiO_3$ and calculated distribution of the d_{xy}, d_{xz}, d_{yz} orbitals. Electrons in d_{xy} are confined closer to the interface, while the d_{xz}, d_{yz} electron wavefunctions extend up to the sixth STO layer below the interface. (d) Calculated t_{2g} (dashed) and d_{xy} (solid) charge densities per unit area as a function of chemical potential. Extracted from [Delugas 2011].

When the $LaAlO_3$ is deposited on the $SrTiO_3$ layer by layer, the interface crystal field breaks the inversion symmetry. The electronic states at the interface are modulated by several parameters such as the lattice distortion induced by the lattice mismatch between $LaAlO_3$ and $SrTiO_3$ together with the confining potential (which must be taken into account self-consistently). Thus, the degeneracy of both the t_{2g} and the e_g bands are further lifted. The out-of-plane orbitals are pushed up in energy, making the d_{xy} orbitals at the origin of the lowest energy conduction band. As a result, the $3d$ orbitals of Ti ions at the interface have an energy hierarchy as shown in Fig. 4.3, as experimentally observed by x-ray absorption spectroscopy. The energy gap between the lower energy d_{xy} and higher d_{xz} and d_{yz} bands were reported to be around 50 meV [Salluzzo 2009]. This effect has been reproduced by several theoritical works [Popović 2008, Lee 2008, Janicka 2009, Delugas 2011]. Delugas *et al.* [Delugas 2011] showed that the electrons reside on the STO side and spread over several Ti layers near the interface. More precisely, the extension of the electron's wavefunction depends on its sub-bands occupation: electrons in the d^i_{xy} (d^i_{xy} is defined as the d_{xy} in the ith STO layer) bands are confined over 3 or 4 STO unit cells whereas those in the d^i_{xz} and d^i_{yz} (d^i_{xz} and d^i_{yz} are defined as the d_{xz}/d_{yz} in the i^{th} STO layer) bands spread over roughly 6 unit cells as shown in Fig. 4.20.

The electrons in the d_{xy} bands have light effective mass ($\simeq 0.7m_e$) with an isotropic Fermi surface. On the other hand, the electrons in the d_{xz} and d_{yz} degenerate bands have heavier effective mass ($\simeq 1.3m_e$) with a star-like Fermi surface (Fig. 4.4(b)). When the carrier density is low (below a critical carrier density [Joshua 2012]), the electrons will only occupy the d_{xy} bands. Then they start to occupy the higher energy bands d_{xz}/d_{yz} bands (shown in Fig. 4.20).

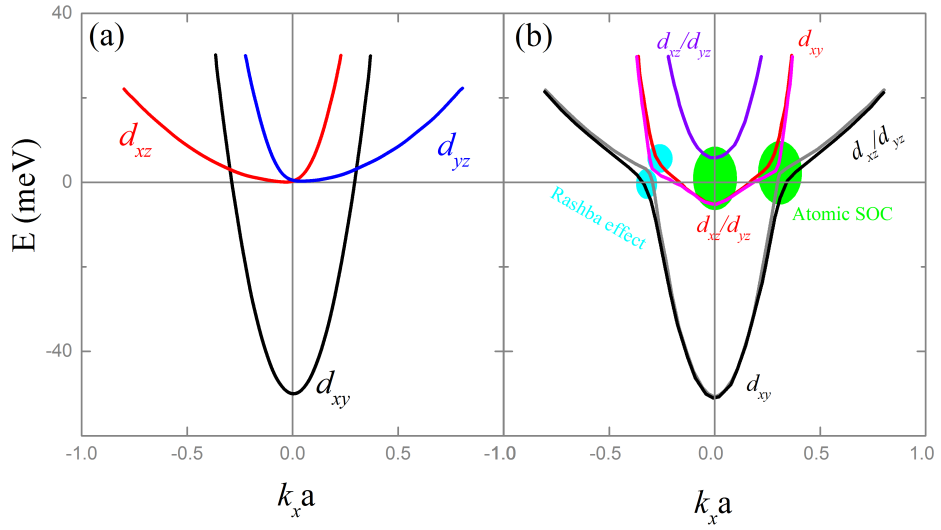

Figure 4.5: (a) Simplified band structure of the t_{2g} bands in $LaAlO_3/SrTiO_3$ interface without any spin-orbit coupling (SOC). The d_{xy} band has a lower energy than the d_{xz}/d_{yz} bands with a gap of 50 meV. (b) The band struture of the t_{2g} orbitals with the presence of SOC. The atomic SOC mixes the t_{2g} bands and lifts the Γ-point degeneracy of the d_{xz} and d_{yz} bands (highlighted by the green area). The interplay between the SOC and the broken inversion symmetry splits the two different spin states for all the bands. The strongest splitting occurs at the points when the d_{xy} band crosses the d_{xz}/d_{yz} bands (highlighted by cyan area). Extracted from [Kim 2013].

In addition to the ladder-like multiple sub-bands at the interface, the presence of a strong spin-orbit coupling (SOC) has been evidenced [Shalom 2010, Caviglia 2010a] and subsequently studied theoretically by many groups [Khalsa 2013, Kim 2013, Zhong 2013, Diez 2015, Khalsa 2013]. The SOC adds complexity to the band structure of this 2DEG system. The atomic SOC hybridizes the three different orbitals and reconstructs the band structure as shown in Fig. B.12. The band mixing has been observed by ARPES measurements [McKeown Walker 2016]. The interplay between SOC and the broken inversion symmetry at the interface gives rise to the Rashba effect [Bychkov 1984]. The Rashba Hamiltonian is written as $H_R = \alpha(\boldsymbol{\sigma} \times \boldsymbol{k}) \cdot \hat{\boldsymbol{z}}$ where α is the Rashba constant, $\boldsymbol{\sigma}$ are the Pauli matrices, $\boldsymbol{k}$

the electron wave vector and $\hat{z}$ the unit vector perpendicular to the interface. This effect modifies the electron parabolic dispersion relation, which is divided into two spin branches shifted along the k_x and k_y direction. The strongest splitting is predicted to occur at the crossing points of the d_{xy} and d_{xz}/d_{yz} orbitals, which is about 10 times larger than that around the Γ point [Zhong 2013]. Since the Rashba effect strongly depends on the electric field at the interface, the Rashba constant α can be tuned by an external electric field [Caviglia 2010a].

4.2 Sample preparation and characterization

4.2.1 Sample preparation

The $LaAlO_3/SrTiO_3$ heterostructures are mainly grown by pulsed laser deposition (PLD) [Ohtomo 2004]. Other methods such as molecular beam epitaxy (MBE) [Segal 2009], atomic layer deposition (ALD) [Sbrockey 2012] are also used. The PLD method is very efficient for the growth of high quality interface in different gaseous environment and with excellent thickness control [Rijnders 1997].

During my thesis, the samples were grown by PLD by the group of Prof. Ariando in National University of Singapore. A few unit cells of LAO were deposited on (001)-orientated STO substrate. Prior to the PLD growth, some preparation works need to be done: (1) preparation of the single LAO crystal for the targets; (2) HF treatment of the STO substrate to make sure the substrate is TiO_2 terminated; (3) reverse lithography on the STO to define the Hall bar geometry; (4) deposition of amorphous AlN as hard mask. The width of the Hall bar is 50 μm and its length is 500 μm, the distance between two voltage probes is 160 μm. A six-probes configuration of the Hall bar allows for the measurement of both longitudinal and Hall resistance (shown in the inset of Fig.4.6). After the patterning process, the patterned STO substrates are put into a PLD chamber for the deposition of LAO.

Fig. 4.6(a) shows the principle of the PLD. During the deposition, the substrate is heated up to a desired temperature (700 - 950 °C) necessary for the LAO crystal growth. A pulsed laser is focused on the LAO target to produce a plume of LAO plasma state. The high temperature plume moves towards the substrate which is located above the target with a very short distance. Repeating the pulses several times, the LAO is deposited at the STO surface layer by layer with very high crystalline quality. After the growth, the sample can be annealed in the chamber at a high temperature with a high oxygen partial pressure to remove the oxygen vacancies introduced by high-energy plasma bombardment during the deposition. The parameters such as the laser energy and pulse rate, the substrate temperature, the vacuum and the oxygen partial pressure are optimized in order to grow high interface quality sample. During the deposition, an *in-situ* reflection high energy electron diffraction (RHEED) probe is used to monitor the LAO thickness deposited [Ariando 2011]. For example, Fig. 4.6(b) shows obvious oscillations with 8 maxima, indicating an atomic scale layer-by-layer growth of a sample with 8 stoichiometric

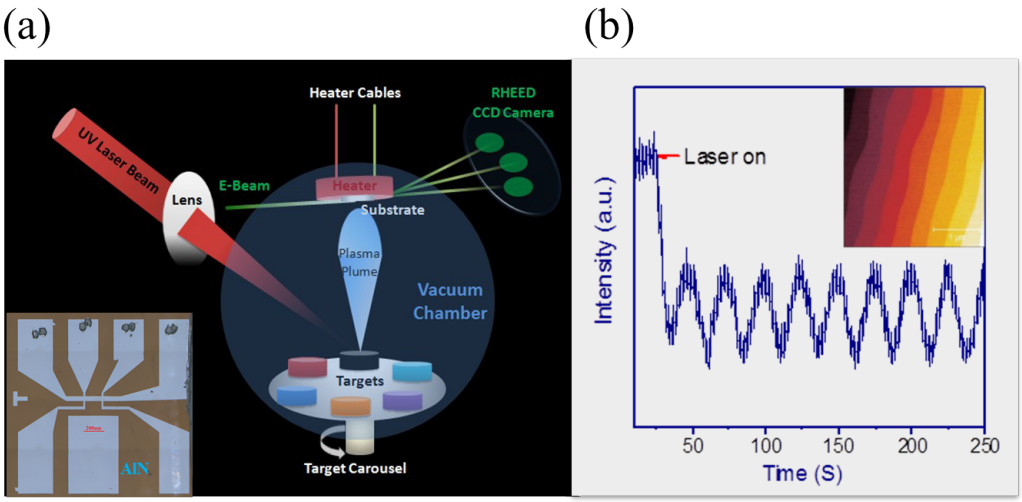

Figure 4.6: (a) Scheme of Pulsed Laser Deposition(PLD) of $LaAlO_3/SrTiO_3$ and the Hall bar (inset). (b) The RHEED pattern during the LAO deposition. The well resolved oscillation indicates the layer-by-layer $LaAlO_3$ deposition. The inset is an AFM image of the STO substrate.

unit cells of LAO deposited on the STO substrate.

4.2.2 Resistance vs temperature characteristics

The temperature dependence of the sample resistance was systematically measured during both the cooling and the heating processes. All the LAO/STO samples show a very strong temperature dependence: the room temperature resistance is of the order of a few hundreds of kilo-Ohms whereas the low temperature resistance is around a few hundreds Ohms. Fig. 4.7 shows a typical resistance vs temperature of one of the samples studied during this thesis. We observe a metallic behavior as the resistance drops from 50 k$\Omega/\square$ at room temperature to 200 $\Omega/\square$ at 4.2 K respectively, in line with the typical values reported in the literature [Ariando 2011]. The carrier density was reported to decrease as the temperature decreases [Huijben 2006, Kalabukhov 2007], which probably results from the electron localization on the oxygen vacancies. At the same time, the mobility was reported to rise by several orders of magnitude when the sample is cooled down to helium temperature. The origin of the very low mobility (a few cm^2/Vs) is believed to result from the long range electron-phonon interactions with soft transverse optical (TO) phonons associated with the lattice distortion of polar atomic displacement in STO [Cancellieri 2016]. This suggestion is in agreement with the strong temperature dependence and the presence of high mobility conduction properties at low temperature.

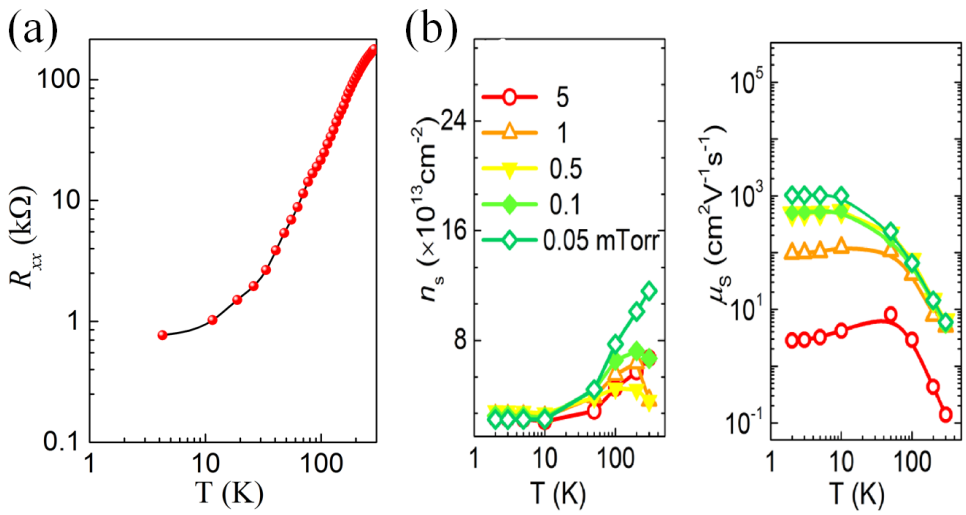

Figure 4.7: (a) A typical temperature dependence of R_{xx} in $LaAlO_3/SrTiO_3$. (b) Typical temperature dependence of carrier density and mobility in LAO/STO samples under different oxygen partial pressure during growth. Extracted from [Han 2016]

4.3 Magneto-transport and electronic properties

In this section, we focus on the transport and electronic properties of $LaAlO_3/SrTiO_3$ samples. The transport properties, mainly characterized by the carrier density and mobility, are extracted from the classical (Drude) transport theory. On the other hand, the electronic properties (and ultimately the band-structure), are deduced from the analysis of the magneto-resistance behavior and the SdH oscillations under high magnetic field. First, we will discuss the case of samples with low or moderate carrier density ($n < 1.5 \times 10^{13}$ cm^{-2}) measured at a temperature of 1.6 K and under a maximum magnetic field of 55 T [Yang 2016b]. These samples show also a low mobility ($\mu \sim$1000 cm^2/Vs). The use of such a high magnetic field allows the observation of many oscillating features despite the relatively low mobility. The analysis of the data emphasizes the role of the spin-orbit coupling and suggests the presence of at least two conducting bands (as a minimal model), to reproduce the main experimental features.

4.3.1 Monotonous magnetoresistance and Hall effect

$LaAlO_3/SrTiO_3$ samples display a positive magneto-resistance (MR) when a high magnetic field is applied perpendicular to the plane of the sample. The amplitude of this generic feature varies from sample to sample, and is decorated with faint Shubnikov-de Haas oscillations for high mobility samples. At first sight, the positive MR background is expected within the Bolzmann model of transport as

well as the linear Hall effect over full magnetic field range. As the magnetic field is rotated from perpendicular to parallel to the plane of the sample, the MR shows a transition from positive to negative (see Fig. 4.8(a)). On the other hand, the Hall resistance remains linear with a slope being reduced by the cosine of the tilt angle, as anticipated considering the Hall bar geometry. A rough estimation of the carrier density from the Hall coefficient R_H gives $n = 1.48 \times 10^{13}$ cm^{-2}, in line with the carrier density range of $LaAlO_3/SrTiO_3$ sample reported in the literature [Caviglia 2010b, Jalan 2010, Lee 2011, McCollam 2014, Maniv 2015].

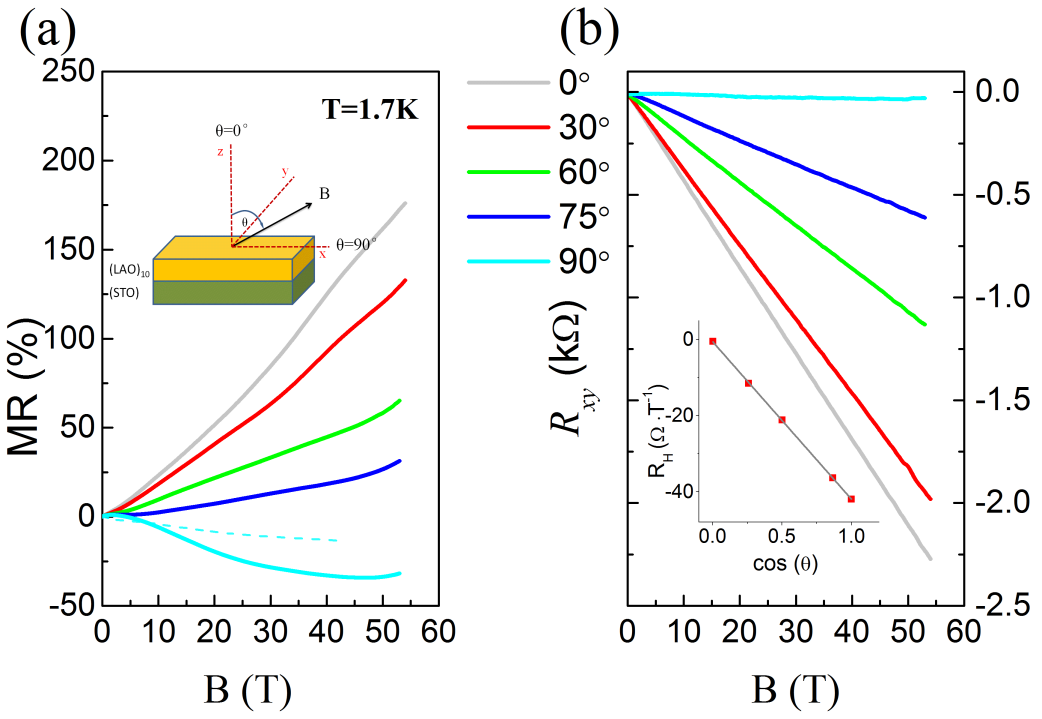

Figure 4.8: Longitudinal magnetoresistance (a) and Hall resistance (b) at T=1.7 K as a function of the tilt angle between the sample's plane and the magnetic field. Inset of (b) displays the linear variation of the Hall coefficient versus the cosine of the tilt angle. The dashed dark cyan line in (a) is the MR recorded at 20 K under parallel magnetic field.

A negative MR under parallel magnetic field was reported by many groups and several explanations were developed. Lee *et al.* [Lee 2011] suggests that the negative MR is due to Kondo effect, where the itinerant electrons are scattered by the localized magnetic moments at the interface. As the magnetic field increases, spin-flip scattering is progressively reduced and translates into a decrease of resistance. According to this hypothesis, the saturation of the magnetoresistance is roughly expected when the Zeeman energy $\epsilon_Z = g\mu_B B_{\parallel}^*$ matches the spin-orbit

coupling energy $\epsilon_{SO} = \frac{m^*\alpha^2}{2\hbar^2}$. Using the parameters derived later in this thesis ($g = 5$, $m^* = 1.9m_e$ and $\alpha = 5.45 \times 10^{-12}$eVm), we extracted a characteristic field $B_c \simeq$1.4 T, which is one order of magnitude lower than the experimental one. Furthermore, the negative MR of 15 % survives at 20 K and under a parallel magnetic field up to 40 T (dashed cyan line in Fig. 4.8) also indicates that the Kondo model is unlikely to account for the negative MR in our case. The second explanation is the diamagnetic shift under parallel magnetic field, where the parallel magnetic field moves upward the confining energies and depopulates the highest subband. The inter-subband scattering contribution is then suppressed and the MR shows a negative behavior up to a certain field until the highest subband is completely empty [McCollam 2014]. This hypothesis is welcomed but difficult to quantify in our study. The third hypothesis is the strong spin-orbit coupling in the interface, suggested by the theoretical work of Diez *et al.* [Diez 2015]. The presence of the Rashba spin-orbit coupling is consistent with the negative magnetoresistance of the order of 35% when the magnetic field is parallel to the plane of the sample. The interplay between electron scattering and spin-orbit coupling in the framework of the Boltzmann formalism applicable to disordered samples can yield a giant negative magnetoresistance as experimentally observed. The growth conditions certainly have a large impact on the sample's magnetoresistance response, so that a direct comparison of our data with the results of reference [Diez 2015] is impractical, however the magnitude of the magnetoresistance and the saturation field, which strongly depends on the carrier density, are in qualitative agreement.

4.3.2 Shubnikov-de Haas oscillations

We now turn our attention to the SdH oscillations which are barely visible in the raw data of Fig. 4.8 since their amplitude is only 1% of the sheet resistance. After a subtraction of a polynomial background, the SdH oscillations are displayed in Fig. 4.9. Interestingly, they show clearly an imperfect periodicity when plotted as a function of inverse magnetic field. Fast Fourier transforms (FFT) were performed for the two samples and show only one broad peak (shown in insets of Fig. 4.9). However, the fitting of the oscillatory part of ΔR_{xx} based on the LK formula (Eq. 1.54) with the main FFT frequency can not reproduce the oscillations in both samples, even qualitatively (main panels in Fig. 4.9). Indeed, careful experimental analysis indicates a separation between successive maxima which increases by ~ 2 T^{-1} as the magnetic field decreases. Traditionally, non-periodic oscillating features are interpreted in terms of the presence of several charge carriers channels, originating from different sub-bands, contributing to SdH oscillations with different periods. Usually, a FFT of the signal allows the extraction of the frequency peaks associated with each subband. In the present case however, this procedure fails mainly because of the small number of oscillations and their *almost periodic* character.

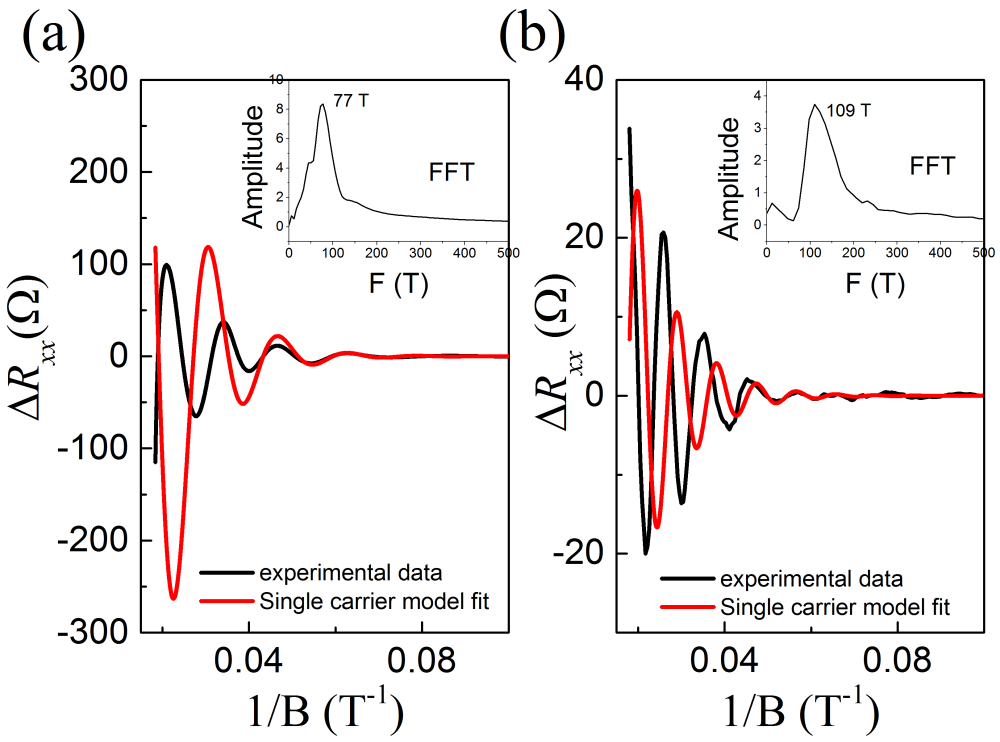

Figure 4.9: Comparison of $\Delta R_{xx}(1/B)$ between the experimental data (black) and calculation (red) using a single oscillation frequency corresponding to the FFT peak for two similar samples issued from the same batch. The qualitative failure of this simple model calls for alternative scenario.

In order to evaluate the effective mass, we derive the carrier's effective mass (as well as the quantum mobility $\mu_q = e\tau_q/m^*$) by studying the temperature dependence of the SdH oscillations as a function of inverse magnetic field using the LK formula (Eq. 1.54). The best fit of $\Delta R_{xx}(T)$ is obtained with the following parameters $m^* = 1.9 \pm 0.1 \times m_e$ (where $m_e = 9.1 \times 10^{-31}$ kg is the bare electron mass) and $T_D = 5.5 \pm 0.3$ K, from which one can extract the quantum scattering time $\tau_q = 2.2 \pm 0.1$ ps and the quantum mobility $\mu_q = 203 \pm 15$ cm^2/Vs (see inset of Fig 4.10).

The effective mass of $1.9m_e$ indicates that the oscillations are probably originating from the heavy bands derived from the Ti^{3+} d_{xz} and d_{yz} orbitals instead of the d_{xy} band despite its low effective mass (which is around $0.7m_e$). This can be understood considering the different spatial distribution of the subbands in the interface [Delugas 2011]. Electrons populating the d_{xz} and d_{yz} electrons are reported to reside within a few unit cells of STO below the LAO layers, and experience less scattering from the interface roughness/defects. On the other hand the d_{xy} electrons are confined close to the interface and experience more scattering. As a result, the d_{xz} and d_{xz} electrons have a larger mobility than the d_{xy} electrons, despite their heavier effective mass and show the SdH oscillations under high enough magnetic

field.

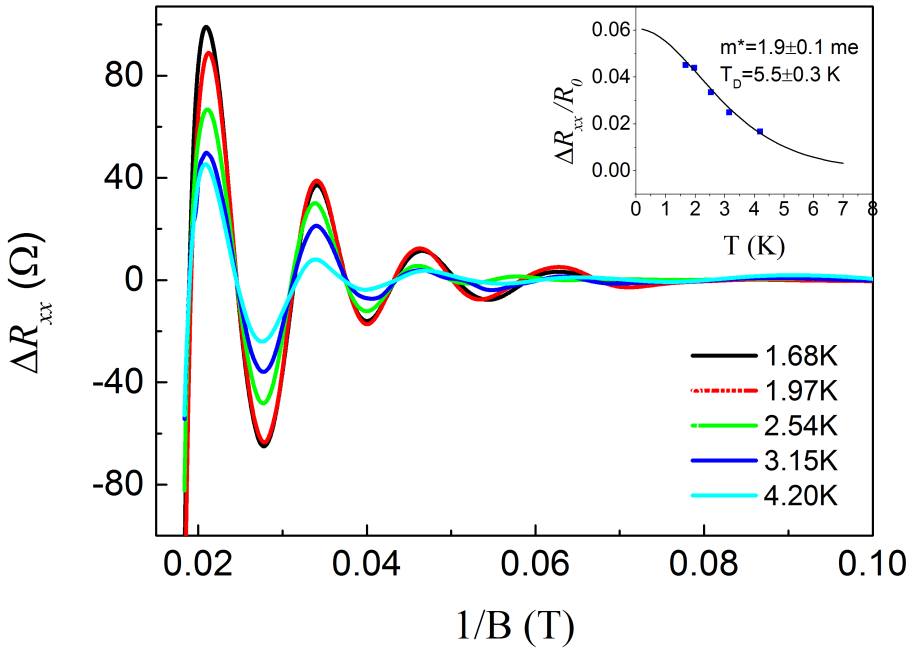

Figure 4.10: Temperature dependence of the Shubnikov-de Haas oscillations as a function of the inverse magnetic field after subtracting a smoothed background. Notice that the oscillations are not exactly $1/B$-periodic. The inset shows the oscillations' amplitude fitted using the LK expression.

4.3.3 Discussion

Although the multi-band scenario cannot be totally excluded, we focus here on an alternative explanation involving spin-orbit coupling. This hypothesis is motivated by the general shape of the oscillations (the exponential-like envelope) which is suggestive of a single band contribution. We would like to stress that, although the Hall carrier density is close to (slightly lower) the threshold of 1.7×10^{13} cm^{-2} (below which only the sub-band derived from d_{xy} are supposed to be populated, giving rise to a genuine 2DEG), our interpretation of SdH oscillations below relies on the contribution of a single heavy sub-band with Rashba effect, whereas the d_{xy} orbitals do not contribute. Several authors [Caviglia 2010a, Diez 2015, Fête 2012, Fête 2014] have considered the influence of the Rashba spin-orbit coupling at the LAO/STO interface, arising from the interfacial breaking of inversion symmetry. In the presence of a strong perpendicular magnetic field, the usual Landau level spectrum is

modified and reads [Nitta 1997]

$$\begin{cases} \varepsilon_{(N=0)} &= \kappa_{(B)} \\ \varepsilon^{\pm}_{(N>0)} &= N\hbar\omega_c \mp \sqrt{\kappa^2_{(B)} + N\frac{2\alpha^2 eB}{\hbar}} \end{cases} \tag{4.1}$$

where $\kappa_{(B)} = \frac{1}{2}\hbar\omega_c - \frac{1}{2}g\mu_B B$, N is a positive integer, $\omega_c = \frac{eB}{m^*}$ is the cyclotron pulsation, g is the spin-orbit enhanced Landé factor and α is the strength of the spin-orbit coupling. The Rashba effect will lift the degeneracy of the spin up and spin down bands and split the simple Landau spectrum into two families of non-linear Landau levels which are shown in the fan diagram in Fig. 4.11(a). The LL broadening is taken into account using a Gaussian line shape with a $\sqrt{B}$ variance ($\Gamma_\pm = \gamma^\pm\sqrt{B}$) in Eq. 1.51

$$\begin{aligned} g(\varepsilon^+) &= \frac{m}{2\pi\hbar^2}\frac{\hbar\omega_c}{\pi\Gamma_+}\sum_{N=0}^{\infty} exp\left[-\frac{(\varepsilon-\varepsilon_N^+)^2}{2\Gamma_+^2}\right] \\ g(\varepsilon^-) &= \frac{m}{2\pi\hbar^2}\frac{\hbar\omega_c}{\pi\Gamma_-}\sum_{N=0}^{\infty} exp\left[-\frac{(\varepsilon-\varepsilon_N^-)^2}{2\Gamma_-^2}\right] \end{aligned} \tag{4.2}$$

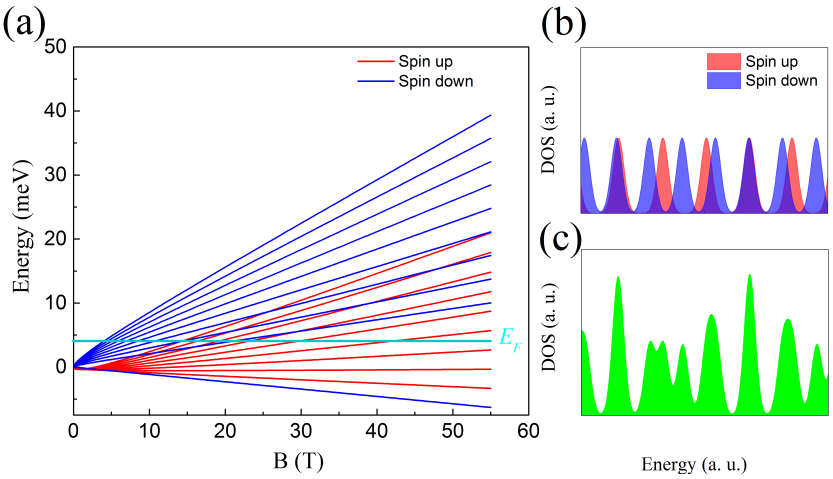

Figure 4.11: (a) The Landau levels for spin up and spin down as a function of magnetic field with the presence of Zeeman effect and Rashba effect. (b) The density of states (DOS) of the spin up and spin down Landau levels with a Gaussian lineshape (Eq. 1.51) broadening with $\sqrt{B}$ variance. (c) The total DOS of the spin up and spin down in (b).

Fig. 4.11(b) shows the DOS for spin up and spin down and Fig. 4.11(c) shows the total DOS for the two spins. From the total DOS we can see the peaks in the DOS are no longer equally separated in energy. By setting the carrier density n as a parameter, we can compute the Fermi energy ε_F by equating the total density of

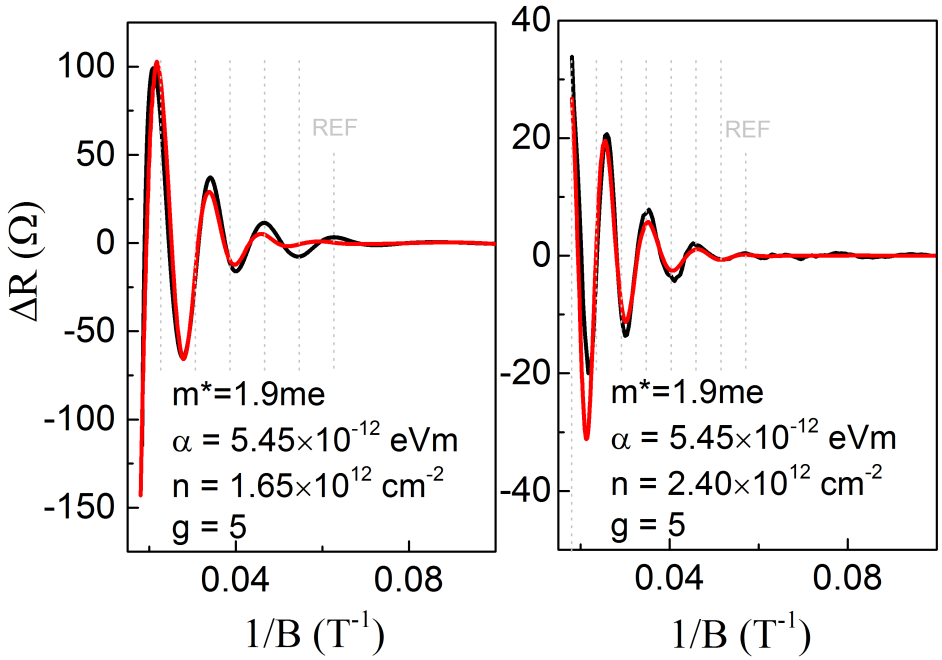

Figure 4.12: Fit (red line) of SdH oscillations for two similar samples issued from the same batch using Eq. 4.1 in the presence of spin-orbit coupling. The black line corresponds to the experimental data. Vertical dotted lines are guide for eyes. "REF" stands for the arbitrary reference for the 1/B periodicity.

states at a given magnetic field to n:

$$n = \int_{-\infty}^{+\infty} d\varepsilon f(\varepsilon - \varepsilon_F) g(\varepsilon).$$

Considering the field-dependent orbital degeneracy of the Landau levels (LLs) and their spectrum given by equation 4.1, the Fermi energy actually evolves non-monotonically within the LL band-structure. As the Fermi energy alternatively crosses a LL or remains in between two LLs, the magnetoresistance oscillates respectively above or below the mean resistance value, giving rise to SdH oscillations. The B-rising amplitude of the oscillations is adjusted using an exponential function.

Fig. 4.12 shows the best fit obtained using this procedure for two samples issued from the same batches from which we extract the free parameters n, g and α. The effective mass value, m^* is constrained to be $1.9m_e$ as found earlier (see inset of Fig. 4.10). Despite an inevitable uncertainty in the determination of the Rashba constant α and g-factor (due to the limited number of oscillations), they both fall in the range of reported values in the literature [Fête 2014, Caviglia 2010a]. We would like to emphasize that the set of parameters $\{\alpha = 5.45 \times 10^{-12}$ eVm, $g = 5\}$ is unique for each sample provided the carrier density remains close to the one

computed using the usual Onsager relation $n = (ed_s)/(hT_{SdH})$. Here, $d_s = 2$ is the spin degeneracy and T_{SdH} is the mean period of the oscillations plotted against inverse magnetic field (neglecting the imperfect periodicity of the SdH oscillations). The obtained carrier density $n \sim 10^{12}$ cm^{-2} is of the same order of magnitude as found in other studies of similar samples [Ben Shalom 2010, Zeng 2016], but remains almost two orders of magnitude lower than the prediction of the polar catastrophe model. Furthermore, it is inconsistent with the value extracted from the linear Hall effect $n_H = 1.48 \times 10^{13}$ cm^{-2} shown in Fig. 4.8.

Since there are 3 free parameters (g, α, n) in the fitting procedure, any change in one of them will affect the oscillation pattern. In order to check the uniqueness of the parameters, we have tried to constrain each parameter and set the rest two to be free parameters. Fig. 4.13 shows some fitting examples when one parameter is slightly modified compared to its optimal values while the two other are determined by the least square method (see the legend for details). The adequation between experimental and theoretical data is, in most cases, not satisfactory, thus establishing the uniqueness set of fitting parameters.

This discrepancy between the carrier density extracted from the SdH oscillations and the Hall effect is actually a long standing issue and several interpretations have been proposed. First, the presence of valley degeneracy has been considered in the literature [Ben Shalom 2010] and would provide a natural explanation involving a complex band-structure. However the odd[1] ratio n_H/n in the present study does not favor this hypothesis. It is worth noting, in addition, that different ratios ranging from roughly 2 to 5 have been reported in the literature [Caviglia 2010b, Ben Shalom 2010, McCollam 2014, Xie 2014] and are therefore likely dependent on the sample's growth conditions rather than being a universal band-structure characteristic.

The difference between n_H and n can be reconciled assuming one or more additional conduction channels which do not contribute to SdH oscillations. In this framework, the Hall resistance can be approached using a minimal two-fluid model, characterized by carrier densities n_1 , n_2 and mobilities $\mu_{t,1}$ and $\mu_{t,2}$. We assume that both carrier densities n_1, n_2 relate to the 2DEG, and that the lower mobility fluid may include several indistinguishable sub-bands. The transverse resistance R_{xy} as a function of B can be written as [Guduru 2013]

$$\begin{aligned} R_{xy}(B) &= \frac{B}{e} \times \frac{\left(n_1\mu_{t,1}^2 + n_2\mu_{t,2}^2\right) + \left(\mu_{t,1}\mu_{t,2}B\right)^2 (n_1 + n_2)}{\left(n_1\mu_{t,1} + n_2\mu_{t,2}\right)^2 + \left(\mu_{t,1}\mu_{t,2}B\right)^2 (n_1 + n_2)^2} \\ R_{(B=0)} &= \frac{L}{W} \times \left(en_1\mu_{t,1} + en_2\mu_{t,2}\right)^{-1}. \end{aligned} \tag{4.3}$$

We note that $\mu_{t,i}$ $(i = 1, 2)$ stands for the transport mobility, which should not be confused with the quantum mobility μ_q defined earlier. It is also worth noting that the magnetic field evolution of $R_{xx}(B)$ is discarded from this analysis since a magnetoresistance contribution is not captured by this simple model. Only

[1] $n_H = 1.48 \times 10^{13} cm^{-2}$ and $n_{SdH} = 1.65 \times 10^{12}$ cm^{-2}, so that $\frac{n_H}{n} = 8.96$.

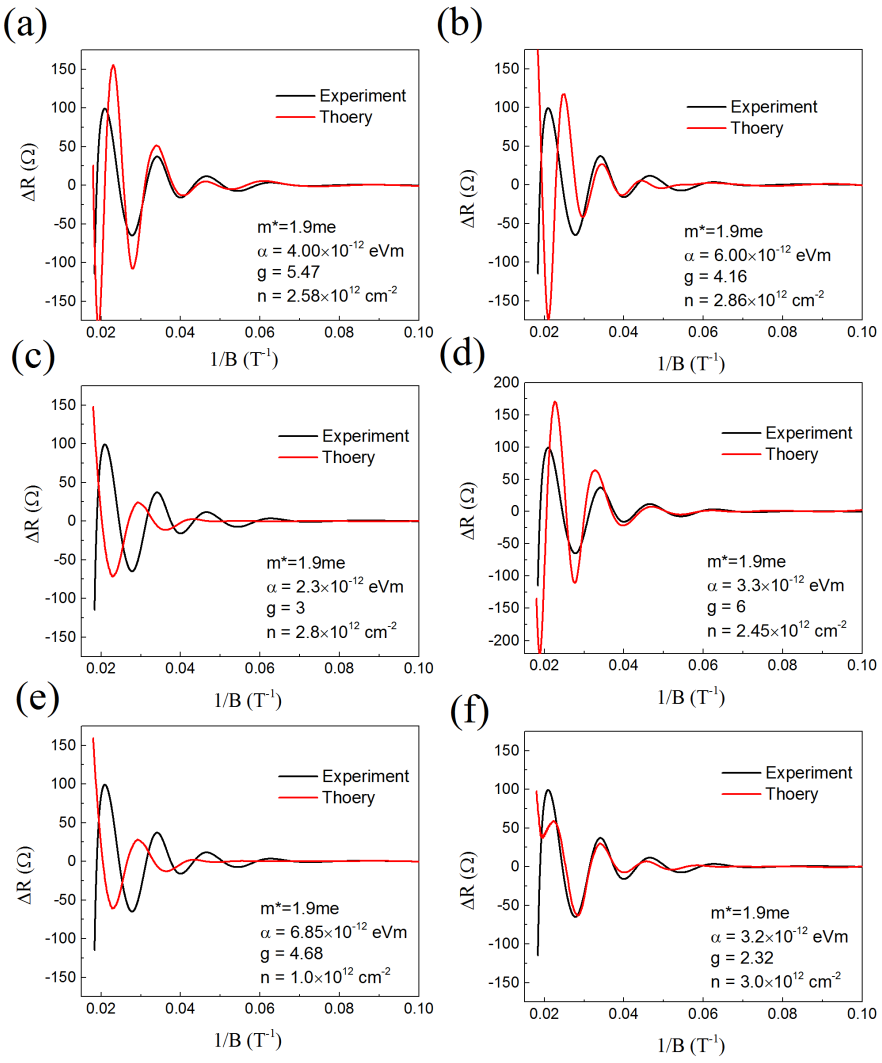

Figure 4.13: The effect of a slight parameter change on the quality of the fit. For all figures, the effective mass is constrained to the value $m^* = 1.9m_e$ extracted from SdH analysis. (a) and (b) The S.O. coupling strength is constrained above and below the best value (5.45×10^{-12} eVm) while the g-factor and carrier density are free parameters, (c) and (d) The g-factor is constrained above and below the best value ($g = 5$) while the S.O. coupling strength and carrier density are free parameters, (e) and (f) The carrier density is constrained above and below the best value ($n = 1.65 \times 10^{12}$ cm^{-2}) while the S.O. coupling strength and g-factor are free parameters.

the zero-field sample resistance $R_{(B=0)}$ is therefore considered. When $\mu_{t,1} \neq \mu_{t,2}$, the two carrier model yields a non-linear Hall effect, contrary to the experimental finding where the linearity of $R_{xy}(B)$ is established for the full magnetic field range (0-55 T). However, the linear B behaviour of the Hall resistance is progressively restored when the ratio $\mu_{t,1}/\mu_{t,2}$ approaches unity.

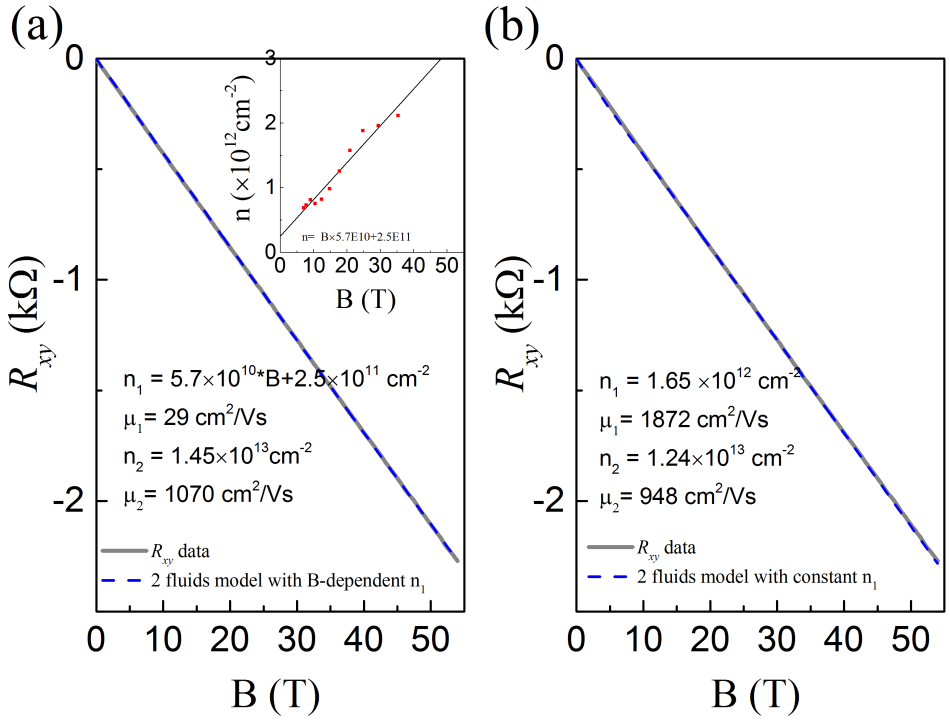

Figure 4.14: (a) Experimental Hall resistance data (black solid line) and two-fluid model fitting (blue dashed line) with a B-dependent carrier density n_1. The best free parameters are $n_2 = 1.45 \times 10^{13}$ cm^{-2}, $\mu_{t,1} = 29$ cm^2/Vs and $\mu_{t,2} = 1070$ cm^2/Vs. The inset shows the carrier density $n_1(B)$ as a function of magnetic field extracted from the Onsager relation. (b) Experimental Hall resistance data (black solid line) and two-fluid model fitting (blue dashed line) with $n_1 = 1.65 \times 10^{12}$ cm^{-2}, $\mu_{t,1} = 1872$ cm^2/Vs, $n_2 = 1.24 \times 10^{13}$ cm^{-2}, $\mu_{t,2} = 948$ cm^2/Vs, where n_1 is extracted from the previous Rashba fitting of the SdH oscillations.

Since a period shift of the SdH oscillations is observed when plotted versus inverse magnetic field, we assume that the carrier density could be magnetic field dependent. This apparent departure from $1/B$ periodic behaviour was also observed in reference [Jalan 2010]. The authors interpreted this result as a change of carrier density with increasing magnetic field, which would be of up to 1250% over the full magnetic field range of the present study. For selected values of B, the carrier density is therefore extracted from two consecutive peaks/valleys of the oscillations using the Onsager relation. The evolution of the carrier density $n_1(B)$ is then interpolated over the full magnetic field range as shown in the inset of Fig. 4.14(a).

$n_1(B)$ is introduced in the two-fluid model in order to fit the Hall resistance. As shown in Fig. 4.14(a), the linear Hall resistance is recovered but the free fitting parameters (n_2, μ_1 and μ_2) are not reliable (notice the very low mobility μ_1=29 cm^2/Vs for carriers giving rise to SdH oscillations). Therefore, the Rashba spin-orbit coupling hypothesis is favored in order to explain the period shift of the SdH oscillations, rather than a magnetic field dependent carrier density.

In the scenario which takes into account the Rashba spin-orbit coupling, we set $n_1 = 1.65 \times 10^{12}$ cm^{-2}, which is derived from the SdH oscillations. The best fit for the Hall resistance is obtained for $n_2 = 1.24 \times 10^{13}$ cm^{-2}, $\mu_{t,2}$=948 cm^2/Vs and $\mu_{t,1}$=1872 cm^2/Vs (shown in Fig. 4.14(b)). The fit is quite good and the fitting parameters are realistic. The minority electrons have a much lower carrier density, which is nearly 10% of the majority part, and a higher mobility. The high mobility electrons give rise to the quantum oscillations in the transport properties and the lower mobility electrons just contribute to the classical transport features (linear Hall effect and magneto-resistance background).

Based on the above analysis, we discuss the origin and transport properties of the two electron fluids. The SdH oscillations originate from heavy-mass carriers ($m^* = 1.9m_e$) which are probably derived from d_{xz} and d_{yz} orbitals extending deep in the STO side of the interface [Fête 2014]ïijĹas shown in Fir. 4.15ïijĽ. These minority carriers have a density of the order of $\sim 10^{12}$ cm^{-2} and a fairly high transport mobility of a few thousands cm^2/Vs. Moreover, their quantum mobility is much lower than their transport mobility by roughly a factor 9, suggesting that long-range scattering is dominant [Coleridge 1991]. Indeed, the quantum mobility is linked to the averaged elastic scattering time whereas the transport mobility is determined by the total scattering weighted by the scattering angle. When long-range scattering is dominant and account for isotropic diffusion processes, the quantum mobility is smaller than its transport counterpart. The presence of charged O^{2-} vacancies close to the interface or in the LAO layer [Petrović 2014] provides strong support for this hypothesis, although their influence is certainly reduced by screening as the charge distribution extends deeper in the STO layer. On the other hand, we attribute the non-oscillatory part of the magnetoresistance to charge carriers lying in the lowest energy sub-band derived from the d_{xy} orbitals (Fig. 4.15). Such carriers are concentrated within a few unit cells of the interface between LAO and STO and certainly experience strong scattering from ionic inter-diffusion and interface reconstruction. Consequently, these charge carriers should display low mobility and are not expected to contribute to SdH oscillations. It is worth noting that even if the two fluid model captures the essence of the underlying physics, it is certainly oversimplified to account for a realistic multi-band system, while a progressive charge distribution from the interface to deep inside the STO layer, involving a continuous crossover from low to high mobility carriers.

Our experimental results in high magnetic field are consistent with recent published studies insofar as they support the presence of at least two conduction channels with different mobility. The high mobility carriers, with twice the bare electron mass, are located deep in the STO material but remain sensitive to charge impuri-

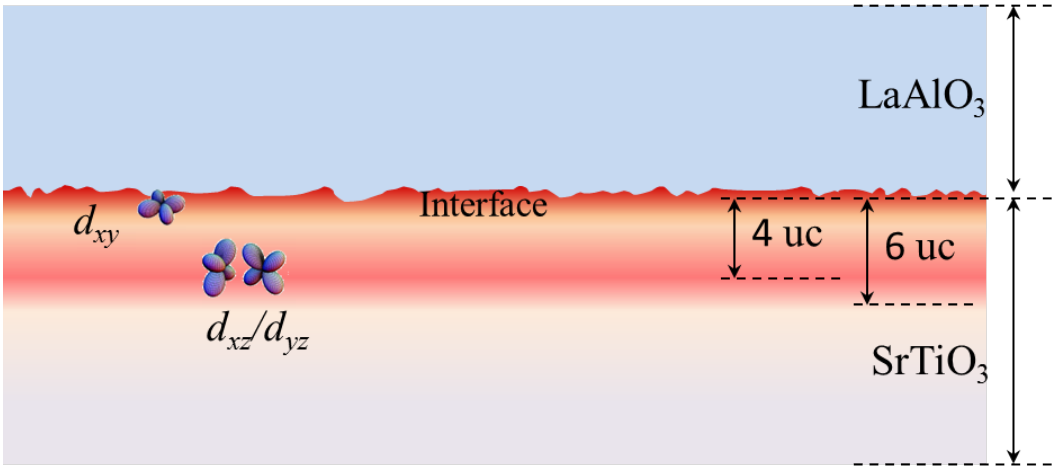

Figure 4.15: The sketch of the simplified two fluids model. The 2DEG in the $LaAlO_3/SrTiO_3$ can be viewed as two parts: the minority part, which is derived from the out of plane d_{xz}/d_{xz} orbitals, has lower carrier density and resides up to 6 unit cells inside the STO substrate. The majority part, which is derived from the in plane d_{xy} orbitals, have higher carrier density and are confined closer to the interface. The minority electrons contribute to the quantum SdH oscillations due to their higher mobility. The majority electrons have lower mobility and don't show SdH oscillations: they only contribute to the MR background and the Hall effect.

ties at the surface. The presence of O^{2-} vacancies is at the origin of a long-range disorder, which translates into a large difference between the Drude and Dingle scattering times. The mobile electron carriers are studied through SdH oscillations with reproducible deviations from $1/B$ periodicity. This effect is interpreted as a consequence of Rashba spin-orbit coupling, consistent with the large negative, saturating magnetoresistance when the field is applied parallel to the sample plane. On the other hand, the low mobility carriers are located close the LAO/STO interface and experience strong scattering, so that the corresponding SdH oscillations remain out of experimental reach even in magnetic fields as high as 55 T. Their contribution is visible in the linear Hall effect, with carrier density roughly one order of magnitude higher than the mobile electrons. In order to validate these conclusions, a magneto-transport study in higher mobility with varying carrier concentration would be required, which will be discussed in the following.

4.4 Band structure spectroscopy

In this section, we focus our attention on the electronic properties of a high mobility $LaAlO_3/SrTiO_3$ sample with 8 unit cells of $LaAlO_3$ measured at sub-Kelvin temperature (40 mK) and under a steady magnetic field of 16 T. Contrary to the previously studied samples, we now take advantage of a high B/T ratio in order

to resolve the band-structure, where the sub-bands are separated from only a few meV. Importantly, we also use a back-gate voltage to tune the carrier density (up to 1.7×10^{13} cm^{-2}) so that the Fermi energy spans an energy window in the vicinity of the band crossing point.

The high mobility sample is obtained under a high growth temperature (850 °C), a low oxygen partial pressure (P_{O_2}= 1.6 × 10^{-5} mbar), and using low laser energy. The deposition rate is therefore quite small and the interface is supposed to host less defects resulting in a higher mobility. The Hall mobility was measured to be 5000 cm^2/Vs , which is about 5 times higher than the ones discussed in section 4.3.1. The back-gate electrode is connected to the sample using silver paste.

4.4.1 Gate dependent magneto-transport at sub-Kelvin temperature

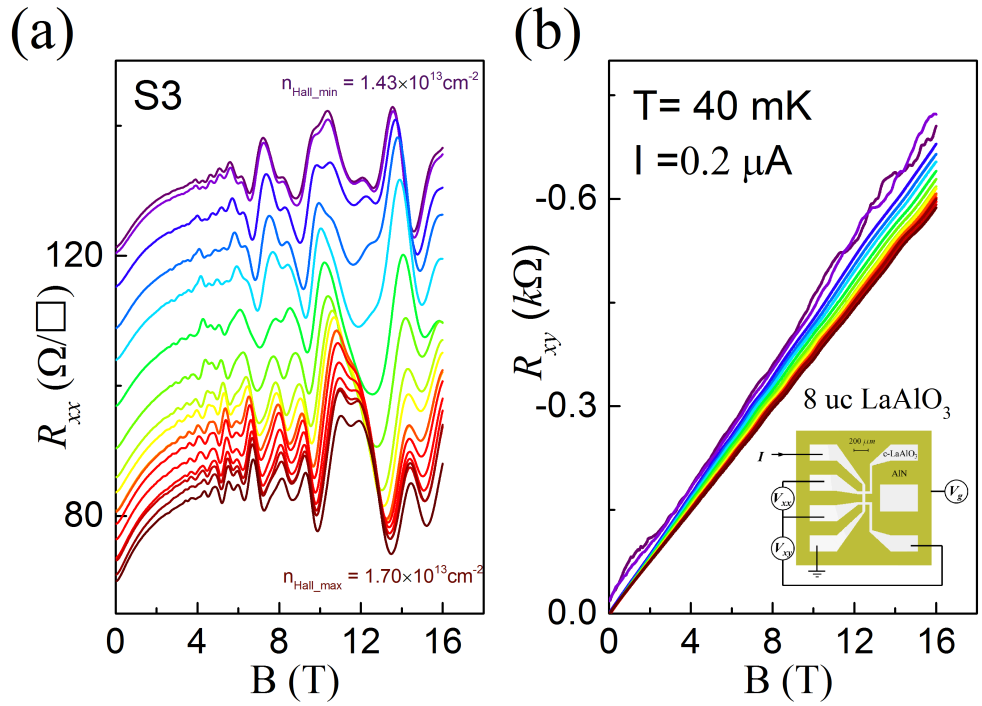

Figure 4.16: (a) The longitudinal resistance R_{xx} and (b) Hall resistance R_{xy} at 40 mK under a DC field up to 16 T with a current $I = 0.2\mu A$. The R_{xx} show complex SdH oscillations at the this temperatures with several frequencies, and the oscillation pattern is clearly gate dependent. The R_{xy} are almost linear up to the 16 T, except some small features superimposed on it, which we think are the parasitic R_{xx} component. The inset shows the sample sketch and the measurement setup.

The temperature dependence of the resistance shows an expected metallic behavior with a sheet resistance varying from 50 kΩ at room temperature to 100 Ω at

helium temperature, respectively. This characteristic is similar to any other samples and will not be discussed further. Fig. 4.16 shows the back-gate dependence of the longitudinal and Hall resistance at T=40 mK. The longitudinal resistance displays a complex SdH oscillation pattern on top of a positive MR background. Remarkably, the MR at 16 T is only of the order of 10% , which is much smaller than the samples previously discussed. The Hall resistance is almost linear over the full magnetic field range, except for some superimposed oscillating features which are probably a small contribution of the MR as expected for multi-band system. For some values of the back-gate voltage when the carrier density is the lowest, the Hall resistance is erratic and noisy. This behavior is reversible when the carrier density is increased. Actually, this phenomenon was already observed in other back-gated $LaAlO_3/SrTiO_3$ samples and was accompanied with a drastic increase of the zero-field resistance, pointing towards a metal to insulator transition. In the present case, we speculate that this transition occurs locally, affecting first some areas in the vicinity of the Hall probes (which therefore behave as a free antenna and produce a noisy signal), and leaving the longitudinal resistance contacts unaltered. In the following, the noisy Hall resistance curves will simply be discarded from the analysis, since the exact physical mechanisms behind this scenario are still under investigation and remain beyond the scope of this present work. Over the full back-gate voltage range (0-100 V), the minimum and maximum Hall carrier densities are respectively 1.43×10^{13} cm^{-2} and 1.7×10^{13} cm^{-2}, with relative transport mobilities 3600 cm^2/Vs and 5000 cm^2/Vs. The relationship between the carrier density and mobility is driven by screening effects, which become prominent and reduce electron-electron scattering as the carrier concentration increases. The mobility range is in agreement with the observation of the first oscillating features of the MR at $B \sim 2$ T, following the criterion $\mu B > 1$ in the regime $\hbar\omega_c > k_B T$. It is worth pointing out that the relationship between the back-gate voltage and the Hall carrier density is not straightforward in LAO/STO samples, as shown in Fig. 4.17. In this experiment, the back-gate voltage was first raised from 0 V to 15 V, then set back to 2 V before being increased again to the maximum value of 100 V. The corresponding Hall carrier density is strongly hysteretic, involving electron trapping states in $SrTiO_3$ according to Tian *et al.* [Tian 2011]. In the following and for clarity, any reference to the back-gate voltage is avoided, when possible, in favor of the carrier density.

Fig. 4.18(a) shows the oscillating part $\Delta R_{xx}(B)$ of the longitudinal resistance (after removing a monotonous background to the MR) for each value of the back-gate voltage. The curves have been separated and successively up-shifted as a function of decreasing carrier density for clarity. Starting from $n_{Hall} = 1.7 \times 10^{13}$ cm^{-2} at $V_g = 80$ V (the highest curve of Fig. 4.18(a)) we notice first a very weak evolution of the oscillating features in agreement with Fig. 4.17 where the carrier density remains fairly constant despite a decreasing back-gate voltage. Accordingly, a net modification of the SdH oscillation pattern arises when the Hall carrier density drops from $\sim 1.65 \times 10^{13}$ cm^{-2} to 1.4×10^{13} cm^{-2}. To interpret the complex SdH oscillation figures, we perform a FFT for each curve plotted as a function

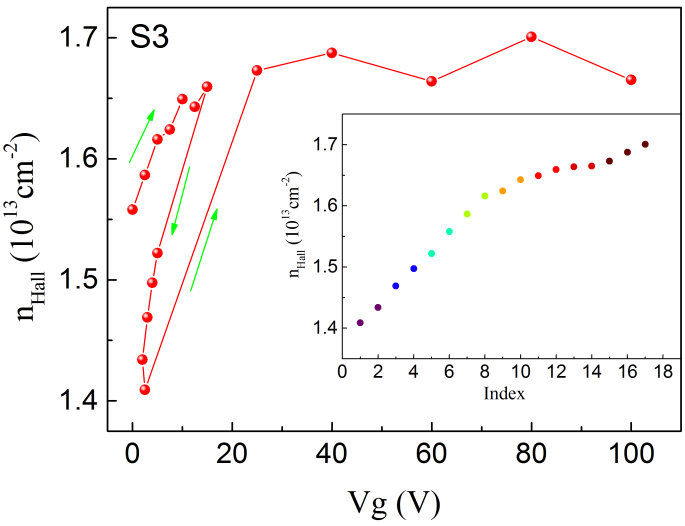

Figure 4.17: The Hall carrier density n_{Hall} as a function of the applied back gate V_g. At low V_g the n_{Hall} is strongly dependent on V_g and almost saturates at high V_g. Another typical behavior is the hysteresis effect of the applied gate, originating from the presence of electrons trapping states in the STO.

of the inverse magnetic field (Fig. 4.18(b)), and we attribute each peak to an oscillation frequency which will later be assigned to a particular sub-band of the band-structure at the Fermi energy. Neglecting the very low frequency regime (< 10 T), we distinguish 9 peaks distributed into 3 pairs and 1 triplet having a different evolution with the carrier density. The peaks are labelled with letter A_i to D_i (where the index i=1, 2, 3 stands for the pairs and triplets) and their evolution is highlighted by dashed lines in Fig. 4.18(b). As the Hall carrier density increases, the values of the peaks $A_{1,2}$ increases; the frequency of the peaks $B_{1,2}$ is unchanged and the frequency of the peaks $C_{1,2}$ varies in a non-monotonous way with a kink at the critical carrier density $n_c = 1.56 \times 10^{13}$ cm^{-2}. According to [Joshua 2012], a Lifshitz transition is expected around $n = 1.68 \times 10^{13}$ cm^2, which falls in the range of n_c, and supports the presence of strong modifications of the FFT spectra in its vicinity. Finally, the peak D_1 disappears at n_c while the peak D_2 shows up at a lower frequency. The peak D_3 follows the same trend as peaks D_1 and D_2, however its amplitude keeps on vanishing as the carrier density increase.

4.4.2 Effective mass versus carrier density

Through the LK (Eq. 1.54) relation, the temperature dependence of the amplitude of the SdH oscillations provides information about the charge carrier's effective mass. In electronic systems where several sub-bands are involved, a detailed analysis is quite demanding since it relies on the temperature evolution of the peak's am-

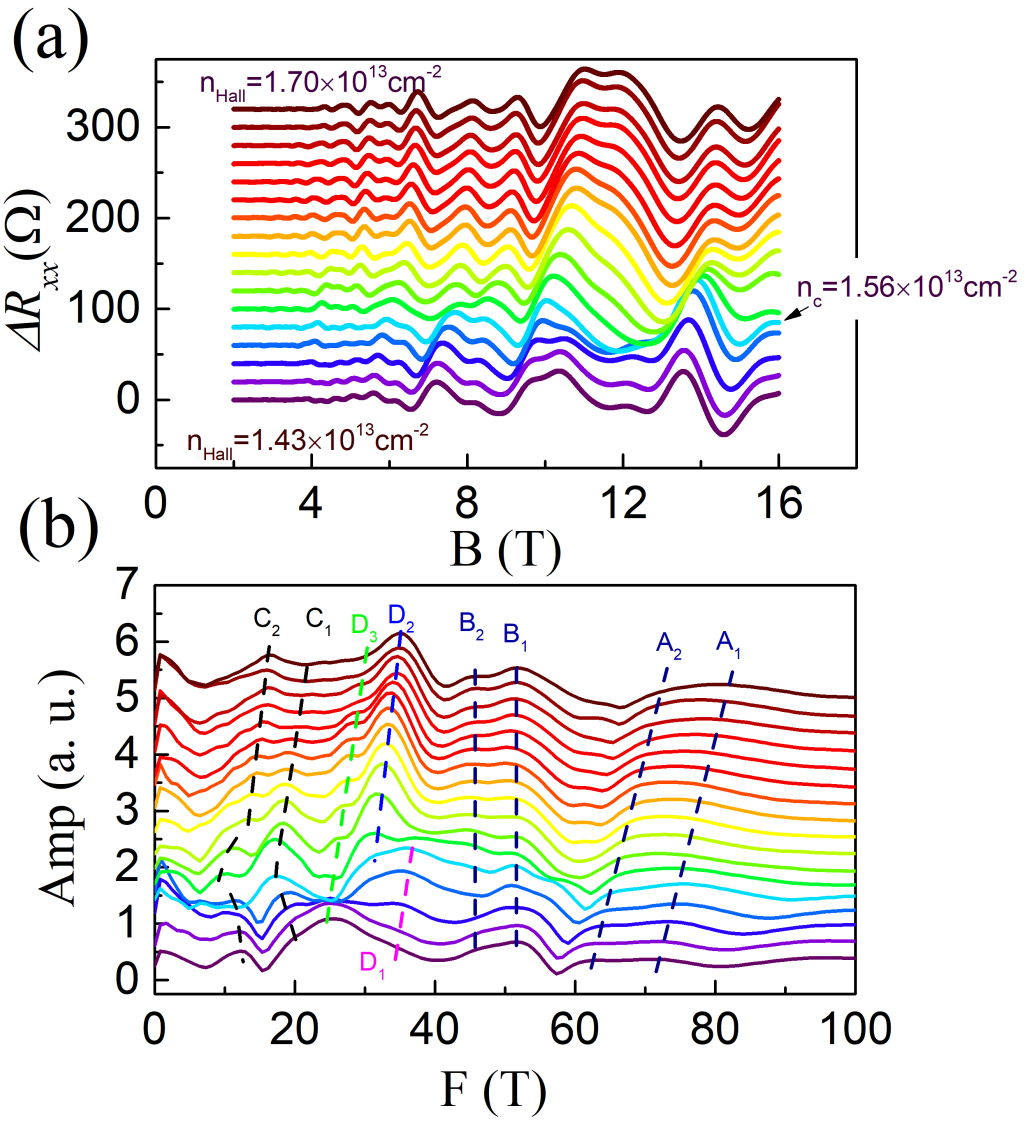

Figure 4.18: (a) Gate dependence of ΔR_{xx} vs B under after background subtractions of R_{xx} in Fig. 4.16(a) by polynomial fits. (b) The FFT spectra of ΔR_{xx} vs $1/B$. The dashed lines indicate the oscillation peaks in the FFT spectra.

plitude of the FFT signal, performed over a limited inverse magnetic field window. This procedure applies only when the SdH oscillation frequencies are high, so that the contributing sub-bands are easily distinguishable from each other. In the present study, however, the oscillation's frequencies are only a few tens of teslas, which is far too small to obtain a reliable FFT spectrum over an inverse magnetic field window of, say[1] 50 mT^{-1}. Therefore, in Fig. 4.19, we directly analyze the temperature evolution of each maxima, without performing any FFT. Actually, each maxima corresponds to a mixture of several contributing sub-bands and the extracted effective mass can be regarded as an undefined pondered average of the individual effective masses of the involved sub-bands. Obviously, such an analysis is rather meaningless, except for the lower and upper bounds which provides an estimation of the lightest and heaviest sub-bands, respectively. In the present case, for the lowest carrier density ($n_{Hall} = 1.43 \times 10^{13}$ cm^{-2} at V_g=0 V), the effective mass is between 0.97 m_e and 2.24 m_e, in line with the typical values expected for the sub-bands derived from d_{xy} and d_{xz}, d_{yz} orbitals [Ben Shalom 2010, Xie 2014, McCollam 2014, Zeng 2016]. This analysis adds further credits to the presence of light and heavy sub-bands crossing the Fermi energy at this particular carrier density. For the highest carrier concentration ($n_H = 1.7 \times 10^{13}$ cm^{-2} at Vg=80 V), the same analysis provides an effective mass bounded between 1.38 m_e and 2.52 m_e. As a general trend, we observe an increase of the effective mass with increasing Fermi energy, suggesting the use of a band-structure model that necessarily goes beyond the parabolic band approximation.

4.4.3 Analysis and model

In 2DEG, the frequency f_{SdH} of the SdH oscillations is directly related to the area of the (2D) Fermi surface S_F through the Onsager relation $f_{SdH} = \hbar S_F / 2\pi e$. In the parabolic band approximation, the dispersion relation reads $E_{(k)} = \hbar^2 k^2 / 2m^*$ so that the Fermi surface is a disk of area $S_F = \pi k_F^2$ and the frequency of the SdH oscillations is $\hbar k_F^2$. Since the Fermi wave-vector is related to the carrier density, which can be tuned by the back-gate voltage, it is possible to gain information about the band-structure of the system by analyzing the evolution of the SdH oscillation frequency while varying the back-gate voltage. However, in the case of $LaAlO_3/SrTiO_3$ interface, theoretical studies suggest the presence of several non-isotropic Fermi surfaces, associated to the d_{xy}, d_{xz} and d_{yz} orbital-derived sub-bands. The band-structure further gains in complexity when one considers the "layer degeneracy lifting" of each sub-band. Indeed, close to the interface, each stoichiometric layer of STO does not experience the same symmetry breaking effect. For instance, in Fig. 4.20, the sub-band labeled d_{xy}^1 lies lower in energy than the d_{xy}^2 sub-band where the superscript 1, 2 indicates the first and second closest

[1] The LK formula requires the magnetic field at which the temperature dependence of the oscillation's maxima is considered. If the analysis focuses on the amplitude of a FFT peak, one uses the average of the (inverse) magnetic field window over which the FFT is performed. This procedure is meaningful only if the (inverse) magnetic field window is small enough compared to the full (inverse) experimental magnetic field range.

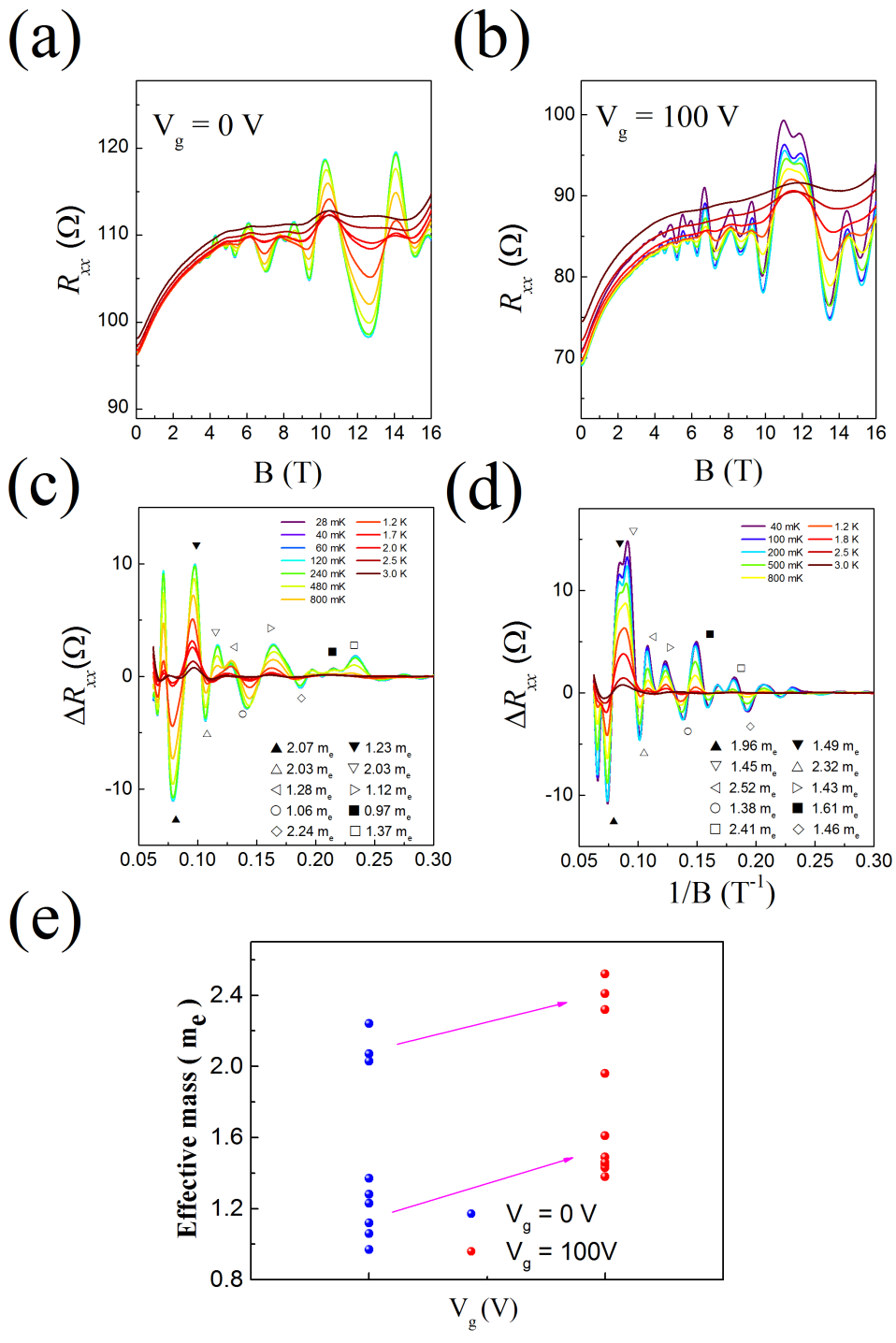

Figure 4.19: (a, b) Temperature dependence of R_{xx} as a function of magnetic field at V_g=0 V and 100 V. (c, d) ΔR_{xx} plotted as a function of inverse magnetic field for V_g=0 V and 100 V, after a background subtraction by polynomial fitting. The effective masses were calculated by the Lifshitz-Kosevich fitting of the temperature dependence of each maxima indicated by the symbols. (e) The effective masses plot for two different gate voltages, which show an enhancement when the carrier density n_{Hall} increases.

stoichiometric $SrTiO_3$ planes to the interface, respectively. We also note that the atomic spin-orbit coupling introduces some band-mixing (anti-crossing effects) at the sub-bands crossing points.

In complex electronic systems, the transport properties and the analysis of the Shubnikov-de Haas oscillations do not allow a direct determination of the band-structure. The exact shape of the Fermi area remains unknown and one must compare the experimental total Fermi area to the predictions of a model. The relation between the carrier density, obtained through the Hall effect, and the Fermi energy also relies on the predicted dispersion relation. Finally, the effect of the temperature and the finite mobility of the charge carriers must also be taken into account when one tries to relate the electronic and transport properties. In the following, we shall restrain our discussion to a qualitative link between the experimental transport measurements and the band-structure model in reference [Joshua 2012]. We attempt to demonstrate that the evolution of the SdH oscillation's frequencies (the FFT peaks) with respect to the Hall carrier density is consistent with the foreseen sub-bands dispersion relation.

In Fig. 4.18(b), the frequency of the FFT peaks A_1 and A_2 increases at the same rate upon increasing the carrier density. We speculate that they originate from the same spin-splitted heavy sub-bands $d^1_{xz/yz}$ (black and grey bands in Fig. 4.20). Indeed, as the Fermi energy increases, the cross-sectional areas of the $d^1_{xz/yz}$ sub-bands with the Fermi line increases quickly. The $A_{1,2}$ FFT peaks are also the highest frequency peaks, in agreement with the $d^1_{xz/yz}$ sub-bands forming the largest Fermi surface. Since these bands hold heavy carriers, we expect a fairly low mobility which translates into quite broad (almost indistinguishable) FFT peaks.

We assign the FFT peaks B_1 and B_2 to the spin-splitted light d^1_{xy} sub-bands. The frequency of the $B_{1,2}$ peaks do not change much with increasing carrier density, in agreement with the high sub-bands' slope in the considered Fermi energy window. On the other hand, the FFT peaks C_1 and C_2 are related to the light $d^1_{xz/yz}$ sub-bands since their low frequencies match with the minimal Fermi surface area. The evolution of the $C_{1,2}$ peaks with carrier density deserves particular attention. As shown in Fig. 4.18, the frequencies of the peaks first decrease when n_{Hall} approaches n_c, and then increase again when n_{Hall} is higher than n_c. This phenomenon can be linked with the band-structure by noting that the bottoms of the bands vary with the carrier concentration, as noted by [Maniv 2015]. This effect is particularly prominent in the quantum transport properties when the Fermi energy lies close to the band bottom, as for the light $d^1_{xz/yz}$ sub-bands. Upon increasing the carrier density, the combined effects of Fermi energy increase and the non-monotonous evolution of the bands' offset provides a natural explanation for the $C_{1,2}$ peaks evolution.

We now turn our attention to the D-bands triplet. Interestingly, the FFT peak D_1 disappears upon approaching n_c while the FFT peak D_2 actually appears for $n_{Hall} > n_c$. On the other hand, the peak D_3 can be more or less distinguished over the full carrier density range with a monotonous frequency increase. In the range

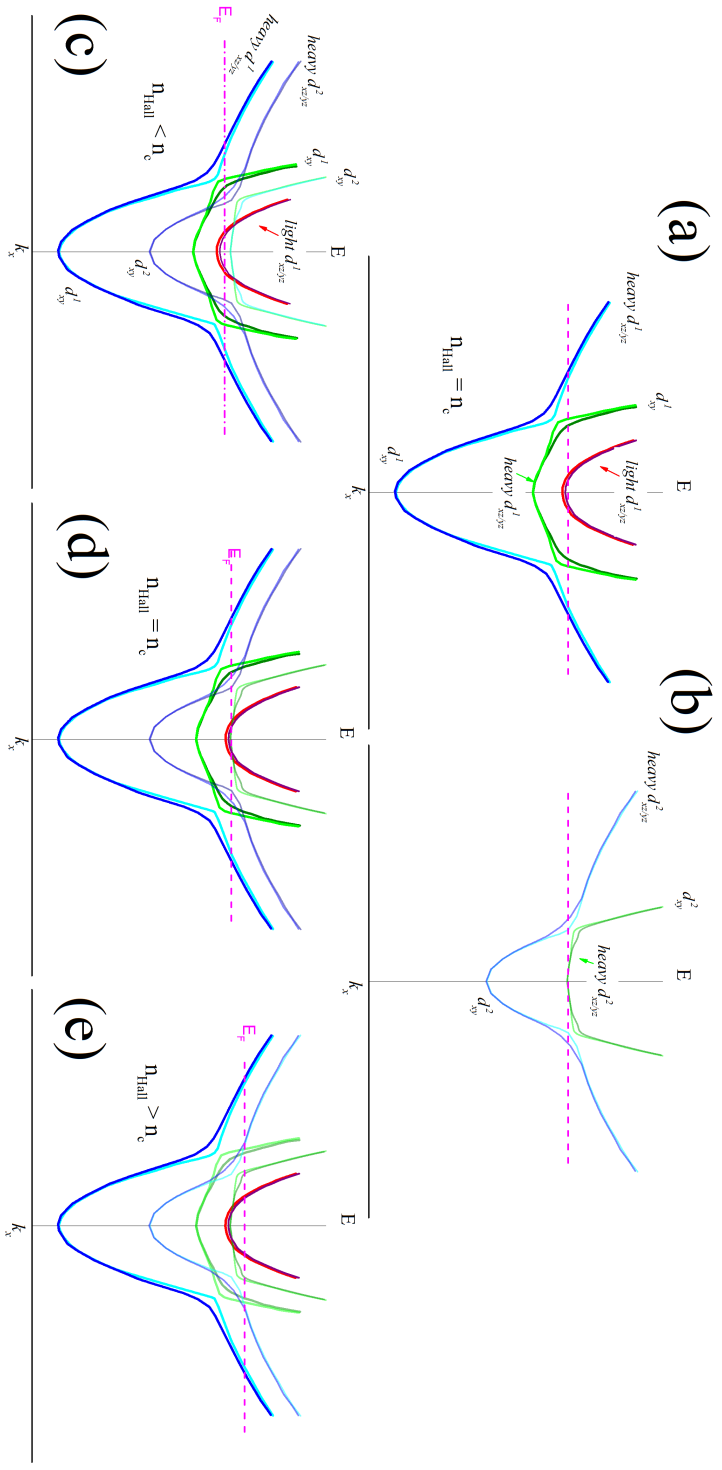

Figure 4.20: The sketch of the band structure and Fermi energy revolution. (a) The 3 lowest subbands of d^1_{xy}, d^1_{xz} and d^1_{yz} based on the model present in [Joshua 2012]. (b) The second lowest subbands of d^2_{xy}, d^2_{xz} and d^2_{yz}. The Fermi energy is set for the carrier density equals to n_c for (a) and (b). (c, d, e) The band structure by combining the lowest and second lowest subbands for different carrier density regime.

$n_{Hall} < n_c$, the peaks D_1 and D_3 are associated to the outer and inner Fermi surface of the d^2_{xy} band splitted by the spin-orbit coupling. The peak D_2, assigned to $d^2_{xz/yz}$ band, is absent since the Fermi energy lies below this band (dotted lines in Fig. 4.20). As the Fermi energy moves up ($n_{Hall} > n_c$), the electrons start populating the flat part of the d^2_{xy} bands: they gain a large effective mass which ultimately leads to the disappearance of the peak D_1. At the same time, the $d^2_{xz/yz}$ band is being filled and the peak D_2 arises. It is worth noting that the peak D_3, associated to the inner Fermi surface of the splitted d^2_{xy} band, is less affected at $n_{Hall} = n_c$ because of the smaller gap between the lower and upper d^2_{xy} bands at the crossing point.

4.4.4 Extension of the experimental results at 55 T and 500 mK

In this section, we present an extension of the above experimental work in magnetic field up to 55 T, performed in a ^{3}He cryostat with base temperature of 500 mK. The back-gate dependent R_{xx} and R_{xy} data are shown in Fig. 4.21. To maintain a reasonable signal-to-noise ratio under pulsed magnetic field, the current passing through the sample has been raised to 50 μA, *i.e.* 250 times larger than in the previous study at 40 mK. Although the electronic temperature is unknown, we assume it is larger than the one provided by the calibrated thermometer (500 mK). As a result, the main SdH oscillations are broadened compared to the low temperature data in the same magnetic field range, while the finest features have disappeared (see Fig. 4.22(c)).

The Hall resistance is quasi-linear with magnetic field except some faint oscillating features(shown in Fig. 4.21(b)), as previously reported. When the back-gate voltage is set to negative, the Hall resistance becomes noisy and ultimately meaningless, which confirms the trend observed in the previous study. The Hall carrier density range from $n_{Hall} = 1.39 \times 10^{13}\text{cm}^{-2}$ to $n_{Hall} = 1.70 \times 10^{13}\text{cm}^{-2}$ as the back-gate voltage is varied from -5 V to 25 V.

Fig. 4.22(b) shows the FFT spectra of the magneto-resistance oscillations for different back-gate voltages, after subtracting a monotonous background and plotting the curves as a function of the inverse magnetic field (Fig. 4.22(a)). Two broad peaks can be distinguished at f_1=72 T and f_2=27 T, but their spectral resolution is too low to observe their sensitiveness to the variations of n_{Hall}. Comparing with the very low temperature results, we assign the FFT peak f_1 and f_2 to the ones previously labeled $A_{1,2}$ and $D_{1,2,3}$, respectively. Naturally, this identification implies that the bands $d^1_{xz/yz}$, $d^2_{zx/yz}$ and d^2_{xy} have the highest ratio mobility/effective mass. This assertion may appear counterintuitive since the $d^1_{xz/yz}$ and $d^2_{xz/yz}$ sub-bands have a large effective mass, however the spatial location of the corresponding electrons (extension of the wave-function) is far from the interface and experience less scattering. The same argument holds for the light d^1_{xy} sub-band (peaks $B_{1,2}$), which mobility is assumed low since the electrons lies the closest to the interface. The peaks $C_{1,2}$, previously assigned to the light sub-bands $d^1_{xz/yz}$, were barely visible in the FFT signals at 40 mK and became undetectable when treating the data

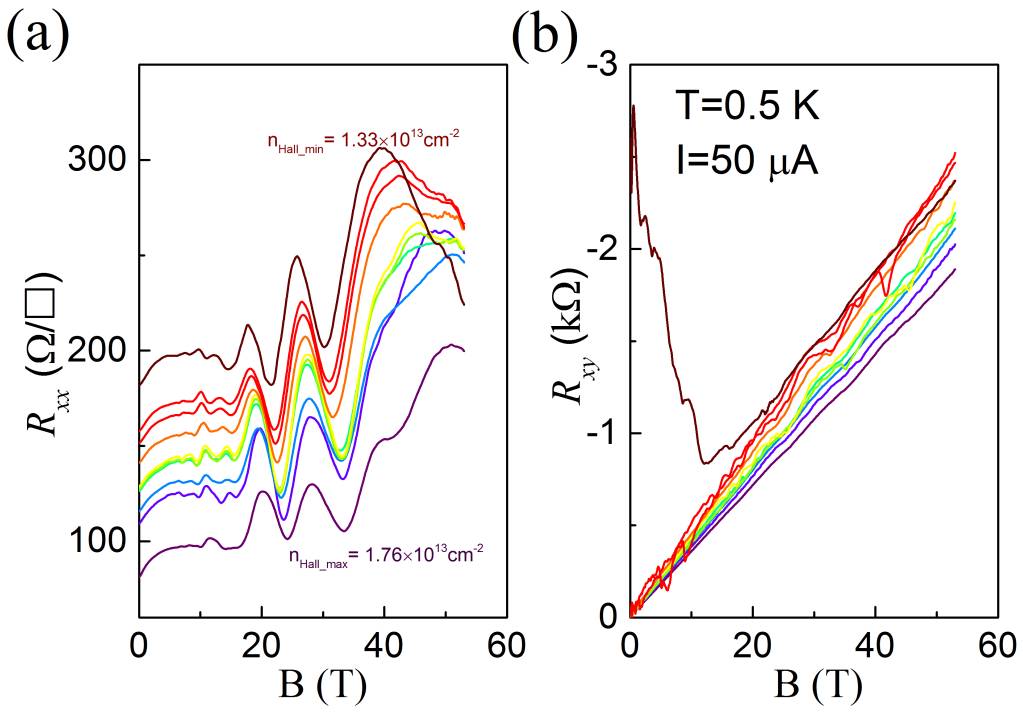

Figure 4.21: (a) The longitudinal resistance R_{xx} and (b) Hall resistance R_{xy} at 500 mK under a pulsed field up to 55 T.

recorded at 500 mK.

4.5 Conclusion

We have studied the transport properties of complex oxide $LaAlO_3/SrTiO_3$ interface under high magnetic field. We observe weak oscillations of the magneto-resistance with altered periodicity when plotted versus inverse magnetic field in samples with low carrier density and low mobility. We assume that this effect is linked to the Rashba spin-orbit coupling which fits reasonably well the experimental data and remains consistent with the large negative magneto-resistance when the field is parallel to the sample's plane. The one order of magnitude difference between the carrier density extracted from the Hall effect and from the pseudo-period of the SdH oscillations is explained by the contribution of at least two conducting channels with different characteristics. Using a minimal two-band model, we estimated the carrier density and the transport mobility of each band. Our results suggest that the majority of charge carriers occupy the lowest energy band, derived from the Ti $t_{2g} - d_{xy}$ orbitals. The electrons populating this band are close to the disordered interface and display low electronic mobility. On the other hand, a minority of carriers populate higher energy bands, which are derived from the Ti $t_{2g} - d_{xz/yz}$

orbitals. These electrons are located deeper in the STO side of the interface and display high mobility, despite the heavy expected effective mass.

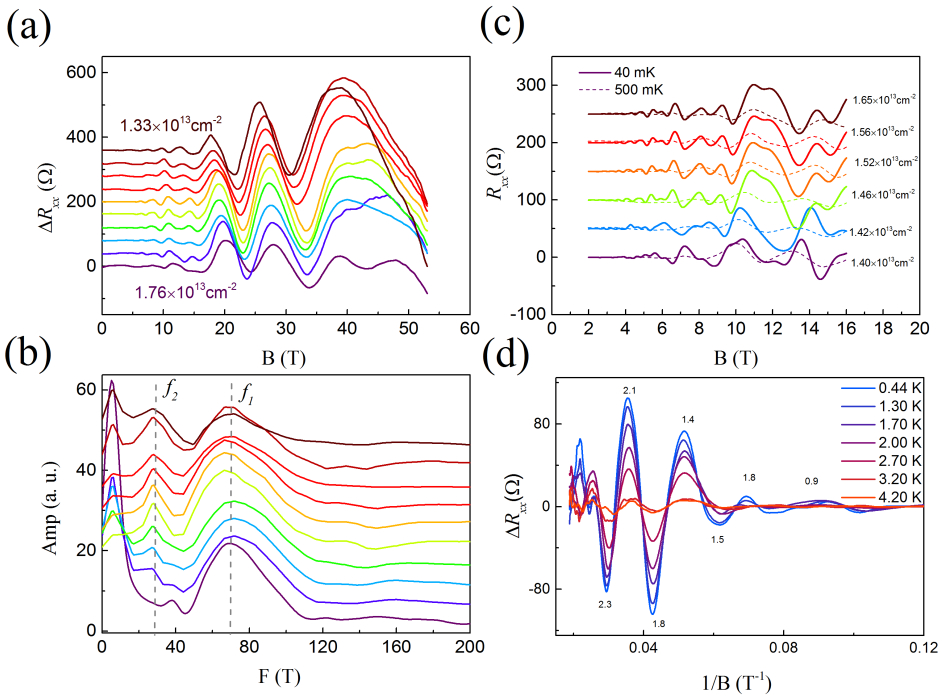

Figure 4.22: (a) Gate dependence of ΔR_{xx} vs B under after background subtractions of R_{xx} in Fig. 4.21(a) by polynomial fits at 500 mK. (b) The FFT spectra of ΔR_{xx} vs $1/B$. The dashed lines indicate the oscillations' peaks in the FFT spectra. The oscillations show only two peaks which are almost not changing with V_g. (c) The comparison between ΔR_{xx} measured at 40 mK (solid lines) and 500 mK (dashed lines) with the same n_{Hall}. The 40 mK data have more oscillations and larger amplitude than the 500 mK data. However, the peaks of the 500 mK data can always find a counterpart in the 40 mK data, indicating the good consistency between the two temperatures. (d) Temperature dependent ΔR_{xx} as a function of 1/B at $V_g = 0$. The numbers near the peaks are the effective masses in unit of m_e, calculated by the LK formula.

In order to obtain more insights into the fine sub-band structure, we continued this research in a high mobility sample under a steady magnetic field up to 16 T at 40 mK. The longitudinal resistance shows a complex SdH oscillation pattern and the Hall resistance is almost linear. The Hall carrier density can be tuned by the application of a back-gate voltage. The FFT of the oscillation pattern at different back-gate voltages show at least nine peaks. By analyzing their evolution, we notice that our experimental data can be well explained by the theoretical band-structure models in the literature, emphasizing the role of spin-orbit coupling and orbital

hybridization close the critical carrier density n_c [Joshua 2012]. Yet, this study does not constitute a proof in itself and more experimental work is required to improve on the FFT resolution, to determine the effective mass of each sub-bands, and to gain more knowledge in the relation between the Hall carrier density and the position of the Fermi energy in the band-structure. The same sample was also investigated under high magnetic field at a base temperature of 500 mK. Despite the larger available magnetic field range, the oscillation's broadening effects (due to the higher temperature) prevented the discovery of new interesting features, but confirmed the data obtained at high B/T ratio.

Conclusion

In this thesis, we have studied the electronic properties of 2DEG under very high magnetic field. This work mainly focuses on two different systems: graphene on SiC and the $LaAlO_3/SrTiO_3$ interface.

The discovery of these 2DEG systems in 2004 constitutes two milestones for research and have both attracted tremendous attention within the scientific community. This great interest is not only focused on the rich novel physics arising from the unique band structure of the two systems, but also on the engineering prospects, covering a broad range of promising applications in next generation of electronic devices.

In graphene on SiC, we have performed magnetotransport measurements under a very high magnetic field up to 78 T. We have observed a quantum Hall plateau at filling factor $\nu = 2$ which extends over an extremely large magnetic field range (from 7 T to 78 T) for the first time. This observation indicates that the carrier density in the sample increases over the full magnetic field range, pining the Fermi level in between the last two Landau levels. The robustness of the $\nu = 2$ quantum Hall plateau has already been studied before by other authors and attributed to a charge transfer from the SiC substrate. The model predicts a saturation of the carrier density after a moderate threshold magnetic field. Through the analysis of the temperature dependence of the quantum Hall effect based on the variable range hopping theory, we have discovered that the carrier density in the sample keeps on increasing without saturation until the Hall plateau departs from its quantized resistance $h/2e^2$.

In the studied sample, the breakdown of the quantum Hall effect occurs at a critical current density which is around 1/10 of the highest reported value in the literature. In the quantum Hall effect breakdown regime, small magnetoresistance oscillations with 1/B periodicity appear while the R_{xy} plateau remains quantized. In order to explain the anomalous magnetoresistance, we propose a model in which natural doping inhomogeneities are introduced in the sample. The presence of highly-doped puddles is justified by local chemical gating failures, which play an important role in the transport properties. The charge transfer not only occurs from the SiC substrate, but also from the highly-doped puddles with 1/B periodicity as the magnetic field increases. This phenomenon translates into 1/B magnetoresistance oscillations. This result can inspire the conception of new devices with embedded charge reservoir to enhance the stability of the quantum Hall effect, or to study specifically the breakdown mechanisms.

The transport properties of low mobility $LaAlO_3/SrTiO_3$ samples were studied under a magnetic field up to 55 T at helium temperature. We observed very weak SdH oscillations, which show a quasi-1/B periodicity when plotted versus inverse magnetic field. We assume that this effect is linked to the Rashba spin-orbit coupling which fits reasonably well the experimental data and remains consistent with a large

negative magnetoresistance when the field is parallel to the sample's plane. At the same time, a linear Hall resistance is observed in the full magnetic field range. The carrier density extracted from the SdH oscillations is one order of magnitude lower than that extracted from the linear Hall effect, which is a long-standing problem for this system. This inconsistency is an indication of the presence of at least two conduction channels with different mobility. Using a minimal two-bands model, we estimate the carrier density and transport mobility for electrons in each channel. This model reconciles the experimentally obtained values from Hall effect and SdH oscillations. Moreover, the effective mass deduced from the SdH oscillations allowed us to identify the sub-bands involved in electronic transport. The results suggest that the majority of charge carriers occupy the lowest energy band derived from Ti $t_{2g} - d_{xy}$ orbitals whereas a highly mobile minority of carriers populate higher energy bands derived from Ti $t_{2g} - d_{xz}/d_{yz}$ orbitals.

We have also performed sub-Kelvin transport measurements in a high mobility $LaAlO_3/SrTiO_3$ sample with varying back-gate voltage in order to reveal the sub-band structure. Complex SdH oscillations with clear back-gate evolution are observed. In the FFT spectra, we identify at least 9 frequency peaks, which we divide into 4 groups based on their gate dependence. We propose a four sub-band model with the presence of strong atomic spin-orbit coupling and Rashba effect. By combining the different orbital symmetry and their different spatial distribution we tentatively explain the gate voltage dependence of the oscillations at moderate magnetic field. The measurements have been repeated in pulsed magnetic field at 500 mK (^{3}He system). Even if the oscillations are damped, these complementary data remain consistent with the low temperature results.

Appendix A

List of works

Publication list

1. A. Nachawaty, **Ming Yang**, W. Desrat, S. Nanot, B. Jabakhanji, D. Kazazis, R. Yakimova, A. Cresti, W. Escoffier, and B. Jouault*.
"Magnetic field driven ambipolar quantum Hall effect in epitaxial graphene close to the charge neutrality point"
Phys. Rev. B 96, 075442(2017).

2. K. Han, Z. Huang*, S. W. Zeng, **Ming Yang**, C. J. Li, W. X. Zhou, X. Renshaw Wang, T. Venkatesan, J. M. D. Coey, M. Goiran, W. Escoffier, and Ariando*.
"Electrical properties and subband occupancy at the (La,Sr)(Al,Ta)O_3/$SrTiO_3$ interface"
Phys. Rev. Material. 1, 011601(2017).

3. **Ming Yang**, O. Couturaud, W. Desrat, C. Consejo, D. Kazazis, R. Yakimova, M. Syväjärvi, M. Goiran, J. Béard, P. Frings, M. Pierre, A. Cresti, W. Escoffier, and B. Jouault*.
"Puddle-Induced Resistance Oscillations in the Breakdown of the Graphene Quantum Hall Effect"
Phys. Rev. Lett. 117, 237702(2016).

4. **Ming Yang***, Kun Han, Olivier Torresin, Mathieu Pierre, Shengwei Zeng, Zhen Huang, T. V. Venkatesan, Michel Goiran, J. M. D. Coey, Ariando*, and Walter Escoffier.
"High field magneto-transport in two-dimensional electron gas $LaAlO_3$/$SrTiO_3$"
Appl. Phys. Lett. 109, 122106 (2016).

5. Yasemin Çelik*, Walter Escoffier, **Ming Yang**, Emmanuel Flahaut, Ender Suvaci.
"Relationship between heating atmosphere and copper foil impurities during graphene growth via low pressure chemical vapor deposition"
Carbon 109 (2016) 529541.

6. Louis Veyrat*, Fabrice Iacovella, Joseph Dufouleur, Christian Nowka, Hannes Funke, **Ming Yang**, Walter Escoffier, Michel Goiran, Barbara Eichler, Oliver G. Schmidt, Bernd Büchner, Silke Hampel, and Romain Giraud.

"Band Bending Inversion in Bi_2Se_3 Nanostructures"
Nano Lett. 2015, 15, 7503-7507.

Oral Presentations

1. **APS March meeting 2018**
   Mar. 05 - 09, 2018, Los Angeles, United States
   "Revealing the complex band structure of $LaAlO_3/SrTiO_3$ interface by high magnetic field quantum transport"

2. **EMFL Days 2016**
   Sep. 14 - 16, 2016, Frankfurt am Main, Germany
   "High field magneto-transport in two-dimensional electron gas $LaAlO_3/SrTiO_3$"

3. **GDR - Matériaux, Etats ElecTronIques et Couplages non-Conventionnels 2016 (GDR-Metticc2016)**
   May. 17 - 20, 2016, Aussois, France
   "High field magneto-transport in two-dimensional electron gas $LaAlO_3/SrTiO_3$"

Poster Presentations

1. **22nd International Conference on Electronic Properties of Two Dimensional Systems (EP2DS-22) & 18th International Conference on Modulated Semiconductor Structures (MSS-18)**
   Jul. 31 - Aug. 4, 2017, Penn State, United States
   "Revealing the complex band structure of $LaAlO_3/SrTiO_3$ interface by high magnetic field quantum transport"
   "Ultra-large quantum Hall plateau in graphene on SiC"

2. **4th International School of Oxide Electronics(ISOE2017)**
   Apr. 10 - 22, 2017, Cargèse, France
   "Revealing the complex band structure of $LaAlO_3/SrTiO_3$ interface by high magnetic field quantum transport"

3. **GDR - Matériaux, Etats ElecTronIques et Couplages non-Conventionnels 2017 (GDR-Metticc2017)**
   Mar. 28 - 31, 2017, Bordeaux, France
   "Revealing the complex band structure of $LaAlO_3/SrTiO_3$ interface by high magnetic field quantum transport"

4. **EMFL Days 2016**
   Sep. 14 - 16, 2016, Frankfurt am Main, Germany
   "High field magneto-transport in two-dimensional electron gas $LaAlO_3/SrTiO_3$"

5. **7th symposium on two-dimensional materials (Carbonhagen2016)**
   Aug. 17 - 18, 2016, Copenhagen, Denmark
   "Ultra-large quantum Hall plateau in graphene on SiC"

6. **The 22nd International Conference on High Magnetic Fields in Semiconductor Physics (HMF22)**
   Jul. 24 - 29, 2016, Sapporo, Japan
   "High field magneto-transport in two-dimensional electron gas $LaAlO_3/SrTiO_3$"
   "Ultra-large quantum Hall plateau in graphene on SiC"

7. **GDR Physique Quantique Mésoscopique - GDR-I graphene & Nanotubes - Sessions Plénières 2015**
   Nov. 29 - Dec. 04, 2015, Aussois, France
   "High field magneto-transport in graphene grown by chemical vapor deposition on SiC"

8. **16th edition of Trends in Nanotechnology International Conference (TNT2015)**
   Sep. 07 - 11, 2015, Toulouse, France
   "High field magneto-transport in graphene grown by chemical vapor deposition on SiC"

9. **The 11th International Conference on Research in High Magnetic Fields (RHMF2015)**
   Jul. 01 - 04, 2015, Grenoble, France
   "High field magneto-transport in graphene grown by chemical vapor deposition on SiC"

Appendix B

Résumé de la thèse en français

Dans cette anexe nous présentons un résumé en français de ce travail de thèse. Le lecteur ne trouvera aucune nouvelle information et les figures utilisées sont les mêmes que dans la version anglaise.

B.1 Gaz d'életons bidimensionnel

Ce chapitre décrit les modèles théoriques permettant d'expliquer la dynamique des électrons dans les matériaux bidimensionnels. Dans les matériaux diffusifs, les électrons sont traités comme un gaz de particules chargées susceptibles d'être accélérées par un champ électrique. Il s'agit du modèle de Drude qui, par la suite, est complété en introduisant une fonction de distribution afin de tenir compte des effets de la température. Ce modèle classique est comparé au modèle semi-classique qui tient compte de la nature ondulatoire des électrons et des phénomènes d'interférence quantiques. En présence d'un champ magnétique, l'énergie des électrons est quantifiée en " niveaux de Landau ", permettant d'expliquer et d'exploiter les oscillations de la magnétorésistance observées à basse température. Enfin ce chapitre rappelle les notions théoriques de l'effet Hall quantique qui sont nécessaires dans l'étude du graphène sur carbure de silicium présenté dans le chapitre suivant.

La conductivité d'un matériau est régie par le mouvement des porteurs de charge, c'est à dire des électrons et / ou des trous. Le modèle le plus simple décrivant le transport des charges est le modèle de Drude dans lequel les électrons sont considérés comme des particules ponctuelles. Dans ce cadre, la conductivité est proportionnelle au produit de la densité de porteurs et de leur mobilité. En tenant compte de la fonction de distribution statistique des électrons et en résolvant l'équation de transport de Boltzmann, il est possible d'affiner le modèle et d'extraire une relation plus complète, tenant en compte les effets de la température, et plus exacte pour décrire le transport électrique. à basse température, alors que la longueur de cohérence de phase augmente sensiblement, la nature ondulatoire des électrons et leur capacité à réaliser des interférences commencent à influer sur la conductivité. Les corrections quantiques de la conductivité sont principalement associées à deux effets observables expérimentalement : la localisation faible et l'anti-localisation faible.

La dynamique des électrons est fortement modifiée en présence d'un champ magnétique. Lorsque ce dernier est suffisamment fort, il ne peut pas être traité comme une perturbation et doit être totalement intégré dans le Hamiltonien du

système. Les ondes de Bloch décrivant habituellement les électrons dans un crystal à champ magnétique nul ne sont plus des fonctions d'onde propres du système et sont abandonnées au profit des états de Landau [Girvin 1999]. Dans ce nouvel espace de description, l'énergie des électrons associée à leur mouvement dans un plan perpendiculaire au champ magnétique est quantifiée en niveaux de Landau. La séparation énergétique entre deux niveaux de Landau voisins est donnée par $\Delta E = \hbar\omega_c$. L'énergie des niveaux de Landau ne dépend pas du vecteur d'onde, ce qui implique une dégénérescence importante et proportionnelle au champ magnétique. En présence de désordre et en considérant les interactions électron-électron, l'énergie des niveaux de Landau n'est plus exactement quantifiée, mais est élargie sur un intervalle plus ou moins important. Lorsque le champ magnétique est suffisamment élevé, de manière à ce que l'écart énergétique entre deux niveaux de Landau consécutifs soit supérieur à leur élargissement, il existe entre les niveaux de Landau des énergies pour lesquelles la densité d'états est nulle. Au centre des niveaux de Landau, la densité d'états est forte et concentre les états dits "étendus". Au contraire, les états dits "localisés" sont situés en périphérie du centre des niveaux de Landau, là où la densité d'états est plus faible. La limite énergétique entre les états étendus et les états localisés est appelée la "limite de mobilité". Les propriétés de transport sont régies par la dynamique des électrons au niveau de Fermi. Expérimentalement, lorsqu'un champ magnétique croissant est appliqué sur un échantillon, les niveaux de Landau se forment progressivement et croisent successivement l'énergie Fermi qui ne dépend, quant à elle, que de la densité de porteurs. Les électrons au niveau de Fermi sont successivement dans des états "localisés " ou "étendus", ce qui donne lieu à des oscillations de la magnétorésistance, dites aussi "oscillations de Shubnikov-de Haas".

Lorsque le champ magnétique est très intense, un phénomène physique original appelé "l'effet Hall quantique entier" s'établit dans les systèmes électroniques bidimensionnels. Expérimentalement, la résistance de Hall développe une série de plateaux à $R_H = \dfrac{h}{\nu e^2}$ où ν est un nombre entier. Dans ce régime de transport, le niveau de Fermi est situé entre deux niveaux de Landau bien distincts. Les électrons à l'intérieur de l'échantillon sont dans des états localisés et ne participent pas au transport des charges. Cependant les électrons situés sur les bords de l'échantillon sont, quant à eux, soumis à un potentiel additionnel (une barrière de potentiel infinie qui représente le bord de l'échantillon) qui modifie leur dynamique et permet leur propagation. D'un point de vue classique, le champ magnétique courbe perpétuellement la trajectoire des électrons et les renvoie contre les bords de l'échantillon sur lesquels ils rebondissent. Ces électrons dits "de bord" ne peuvent pas être rétrodiffusés et transportent le courant électrique sans dissipation le long des bords de l'échantillon. Il s'agit du régime d'effet Hall quantique dans lequel la conductance intrinsèque de l'échantillon est strictement nulle, tandis que la conductance de Hall est un multiple entier du quantum de conductance. Au contraire, pour des valeurs particulières du champ magnétique et en particulier lorsque le niveau de Fermi est aligné avec un niveau de Landau, les électrons sont dans des états quantiques éten-

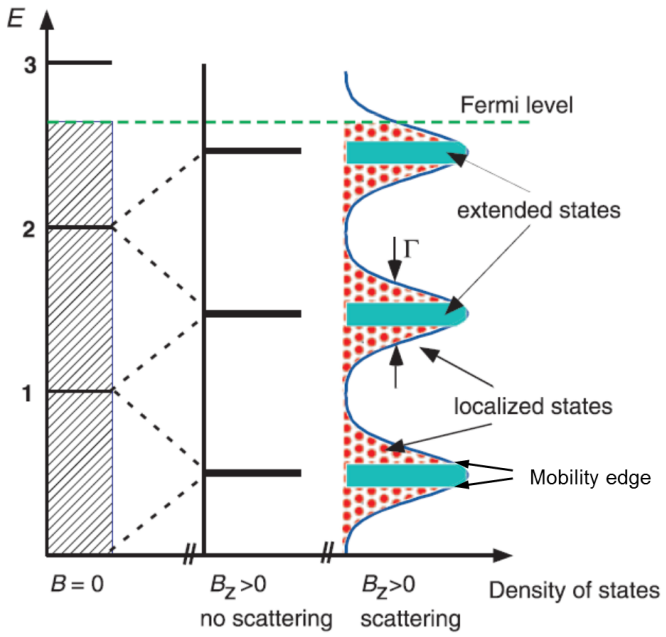

Figure B.1: Quantification en niveaux de Landau d'un gaz d'électrons 2D sans spin. La densité d'états constante 2D (à gauche) se développe en présence d'un champ magnétique en une série de pics ou "niveaux de Landau" en l'absence de désordre (au milieu). L'introduction du désordre dans le système élargit les niveaux de Landau en forme de ligne de crête, permettant une densité d'états faible mais non nulle entre les niveaux de Landau. L'élargissement des niveaux de Landau peut être modélisé par une fonction gaussienne ou lorentzienne avec un paramètre typique Γ , qui est lié au temps de diffusion quantique des électrons. Les états quantiques situés au centre des niveaux de Landau sont appelés états étendus, et les états éloignés du centre sont des états localisés. Les états étendus et les états localisés sont séparés par la limite de mobilité. Extrait de [Jeckelmann 2001].

dus. Ils transportent le courant de manière diffusif dans l'ensemble de l'échantillon et leur dynamique est régie par l'équation classique de Boltzmann en présence d'un champ magnétique.

Le régime d'effet Hall quantique est susceptible d'être détruit par le désordre de l'échantillon (caractérisé macroscopiquement par la mobilité électronique), par la température et par le courant électrique. Lorsque l'un de ces paramètres varie, le système transite de l'état d'effet Hall quantique vers l'état classique. Cette transition fait intervenir un régime de conduction par "sauts" des électrons entre des états localisés spatialement distincts. Grâce au modèle de conduction par "sauts", l'analyse de la résistance électrique au cours de cette transition permet d'obtenir des grandeurs caractéristiques du système telle que la longueur de localisation.

B.2 Techniques expérimentales

Dans ce chapitre, je présente les techniques expérimentales qui ont été utilisées au cours de cette thèse. Un champ magnétique intense et pulsé est généré par un banc de capacités connectées en parallèle (permettant de stocker au maximum 14 MJ) et des bobines conçues et fabriquées au laboratoire. Les échantillons sont mesurés à très basse température en utilisant des cryostats fonctionnant avec de l'hélium 4 ou de l'hélium 3 liquide. Je décris aussi les précautions particulières pour la mesure de la magnétorésistance sous champ magnétique pulsé, afin de limiter la tension induite pendant l'impulsion de champ magnétique. Les cannes de mesure sont conÃğues en tenant compte de la particularité de l'environnement extrême de champ magnétique intense et des basses températures au cours de la mesure. Enfin je compare deux techniques de mesure de la magnétorésistance des échantillons : l'une en utilisant une source de courant continu et l'autre une source de courant alternatif.

B.3 Graphène sur carbure silisium

Dans ce chapitre, je présente l'étude de magnétotransport à fort champ sur le graphène/SiC jusqu'à 80 T. Cet échantillon montre un plateau de Hall quantique large et des oscillations de magnétorésistance anormales dans le régime de rupture de Hall quantique. Nous avons proposé un modèle basé sur l'inhomogénéité de l'échantillon et le mécanisme de transfert de charges dans ce système pour expliquer les résultats expérimentaux.

B.3.1 Introduction au graphène

Le graphène est un matériau bidimensionnel formé par des atomes de carbone organisés dans un réseau hexagonal en forme de nid d'abeille. Sa cellule unitaire primitive contient deux atomes non équivalents et le réseau réciproque est également un réseau hexagonal. La structure de bande, calculée en utilisant le modèle des liaisons fortes par [Wallace 1947] est représentée dans l'encadré gauche de la figure B.2. La bande de conduction et la bande de valence se croisent aux trois points K et K' de la première zone Brillouin. Ces points sont aussi appelés " points de Dirac " et la relation de dispersion linéaire autour du point de Dirac forme le " cône de Dirac ". La dynamique des porteurs de charges dans le graphène imite le comportement des particules relativistes sans masse et à spin demi-entier, tels que les neutrinos en physique des hautes énergies. La structure électronique particulière du graphène joue un rôle central dans les propriétés de transport, sans analogue en physique de la matière condensée. La structure des niveaux de Landau dans le graphène est très différente de celle des fermions de SchrÃűdinger. En effet, les niveaux de Landau sont énergétiquement non-équidistants et il existe un niveau de Landau à énergie nulle, non dispersif avec le champ magnétique.

L'effet Hall quantique dans le graphène a été étudié par de nombreuses équipes

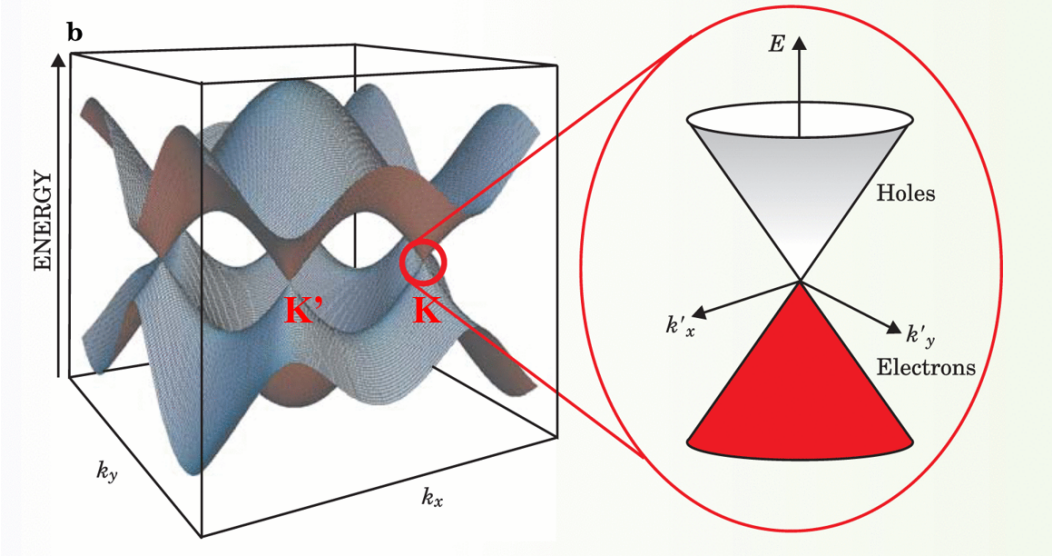

Figure B.2: Structure de bande électronique du graphène dans la première zone de Brillouin calculée avec la méthode des liaisons fortes (à gauche). Un zoom sur l'un des points de Dirac est montré (à droite), où le cône de Dirac est mis en évidence. Extrait de [Wilson 2006].

de recherche depuis sa découverte. La résistance de Hall montre une série de plateaux pour des facteurs de remplissage $\nu = 4(N + 1/2)$ ou N est un entier. Le facteur 4 est lié à la dégénérescence de spin et de vallée tandis que le nombre 1/2 est intrinsèquement lié à la présence d'un niveau de Landau à énergie nulle, peuplé à la fois par les électrons et des trous. Sous un champ magnétique très élevé et dans des échantillons de haute mobilité, la dégénérescence de spins et de vallée peut être levée [Zhang 2006, Jiang 2007].

B.3.2 Graphène sur carbure de silisium

Dans le régime d'effet Hall quantique, le graphène est un matériau prometteur pour remplacer les hétérostructures à base de semiconducteurs Si-FET et III-V permettant de définir le standard international de résistance. Les échantillons de graphène issus du graphite exfolié ont des tailles trop modestes et ne peuvent pas satisfaire à l'exigence de précision dans le domaine de la métrologie. En effet, ses dimensions latérales sont de l'ordre de la dizaine de microns au mieux, ce qui limite fortement l'intensité du courant non dissipatif maximum pouvant être atteint dans le régime d'effet Hall quantique.

Ces dernières années, le développement des méthodes de fabrication du graphène, et en particulier le dépôt en phase vapeur (CVD) du graphène sur un substrat de carbure de silicium (SiC) ou la sublimation du SiC permettent d'atteindre une qualité d'échantillon suffisante sur de grandes dimensions (plusieurs centimètres). Par conséquent, le graphène sur SiC a été proposé [Tzalenchuk 2010] comme candidat

pour des applications de métrologie quantique. Cette proposition a été expérimentalement confirmée quelques années plus tard [Ribeiro-Palau 2015].

L'échantillon que nous avons étudié durant cette thèse a été réalisé par sublimation du SiC. Un substrat de SiC est chauffé à très haute température (au dessus de 1500 °C) sous ultra vide. Les atomes de silicium à la surface du SiC se subliment et laissent un excès d'atomes de carbone qui finissent par s'organiser en formant des couches de graphène. Le graphène présent sur la face Si du substrat de SiC sont toujours dopées "n" avec une mobilité de l'ordre de 1300-1600 cm^2/Vs. Ce dopage est lié à la présence d'une couche de carbone non conductrice intercalée entre les atomes Si du SiC et la couche de graphène, susceptible de transférer des charges dans cette dernière.

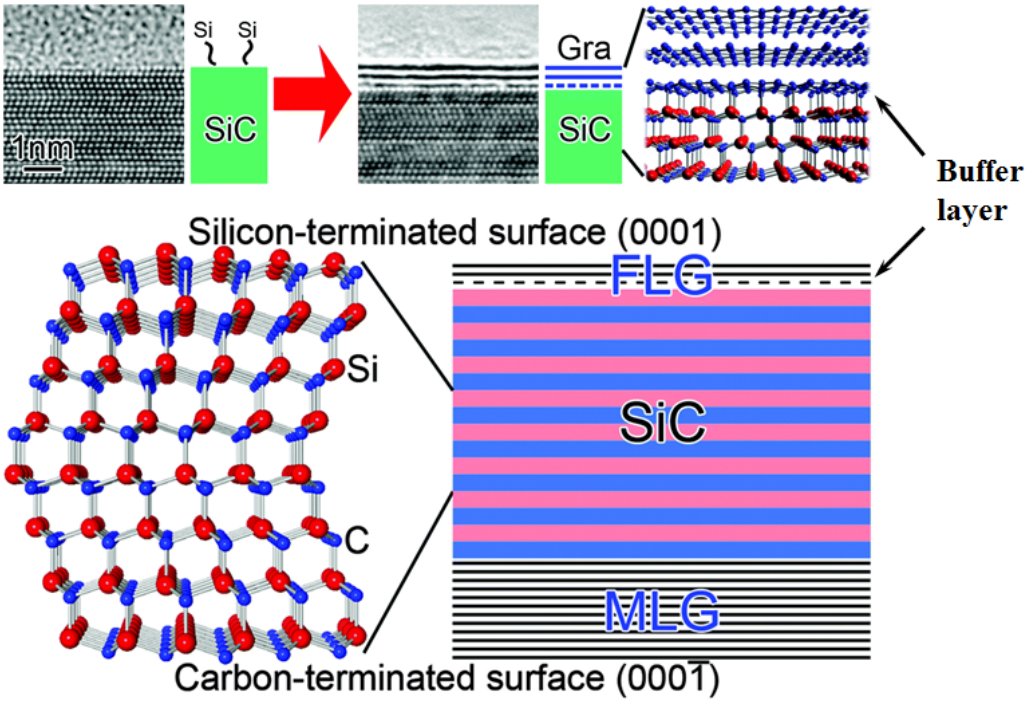

Figure B.3: Croissance épitaxiale du graphène par la méthode de sublimation du SiC. A très haute température, les atomes de Silicium se subliment de la surface du SiC, laissant un excès d'atomes de carbone. Sur la face C du substrat, le taux de croissance est rapide et donne du graphène multicouche. Au contraire, la formation du graphène sur la face Si est lente et mieux contrôlée, il existe une couche tampon intercalée entre les atomes Si et la couche de graphène. Extrait de [Norimatsu 2014].

Les échantillons sont recouverts d'une couche de PMMA (poly méthylméthacrylate-co-méthacrylate) afin de les structurer en barre de Hall en utilisant des techniques de lithographie électronique. Ensuite, une barrière photo-chimique est appliquée en étalant une résine (poly méthylstyrène-co-chlor-ométhylacrylate - nom commercial ZEP520A) de 300 nm d'épaisseur sur le dessus de la couche de protection en PMMA [Lara-Avila 2011, Tzalenchuk 2011]. Lorsque la résine ZEP520A est illuminée par

une lumière ultraviolette, elle subit une réaction chimique qui absorbe les électrons environnants, diminuant ainsi le dopage de type “n” du graphène.

La présence de la couche tampon d'atomes de carbone sous la première couche de graphène joue un rôle très important dans la stabilisation du plateau de Hall quantique à v = 2 dans une large gamme de champ magnétique. En effet, les deux couches ne sont séparées que d'une distance $d = 0.3$ nm et interagissent fortement entre elles. Un transfert de charge dépendant du champ magnétique entre la couche tampon et le graphène augmente la densité de porteurs dans ce dernier et stabilise le facteur de remplissage à $\nu = 2$ dans une grande plage de champ magnétique. Cette hypothèse, présentée par [Kopylov 2010, Janssen 2011], suppose que l'énergie de Fermi reste toujours entre les niveaux de Landau $N = 0$ et $N = 1$.

B.3.3 Electronic properties of graphene on SiC

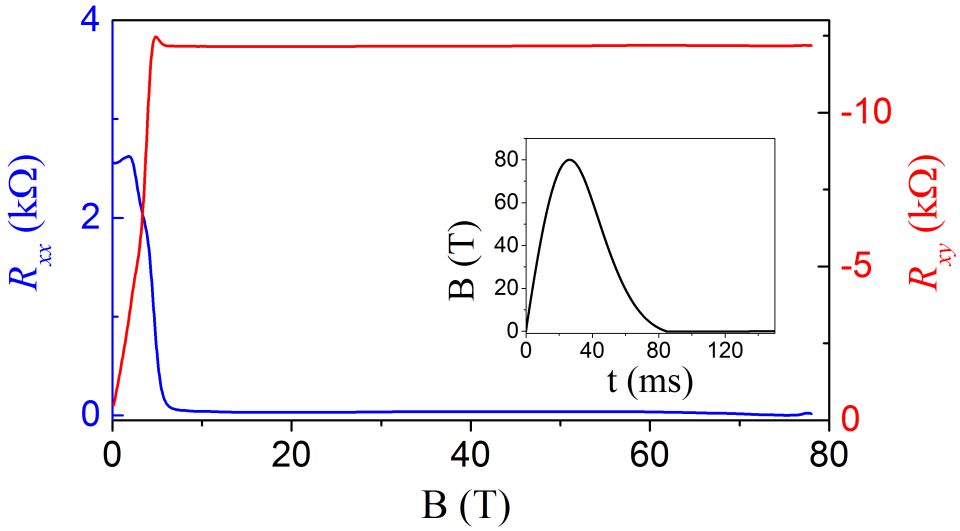

Figure B.4: Résistance longitudinale R_{xx} et résistance Hall R_{xy} mesurées à T = 4,2 K jusqu'à $B = 78$ T, avec un courant $I = 20$ μA. Encart: impulsion du champ magnétique utilisé dans cette expérience.

Fig. B.4 montre les résistances longitudinales et de Hall (respectivement R_{xx} et R_{xy}) mesurées en fonction du champ magnétique à la température T = 4,2 K. La résistance longitudinale est normalisée à un carré. Pour $B \sim 7$ T, un plateau de Hall quantique extrêmement large à $R_{xy} = h/2e^2$ est observé jusqu'au champ magnétique expérimental le plus élevé (78 T). Comme prévu, le plateau de Hall quantique coïncide avec une annulation complète de la résistance longitudinale R_{xx}.

Fig. B.5 montre les magnétorésistances à différentes températures. La résistance longitudinale R_{xx} a un minimum autour de $B_{min} = 18$ T lorsque la température augmente au-dessus de 30 K. Nous supposons que, comme dans les systèmes

semi-conducteurs bidimensionnels, ce minimum se produit lorsque l'énergie de Fermi est exactement entre deux niveaux Landau adjacents. Ainsi, le facteur de remplissage est exactement égal à 2 à Bmin. Nous en déduisons que la densité de porteurs a augmenté de $3,4 \times 10^{11}\mathrm{cm}^{-2}$ (la densité porteuse initiale à champ magnétique nul extraite de l'effet Hall classique) jusqu'à $8,5 \times 10^{11} cm^{-2}$ à $B = B_{min}$.

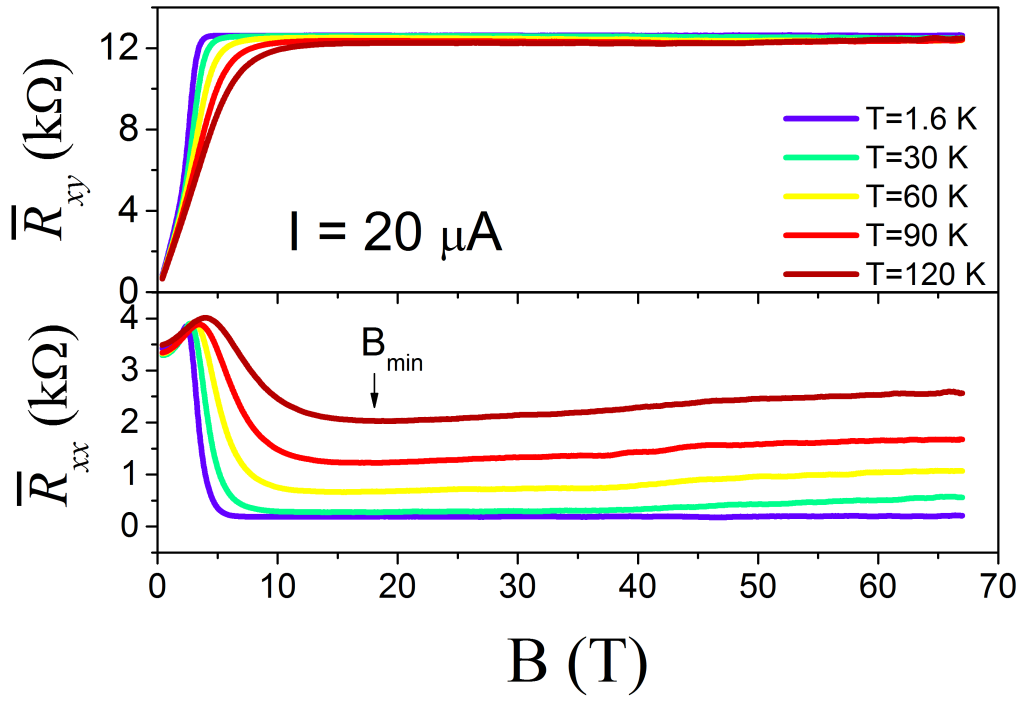

Figure B.5: Résistances longitudinales (bas) et transversales (haut) de T = 1,6 K jusqu'à T = 120 K. Un courant de 20 μA a été utilisé.

À température finie, le transport de charge dans le régime d'effet Hall quantique est décrit par la théorie de "sauts à distances variables" d'Efros-Shklovskii (ES-VRH) [Efros 1975, Shklovskii 1984], dont les signes expérimentaux ont déjà été observés dans divers échantillons de graphène pour T = 100 K [Lafont 2015, Giesbers 2008, Bennaceur 2012, Janssen 2013]. L'analyse présentée sur la Fig. B.6(a) utilise uniquement les données expérimentales pour $T>$ 30 K, où les erreurs de mesure sont négligeables, et $T <$ 120 K, où la conduction par activation aux états étendus peut être raisonnablement négligée. L'accord entre les résultats expérimentaux et les prédictions du modèle théorique est très satisfaisant et permet d'extraire, pour chaque valeur du champ magnétique, la longueur de localisation et la température caractéristique de saut $T0$.

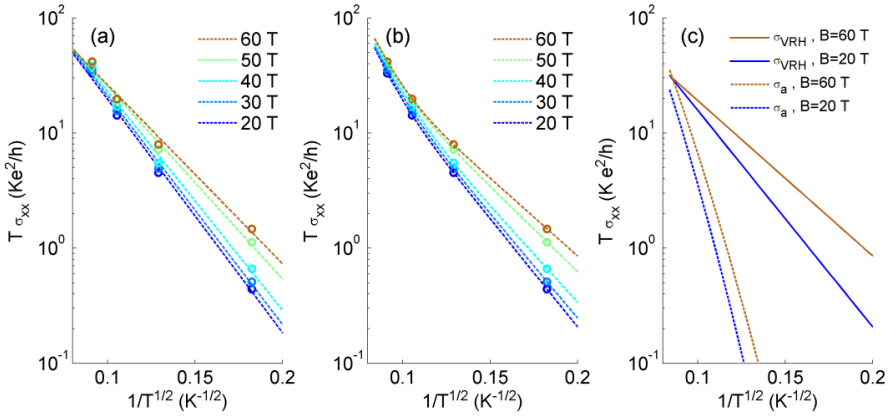

Figure B.6: (a) Symboles ouverts: conductivité mesurée $T\sigma_{xx}$ vs $T^{-1/2}$ de $B = 20$ T à $B = 60$ T avec un pas de 10 T. Lignes pointillées: ajustement linéaires avec le modèle ES-VRH. Les données de [Lafont 2015] à $B = 19$ T sont présentées à titre de comparaison (ligne pointillée rouge). (b) Ajustement théorique des mêmes données que (a) en considérant l'effet de l'activation thermique. L'ajustement théorique est amélioré pour une plage de température élevée ($T > 100$ K). (c) La contribution du modèle ES-VRH et de l'activation thermique à la conductivité à $B = 20$ T et 60 T. La composante d'activation thermique est négligeable par rapport à celle du modèle ES-VRH à basse température (T <100 K).

Pour des champs magnétiques inférieurs à 20 T, la longueur de localisation ξ est comparable à la longueur magnétique $l_B = \sqrt{\hbar/eB}$. Sous champ magnétique plus élevé, elle n'augmente que très légèrement. Dans le régime de Hall quantique, la longueur de localisation devrait varier selon $\xi \propto \Delta E^{-\gamma}$ où ΔE est l'écart de mobilité entre les états délocalisés les plus proches et l'énergie de Fermi et $\gamma = 2.3$ est l'exposant de percolation quantique [Huckestein 1995]. En supposant une densité de charge constante et une densité d'états localisés indépendants de l'énergie, la longueur de localisation varierait comme $1/\nu^{2.3} \sim B^{2.3}$, donnant $\xi_{B=60T}/\xi_{B=20T} \simeq 12$. En revanche, la variation expérimentale de $\xi_{B=60T}/\xi_{B=20T} \simeq 2$ dans la gamme 20-60 T est différente des prédictions du modèle, suggérant une augmentation de la densité de porteurs à mesure que le champ mangtique augmente.

B.3.4 Oscillations anormales de la magnétorésistance

Dans cette partie, le régime d'effet Hall quantique a été étudié en faisant varier le courant entre 50 μA et 400 μA (voir Fig. B.7). Des écarts significatifs de R_{xx} et R_{xy} par rapport aux prédictions théoriques sont constatés lorsque le courant est important. Pour $I = 100$ μA, $R_{xx} > 3$ Ω sur toute la plage du champ magnétique, produisant une tension longitudinale ($V_{xx} > 300$ μV) trop importante pour être compatible avec des mesures métrologiques. Cela implique une densité de courant critique $j_c \simeq 1$ A/m, soit un ordre de grandeur inférieur aux valeurs les plus élevées rapportées pour le graphène sur SiC [Alexander-Webber 2013].

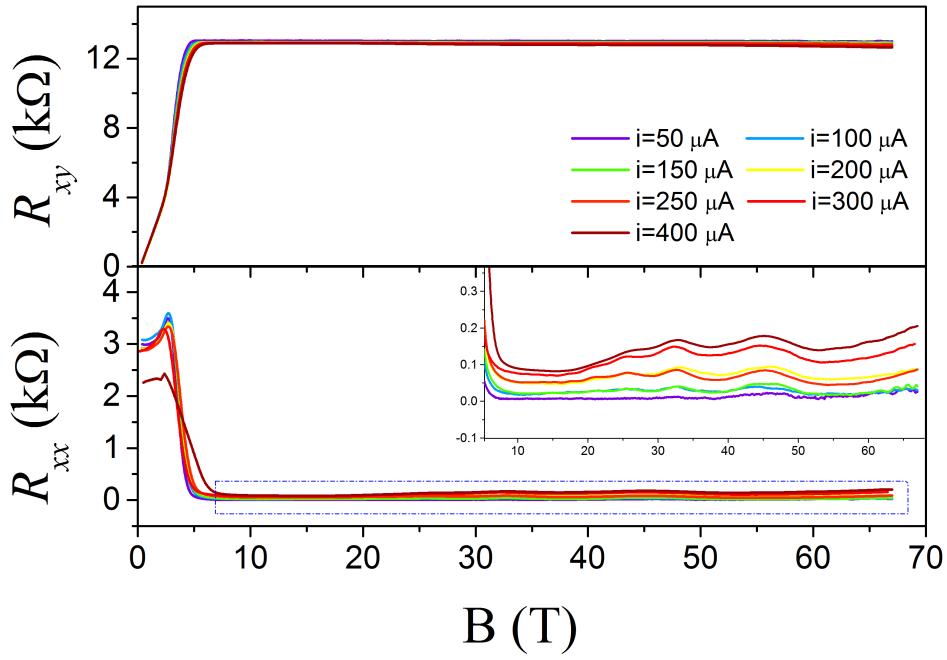

Figure B.7: Résistance longitudinale et transversale en fonction du courant injecté dans l'échantillon. L'encart est un agrandissement de la zone encadrée en pointillés. De faibles oscillations de la résistance longitudinale sont visibles dont l'amplitude augmente à mesure que le courant augmente.

A courant élevé, de faibles oscillations de la résistance longitudinale, périodiques en fonction de l'inverse du champ magnétique, sont visibles. Afin de mieux comprendre leur origine, des mesures de dépendance thermique ont été effectuées pour un courant de $I = 150$ μA. L'amplitude des oscillations est la plus forte à T =40 K et persistent jusqu'à T = 120 K. La dépendance en température de l'amplitude des oscillations est contraire aux prédictions de la théorie de Shubnikov-de Haas. Pour poursuivre l'analyse, nous suivons la pratique habituelle en définissant un indice B_N pour chaque minimum des oscillations de R_{xx} et nous traçons l'inverse du champ magnétique correspondant en fonction de cet indice. Ici, l'indice N correspond au nombre de niveaux de Landau remplis sous le niveau de Fermi. Les données donnent une droite (indiquant que les oscillations sont périodiques en fonction de 1/B) dont la pente est directement reliée à la densité de porteurs et qui intercepte l'axe de l'indice à N=0. Cette caractéristique (la phase des oscillations) correspond aux propriétés des fermions de Schrödinger, pour lesquels il existe un nombre entier de niveaux de Landau dégénérés sous le niveau de Fermi. Au contraire, celui-ci est demi-entier dans le cas du graphène (car le niveau de Landau à énergie nulle est partagé à la fois par les électrons et les trous). Ce résultat contre-

intuitif suggère à nouveau que les oscillations de la magnéto-résistance observées ne sont pas des oscillations de Shubnikov-de Haas, malgré leur caractère périodique en 1/B. Nous remarquons finalement que les oscillations ne sont pas reproductibles après un ou plusieurs cycles thermiques. Une observation au microscope optique de l'échantillon avant et après un cycle thermique montre une altération de la résine déposée à la surface de l'échantillon. Cette dernière permet de maîtriser le dopage de l'échantillon de graphène. Nous faisons l'hypothèse que les oscillations décrites ci-dessus sont liées à l'altération de la résine, qui introduit un dopage inhomogène au sein de l'échantillon.

B.3.5 Modèle et simulations

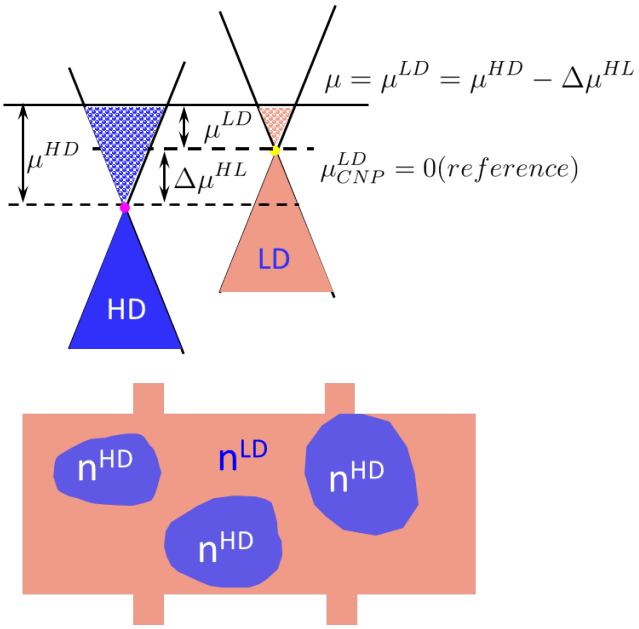

Figure B.8: Schéma d'un échantillon inhomogène avec la présence de régions fortement dopées (HD) dans une matrice faiblement dopée (LD). Le potentiel chimique au point de neutralité de charge constitue la référence énergétique.

Le modèle décrit ci-dessous est basé sur un transfert de charge proposé par Kopylov et al. Il prend en compte la présence de zones fortement dopées (HD) dans une matrice de graphène faiblement dopée (LD). Nous supposons ainsi que la couche de graphène est dopée de manière inhomogène à cause de l'altération locale de la résine qui le recouvre. La présence de seulement deux dopages différents est essentielle dans ce modèle. En effet, une large distribution de dopages différents neutraliserait les effets liés au transfert de charge, comme par exemple dans le cas du graphène sur oxyde de silicium. Lorsque le champ magnétique augmente, les électrons se redistribuent entre les zones LD et HD pour maintenir le même potentiel chimique dans l'échantillon. Cette assertion peut être mise en équation et résolue

de manière numérique, afin d'obtenir l'évolution du potentiel chimique en fonction du champ magnétique. Cette méthode permet aussi d'extraire l'évolution de la densité de porteurs dans les régions LD et HD (figure B.9) en fonction du champ magnétique. Nous observons que la concentration des électrons dans la région de LD augmente sans jamais saturer, impliquant un transfert de charge entre le graphène et le substrat de SiC. Ce processus est responsable de la stabilité du plateau de Hall $\nu = 2$ pour $B > B_{min}$. Au contraire, la densité de porteurs de charge dans la région HD oscille avec une périodicité inverse au champ magnétique et implique un transfert de charge entre les régions LD et HD. Les oscillations de la densité de porteurs dans les zones HD sont à l'origine des oscillations de la magnétorésistance observées expérimentalement.

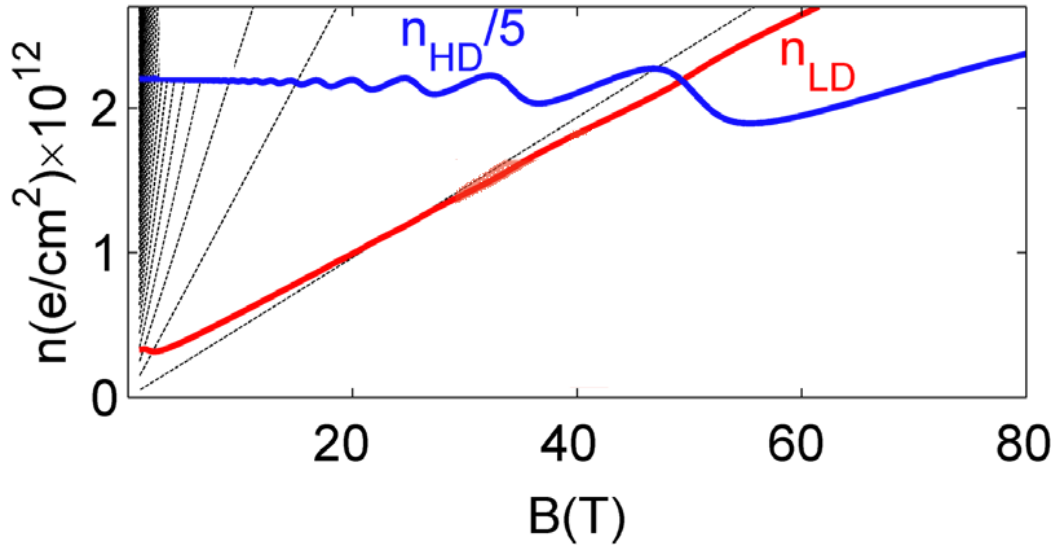

Figure B.9: Densités de porteurs dans les régions LD et HD obtenues à partir du modèle théorique. La densité de porteurs dans la région LD augmente sans saturation alors qu'elle oscille dans la région HD.

En effet, les régions HD ont une conductivité élevée par rapport à la matrice LD et se comportent comme une surface équipotentielle. Le champ électrique est perpendiculaire à l'interface HD/LD. Dans le régime d'effet Hall quantique, le courant est quasi-perpendiculaire au champ électrique et ne peut donc pas entrer dans les régions HD, qui se comportent comme des isolants. Etant donné que le courant traversant la barre Hall est constant, les zones HD agissent tel un goulot d'étranglement et provoquent une augmentation de la densité de courant locale. Macroscopiquement, cet effet se traduit par une réduction de la largeur effective de la barre de Hall W_{eff}, qui évolue périodiquement avec le champ magnétique, et qui est en lien direct avec la disparition (transition) de l'effet Hall quantique [Lafont 2015, Furlan 1998].

Le modèle présenté ci-dessus reproduit les oscillations de la magnétorésistance

avec la bonne phase et le bon ordre de grandeur pour l'amplitude. Le meilleur accord avec les données expérimentales est trouvé en choisissant un recouvrement de 30 % de la surface de l'échantillon par des zones HD.

B.4 L'interface entre $LaAlO_3/SrTiO_3$

Dans ce chapitre, l'étude du magnétotransport sur le gaz bidimensionnel à l'interface $LaAlO_3/SrTiO_3$ est présentée. A partir des données expérimentales sous fort champ, nous abordons les propriétés électroniques et le rôle de l'effet Rashba. L'étude en fonction de la tension de grille, appliquée sur la face arrière, dans une gamme de température sub-Kelvin nous permet d'explorer la structure de bande complexe dans ce système. Nous proposons une interprétation des résultats expérimentaux fondée sur un modèle de structure de la bande proposé dans la littérature.

B.4.1 Introduction au système $LaAlO_3/SrTiO_3$

En 2004, Ohtomo et Hwang [Ohtomo 2004] ont rapporté la présence d'un gaz d'électrons bidimensionnel conducteur de haute mobilité (2DEG) à l'interface entre deux isolants de bande, $LaAlO_3$ et $SrTiO_3$. Cette observation a immédiatement déclenché un grand nombre d'études sur cette famille d'hétérostructures. Les deux composés parents, $LaAlO_3$ et $SrTiO_3$, ont une structure pérovskite représentée sur la Fig. B.10(b).

L'origine du gaz bidimensionnel est une question controversée et un sujet de nombreuses études expérimentales et théoriques: la catastrophe polaire, les lacunes d'oxygène, ou encore l'interdiffusion des ions à l'interface sont des mécanismes qui peuvent conduire ou contribuer à la création de ce gaz 2D. Jusqu'à présent, la catastrophe polaire est considérée comme le mécanisme le plus efficace pour expliquer l'origine du 2DEG à l'interface $LaAlO_3/SrTiO_3$.

Tous les échantillons étudiés au cours de cette thèse ont été recuits sous atmosphère d'oxygène après la croissance afin de réduire la contribution des lacunes d'oxygène.

Une analyse théorique détaillée montre que le gaz 2D se situe du côté du STO et s'étend sur plusieurs couches stœchiométriques à l'intérieur de ce matériau. Le modèle de la catastrophe polaire prévoir qu'il soit confiné à la première couche [Delugas 2011]. Dans un premier nous décrivons la structure de bande de $SrTiO_3$. Cette structure de bande est complexe puisqu'elle émerge de combinaisons d'orbitales atomiques 3d $Ti^{3+/4+}$, avec de fortes interactions électroniques.

La bande de conduction de $SrTiO_3$ massif est dérivée des orbitales $3d$ des atomes de Ti (d_{xy}, d_{xz}, d_{yz}, d_{z^2} et $d_{x^2-y^2}$). Pour les atomes de Ti isolés sans champ cristallin, les orbitales Ti $3d$ sont dégénérées 5 fois. Le champ cristallin cubique lève la dégénérescence du quintuplet en un triplet t_{2g} (d_{xy}, d_{xz}) et un doublet e_g ($d_{3z^2-r^2}$ and $d_{x^2-y^2}$). Lorsque $LaAlO_3$ est déposé sur $SrTiO_3$, le champ cristallin à l'interface rompt la symétrie d'inversion. La dégénérescence des bandes t_{2g} et e_g est

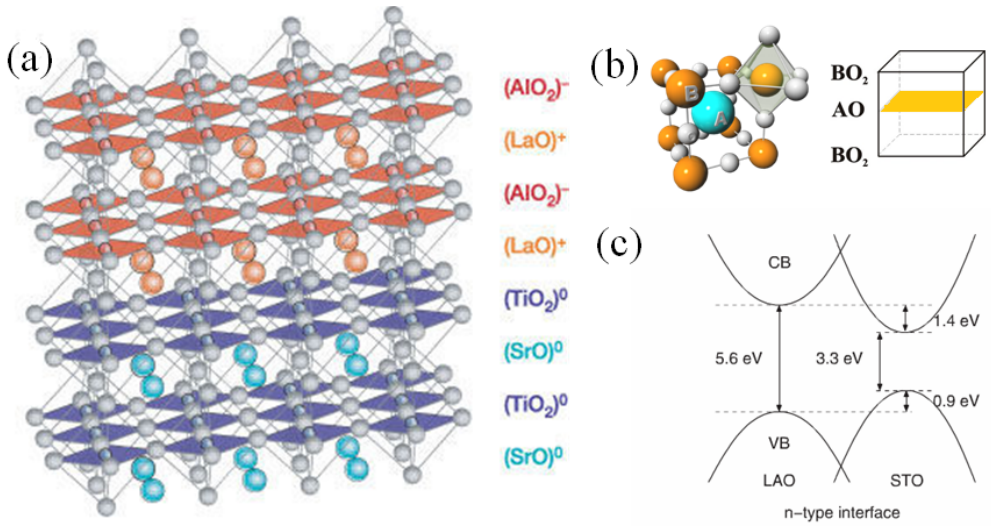

Figure B.10: (a) Schéma de l'interface LAO/STO, montrant la composition de chaque couche et l'état de charge ionique de chaque couche. (b) La structure de la pérovskite ABO_3, où A est soit un atome de La ou de Sr, B est soit un atome de Al ou de Ti. (c) L'alignement de bande de deux isolants: LAO et STO. Extrait de [Ohtomo 2004, Popović 2008].

elle aussi levée. La sous-bande d_{xy} devient la sous-bande fondamentale et les sous-bandes d_{xz}/d_{yz} ont une énergie plus élevée. Delugas *et al.* [Delugas 2011] a montré que les électrons résident du côté STO de l'hétérojonction et que le gaz d'électrons s'étale sur plusieurs couches de TiO_2 à proximité de l'interface. Plus précisément, l'extension des fonctions d'onde de électroniques dépend du type de sous-bandes occupée: les électrons des bandes d_{xy} sont confinés sur 3 ou 4 cellules unitaires du STO alors que ceux des bandes d_{xz} et d_{yz} s'étendent sur environ 6 cellules unitaires. Les électrons dans les bandes d_{xy} ont une masse effective légère ($0.7m_e$) avec une surface de Fermi isotrope. D'autre part, les électrons dans les bandes dégénérées d_{xz} et d_{yz} ont une masse efficace plus lourde ($1.3m_e$) avec une surface de Fermi en étoile (figure B.11(b)). De plus, la présence d'un fort couplage spin-orbite (SOC) ajoute de la complexité à la structure de bande de ce système. Le couplage spin-orbite atomique hybride les trois orbitales différentes et reconstruit la structure de la bande. En outre l'interaction entre le couplage spin-orbite et la brisure de la symétrie d'inversion à l'interface donne lieu à l'effet Rashba [Bychkov 1984]. Cet effet modifie la relation de dispersion parabolique électronique, qui est divisée en deux branches de spins décalées le long des directions k_x et k_y.

B.4.2 Préparation des échantillons et caractérisations

Les échantillons de $LaAlO_3/SrTiO_3$ ont été élaborés par ablation laser pulsé (PLD en anglais : Pulsed Laser Deposition) par le groupe du Prof. Ariando à

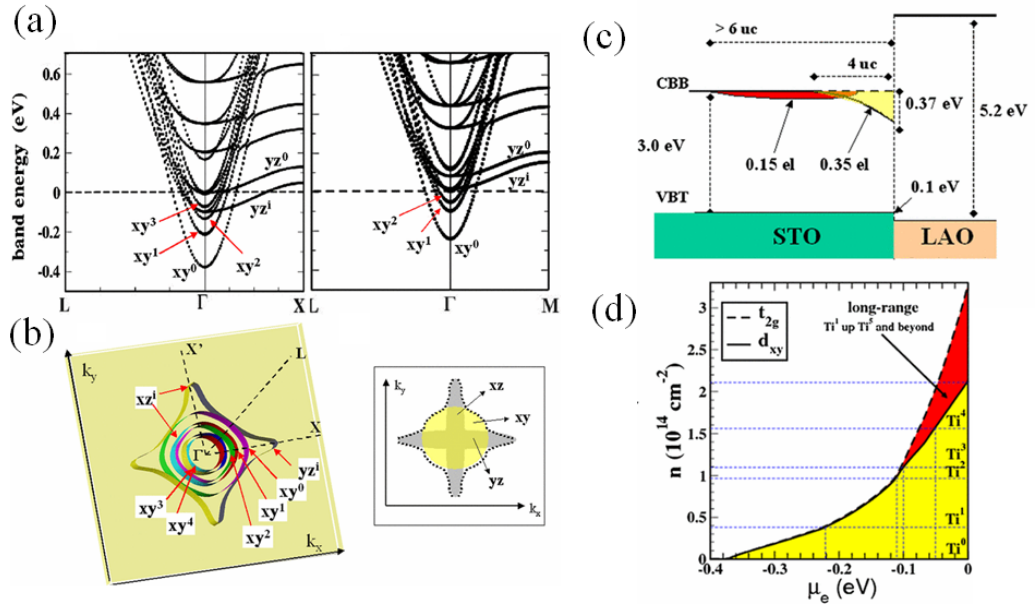

Figure B.11: (a) Bandes d'énergie calculées pour une densité de porteurs élevée (gauche) et basse (droite). (b) Surfaces de Fermi du 2DEG à l'interface de $LaAlO_3/SrTiO_3$. (c) L'alignement de la bande de $LaAlO_3/SrTiO_3$ et la distribution calculée des orbitales d_{xy}, d_{xz}, d_{yz}. Les électrons qui occupent les orbitales d_{xy} sont proches de l'interface, tandis que les fonctions d'onde d_{xz}, d_{yz} s'étendent jusqu'à la sixième couche de STO sous l'interface. (d) Calcul des densités de charge t2g (pointillé) et d_{xy} (solide) par unité de surface en fonction du potentiel chimique. Extrait de [Delugas 2011].

l'Université Nationale de Singapour. Quelques plans de LAO ont été déposées sur un substrat STO orienté (001). Les dispositifs en forme de barre Hall, à six contacts, de largeur 50 μm et de longueur 180 μm entre les sondes longitudinales ont été fabriqués par photolithographie conventionnelle en utilisant des dépôts de AlN amorphes pour réaliser les masques. Pendant le dépôt, la diffraction d'électrons à haute énergie (RHEED) a été utilisée pour contrôler avec précision la croissance couche par couche de LAO. Les échantillons ont ensuite été recuits dans un four tubulaire sous pression partielle d'oxygène afin d'éliminer les lacunes d'oxygène dans les substrats STO introduits par bombardement plasma à haute énergie pendant le dépôt. La dépendance en température de la résistance de l'échantillon a été mesurée systématiquement pendant les processus de refroidissement et de chauffage. Tous les échantillons LAO/STO montrent une très forte dépendance à la température: la résistance à température ambiante est de l'ordre de quelques centaines de kilo-ohms tandis que la résistance à basse température est de l'ordre de quelques centaines d'ohms.

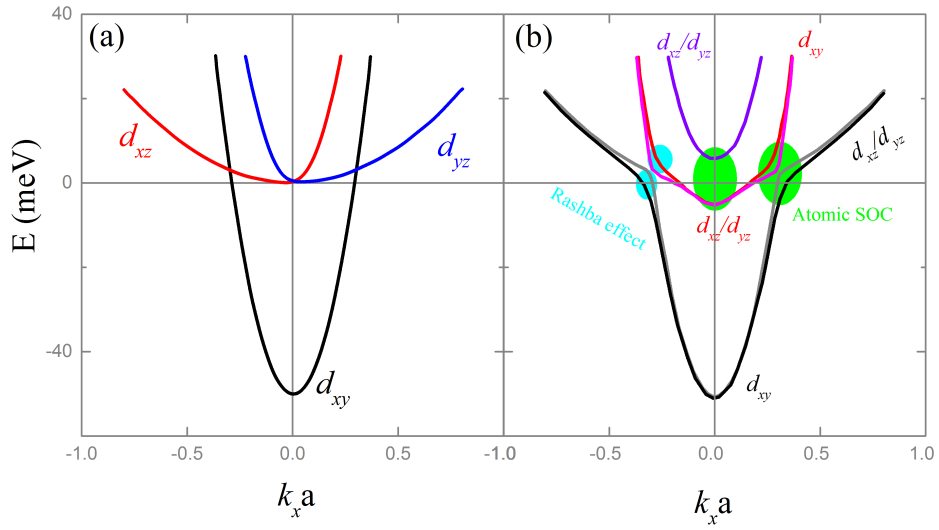

Figure B.12: (a) Structure simplifiée des bandes t_{2g} à l'interface LaAlO $_3$/SrTiO $_3$ sans aucun couplage spin-orbite (SOC). La bande d_{xy} a une énergie inférieure de 50 meV Ãă celle des bandes d_{xz}/d_{yz}. (b) La struture de bande des orbitales t_{2g} en présence de couplage spin-orbite (SOC). Le SOC atomique combine les bandes t_{2g} et lève la dégénérescence Γ-point des bandes d_{xz} et d_{yz} (mise en évidence par la zone verte). L'interaction entre le SOC et la brisure de la symétrie d'inversion clive les deux états de spin pour toutes les bandes. Le clivage le plus important se produit aux points où la bande d_{xy} croise les bandes d_{xz}/d_{yz} (mise en évidence par la zone cyan). Extrait de [Kim 2013].

B.4.3 Magnéto-transport et propriétés électroniques

Dans cette section, nous nous intéressons aux propriétés de transport et aux propriétés électroniques des échantillons $LaAlO_3/SrTiO_3$. Les échantillons présentent une magnétorésistance positive (MR) lorsqu'un champ magnétique élevé est appliqué perpendiculairement au plan de l'échantillon. L'amplitude de cette caractéristique générique varie d'un échantillon à l'autre et est décorée de faibles oscillations de Shubnikov-de Haas pour les échantillons à mobilité élevée. Lorsque le champ magnétique est orienté progressivement perpendiculairement au plan de l'échantillon, la MR montre une évolution de positive à négative (voir Fig. B.14). D'autre part, la résistance de Hall reste linéaire avec une pente réduite par le cosinus de l'angle d'inclinaison, comme prévu en considérant la géométrie de la barre de Hall. Une estimation grossière de la densité de porteurs à partir du coefficient de Hall R_H donne $n_H = 1.48 \times 10^{13}$ cm^{-2}.

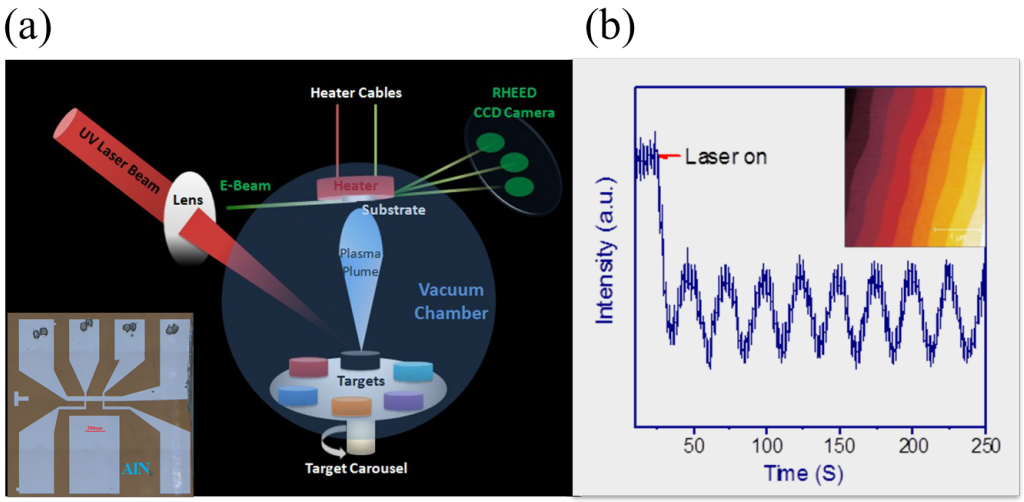

Figure B.13: (a) Schéma du dépôt laser pulsé (PLD) de $LaAlO_3/SrTiO_3$ et la barre de Hall (encart). (b) Le profil RHEED pendant le dépôt de LAO. Les maxima/minima d'oscillation indiquent que le dépôt de $LaAlO_3$ s'effectue couche par couche. L'encart est une image AFM du substrat $SrTiO_3$.

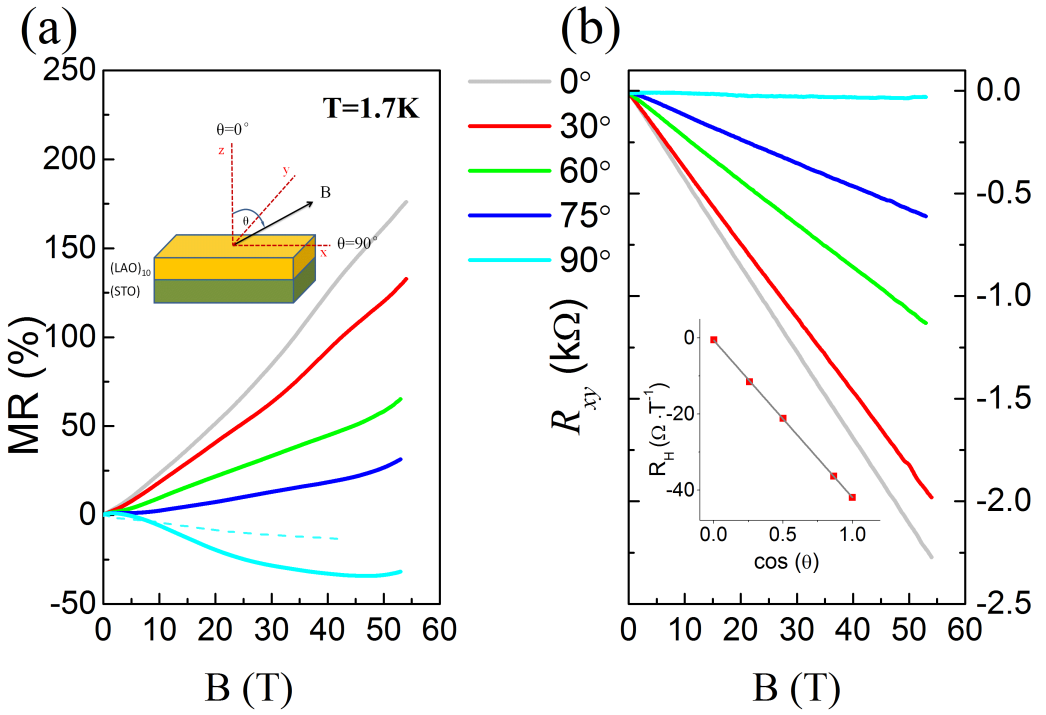

Figure B.14: Magnétorésistance longitudinale (a) et résistance de Hall (b) à T = 1,7 K en fonction de l'angle d'inclinaison entre le plan de l'échantillon et le champ magnétique. L'encadré de (b) affiche la variation linéaire du coefficient de Hall par rapport au cosinus de l'angle d'inclinaison. La ligne cyan foncé en pointillés de (a) est la RM enregistrée Ãă 20 K sous un champ magnétique parallÃÍle.

La Fig. B.16 montre le meilleur ajustement obtenu en utilisant cette procédure pour deux échantillons issus des mêmes lots à partir desquels on extrait les paramètres libres n, g et Γ. La valeur de masse effective, m^* est fixée à 1.9 m_e à partir de l'évolution de l'amplitudes des oscillations présentée plus haut. La densité de porteurs obtenue $n = 1.65 \times 10^{12}\text{cm}^{-2}$ est du même ordre de grandeur que celle rapportées dans d'autres études réalisées sur des échantillons similaires[Ben Shalom 2010, Zeng 2016], mais reste néanmoins près de deux ordres de grandeur inférieure aux prédictions du modèle de catastrophe polaire. De plus, cette valeur n'est pas en accord avec la valeur extraite de l'effet Hall linéaire $n_H = 1.48 \times 10^{13}$ cm^{-2}.

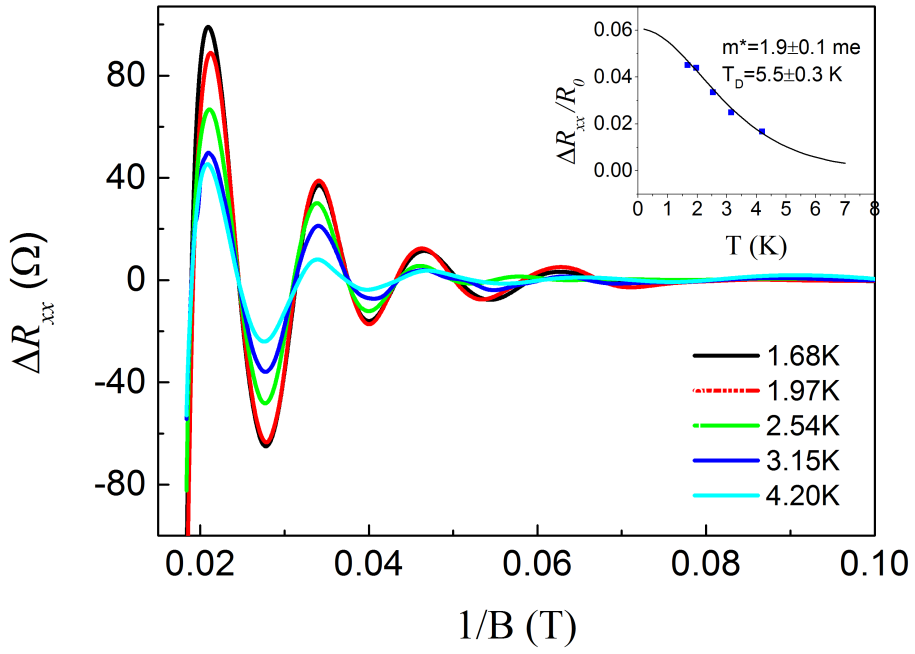

Figure B.15: Dépendance en température des oscillations de Shubnikov-de Haas en fonction du l'inverse du champ magnétique après soustraction d'une composante monotone. Notez que les oscillations ne sont pas exactement périodiques en 1/B. L'encart montre l'amplitude des oscillations en fonction de la température et leur ajustement en utilisant l'expression de LK.

B.4.4 Spectroscopie de la structure de bande

Dans cette section, nous concentrons notre attention sur les propriétés électroniques d'un échantillon $LaAlO_3/SrTiO_3$ à mobilité élevée avec 8 cellules unitaires de LaAlO3. Les mesures sont effectuées dans une gamme de température inférieure au kelvin (40 mK) et sous un champ magnétique constant de 16 T. Une grille réalisée

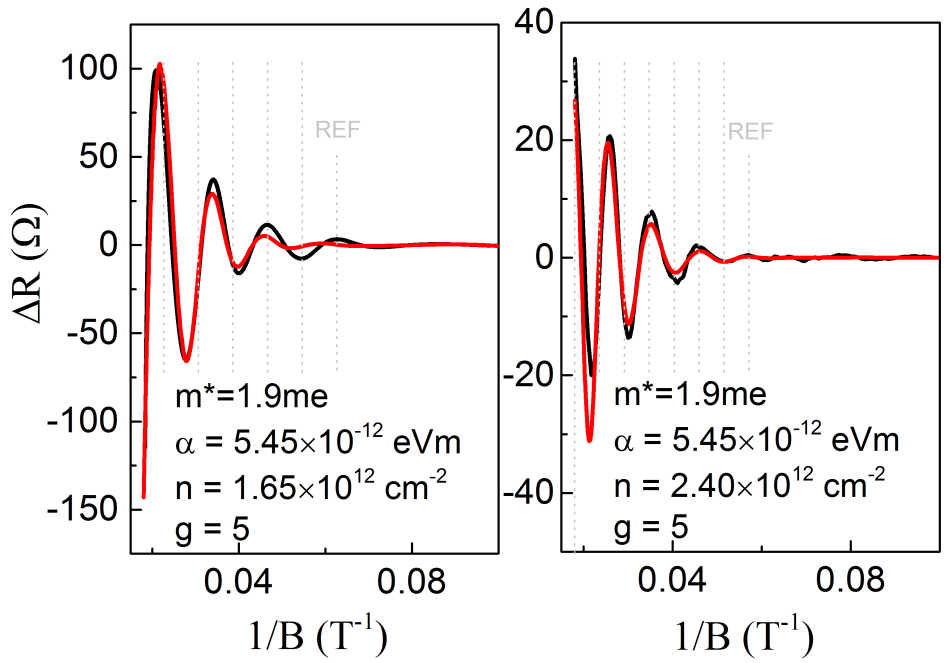

Figure B.16: Ajustement (ligne rouge) des oscillations SdH pour deux échantillons similaires issus du même lot en présence d'un couplage spin-orbite. La ligne noire correspond aux données expérimentales. Les lignes pointillées verticales sont un guide pour les yeux. "REF" représente la référence arbitraire pour la périodicité 1/B.

sur la face arrière (back-gate) permet par l'application d'une tension de faire varier la densité de porteurs à l'interface LAO/STO.

La Fig. B.18 montre la dépendance de la résistance longitudinale et de la résistance de Hall à T = 40 mK. La résistance longitudinale affiche un diagramme d'oscillation SdH complexe superposé à une faible MR positive à bas champ. La résistance de Hall est quasiment linéaire sur toute la gamme des champs magnétiques, avec de faibles oscillations superposées à ce comportement linéaire qui sont probablement dues à une contribution de la MR comme prévu pour un système multi-bandes. Sur toute la plage de tensions de grille scrutée (0-100 V), les densités minimales et maximales de porteurs sont respectivement de 1.43×10^{13} cm^{-2} et 1.7×10^{13} cm^{-2}, les mobilités correspondantes sont 3600 cm^2/Vs et 5000 cm^2/Vs.

Dans ce qui suit, nous limiterons notre discussion à un lien qualitatif entre les mesures de transport expérimentales et le modèle de structure de bande (Fig. B.20 d'après [Joshua 2012].) Nous démontrons ici que, dans la plage de densités électroniques déterminée par effet Hall, l'évolution des fréquences d'oscillations de SdH (les pics FFT) est cohérente avec la structure de bandes prévue théoriquement

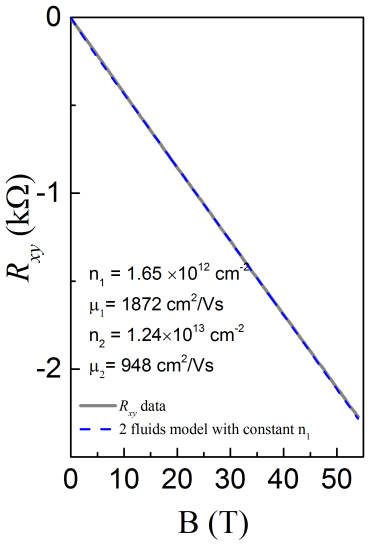

Figure B.17: Résistance de Hall mesurée (trait plein noir) et ajustement avec un modèle à deux fluides (ligne pointillée bleue) avec $n_1 = 1.65 \times 10^{12}$ cm^{-2}, $\mu_{t,1}$=1872 cm^2/Vs, $n_2 = 1.24 \times 10^{13}$ cm^{-2}, $\mu_{t,2}$=948 cm^2/Vs. La valeur de n_1 est extraite du précédent ajustement des oscillations de SdH prenant en compte l'effet Rashba.

pour l'hétérostructure LAO/STO. La plage de densité électronique scrutée dans ces expériences se situe au voisinage de n_c, densité critique où la structure des états aux niveaux de Fermi varie rapidement avec la densité.

Sur la Fig. B.19(b), les fréquences des pics de FFT A_1 et A_2 augmentent de la même façon lors de l'augmentation de la densité de porteurs. Elles peuvent être associées aux sous-bandes résolues en spin $d^1_{xz/yz}$ (bandes noires et grises sur la Fig. B.19(b)). Lorsque la densité de porteurs augmente, la section de la surface de Fermi perpendiculaire au champ croït notablement pour ces bandes ce qui correspond à une augmentation de la fréquences des pics A_1 et A_2. Nous assignons les pics B_1 et B_2 aux sous-bandes "légères" résolues en spin d^1_{xy}. Pour ces bandes la section de la surface de Fermi perpendiculaire au champ n'évolue pas ou peu lorsque le niveau de Fermi est au voisinage de la densité critique n_c. D'autre part, les pics C_1 et C_2 sont liés aux sous-bandes "légères" $d^2_{xz/yz}$, leurs fréquences basses correspondent à la surface de Fermi minimale. Comme le montre la Fig. B.19(b), les fréquences des pics décroissent d'abord lorsque nHall approche n_c, puis augmentent à nouveau lorsque nHall est supérieur à n_c. Ce phénomène peut être lié à la structure de bande en notant que les minima des bandes varient avec la concentration de porteurs, comme indiqué par [Maniv 2015]. Les pics D_1 et D_3 sont associés à la surface de Fermi externe et interne de la bande d^2_{xy} clivée par le couplage spin-orbite. Le pic D_2, assigné à la bande $d^2_{xz/yz}$, est absent puisque l'énergie de Fermi se trouve en dessous de cette bande (ligne pointillée sur la Fig. B.20). Lorsque l'énergie de Fermi augment ($n_{Hall} > n_c$), les électrons commencent à peupler les bandes d^2_{xy}:

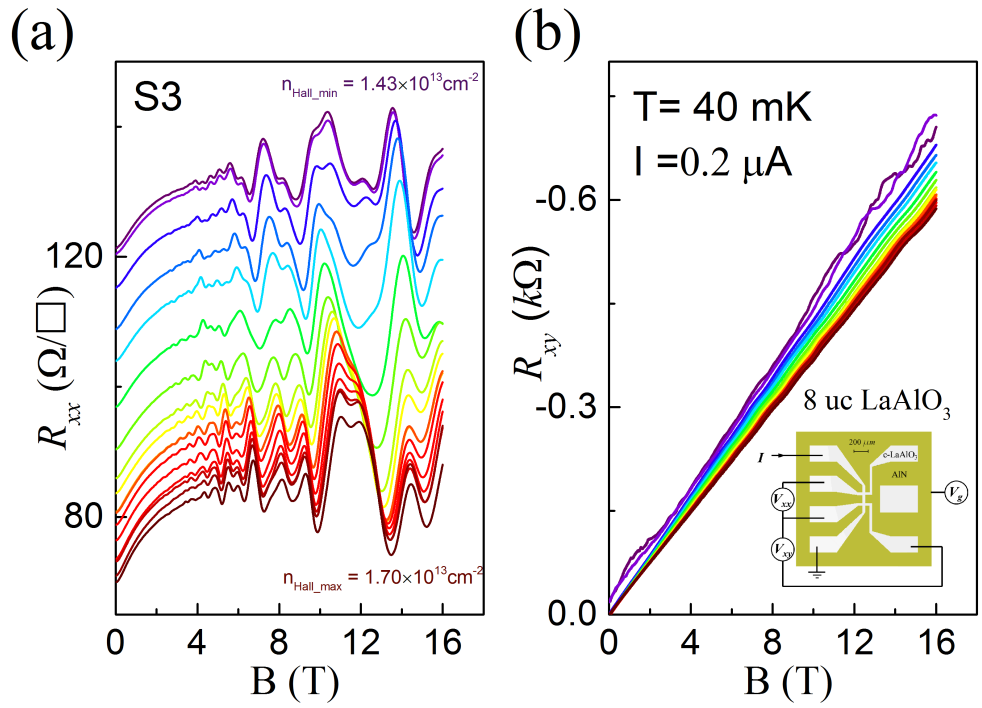

Figure B.18: (a) La résistance longitudinale R_{xx} et (b) la résistance de Hall R_{xy} à 40 mK sous un champ continu jusqu'à 16 T avec un courant I= 0,2 μA. Les R_{xx} montrent des oscillations SdH complexes à ces températures avec plusieurs fréquences, et le diagramme d'oscillation dépend clairement de la porte. Les R_{xy} sont presque linéaires jusqu'au 16 T, à l'exception de quelques petites entités superposées, que nous pensons être le composant R_{xx} parasite. L'encart montre l'esquisse de l'échantillon et la configuration de la mesure.

elles acquièrent une masse effective plus élevée (qui se traduit par une mobilité réduite) qui conduit finalement à la disparition du pic D_1. Dans le même temps, la bande $d^2_{xz/yz}$ est peuplée et le pic D_2 apparaït. Il convient de noter que le pic D_3, associé à la surface de Fermi interne de la bande d^2_{xy} clivée par l'interaction spin-orbite, est moins affecté à au voisinage de $n_{Hall} = n_c$ en raison du plus petit écart entre les bandes d^2_{xy} inférieure et supérieure au point de croisement.

Nous étendons le travail expérimental ci-dessus dans un champ magnétique pulsé jusqu'à 55 T, avec une température de base de 500 mK. Les oscillations observées sont moins bien résolues ou non détectées par rapport aux expériences à très basse température et en champ statique. Celles qui persistent à cette température sont élargies. Bien que la température électronique soit inconnue, nous supposons qu'elle est supérieure à celle fournie par le thermomètre calibré (500 mK), en effet pour les expériences en champ transitoire il est nécessaire d'augmenter le courant. Les oscillations principales sont néanmoins reproduites dans ces expériences sous

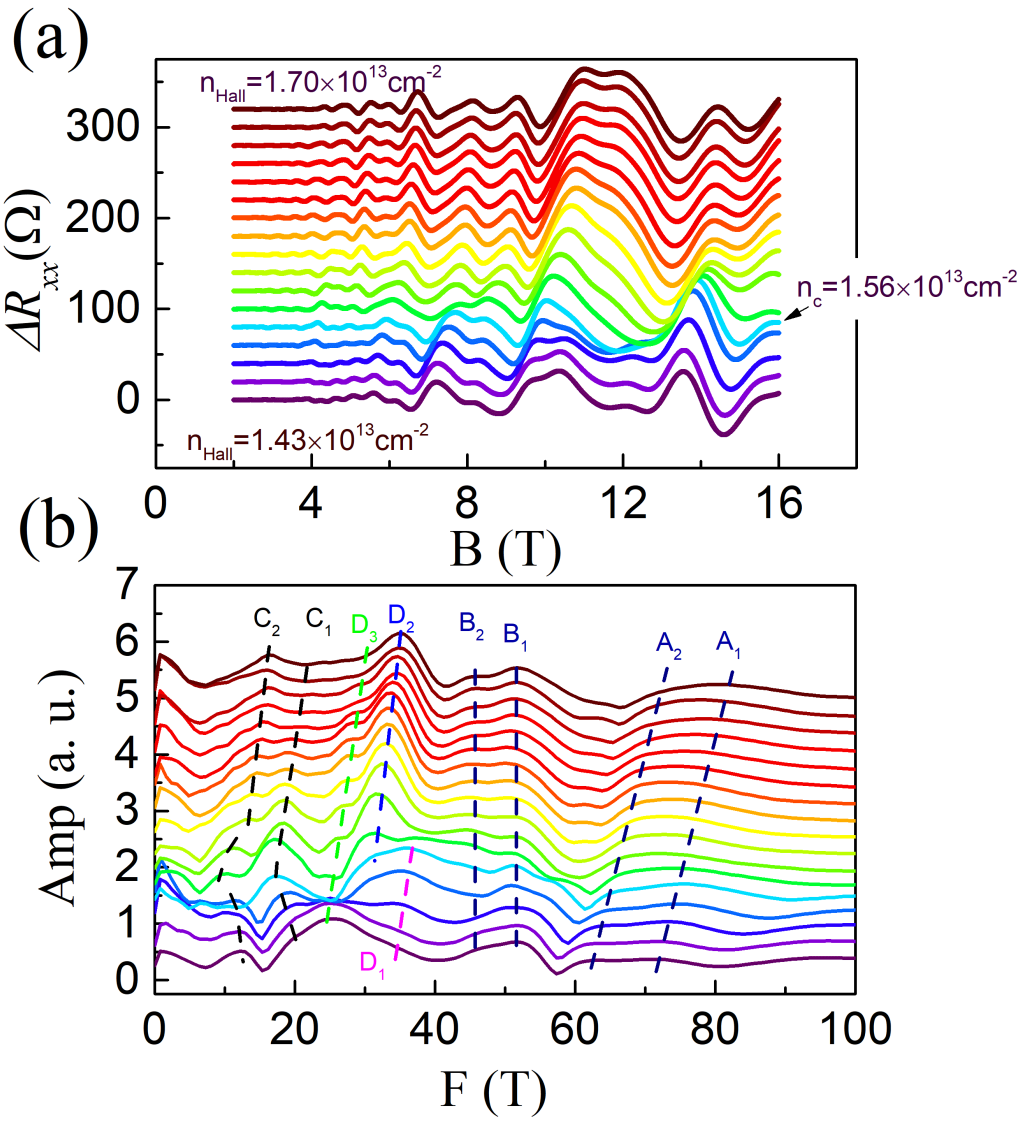

Figure B.19: (a) Dépendance de R_{xx} en fonction de B après soustractions de la composante monotone. (b) Spectres FFT de R_{xx} en fonction de 1/B. Les lignes pointillées indiquent les pics principaux dans les spectres de Fourier.

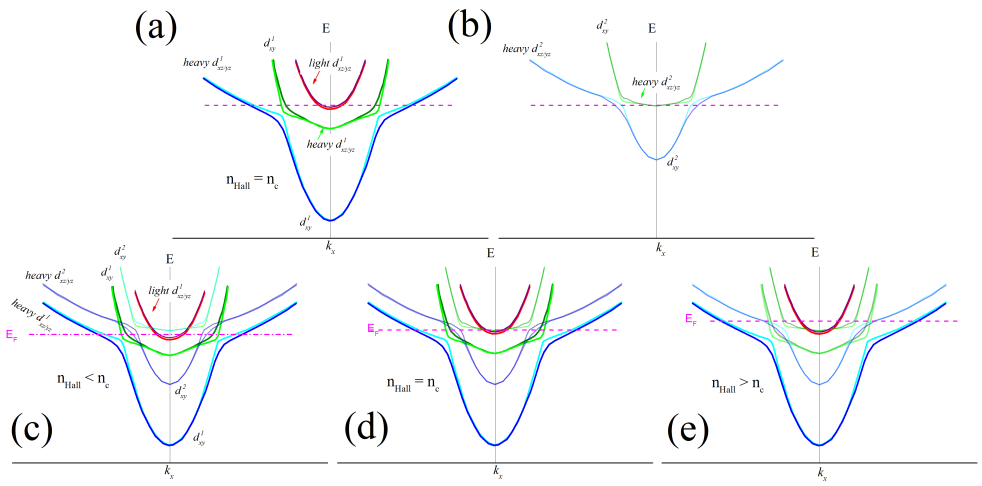

Figure B.20: Schéma de la structure de bande au voisinage du niveau de Fermi. (a) Les 3 bandes fondamentales d^1_{xy}, d^1_{xz} et d^1_{yz} d'après le modèle proposé dans [Joshua 2012] situées dans la première couche de STO. (b) Sous-bandes fondamentales d^2_{xy}, d^2_{xz} and d^2_{yz} situées dans la deuxième couche de STO. L'énergie de Fermi est définie pour la densité de porteurs égale à nc pour (a) et (b). (c, d, e) Structure de bande obtenue en combinant les sous-bandes fondamentales des deux premières couches de STO, le niveau de Fermi correspond à différentes densité électroniques

fort champ magnétique.

B.5 Conclusion

Dans cette thèse, nous avons étudié les propriétés électroniques de gaz d'électrons bidimensionnel sous champ magnétique très élevé. Ce travail se concentre principalement sur deux systèmes : le graphène sur SiC et l'interface $LaAlO_3/SrTiO_3$.

Dans le graphène sur SiC, nous avons effectué des mesures de magnétotransport sous un champ magnétique jusqu'à 78 T. Nous avons observé pour la première fois un plateau de Hall quantique pour un facteur de remplissage $\nu = 2$ qui s'étend sur une très large plage de champ magnétique (de 7 T à 78 T). Dans le régime de rupture de l'effet Hall quantique, des oscillations de la magnétorésistance de faible amplitude et périodiques en 1/B apparaissent alors que le plateau R_{xy} reste quantifié. Nous proposons un modèle dans lequel des inhomogénéités de dopage naturelles sont introduites dans l'échantillon. Ce modèle explique avec succès le long plateau de Hall et les oscillations anormales de la magnétorésistance dans un champ magnétique intense.

Les propriétés de transport des échantillons de $LaAlO_3/SrTiO_3$ de faible mobilité ont été étudiées sous un champ magnétique allant jusqu'à 55 T à la température de l'hélium liquide. Nous avons observé des oscillations de SdH de très faible amplitude et quasi-périodiques en 1/B. Nous attribuons ces oscillations à l'effet Rashba

présent à l'interface de l'hétérostructure LAO/STO. La différence de densités de porteurs déterminées par les oscillations de SdH et l'effet Hall est expliquée en utilisant un modèle simple à deux bandes. A très basse température, (40mK) et sous champ statique, des oscillations de SdH complexes avec une évolution claire en fonction de la position du niveau de Fermi (ajusté par une tension de grille) sont observées. Ces résultats sont en bon accord qualitatif avec le modèle de structure de bande à l'interface LAO/STO proposé par [Joshua 2012]. Ce modèle prend inclut les différentes sous bandes ainsi que le couplage spin-orbite atomique et l'effet Rashba. En prenant en compte les symétries des différentes orbitales et leur distribution spatiale, nous expliquons la dépendance oscillations de SdH en fonction de la densité de porteurs.

Bibliography

[Alexander-Webber 2012] J. A. Alexander-Webber, A. M. R. Baker, P. D. Buckle, T. Ashley and R. J. Nicholas. *High-current breakdown of the quantum Hall effect and electron heating in InSb/AlInSb.* Physical Review B, vol. 86, page 045404, Jul 2012. (Cited on page 27.)

[Alexander-Webber 2013] J. A. Alexander-Webber, A. M. R. Baker, T. J. B. M. Janssen, A. Tzalenchuk, S. Lara-Avila, S. Kubatkin, R. Yakimova, B. A. Piot, D. K. Maude and R. J. Nicholas. *Phase Space for the Breakdown of the Quantum Hall Effect in Epitaxial Graphene.* Physical Review Letters, vol. 111, page 096601, Aug 2013. (Cited on pages 45, 52, 55 and 119.)

[Annadi 2013] A. Annadi, Q. Zhang, X. Renshaw Wang, Nikolina Tuzla, K. Gopinadhan, W. M. Lü, A. Roy Barman, Z. Q. Liu, A. Srivastava, S. Saha*et al.* *Anisotropic two-dimensional electron gas at the $LaAlO_3/SrTiO_3$ (110) interface.* Nature Communications, vol. 4, page 1838, 2013. (Cited on page 74.)

[Ariando 2011] Ariando, X. Wang, G Baskaran, ZQ Liu, J Huijben, JB Yi, A Annadi, AR Barman, A Rusydi, S Dhar, YP Feng, J Ding, H Hilgenkamp and T Venkatesan. *Electronic phase separation at the $LaAlO_3/SrTiO_3$ interface.* Nature Communications, vol. 2, page 188, 2011. (Cited on pages 75, 79 and 80.)

[Ashcroft 2010] Neil W Ashcroft and N David Mermin. *Solid State Physics (Saunders College, Philadelphia, 1976).* Google Scholar, page 29, 2010. (Cited on page 8.)

[Assmann 2013] Elias Assmann, Peter Blaha, Robert Laskowski, Karsten Held, Satoshi Okamoto and Giorgio Sangiovanni. *Oxide Heterostructures for Efficient Solar Cells.* Physical Review Letters, vol. 110, page 078701, Feb 2013. (Cited on page 71.)

[Bae 2010] Sukang Bae, Hyeongkeun Kim, Youngbin Lee, Xiangfan Xu, Jae-Sung Park, Yi Zheng, Jayakumar Balakrishnan, Tian Lei, Hye Ri Kim, Young Il Song*et al.* *Roll-to-roll production of 30-inch graphene films for transparent electrodes.* Nature Nanotechnology, vol. 5, no. 8, pages 574–578, 2010. (Cited on page 45.)

[Balaban 1993] N. Q. Balaban, U. Meirav, H. Shtrikman and Y. Levinson. *Scaling of the critical current in the quantum Hall effect: A probe of current distribution.* Physical Review Letters, vol. 71, pages 1443–1446, Aug 1993. (Cited on page 27.)

[Béard 2013a] J. Béard, J. Billette, P. Frings, M. Suleiman and F. Lecouturier. *Special Coils Development at the National High Magnetic Field Laboratory in Toulouse*. Journal of Low Temperature Physics, vol. 170, no. 5, pages 442–446, 2013. (Cited on page 30.)

[Béard 2013b] J. Béard and F. Debray. *The French High Magnetic Field Facility*. Journal of Low Temperature Physics, vol. 170, no. 5, pages 541–552, 2013. (Cited on page 30.)

[Belin 2005] T. Belin and F. Epron. *Characterization methods of carbon nanotubes: a review*. Materials Science and Engineering: B, vol. 119, no. 2, pages 105 – 118, 2005. (Cited on page 38.)

[Bell 2009] C. Bell, S. Harashima, Y. Kozuka, M. Kim, B. G. Kim, Y. Hikita and H. Y. Hwang. *Dominant Mobility Modulation by the Electric Field Effect at the $LaAlO_3/SrTiO_3$ Interface*. Physical Review Letters, vol. 103, page 226802, Nov 2009. (Cited on page 72.)

[Ben Shalom 2010] M. Ben Shalom, A. Ron, A. Palevski and Y. Dagan. *Shubnikov–De Haas Oscillations in $SrTiO_3/LaAlO_3$ Interface*. Physical Review Letters, vol. 105, page 206401, Nov 2010. (Cited on pages 88, 97 and 128.)

[Bennaceur 2012] K. Bennaceur, P. Jacques, F. Portier, P. Roche and D. C. Glattli. *Unveiling quantum Hall transport by Efros-Shklovskii to Mott variable-range hopping transition in graphene*. Physical Review B, vol. 86, page 085433, Aug 2012. (Cited on pages 54 and 118.)

[Berger 2006] Claire Berger, Zhimin Song, Xuebin Li, Xiaosong Wu, Nate Brown, Cécile Naud, Didier Mayou, Tianbo Li, Joanna Hass, Alexei N Marchenkov*et al.* *Electronic confinement and coherence in patterned epitaxial graphene*. Science, vol. 312, no. 5777, pages 1191–1196, 2006. (Cited on page 45.)

[Bishop 1982] D. J. Bishop, R. C. Dynes and D. C. Tsui. *Magnetoresistance in Si metal-oxide-semiconductor field-effect transitors: Evidence of weak localization and correlation*. Physical Review B, vol. 26, pages 773–779, Jul 1982. (Cited on page 4.)

[Boisen 1994] A. Boisen, P. Bo/ggild, A. Kristensen and P. E. Lindelof. *Nonlinear current-voltage characteristics at quantum Hall resistance minima*. Physical Review B, vol. 50, pages 1957–1960, Jul 1994. (Cited on page 27.)

[Bolotin 2009] KI Bolotin, F Ghahari, MD Shulman, HL Stormer and P Kim. *Observation of the fractional quantum Hall effect in graphene*. Nature, vol. 462, no. 7270, pages 196–199, 2009. (Cited on page 38.)

[Boyko 1999] B. A. Boyko, A. I. Bykov, M. I. Dolotenko, N. P. Kolokolchikov, I. M. Markevtsev, O. M. Tatsenko and K. Shuvalov. *With record magnetic fields*

to the 21st Century. Digest of Technical Papers. 12th IEEE International Pulsed Power Conference. (Cat. No.99CH36358), vol. 2, pages 746–749 vol.2, June 1999. (Cited on page 30.)

[Breitschaft 2010] M. Breitschaft, V. Tinkl, N. Pavlenko, S. Paetel, C. Richter, J. R. Kirtley, Y. C. Liao, G. Hammerl, V. Eyert, T. Kopp and J. Mannhart. *Two-dimensional electron liquid state at $LaAlO_3 - SrTiO_3$ interfaces*. Physical Review B, vol. 81, page 153414, Apr 2010. (Cited on page 72.)

[Brinkman 2007] A Brinkman, M Huijben, M Zalk, J Huijben, U Zeitler, JC Maan, WG Wiel, G Rijnders, DHA Blank and H Hilgenkamp. *Magnetic effects at the interface between nonmagnetic oxides*. Nature Materials, vol. 6, no. 7, pages 493–496, 2007. (Cited on pages 72 and 75.)

[Büttiker 1988] M. Büttiker. *Absence of backscattering in the quantum Hall effect in multiprobe conductors*. Physical Review B, vol. 38, pages 9375–9389, Nov 1988. (Cited on page 25.)

[Bychkov 1984] Yu A Bychkov and Emmanuel I Rashba. *Oscillatory effects and the magnetic susceptibility of carriers in inversion layers*. Journal of Physics C: Solid State Physics, vol. 17, no. 33, page 6039, 1984. (Cited on pages 78 and 124.)

[Cancellieri 2016] Claudia Cancellieri, Andrei S Mishchenko, Ulrich Aschauer, Alessio Filippetti, Carina Faber, OS Barišić, VA Rogalev, Thorsten Schmitt, Naoto Nagaosa and Vladimir N Strocov. *Polaronic metal state at the $LaAlO_3/SrTiO_3$ interface*. Nature Communications, vol. 7, page 10386, 2016. (Cited on page 80.)

[Castro Neto 2006] A. H. Castro Neto, Francisco Guinea and Nuno Miguel Peres. *Drawing conclusions from graphene*. Physics World, vol. 19, no. 11, page 33, 2006. (Cited on page 39.)

[Castro Neto 2009] A. H. Castro Neto, F. Guinea, N. M. R. Peres, K. S. Novoselov and A. K. Geim. *The electronic properties of graphene*. Reviews of Modern Physics Review, vol. 81, pages 109–162, Jan 2009. (Cited on page 40.)

[Caviglia 2008] A. D. Caviglia, Stefano Gariglio, Nicolas Reyren, Didier Jaccard, T Schneider, M Gabay, S Thiel, G Hammerl, Jochen Mannhart and J-M Triscone. *Electric field control of the $LaAlO_3/SrTiO_3$ interface ground state*. Nature, vol. 456, no. 7222, pages 624–627, 2008. (Cited on pages 72 and 75.)

[Caviglia 2010a] A. D. Caviglia, M. Gabay, S. Gariglio, N. Reyren, C. Cancellieri and J.-M. Triscone. *Tunable Rashba Spin-Orbit Interaction at Oxide Interfaces*. Physical Review Letters, vol. 104, page 126803, Mar 2010. (Cited on pages 72, 78, 79, 85 and 87.)

[Caviglia 2010b] A. D. Caviglia, S. Gariglio, C. Cancellieri, B. Sacépé, A. Fête, N. Reyren, M. Gabay, A. F. Morpurgo and J.-M. Triscone. *Two-Dimensional Quantum Oscillations of the Conductance at $LaAlO_3/SrTiO_3$ Interfaces.* Physical Review Letters, vol. 105, page 236802, Dec 2010. (Cited on pages 22, 72, 75, 82 and 88.)

[Cen 2008] Cheng Cen, S. Thiel, G. Hammerl, C. W. Schneider, K. E. Andersen, C. S. Hellberg, J. Mannhart and J Levy. *Nanoscale control of an interfacial metal–insulator transition at room temperature.* Nature Materials, vol. 7, no. 4, pages 298–302, 2008. (Cited on page 72.)

[Chen 2011] Yunzhong Chen, Nini Pryds, Josée E Kleibeuker, Gertjan Koster, Jirong Sun, Eugen Stamate, Baogen Shen, Guus Rijnders and Søren Linderoth. *Metallic and insulating interfaces of amorphous $SrTiO_3$-based oxide heterostructures.* Nano Letters, vol. 11, no. 9, pages 3774–3778, 2011. (Cited on page 74.)

[Chen 2013] YZ Chen, N Bovet, Felix Trier, DV Christensen, FM Qu, Niels Hessel Andersen, Takeshi Kasama, Wei Zhang, R Giraud, J Dufouleur*et al. A high-mobility two-dimensional electron gas at the spinel/perovskite interface of γ-$Al_2O_3/SrTiO_3$.* Nature Communications, vol. 4, page 1371, 2013. (Cited on page 22.)

[Coleridge 1991] P. T. Coleridge. *Small-angle scattering in two-dimensional electron gases.* Physical Review B, vol. 44, pages 3793–3801, Aug 1991. (Cited on page 91.)

[Dean 2011] C. R. Dean, A. F. Young, P. Cadden-Zimansky, L. Wang, H. Ren, K. Watanabe, T. Taniguchi, P. Kim, J. Hone and K. L. Shepard. *Multicomponent fractional quantum Hall effect in graphene.* Nature Physics, vol. 7, pages 693–696, 2011. (Cited on page 38.)

[Delahaye 2003] F Delahaye and B Jeckelmann. *Revised technical guidelines for reliable dc measurements of the quantized Hall resistance.* Metrologia, vol. 40, no. 5, pages 217–223, 2003. (Cited on page 45.)

[Delugas 2011] Pietro Delugas, Alessio Filippetti, Vincenzo Fiorentini, Daniel I. Bilc, Denis Fontaine and Philippe Ghosez. *Spontaneous 2-Dimensional Carrier Confinement at the n-Type $SrTiO_3/LaAlO_3$ Interface.* Physical Review Letters, vol. 106, page 166807, Apr 2011. (Cited on pages 76, 77, 84, 123, 124 and 125.)

[Diez 2015] M. Diez, A.M.R.V.L. Monteiro, G. Mattoni, E. Cobanera, T. Hyart, E. Mulazimoglu, N. Bovenzi, C. W.H. Beenakker and A. D. Caviglia. *Giant Negative Magnetoresistance Driven by Spin-Orbit Coupling at the $LaAlO_3/SrTiO_3$ Interface.* Physical Review Letters, vol. 115, no. 1, 2015. (Cited on pages 78, 83 and 85.)

[Dingle 1974] Raymond Dingle, William Wiegmann and Charles H Henry. *Quantum states of confined carriers in very thin $Al_xGa_{1-x}As$-$GaAsAl_xGa_{1-x}As$ heterostructures.* Physical Review Letters, vol. 33, no. 14, page 827, 1974. (Cited on page 4.)

[Dresselhaus 1992] M. S. Dresselhaus, G. Dresselhaus and Riichiro Saito. *Carbon fibers based on C_{60} and their symmetry.* Physical Review B, vol. 45, pages 6234–6242, Mar 1992. (Cited on page 38.)

[Ebert 1982] G. Ebert, K.v. Klitzing, C. Probst and K. Ploog. *Magneto-quantumtransport on $GaAs$-$Al_xGa_{1-x}As$ heterostructures at very low temperatures.* Solid State Communications, vol. 44, no. 2, pages 95 – 98, 1982. (Cited on page 23.)

[Eda 2008] Goki Eda, Giovanni Fanchini and Manish Chhowalla. *Large-area ultrathin films of reduced graphene oxide as a transparent and flexible electronic material.* Nature Nanotechnology, vol. 3, no. 5, pages 270–274, 2008. (Cited on page 45.)

[Efros 1975] A L Efros and B I Shklovskii. *Coulomb gap and low temperature conductivity of disordered systems.* Journal of Physics C: Solid State Physics, vol. 8, no. 4, page L49, 1975. (Cited on pages 28, 53 and 118.)

[Eriksson 2012] Jens Eriksson, Ruth Pearce, Tihomir Iakimov, Chariya Virojanadara, Daniela Gogova, Mike Andersson, Mikael Syväjärvi, Anita Lloyd Spetz and Rositza Yakimova. *The influence of substrate morphology on thickness uniformity and unintentional doping of epitaxial graphene on SiC.* Applied Physics Letters, vol. 100, no. 24, page 241607, 2012. (Cited on page 59.)

[Eto 2010] Kazuma Eto, Zhi Ren, A. A. Taskin, Kouji Segawa and Yoichi Ando. *Angular-dependent oscillations of the magnetoresistance in Bi_2Se_3 due to the three-dimensional bulk Fermi surface.* Physical Review B, vol. 81, page 195309, May 2010. (Cited on page 22.)

[Fawcett 1964] E. Fawcett. *High-field galvanomagnetic properties of metals.* Advances in Physics, vol. 13, no. 50, pages 139–191, 1964. (Cited on page 8.)

[Fazilleau 2012] P. Fazilleau, C. Berriaud, R. Berthier, F. Debray, B. Hervieu, W. Joss, F. P. Juster, M. Massinger, C. Mayri, Y. Queinec, C. Pes, R. Pfister, P. Pugnat, L. Ronayette and C. Trophime. *Final Design of the New Grenoble Hybrid Magnet.* IEEE Transactions on Applied Superconductivity, vol. 22, no. 3, pages 4300904–4300904, June 2012. (Cited on page 30.)

[Fête 2012] A. Fête, S. Gariglio, A. D. Caviglia, J.-M. Triscone and M. Gabay. *Rashba induced magnetoconductance oscillations in the $LaAlO_3/SrTiO_3$ heterostructure.* Physical Review B, vol. 86, no. 20, 2012. (Cited on page 85.)

[Fête 2014] A Fête, S Gariglio, C Berthod, D Li, D Stornaiuolo, M Gabay and J-M Triscone. *Large modulation of the Shubnikov-de Haas oscillations by the Rashba interaction at the $LaAlO_3/SrTiO_3$ interface.* New Journal of Physics, vol. 16, no. 11, page 112002, 2014. (Cited on pages 72, 85, 87 and 91.)

[Feynman 2010] Richard P Feynman, Albert R Hibbs and Daniel F Styer. Quantum mechanics and path integrals. Courier Corporation, 2010. (Cited on page 14.)

[Finnis 2003] Mike Finnis. Interatomic forces in condensed matter, volume 1. OUP Oxford, 2003. (Cited on page 40.)

[Fontein 1991] P. F. Fontein, J. A. Kleinen, P. Hendriks, F. A. P. Blom, J. H. Wolter, H. G. M. Lochs, F. A. J. M. Driessen, L. J. Giling and C. W. J. Beenakker. *Spatial potential distribution in $GaAs/Al_xGa_{1-x}As$ heterostructures under quantum Hall conditions studied with the linear electro-optic effect.* Physical Review B, vol. 43, pages 12090–12093, May 1991. (Cited on page 27.)

[Förg 2012] B. Förg, C. Richter and J. Mannhart. *Field-effect devices utilizing $LaAlO_3/SrTiO_3$ interfaces.* Applied Physics Letters, vol. 100, no. 5, page 053506, 2012. (Cited on page 72.)

[Fowler 1966] Alan B Fowler, Frank F Fang, William E Howard and Philip J Stiles. *Magneto-oscillatory conductance in silicon surfaces.* Physical Review Letters, vol. 16, no. 20, page 901, 1966. (Cited on page 4.)

[Frings 2008] P. Frings, H. Witte, H. Jones, J. Beard and T. Hermannsdoerfer. *Rapid Cooling Methods for Pulsed Magnets.* IEEE Transactions on Applied Superconductivity, vol. 18, no. 2, pages 612–615, June 2008. (Cited on page 30.)

[Furlan 1998] M. Furlan. *Electronic transport and the localization length in the quantum Hall effect.* Physical Review B, vol. 57, pages 14818–14828, Jun 1998. (Cited on pages 54, 64 and 122.)

[Geim 2007] A. K. Geim and K. S. Novoselov. *The rise of graphene.* Nature Materials, vol. 6, no. 3, pages 183–91, 2007. (Cited on page 38.)

[Geller 1956] S. Geller and V. B. Bala. *Crystallographic studies of perovskite-like compounds. II. Rare earth alluminates.* Acta Crystallographica, vol. 9, no. 12, pages 1019–1025, 1956. (Cited on page 73.)

[Giesbers 2008] A. J. M. Giesbers, G. Rietveld, E. Houtzager, U. Zeitler, R. Yang, K. S. Novoselov, A. K. Geim and J. C. Maan. *Quantum resistance metrology in graphene.* Applied Physics Letters, vol. 93, no. 22, page 222109, 2008. (Cited on pages 54 and 118.)

[Girvin 1999] Steven M. Girvin. The quantum hall effect: novel excitations and broken symmetries. Springer, 1999. (Cited on pages 16 and 112.)

[Goerbig 2011] M. O. Goerbig. *Electronic properties of graphene in a strong magnetic field*. Review of Modern Physics, vol. 83, pages 1193–1243, Nov 2011. (Cited on page 38.)

[Golub 2016] L. E. Golub, I. V. Gornyi and V. Yu. Kachorovskii. *Weak antilocalization in two-dimensional systems with large Rashba splitting*. Physical Review B, vol. 93, page 245306, Jun 2016. (Cited on page 16.)

[Guduru 2013] V. K. Guduru, A. Granados del Aguila, Sander Wenderich, M. K. Kruize, A. McCollam, P. C. M. Christianen, U. Zeitler, Alexander Brinkman, G. Rijnders, H. Hilgenkamp*et al. Optically excited multi-band conduction in* $LaAlO_3/SrTiO_3$ *heterostructures*. Applied Physics Letters, vol. 102, no. 5, page 051604, 2013. (Cited on page 88.)

[Guignard 2012] J. Guignard, D. Leprat, D. C. Glattli, F. Schopfer and W. Poirier. *Quantum Hall effect in exfoliated graphene affected by charged impurities: Metrological measurements*. Physical Review B, vol. 85, page 165420, Apr 2012. (Cited on page 45.)

[Halperin 1982] B. I. Halperin. *Quantized Hall conductance, current-carrying edge states, and the existence of extended states in a two-dimensional disordered potential*. Physical Review B, vol. 25, pages 2185–2190, Feb 1982. (Cited on page 24.)

[Han 2016] Kun Han. *High-monility two-dimensional electron gases at the* $(LaAlO_3)_{0.3}(SrAl_{0.5}Ta_{0.5}O_3)_{0.7}/SrTiO_3$ *and* $SrAl_{0.5}Ta_{0.5}O_3/SrTiO_3$ *Interface*. PhD thesis, National Unversity of Singapore, 2016. (Cited on page 81.)

[Hanai 2014] S. Hanai, T. Tsuchihashi, Y. Minemoto, S. Ioka, K. Watanabe, S. Awaji and H. Oguro. *Upgraded Cryogen-Free 20 T Superconducting Magnet*. IEEE Transactions on Applied Superconductivity, vol. 24, no. 3, pages 1–4, June 2014. (Cited on page 30.)

[Hernandez 2008] Yenny Hernandez, Valeria Nicolosi, Mustafa Lotya, Fiona M Blighe, Zhenyu Sun, Sukanta De, IT McGovern, Brendan Holland, Michele Byrne, Yurii K Gun'Ko*et al. High-yield production of graphene by liquid-phase exfoliation of graphite*. Nature Nanotechnology, vol. 3, no. 9, pages 563–568, 2008. (Cited on page 45.)

[Herranz 2007] G Herranz, M Basletić, M Bibes, C Carrétéro, E Tafra, E Jacquet, K Bouzehouane, C Deranlot, A Hamzić, J -M Broto, A Barthélémy and A Fert. *High Mobility in* $LaAlO_3/SrTiO_3$ *Heterostructures: Origin, Dimensionality, and Perspectives*. Physical Review Letters, vol. 98, no. 21, 2007. (Cited on page 75.)

[Huang 2013] Z. Huang, X. Renshaw Wang, Z. Q. Liu, W. M. Lü, S. W. Zeng, A. Annadi, W. L. Tan, X. P. Qiu, Y. L. Zhao, M. Salluzzo, J. M. D. Coey, T. Venkatesan and Ariando. *Conducting channel at the $LaAlO_3/SrTiO_3$ interface*. Physical Review B, vol. 88, no. 16, 2013. (Cited on page 72.)

[Huckestein 1995] Bodo Huckestein. *Scaling theory of the integer quantum Hall effect*. Review of Modern Physics, vol. 67, pages 357–396, Apr 1995. (Cited on pages 55 and 119.)

[Huijben 2006] Mark Huijben, Guus Rijnders, Dave HA Blank, Sara Bals, Sandra Van Aert, Jo Verbeeck, Gustaaf Van Tendeloo, Alexander Brinkman and Hans Hilgenkamp. *Electronically coupled complementary interfaces between perovskite band insulators*. Nature Materials, vol. 5, no. 7, pages 556–560, 2006. (Cited on page 80.)

[Huijben 2013] Mark Huijben, Gertjan Koster, Michelle K Kruize, Sander Wenderich, Jo Verbeeck, Sara Bals, Erik Slooten, Bo Shi, Hajo JA Molegraaf, Josee E Kleibeuker*et al. Defect engineering in oxide heterostructures by enhanced oxygen surface exchange*. Advanced Functional Materials, vol. 23, no. 42, pages 5240–5248, 2013. (Cited on page 72.)

[Hwang 2012] Harold Y Hwang, Yoh Iwasa, Masashi Kawasaki, Bernhard Keimer, Naoto Nagaosa and Yoshinori Tokura. *Emergent phenomena at oxide interfaces*. Nature Materials, vol. 11, no. 2, page 103, 2012. (Cited on page 71.)

[Jackson 1999] John David Jackson and Ronald F Fox. Classical electrodynamics, volume 67. American Association of Physics Teachers, 1999. (Cited on page 16.)

[Jalan 2010] Bharat Jalan, Susanne Stemmer, Shawn Mack and James S Allen. *Two-dimensional electron gas in δ-doped $SrTiO_3$*. Physical Review B, vol. 82, no. 8, 2010. (Cited on pages 82 and 90.)

[Janicka 2009] Karolina Janicka, Julian P Velev and Evgeny Y Tsymbal. *Quantum nature of two-dimensional electron gas confinement at $LaAlO_3/SrTiO_3$ interfaces*. Physical Review Letters, vol. 102, no. 10, page 106803, 2009. (Cited on page 77.)

[Janssen 2011] T. J. B. M. Janssen, A. Tzalenchuk, R. Yakimova, S. Kubatkin, S. Lara-Avila, S. Kopylov and V. I. Fal'ko. *Anomalously strong pinning of the filling factor $\nu = 2$ in epitaxial graphene*. Physical Review B, vol. 83, page 233402, Jun 2011. (Cited on pages 45, 47, 50, 52 and 117.)

[Janssen 2013] T J B M Janssen, A Tzalenchuk, S Lara-Avila, S Kubatkin and V I Fal'ko. *Quantum resistance metrology using graphene*. Reports on Progress in Physics, vol. 76, no. 10, page 104501, 2013. (Cited on pages 54 and 118.)

[Jeckelmann 2001] B Jeckelmann and B Jeanneret. *The quantum Hall effect as an electrical resistance standard*. Reports on Progress in Physics, vol. 64, no. 12, page 1603, 2001. (Cited on pages 19 and 113.)

[Jiang 2007] Z. Jiang, Y. Zhang, H. L. Stormer and P. Kim. *Quantum Hall States near the Charge-Neutral Dirac Point in Graphene*. Physical Review Letters, vol. 99, page 106802, Sep 2007. (Cited on pages 43, 44 and 115.)

[Jnawali 2017] Giriraj Jnawali, Mengchen Huang, Jen-Feng Hsu, Hyungwoo Lee, Jung-Woo Lee, Patrick Irvin, Chang-Beom Eom, Brian D'Urso and Jeremy Levy. *Room-Temperature Quantum Transport Signatures in Graphene/$LaAlO_3$/$SrTiO_3$ Heterostructures*. Advanced Materials, vol. 29, no. 9, 2017. (Cited on page 15.)

[Jobst 2010] Johannes Jobst, Daniel Waldmann, Florian Speck, Roland Hirner, Duncan K Maude, Thomas Seyller and Heiko B Weber. *Quantum oscillations and quantum Hall effect in epitaxial graphene*. Physical Review B, vol. 81, no. 19, page 195434, 2010. (Cited on page 45.)

[Joshua 2012] Arjun Joshua, S Pecker, J Ruhman, E Altman and S Ilani. *A universal critical density underlying the physics of electrons at the $LaAlO_3/SrTiO_3$ interface*. Nature Communications, vol. 3, page 1129, 2012. (Cited on pages 78, 95, 99, 100, 104, 129, 133 and 134.)

[Kalabukhov 2007] Alexey Kalabukhov, Robert Gunnarsson, Johan Börjesson, Eva Olsson, Tord Claeson and Dag Winkler. *Effect of oxygen vacancies in the $SrTiO_3$ substrate on the electrical properties of the $LaAlO_3/SrTiO_3$ interface*. Physical Review B, vol. 75, page 121404, Mar 2007. (Cited on pages 74, 75 and 80.)

[Khalsa 2013] Guru Khalsa, Byounghak Lee and A. H. MacDonald. *Theory of t_{2g} electron-gas Rashba interactions*. Physical Review B, vol. 88, page 041302, Jul 2013. (Cited on page 78.)

[Kim 2013] Younghyun Kim, Roman M. Lutchyn and Chetan Nayak. *Origin and transport signatures of spin-orbit interactions in one- and two-dimensional $SrTiO_3$-based heterostructures*. Physical Review B, vol. 87, page 245121, Jun 2013. (Cited on pages 78 and 126.)

[Klitzing 1980] K. v. Klitzing, G. Dorda and M. Pepper. *New Method for High-Accuracy Determination of the Fine-Structure Constant Based on Quantized Hall Resistance*. Physical Review Letters, vol. 45, pages 494–497, Aug 1980. (Cited on pages 4, 22 and 43.)

[Komiyama 2000] Susumu Komiyama and Yasushi Kawaguchi. *Heat instability of quantum Hall conductors*. Physical Review B, vol. 61, pages 2014–2027, Jan 2000. (Cited on page 27.)

[Kopylov 2010] Sergey Kopylov, Alexander Tzalenchuk, Sergey Kubatkin and Vladimir I Fal'ko. *Charge transfer between epitaxial graphene and silicon carbide.* Applied Physics Letters, vol. 97, no. 11, page 112109, 2010. (Cited on pages 45, 47, 49, 52 and 117.)

[Kozuka 2009] Y Kozuka, M Kim, C Bell, Bog G Kim, Y Hikita and HY Hwang. *Two-dimensional normal-state quantum oscillations in a superconducting heterostructure.* Nature, vol. 462, no. 7272, pages 487–490, 2009. (Cited on pages 72 and 75.)

[Kroto 1985] Harold W Kroto, James R Heath, Sean C O'Brien, Robert F Curl and Richard E Smalley. *C_{60}: Buckminsterfullerene.* Nature, vol. 318, no. 6042, pages 162–163, 1985. (Cited on page 38.)

[Kunc 2015] J. Kunc, B. A. Piot, D. K. Maude, M. Potemski, R. Grill, C. Betthausen, D. Weiss, V. Kolkovsky, G. Karczewski and T. Wojtowicz. *Magnetoresistance quantum oscillations in a magnetic two-dimensional electron gas.* Physical Review B, vol. 92, page 085304, Aug 2015. (Cited on page 20.)

[Lafont 2015] F Lafont, Ribeiro-Palau, R, D Kazazis, A Michon, O Couturaud, C Consejo, T Chassagne, M Zielinski, M Portail, B Jouault, F Schopfer and W Poirier. *Quantum Hall resistance standards from graphene grown by chemical vapour deposition on silicon carbide.* Nature Communications, vol. 6, page 6806, 2015. (Cited on pages 45, 52, 54, 64, 118, 119 and 122.)

[Lara-Avila 2011] Samuel Lara-Avila, Kasper Moth-Poulsen, Rositza Yakimova, Thomas Bjørnholm, Vladimir Fal'ko, Alexander Tzalenchuk and Sergey Kubatkin. *Non-Volatile Photochemical Gating of an Epitaxial Graphene/Polymer Heterostructure.* Advanced Materials, vol. 23, no. 7, pages 878–882, 2011. (Cited on pages 46, 48 and 116.)

[Lee 2008] Jaekwang Lee and Alexander A Demkov. *Charge origin and localization at the n-type $SrTiO_3/LaAlO_3$ interface.* Physical Review B, vol. 78, no. 19, page 193104, 2008. (Cited on page 77.)

[Lee 2011] Menyoung Lee, J. R. Williams, Sipei Zhang, C. Daniel Frisbie and D. Goldhaber-Gordon. *Electrolyte Gate-Controlled Kondo Effect in $SrTiO_3$.* Physical Review Letters, vol. 107, page 256601, Dec 2011. (Cited on page 82.)

[Liu 2013] Z. Q. Liu, C. J. Li, W. M. Lü, X. H. Huang, Z. Huang, S. W. Zeng, X. P. Qiu, L. S. Huang, A. Annadi, J. S. Chen, J. M. D. Coey, T. Venkatesan and Ariando. *Origin of the Two-Dimensional Electron Gas at $LaAlO_3/SrTiO_3$ Interfaces: The Role of Oxygen Vacancies and Electronic Reconstruction.* Physical Review X, vol. 3, page 021010, May 2013. (Cited on page 74.)

[Low 2012] T. Low, V. Perebeinos, J. Tersoff and Ph. Avouris. *Deformation and Scattering in Graphene over Substrate Steps.* Physical Review Letters, vol. 108, page 096601, Mar 2012. (Cited on page 59.)

[Maniv 2015] E Maniv, M Ben Shalom, A Ron, M Mograbi, A Palevski, M Goldstein and Y Dagan. *Strong correlations elucidate the electronic structure and phase diagram of $LaAlO_3/SrTiO_3$ interface.* Nature Communications, vol. 6, 2015. (Cited on pages 82, 99 and 130.)

[Mannhart 2008] J. Mannhart, D.H.A. Blank, H.Y. Hwang, A.J. Millis and J.-M. Triscone. *Two-Dimensional Electron Gases at Oxide Interfaces.* MRS Bulletin, vol. 33, no. 11, pages 1027–1034, 2008. (Cited on page 71.)

[Mannhart 2010] Jochen Mannhart and DG Schlom. *Oxide interfaces-an opportunity for electronics.* Science, vol. 327, no. 5973, pages 1607–1611, 2010. (Cited on page 71.)

[Mao 2003] Shaolin Mao, Cesar A Luongo and John R Miller. *Analysis of the NHMFL 45-T hybrid magnet thermal behavior.* Cryogenics, vol. 43, no. 3 - 5, pages 153 – 163, 2003. (Cited on page 30.)

[McCann 2006] E. McCann, K. Kechedzhi, Vladimir I. Fal'ko, H. Suzuura, T. Ando and B. L. Altshuler. *Weak-Localization Magnetoresistance and Valley Symmetry in Graphene.* Physical Review Letters, vol. 97, page 146805, Oct 2006. (Cited on page 51.)

[McClure 1956] J. W. McClure. *Diamagnetism of Graphite.* Physical Review, vol. 104, pages 666–671, Nov 1956. (Cited on pages 39 and 43.)

[McCollam 2014] A. McCollam, S. Wenderich, M. K. Kruize, V. K. Guduru, H. J. A. Molegraaf, M. Huijben, G. Koster, D. H. A. Blank, G. Rijnders, A. Brinkman, H. Hilgenkamp, U. Zeitler and J. C. Maan. *Quantum oscillations and subband properties of the two-dimensional electron gas at the $LaAlO_3/SrTiO_3$ interface.* APL Materials, vol. 2, no. 2, page 022102, 2014. (Cited on pages 72, 82, 83, 88 and 97.)

[McKeown Walker 2016] S. McKeown Walker, S. Riccò, F. Y. Bruno, A. de la Torre, A. Tamai, E. Golias, A. Varykhalov, D. Marchenko, M. Hoesch, M. S. Bahramy, P. D. C. King, J. Sánchez-Barriga and F. Baumberger. *Absence of giant spin splitting in the two-dimensional electron liquid at the surface of $SrTiO_3$ (001).* Physical Review B, vol. 93, page 245143, Jun 2016. (Cited on page 78.)

[Morozov 2006] S. V. Morozov, K. S. Novoselov, M. I. Katsnelson, F. Schedin, L. A. Ponomarenko, D. Jiang and A. K. Geim. *Strong Suppression of Weak Localization in Graphene.* Physical Review Letters, vol. 97, page 016801, Jul 2006. (Cited on page 51.)

[Morpurgo 2006] A. F. Morpurgo and F. Guinea. *Intervalley Scattering, Long-Range Disorder, and Effective Time-Reversal Symmetry Breaking in Graphene.* Physical Review Letters, vol. 97, page 196804, Nov 2006. (Cited on page 51.)

[Mott 1968] N. F. Mott. *Conduction in non-crystalline systems.* Philosophical Magazine, vol. 17, no. 150, pages 1259–1268, 1968. (Cited on page 28.)

[Mousavi 2014] Hamze Mousavi and Jabbar Khodadadi. *Flake Electrical Conductivity of Few-Layer Graphene.* Sci World J, vol. 2014, pages 1–6, 2014. (Cited on page 40.)

[Nachawaty 2017] A. Nachawaty, M. Yang, W. Desrat, S. Nanot, B. Jabakhanji, D. Kazazis, R. Yakimova, A. Cresti, W. Escoffier and B. Jouault. *Magnetic field driven ambipolar quantum Hall effect in epitaxial graphene close to the charge neutrality point.* Physical Review B, vol. 96, page 075442, Aug 2017. (Cited on page 67.)

[Nakagawa 2006] Naoyuki Nakagawa, Harold Y Hwang and David A Muller. *Why some interfaces cannot be sharp.* Nature Materials, vol. 5, pages 204–209, 2006. (Cited on pages 74 and 75.)

[Nakamura 2013] D. Nakamura, H. Sawabe, Y. H. Matsuda and S. Takeyama. *Precise measurement of a magnetic field generated by the electromagnetic flux compression technique.* Review of Scientific Instruments, vol. 84, no. 4, page 044702, 2013. (Cited on page 30.)

[Nitta 1997] Junsaku Nitta, Tatsushi Akazaki, Hideaki Takayanagi and Takatomo Enoki. *Gate Control of Spin-Orbit Interaction in an Inverted $In_{0.53}Ga_{0.47}As/In_{0.52}Al_{0.48}As$ Heterostructure.* Physical Review Letters, vol. 78, no. 7, page 1335, 1997. (Cited on page 86.)

[Norimatsu 2014] Wataru Norimatsu and Michiko Kusunoki. *Epitaxial graphene on SiC0001: advances and perspectives.* Physical Chemistry Chemical Physics, vol. 16, pages 3501–3511, 2014. (Cited on pages 47 and 116.)

[Novoselov 2004] KS Novoselov, AK Geim, SV Morozov, D Jiang, Y Zhang, SV Dubonos, IV Grigorieva and AA Firsov. *Electric Field Effect in Atomically Thin Carbon Films.* Science, vol. 306, no. 5696, pages 666–669, 2004. (Cited on page 38.)

[Novoselov 2005] KS Novoselov, AK Geim, SV Morozov, D Jiang, MI Katsnelson, IV Grigorieva, SV Dubonos and AA Firsov. *Two-dimensional gas of massless Dirac fermions in graphene.* Nature, vol. 438, no. 7065, pages 197–200, 2005. (Cited on pages 43, 44 and 57.)

[Novoselov 2007] Konstantin S Novoselov, Z Jiang, Y Zhang, SV Morozov, Horst L Stormer, U Zeitler, JC Maan, GS Boebinger, Philip Kim and Andre K

Geim. *Room-temperature quantum Hall effect in graphene.* Science, vol. 315, no. 5817, pages 1379–1379, 2007. (Cited on pages 38 and 43.)

[Ohtomo 2004] A Ohtomo and HY Hwang. *A high-mobility electron gas at the $LaAlO_3/SrTiO_3$ heterointerface.* Nature, vol. 427, pages 423–426, 2004. (Cited on pages 71, 72, 73, 79, 123 and 124.)

[Pallecchi 2014] E Pallecchi, F Lafont, V Cavaliere, F Schopfer, D Mailly, W Poirier and A Ouerghi. *High Electron Mobility in Epitaxial Graphene on 4H-SiC (0001) via post-growth annealing under hydrogen.* Scientific Reports, vol. 4, 2014. (Cited on page 52.)

[Panchal 2016] Vishal Panchal, Cristina E Giusca, Arseniy Lartsev, Nicholas A Martin, Nathan Cassidy, Rachael L Myers-Ward, D Kurt Gaskill and Olga Kazakova. *Atmospheric doping effects in epitaxial graphene: correlation of local and global electrical studies.* 2D Materials, vol. 3, no. 1, page 015006, 2016. (Cited on page 59.)

[Pentcheva 2010] Rossitza Pentcheva, Mark Huijben, Katrin Otte, Warren E Pickett, JE Kleibeuker, J Huijben, H Boschker, D Kockmann, W Siemons, Gertjan Koster*et al. Parallel electron-hole bilayer conductivity from electronic interface reconstruction.* Physical Review Letters, vol. 104, no. 16, page 166804, 2010. (Cited on page 72.)

[Petrović 2014] Alexander Paul Petrović, A Paré, Tula R Paudel, K Lee, S Holmes, Crispin HW Barnes, A David, T Wu, Evgeny Y Tsymbal and C Panagopoulos. *Long-range electronic reconstruction to a $d_{xz,yz}$-dominated Fermi surface below the $LaAlO_3/SrTiO_3$ interface.* Scientific Reports, vol. 4, 2014. (Cited on page 91.)

[Polyakov 1994] D. G. Polyakov and B. I. Shklovskii. *Activated Conductivity in the Quantum Hall Effect.* Physical Review Letters, vol. 73, pages 1150–1153, Aug 1994. (Cited on page 28.)

[Popović 2008] Zoran S Popović, Sashi Satpathy and Richard M Martin. *Origin of the two-dimensional electron gas carrier density at the $LaAlO_3/SrTiO_3$ interface.* Physical Review Letters, vol. 101, no. 25, page 256801, 2008. (Cited on pages 73, 77 and 124.)

[Portugall 1999] O Portugall, N Puhlmann, H U Müller, M Barczewski, I Stolpe and M von Ortenberg. *Megagauss magnetic field generation in single-turn coils: new frontiers for scientific experiments.* Journal of Physics D: Applied Physics, vol. 32, no. 18, page 2354, 1999. (Cited on page 30.)

[Poumirol 2010] Jean-Marie Poumirol, Walter Escoffier, Amit Kumar, Bertrand Raquet and Michel Goiran. *Impact of disorder on the $\nu = 2$ quantum Hall plateau in graphene.* Physical Review B, vol. 82, page 121401, Sep 2010. (Cited on pages 38 and 67.)

[Reich 2002] S. Reich, J. Maultzsch, C. Thomsen and P. Ordejón. *Tight-binding description of graphene.* Physical Review B, vol. 66, page 035412, Jul 2002. (Cited on page 41.)

[Reyren 2007] N. Reyren, S. Thiel, A. D. Caviglia, L. Fitting Kourkoutis, G. Hammerl, C. Richter, C. W. Schneider, T. Kopp, A.-S. Rüetschi, D. Jaccard, M. Gabay, D. A. Muller, J.-M. Triscone and J. Mannhart. *Superconducting Interfaces Between Insulating Oxides.* Science, vol. 317, no. 5842, pages 1196–1199, 2007. (Cited on page 72.)

[Ribeiro-Palau 2015] R. Ribeiro-Palau, F. Lafont, J. Brun-Picard, D. Kazazis, A. Michon, F. Cheynis, O. Couturaud, C. Consejo, B. Jouault and Wilfrid Poirier. *Quantum Hall resistance standard in graphene devices under relaxed experimental conditions.* Nature Nanotechnology, vol. 10, no. 11, page 965, 2015. (Cited on pages 45 and 116.)

[Rijnders 1997] Guus JHM Rijnders, Gertjan Koster, Dave HA Blank and Horst Rogalla. *In situ monitoring during pulsed laser deposition of complex oxides using reflection high energy electron diffraction under high oxygen pressure.* Applied physics Letters, vol. 70, no. 14, pages 1888–1890, 1997. (Cited on page 79.)

[Rosenbaum 1991] Ralph Rosenbaum. *Crossover from Mott to Efros-Shklovskii variable-range-hopping conductivity in In_xO_y films.* Physical Review B, vol. 44, pages 3599–3603, Aug 1991. (Cited on page 28.)

[Salluzzo 2009] M. Salluzzo, J. C. Cezar, N. B. Brookes, V. Bisogni, G. M. De Luca, C. Richter, S. Thiel, J. Mannhart, M. Huijben, A. Brinkman, G. Rijnders and G. Ghiringhelli. *Orbital Reconstruction and the Two-Dimensional Electron Gas at the $LaAlO_3/SrTiO_3$ Interface.* Physical Review Letters, vol. 102, page 166804, Apr 2009. (Cited on page 77.)

[Sbrockey 2012] Nick M Sbrockey, Michael Luong, Eric M Gallo, Jennifer D Sloppy, Guannan Chen, Christopher R Winkler, Stephanie H Johnson, Mitra L Taheri, Gary S Tompa and Jonathan E Spanier. *$LaAlO_3/SrTiO_3$ epitaxial heterostructures by atomic layer deposition.* Journal of Electronic Materials, vol. 41, no. 5, pages 819–823, 2012. (Cited on page 79.)

[Schooley 1965] J. F. Schooley, W. R. Hosler, E. Ambler, J. H. Becker, Marvin L. Cohen and C. S. Koonce. *Dependence of the Superconducting Transition Temperature on Carrier Concentration in Semiconducting $SrTiO_3$.* Physical Review Letters, vol. 14, pages 305–307, Mar 1965. (Cited on page 74.)

[Schumann 2012] T. Schumann, K.-J. Friedland, M. H. Oliveira, A. Tahraoui, J. M. J. Lopes and H. Riechert. *Anisotropic quantum Hall effect in epitaxial graphene on stepped SiC surfaces.* Physical Review B, vol. 85, page 235402, Jun 2012. (Cited on page 52.)

[Segal 2009] Y. Segal, J. H. Ngai, J. W. Reiner, F. J. Walker and C. H. Ahn. *X-ray photoemission studies of the metal-insulator transition in $LaAlO_3/SrTiO_3$ structures grown by molecular beam epitaxy.* Physical Review B, vol. 80, page 241107, Dec 2009. (Cited on page 79.)

[Shalom 2010] M. Ben Shalom, M. Sachs, D. Rakhmilevitch, A. Palevski and Y. Dagan. *Tuning Spin-Orbit Coupling and Superconductivity at the $SrTiO_3/LaAlO_3$ Interface: A Magnetotransport Study.* Physical Review Letters, vol. 104, no. 12, 2010. (Cited on page 78.)

[Shankar 2012] Ramamurti Shankar. Principles of quantum mechanics. Springer Science & Business Media, 2012. (Cited on page 17.)

[Shen 2009] T Shen, JJ Gu, M Xu, YQ Wu, ML Bolen, MA Capano, LW Engel and PD Ye. *Observation of quantum-Hall effect in gated epitaxial graphene grown on SiC (0001).* Applied Physics Letters, vol. 95, no. 17, page 172105, 2009. (Cited on page 45.)

[Shklovskii 1984] Boris I Shklovskii and Alex L Efros. Electronic properties of doped semiconductors. Springer, 1984. (Cited on pages 28, 53 and 118.)

[Siemons 2007] Wolter Siemons, Gertjan Koster, Hideki Yamamoto, Walter A. Harrison, Gerald Lucovsky, Theodore H. Geballe, Dave H. A. Blank and Malcolm R. Beasley. *Origin of Charge Density at $LaAlO_3$ on $SrTiO_3$ Heterointerfaces: Possibility of Intrinsic Doping.* Physical Review Letters, vol. 98, page 196802, May 2007. (Cited on page 74.)

[Sims 2008] J. R. Sims, D. G. Rickel, C. A. Swenson, J. B. Schillig, G. W. Ellis and C. N. Ammerman. *Assembly, Commissioning and Operation of the NHMFL 100 Tesla Multi-Pulse Magnet System.* IEEE Transactions on Applied Superconductivity, vol. 18, no. 2, pages 587–591, June 2008. (Cited on page 30.)

[Störmer 1979] HL Störmer, R Dingle, AC Gossard, W Wiegmann and MD Sturge. *Two-dimensional electron gas at a semiconductor-semiconductor interface.* Solid State Communications, vol. 29, no. 10, pages 705–709, 1979. (Cited on page 4.)

[Stornaiuolo 2015] D. Stornaiuolo, C. Cantoni, G. M. De Luca, R. Di Capua, E. Di. Gennaro, G. Ghiringhelli, B. Jouault, D. Marrè, D. Massarotti, F. Miletto Granozio, I. Pallecchi, C. Piamonteze, S. Rusponi, F. Tafuri and M. Salluzzo. *Tunable spin polarization and superconductivity in engineered oxide interfaces.* Nature Materials, 2015. (Cited on page 72.)

[Thiel 2006] Stefan Thiel, German Hammerl, A Schmehl, CW Schneider and Jochen Mannhart. *Tunable quasi-two-dimensional electron gases in oxide heterostructures.* Science, vol. 313, no. 5795, pages 1942–1945, 2006. (Cited on pages 72 and 74.)

[Tian 2011] HF Tian, YG Zhao, XL Jiang, JP Shi, HJ Zhang and JR Sun. *Resistance switching effect in $LaAlO_3$/Nb-doped $SrTiO_3$ heterostructure.* Applied Physics A, vol. 102, no. 4, pages 939–942, 2011. (Cited on page 94.)

[Tsui 1982] D. C. Tsui, H. L. Stormer and A. C. Gossard. *Two-Dimensional Magnetotransport in the Extreme Quantum Limit.* Physical Review Letters, vol. 48, pages 1559–1562, May 1982. (Cited on pages 4 and 23.)

[Tzalenchuk 2010] Alexander Tzalenchuk, Samuel Lara-Avila, Alexei Kalaboukhov, Sara Paolillo, Mikael Syväjärvi, Rositza Yakimova, Olga Kazakova, TJBM Janssen, Vladimir Fal'Ko and Sergey Kubatkin. *Towards a quantum resistance standard based on epitaxial graphene.* Nature Nanotechnology, vol. 5, no. 3, pages 186–189, 2010. (Cited on pages 38, 45 and 115.)

[Tzalenchuk 2011] Alexander Tzalenchuk, Samuel Lara-Avila, Karin Cedergren, Mikael Syväjärvi, Rositza Yakimova, Olga Kazakova, TJBM Janssen, Kasper Moth-Poulsen, Thomas Bjørnholm, Sergey Vladimir FalâĂŹko Kopylov and Sergey Kubatkin. *Engineering and metrology of epitaxial graphene.* Solid State Communications, vol. 151, no. 16, pages 1094–1099, 2011. (Cited on pages 46 and 116.)

[Usher 2009] Alan Usher and Martin Elliott. *Magnetometry of low-dimensional electron and hole systems.* Journal of Physics: Condensed Matter, vol. 21, no. 10, page 103202, 2009. (Cited on page 19.)

[Van Benthem 2001] K Van Benthem, C Elsässer and RH French. *Bulk electronic structure of $SrTiO_3$: experiment and theory.* Journal of Applied Physics, vol. 90, no. 12, pages 6156–6164, 2001. (Cited on page 73.)

[Wallace 1947] P. R. Wallace. *The Band Theory of Graphite.* Physical Review, vol. 71, pages 622–634, May 1947. (Cited on pages 38, 39 and 114.)

[Willmott 2007] P. R. Willmott, S. A. Pauli, R. Herger, C. M. Schlepütz, D. Martoccia, B. D. Patterson, B. Delley, R. Clarke, D. Kumah, C. Cionca and Y. Yacoby. *Structural Basis for the Conducting Interface between $LaAlO_3$ and $SrTiO_3$.* Physical Review Letters, vol. 99, page 155502, Oct 2007. (Cited on page 75.)

[Wilson 2006] Mark Wilson. *Electrons in atomically thin carbon sheets behave like massless particles.* Physics Today, vol. 59, no. 1, pages 21–23, 2006. (Cited on pages 41 and 115.)

[Woszczyna 2012] Mirosław Woszczyna, Miriam Friedemann, Martin Götz, Eckart Pesel, Klaus Pierz, Thomas Weimann and Franz J Ahlers. *Precision quantization of Hall resistance in transferred graphene.* Applied Physics Letters, vol. 100, no. 16, page 164106, 2012. (Cited on page 45.)

[Wu 2007] Xiaosong Wu, Xuebin Li, Zhimin Song, Claire Berger and Walt A. de Heer. *Weak Antilocalization in Epitaxial Graphene: Evidence for Chiral Electrons.* Physical Review Letters, vol. 98, page 136801, Mar 2007. (Cited on page 51.)

[Wu 2009] Xiaosong Wu, Yike Hu, Ming Ruan, Nerasoa K Madiomanana, John Hankinson, Mike Sprinkle, Claire Berger and Walt A De Heer. *Half integer quantum Hall effect in high mobility single layer epitaxial graphene.* Applied Physics Letters, vol. 95, no. 22, page 223108, 2009. (Cited on page 45.)

[Xie 2014] Yanwu Xie, Christopher Bell, Minu Kim, Hisashi Inoue, Yasuyuki Hikita and Harold Y Hwang. *Quantum longitudinal and Hall transport at the $LaAlO_3/SrTiO_3$ interface at low electron densities.* Solid State Communications, vol. 197, pages 25–29, 2014. (Cited on pages 88 and 97.)

[Yang 2016a] M. Yang, O. Couturaud, W. Desrat, C. Consejo, D. Kazazis, R. Yakimova, M. Syväjärvi, M. Goiran, J. Béard, P. Frings, M. Pierre, A. Cresti, W. Escoffier and B. Jouault. *Puddle-Induced Resistance Oscillations in the Breakdown of the Graphene Quantum Hall Effect.* Physical Review Letters, vol. 117, page 237702, Dec 2016. (Cited on page 48.)

[Yang 2016b] Ming Yang, Kun Han, Olivier Torresin, Mathieu Pierre, Shengwei Zeng, Zhen Huang, T. V. Venkatesan, Michel Goiran, J. M. D. Coey, Ariando and Walter Escoffier. *High field magneto-transport in two-dimensional electron gas $LaAlO_3/SrTiO_3$.* Applied Physics Letters, vol. 109, no. 12, page 122106, 2016. (Cited on page 81.)

[Young 2012] AF Young, CR Dean, L Wang, H Ren, P Cadden-zimansky, K Watanabe, T Taniguchi, J Hone, KL Shepard and P Kim. *Spin and valley quantum Hall ferromagnetism in graphene.* Nature Physics, vol. 8, no. 7, page 550, 2012. (Cited on page 43.)

[Zeng 2016] Shengwei Zeng, Weiming Lü, Zhen Huang, Zhiqi Liu, Kun Han, Kalon Gopinadhan, Changjian Li, Rui Guo, Wenxiong Zhou, Haijiao Harsan Ma*et al. Liquid-Gated High Mobility and Quantum Oscillation of the Two-Dimensional Electron Gas at an Oxide Interface.* ACS Nano, vol. 10, no. 4, pages 4532–4537, 2016. (Cited on pages 72, 88, 97 and 128.)

[Zhang 2005] Yuanbo Zhang, Yan-Wen Tan, Horst L Stormer and Philip Kim. *Experimental observation of the quantum Hall effect and Berry's phase in graphene.* Nature, vol. 438, no. 7065, pages 201–204, 2005. (Cited on pages 38, 43, 44 and 57.)

[Zhang 2006] Y. Zhang, Z. Jiang, J. P. Small, M. S. Purewal, Y.-W. Tan, M. Fazlollahi, J. D. Chudow, J. A. Jaszczak, H. L. Stormer and P. Kim. *Landau-Level Splitting in Graphene in High Magnetic Fields.* Physical Review Letters, vol. 96, page 136806, Apr 2006. (Cited on pages 43, 44 and 115.)

[Zhong 2013] Zhicheng Zhong, Anna Tóth and Karsten Held. *Theory of spin-orbit coupling at $LaAlO_3/SrTiO_3$ interfaces and $SrTiO_3$ surfaces.* Physical Review B, vol. 87, page 161102, Apr 2013. (Cited on pages 78 and 79.)

Author: Ming YANG

Title: High magnetic field studies of 2DEG in graphene on silicon carbide and at the $LaAlO_3/SrTiO_3$ interface

Supervisors: Michel GOIRAN and Mathieu PIERRE

Specialty: Nanophysics

Laboratory: Laboratoire National des Champs Magnétiques Intenses (LNCMI-T), CNRS-UPR 3228, 143 avenue de Rangueil, 31400, Toulouse, France

Abstract:

This thesis is devoted to the study of the magneto-transport properties of two dimensional electron gas (2DEG), and more specifically graphene on silicon carbide (G/SiC) as well as the interface between two complex oxides $LaAlO_3$ / $SrTiO_3$ (LAO/STO). We take advantage of very high magnetic field (up to 80 T) and very low temperature (down to 40 mK) to investigate the quantum transport properties, which are evocative of the underlying electronic band-structure.

In G/SiC, close to the quantum Hall breakdown regime, we measure an ultra-broad quantum Hall plateau at $R=h/2e^2$ covering a magnetic field range of more than 70 T (from 7 T to 80 T). Accordingly, the longitudinal resistance is close to zero, but displays unexpected weak 1/B-periodic oscillations. Based on microscopic observations, this 2DEG is modeled as a low charge carrier density graphene matrix decorated by micrometers-size puddles with larger doping. Numerical simulations of the transport properties reproduce well both the broad Quantum Hall plateau and the presence of the oscillations. Besides the SiC substrate which acts as a charge reservoir and stabilizes the quantum Hall state at filling factor $\nu=2$, a magnetic field dependent transfer of charges involving the puddles is responsible for the presence of the oscillating features. This original study provides new insights for resistance metrology purposes.

The 2DEG arising at the interface between the complex oxides LAO and STO is nowadays envisioned for future multi-functional devices. Their electronic properties are still a matter of debate and require further investigations. The high field magneto-resistance of this 2DEG displays quasi-periodic Shubnikov-de Haas Oscillations (SdHO) and a linear Hall effect up to 55 T at low temperature. We observe a large discrepancy between the carrier density extracted from the period of the SdHO and the slope of the Hall resistance, which constitutes a strong evidence for the presence of many sub-bands crossing the Fermi energy. The quasi-periodic oscillations of the magneto-resistance are well reproduced by numerical simulations taking into account the strong Rashba effect at the interface. In addition, from the back-gate voltage evolution of the SdHO at sub-kelvin temperature, we identify the electronic sub-bands contributing to transport, the orbital symmetry from which they derive, as well as their spatial localization along the interface.

Keywords: 2DEG, high magnetic field, low temperature, magnetotransport, Quantum Hall effect, Shubnikov-de Haas oscillations, band structure.

Auteur : Ming YANG
Titre : Étude des gaz d'électrons bidimensionnels sous champ magnétique intense dans du graphène sur SiC et à l'interface entre les oxydes complexes $LaAlO_3$ et $SrTiO_3$
Directeurs de thèse : Michel GOIRAN et Mathieu PIERRE

Spécialité : Nanophysique

Laboratoire : Laboratoire National des Champs Magnétiques Intenses (LNCMI-T), CNRS-UPR 3228, 143 avenue de Rangueil, 31400, Toulouse, France

Abstract:
Cette thèse est dédiée à l'étude des propriétés de magnéto-transport des gaz d'électrons bidimensionnel, et plus spécifiquement du graphène sur carbure de silicium (G/SiC) ainsi qu'à l'interface entre les oxydes complexes $LaAlO_3$ (LAO) et $SrTiO_3$ (STO). Nous exploitons la génération d'un champ magnétique intense (jusqu'à 80 T) et les très basses températures (jusqu'à 40 mK) pour étudier les propriétés de transport quantique, qui sont évocatrices de la structure de bandes électroniques sous-jacente.

Dans G/SiC, à la limite du régime d'effet Hall quantique, nous mesurons un plateau de Hall ultra-large quantifié à $R=h/2e^2$ couvrant un champ magnétique de plus de 70 T (de 7 T à 80 T). La résistance longitudinale est proche de zéro mais présente, de manière inattendue, de faibles oscillations périodiques avec l'inverse du champ magnétique. Sur la base d'observations microscopiques, ce gaz d'électrons 2D est modélisé par une matrice de graphène ayant une densité de porteurs de charge faible, parsemée d'ilots de taille micrométrique ayant un dopage plus important. Les simulations numériques des propriétés de transport reproduisent bien le plateau de Hall et la présence des oscillations. Au-delà du substrat de SiC qui agit comme un réservoir de charge et stabilise le facteur de remplissage à $\nu=2$, un transfert de charge dépendant du champ magnétique entre les ilots chargés est responsable de la présence des oscillations de la magnétorésistance. Cette étude originale fournit de nouvelles perspectives pour des applications en métrologie.

Les propriétés remarquables des gaz d'électrons 2D à l'interface entre les oxydes complexes LAO et STO sont aujourd'hui envisagées pour le développement de futurs dispositifs multifonctionnels. Toutefois, leurs propriétés électroniques sont encore mal connues et nécessitent des recherches plus approfondies. Dans ces systèmes, la magnétorésistance montre des oscillations de Shubnikov-de Haas (SdH) quasi-périodiques et un effet Hall linéaire jusqu'à 55 T à basse température. Nous observons une différence d'un ordre de grandeur entre la densité de porteurs extraite de la période des oscillations SdH et la pente de la résistance de Hall, impliquant la présence de nombreuses sous-bandes à l'énergie de Fermi. Les oscillations quasi-périodiques de la magnétorésistance sont bien reproduites par des simulations numériques prenant en compte l'effet Rashba à l'interface. De plus, à partir de l'évolution des oscillations SdH avec la tension de grille à très basse température (40mK), nous identifions les sous-bandes électroniques contribuant au transport, les orbitales atomiques dont elles dérivent, ainsi que leur localisation spatiale dans la profondeur de l'interface.

Mots-clefs : gaz d'électrons bidimensionnels, champ magnétique intense, basse température, magnéto-transport, Effet Hall Quantique, Oscillations de Shubnikov-de Haas, structure de bande.